University of Cyprus

DEPARTMENT OF CIVIL AND ENVIRONMENTAL ENGINEERING

THE MECHANICS OF ARTERIAL SUTURING

DOCTOR OF PHILOSOPHY DISSERTATION

HARALAMBIA P. CHARALAMBOUS

2015

University of Cyprus

DEPARTMENT OF CIVIL AND ENVIRONMENTAL ENGINEERING

THE MECHANICS OF ARTERIAL SUTURING

HARALAMBIA P. CHARALAMBOUS

A Dissertation Submitted to the University of Cyprus in Partial Fulfillment of the Requirements for the Degree of Doctor of Philosophy

May 2015

Validation Page

Doctoral Candidate: Haralambia P. Charalambous

Doctoral Thesis Title: The mechanics of arterial suturing

The present Doctoral Dissertation was submitted in partial fulfillment of the requirements for the Degree of Doctor of Philosophy at the ***Department of Civil and Environmental Engineering*** *and was approved on the 8th of May,2015 by the members of the* ***Examination Committee.***

Examination Committee:

Research Supervisor: ΠΡΟΣΩΠΙΚΑ ΔΕΔΟΜΕΝΑ

Dr. Panayiotis Roussis, *Assistant Professor, Department of Civil and Environmental Engineering, University of Cyprus*

Committee Member: ΠΡΟΣΩΠΙΚΑ ΔΕΔΟΜΕΝΑ

Dr. Panos Papanastasiou, *Professor, Department of Civil and Environmental Engineering, University of Cyprus*

Committee Member: ΠΡΟΣΩΠΙΚΑ ΔΕΔΟΜΕΝΑ

Dr. Dimitrios Loukidis, *Assistant Professor, Department of Civil and Environmental Engineering, University of Cyprus*

Committee Member: ΠΡΟΣΩΠΙΚΑ ΔΕΔΟΜΕΝΑ

Dr. Antonios Giannakopoulos, *Professor, Department of Civil Engineering, University of Thessaly*

Committee Member: ΠΡΟΣΩΠΙΚΑ ΔΕΔΟΜΕΝΑ

Dr. Athanasios Giannoukas, *Professor, Faculty of Medicine, University of Thessaly*

Declaration of Doctoral Candidate

The present doctoral dissertation was submitted in partial fulfillment of the requirements for the degree of Doctor of Philosophy of the University of Cyprus. It is a product of original work of my own, unless otherwise mentioned through references, notes, or any other statements.

Haralambia P. Charalambous

.... **ΠΡΟΣΩΠΙΚΑ ΔΕΔΟΜΕΝΑ** .....

Περίληψη

Οι αγγειοχειρουργικές επεμβάσεις δύνανται να παρουσιάσουν βραχυπρόθεσμες (αμέσως μετά την αποκατάσταση της ροής τού αίματος) και μακροπρόθεσμες (βδομάδες μετά την επέμβαση) επιπλοκές, που σχετίζονται με τη συρραφή ανθρώπινων αρτηριών μεταξύ τους ή με μοσχεύματα. Κατά συνέπεια, η τεχνική τής συρραφής και τα υλικά που χρησιμοποιούνται στην αγγειοχειρουργική είναι υψίστης σημασίας για τη θεραπεία των αγγειακών παθήσεων, όπως η αθηροσκλήρωση και τα ανευρύσματα.

Η διατριβή αυτή επικεντρώνεται στη μαθηματική μοντελοποίηση αρτηριακών αναστομώσεων και στην απόκριση της γραμμής συρραφής τους, ένα διεπιστημονικό θέμα της δομοστατικής και βιοϊατρικής μηχανικής. Η μαθηματική διατύπωση του προβλήματος γίνεται στη βάση δυναμικής ανάλυσης, αλληλεπίδρασης του ράμματος με την αρτηρία και χρήσης διαφόρων καταστατικών νόμων. Σκοπός τής διατριβής είναι η διερεύνηση της απόκρισης διαφορετικών τεχνικών αρτηριακών αναστομώσεων (κατά τρόπο γενικεύσιμο), η εξαγωγή λύσεων κλειστής μορφής (όπου είναι δυνατόν), και η εξαγωγή χρήσιμων συμπερασμάτων όσον αφορά τα βέλτιστα χαρακτηριστικά της συρραφής και του μοσχεύματος για την αποφυγή μετεγχειρητικών επιπλοκών.

Η απόκριση μακριά από την περιοχή της αναστόμωσης μελετάται θεωρώντας γραμμική, υπερελαστική και βισκοελαστική συμπεριφορά τού αρτηριακού ιστού. Η απόκριση της γραμμής συρραφής, για τις διαφορετικές τεχνικές αναστόμωσης, διερευνάται μέσω: (α) ενός μοντέλου που περιγράφει τη δυναμική απόκριση της τελικο-τελικής τεχνικής αναστόμωσης, (β) ενός μοντέλου που περιγράφει την απόκριση της τελικο-πλάγιας τεχνικής αναστόμωσης, και (γ) ενός εξιδανικευμένου κυλινδρικού μοντέλου αναστόμωσης με δύο αρθρώσεις, ώστε να διερευνηθεί η επίδραση της ελαστικής μη-συμβατότητας στην απόκριση αναστομώσεων που σχετίζονται με πλαγιο-πλάγια αναστόμωση, και εμβαλώματος σε αρτηρία. Επιπλέον, καθορίζονται κριτήρια αστοχίας που λαμβάνουν υπόψη βραχυπρόθεσμα και μακροπρόθεσμα σενάρια αστοχίας.

Η απόκριση στην περιοχή και μακριά από την περιοχή της γραμμής συρραφής υπολογίζεται σε όρους κύριων μετατοπίσεων, τάσεων, και/ή πυκνότητας ενέργειας-παραμόρφωσης. Τα αποτελέσματα συγκρίνονται με πειραματικές και αριθμητικές μελέτες διαθέσιμες στη βιβλιογραφία, ώστε να αξιολογηθεί το επίπεδο προσέγγισης των προτεινόμενων αναλυτικών μοντέλων.

Μεγάλος αριθμός ραμμάτων, αυξημένο πάχος ράμματος/χειρουργικού κλιπ, και μέτρο ελαστικότητας του μοσχεύματος ίσο με εκείνο της αρτηρίας, είναι μερικές από τις βασικές

παραμέτρους που αποδείχθηκε ότι μειώνουν την απόκριση της γραμμής συρραφής. Άλλοι παράγοντες που μειώνουν την απόκριση της γραμμής συρραφής είναι σχετικά μικρές τιμές της γωνίας ένωσης μεταξύ της αρτηρίας και του μοσχεύματος (τελικο-πλάγια αναστόμωση), ακτίνα μοσχεύματος μικρότερη από την ακτίνα της αρτηρίας (τελικο-πλάγια αναστόμωση), χρήση επιθεμάτων με μικρό πλάτος (εμβάλωμα σε αρτηρία), κ.λπ. Επιπλέον, μέσα από τα μοντέλα που αναπτύχθηκαν, ο ακριβής μηχανισμός με τον οποίο κάθε παράμετρος επηρεάζει την απόκριση του συστήματος γίνεται κατανοητός.

Η κύρια επιστημονική συνεισφορά της διατριβής αυτής έγκειται στην ανάπτυξη βασικών αναλυτικών μοντέλων που οδηγούν στην πρόβλεψη της συμπεριφοράς αρτηριακών αναστομώσεων στην περιοχή και μακριά από την περιοχή της συρραφής. Η αναλυτική διατύπωση αποκαλύπτει χρήσιμες αλληλεξαρτήσεις μεταξύ των παραμέτρων του προβλήματος, καθιστώντας έτσι το προτεινόμενο μοντέλο ένα πολύτιμο εργαλείο για τη βέλτιστη επιλογή των υλικών και τη βελτιωμένη λειτουργία των ραμμάτων. Δυνάμει της γενικότητας και της αμεσότητας της εφαρμογής τους, τα ευρήματα της διατριβής μπορεί να αποτελέσουν τη βάση για την ανάπτυξη κατευθυντήριων γραμμών που σχετίζονται με την πρόληψη μετεγχειρητικών επιπλοκών σε αρτηριακές αναστομώσεις.

Abstract

Vascular surgeries potentially suffer from short-term (immediately after the blood flow is restored) and long-term (weeks after the operation) post-surgery complications, related to the stitching of human arteries with themselves or with grafts. Accordingly, stitching techniques and related suture materials are of utmost importance in the surgical treatment of vascular disorders, such as atherosclerosis and aneurysms.

This dissertation focuses on the mathematical modeling of arterial anastomoses and their suture-line response, an interdisciplinary topic in structural and biomedical engineering. The mathematical formulation of the problem is carried out on the basis of dynamic analysis, suture-artery interaction, and different material constitutive laws. The aim of this research is to investigate the response of different arterial anastomosis techniques in a general manner, develop closed-form expressions for the problem solution (wherever possible), and provide useful conclusions about the optimum suturing details and graft properties to prevent post-surgery complications.

The far-field arterial response is studied by considering linear, hyperelastic, and viscoelastic material behavior. The suture-line response for different anastomosis techniques is investigated through: (a) a model governing the dynamic response of the end-to-end anastomosis technique; (b) a model describing the response of the end-to-side anastomosis technique; and (c) an idealized two-hinged anastomosis model, aiming to investigate the effect of elastic mismatch on the response of side-to-side related anastomoses and arterial patching. In addition, comprehensive failure criteria that account for short- and long-term failure scenarios are established.

The suture-line and far-field response is calculated in terms of principal displacements, stresses, and/or strain-energy density. Results are compared with experimental and numerical studies available in the literature to evaluate the level of approximation of the developed analytical models.

High number of utilized stitches, increased suture/clip thickness, and graft elasticity modulus equal to that of the host artery, are some of the key parameters found to reduce the suture-line response of arterial anastomoses. Other factors that reduce the suture-line response are low values of the intersecting angle between the artery and the graft (end-to-side anastomosis), graft radius smaller than the artery radius (end-to-side anastomosis), use of patches with small width (artery patching), etc. Moreover, the exact mechanism by which each problem parameter affects the system response is revealed.

The main contribution of this thesis lies in the development of fundamental analytical models to predict the far-field and suture-line behavior of arterial anastomoses. The analytical formulation reveals useful interrelations among the problem parameters, thus making the proposed model a valuable tool for the optimal selection of materials and improved functionality of the sutures. By virtue of their generality and directness of application, the findings of this study can ultimately form the basis for the development of vascular anastomosis guidelines pertaining to the prevention of post-surgery complications.

Acknowledgements

I wish to express my gratitude to the following people for their valued support throughout this project. To my supervisor, Dr. Panayiotis Roussis, Assistant Professor at the Department of Civil and Environmental Engineering at the University of Cyprus, for his help, guidance, constructive suggestions and encouragement during these years. Deepest gratefulness is also due to the member of the examining committee, Dr. Antonios Giannakopoulos, Professor at the Department of Civil Engineering at the University of Thessaly, for his valuable support especially when I attended the University of Thessaly in spring semester 2014. Special thanks to Dr. Panos Tsopelas for his help and for offering me a workplace during my attendance at the University of Thessaly, when he was a Professor at the Department of Civil Engineering at the University of Thessaly.

Sincere gratitude is owed to the member of the examining committee, Dr. Athanasios Giannoukas, Professor at the Faculty of Medicine at the University of Thessaly, for the useful discussions on my work. In addition, my warmest thanks to Dr. Georgios Georghiou, of the Cardiothoracic Surgery Department of American Medical Center (Nicosia, Cyprus), for the constructive suggestions and feedback.

Lastly, I want to express my appreciation to my family and friends for their understanding and valuable support.

To my parents Pantelis and Angela,

and my sisters Xanthi, Georgia, and Irene

Table of Contents

List of Figures

List of Tables

List of Symbols

A	-	Elastic mismatch parameter
A_i	-	Cross sectional area of blood vessel lumen of cross-section i ($i = 1,\ 2,\ 3$)
A_L	-	Cross sectional area of artery
A_{res}	-	Residual value to satisfy equilibrium
A_s	-	Cross sectional area of suture
A^i	-	Cross sectional area of element i of the two-hinged anastomosis model ($i = \mathrm{I}, \mathrm{II}$)
a	-	Stress-like material parameter of Hariton strain-energy function
$\mathbf{B}$	-	Left Cauchy-Green strain matrix
B	-	Stress-like material parameter of Skalak et al. strain-energy function
B_1, B_2, B_3	-	Constants
B^i	-	Parameter of element i of the two-hinged anastomosis model ($i = \mathrm{I}, \mathrm{II}$)
b	-	Stress-like material parameter of Hariton strain-energy function
b_x	-	Width of pin-loaded plate
b_w	-	Wave number
$\mathbf{C}$	-	Right Cauchy-Green strain matrix
C	-	Stress-like material parameter of Skalak et al. strain-energy function
C_i	-	Coefficients of the parametric equations of Shao et al.
C_{n_f}, C_{m_f}	-	Frequency coefficient
C^i	-	Parameter of element i of the two-hinged anastomosis model ($i = \mathrm{I}, \mathrm{II}$)
D_d	-	Blood vessel diameter under diastolic pressure
D_s	-	Blood vessel diameter under systolic pressure
$D_1^{\mathrm{II}}, D_2^{\mathrm{II}}$	-	Parameters of artery patch model

d_1, d_2, d_3 - Stress-like material parameters of Holzapfel and Gasser strain-energy function

d_4 - Dimensionless material parameter of Holzapfel and Gasser strain-energy function

d_{rbc} - Red blood cell diameter

d_r - Thickness/diameter of rigid stitch/clip

d_s - Suture diameter of continuous stitching

E_θ - Young's modulus in the circumferential direction

$E_{\theta a}$ - Young's modulus of arterial segment in the circumferential direction

$E_{\theta g}$ - Young's modulus of graft segment in the circumferential direction

E_θ^0 - Initial tangent Young's modulus in the circumferential direction

E_a - Young's modulus of host artery (isotropic)

E_g - Young's modulus of graft (isotropic)

E_L - Young's modulus in the longitudinal direction

E_{La} - Young's modulus of arterial segment in the longitudinal direction

E_{Lg} - Young's modulus of graft segment in the longitudinal direction

E_x - Young's modulus in the direction of *x*-axis

E_y - Young's modulus in the direction of *y*-axis

E_K - Kinetic energy density

E_t - Total energy density

E_s - Young's modulus of the suture

E^i - Young's modulus of element i of the two-hinged anastomosis model ($i = \mathrm{I}, \mathrm{II}$)

e - Green strain matrix

e - Distance from the center of the hole to the edge of the pin-loaded plate

$e_{\theta\theta}$ - Circumferential Green strain tensor

e_{zz} - Longitudinal Green strain tensor

$\mathbf{F}$ - Deformation gradient matrix

F_L - Tensile force of isocompliant arterial segments, in the longitudinal direction

F_{La} - Tensile force of arterial segment, in the longitudinal direction

F_{Lg} - Tensile force of graft segment, in the longitudinal direction

F_y - Force along the *y*-axis of a pin-loaded plate

f_s - Tensile force of suture

f_s^{cont} - Tensile force of suture (continuous stitching technique)

$f_{s,u}$ - Ultimate tensile force of suture/knot

f_s^0 - Pre-tension force of suture

G_i - Constants to be obtained through boundary conditions ($i = 1,\ 2,\ 3,\ 4$)

G_{xy} - Shear modulus (orthotropic)

H - Undeformed artery thickness

H_a - Thickness of host artery at undeformed state

H_g - Thickness of graft at undeformed state

H_p - Thickness of isocompliant arteries at pre-stressed state

H_{pa} - Thickness of host artery at pre-stressed state

H_{pg} - Thickness of graft at pre-stressed state

h - Deformed artery thickness

$h(t-\tau)$ - Unit-impulse response function

$\mathbf{I}$ - Unit matrix

I - Alternative form of first strain invariant

II - Alternative form of second strain invariant

I_1 - First strain invariant

I_2 - Second strain invariant

I_4 - Fourth strain invariant

I^i - Moment of inertia of element i of the two-hinged anastomosis model ($i = \mathrm{I}, \mathrm{II}$)

J - Determinant of the deformation gradient matrix

k - Parameter of dynamic pinned circular arch model

k_1 - Q_2 / Q_1

k_2 - A_2 / A_1

L - Length of undeformed artery

L_i - Differential terms of dynamic pinned circular arch $i = 1,\ 2,\ 3,\ 4$

L_p - Length of isocompliant arterial segments at pre-stressed state

L_{pa} - Length of host artery segment at pre-stressed state

L_{pg} - Length of graft segment at pre-stressed state

l - Length of deformed artery

l_s - Stitch length

l_u - Unrestrained length of isocompliant segments under applied blood pressure

l_{ua} - Unrestrained length of arterial segment under applied blood pressure

l_{ug} - Unrestrained length of graft segment under applied blood pressure

Δl - Tensile deformation due to stitching stiffness (isocomplaint arterial segments)

Δl_a - Tensile deformation due to stitching stiffness (arterial segment)

Δl_g - Tensile deformation due to stitching stiffness (graft segment)

$\Delta l_s^{\mathrm{int}}$ - Gap between the two blood vessels of an end-to-side anastomosis with rigid/interrupted stitching

Δl_s^{cont} - Gap between the two blood vessels of an end-to-side anastomosis with continuous stitching

N - Axial force along the circumferential direction

N_1 - Minimum number of stitches in order to prevent suture/knot failure

N_2 - Minimum number of stitches in order to prevent arterial tissue failure

N_3 - Minimum number of stitches in order to prevent blood leak

N_{res} - Longitudinal residual axial force

N_s - Number of stitches

n_f - Number of mode (frequency curves analysis)

M - Internal moment of circular element

m - Mass of the unit-length arterial element

m_f - Parameter of frequency curves analysis

$\mathbf{P}$ - Hydrostatic pressure matrix

P - Hydrostatic pressure

P_4 - Product of four dimensionless parameters

p - Blood pressure

p_i - Blood pressure at cross-section i ($i = 1,\ 2,\ 3$)

p_d - Diastolic pressure

p_s - Systolic pressure

Q - Internal shear force of circular element

Q_i - Average flow rate at cross-section i ($i = 1,\ 2,\ 3$)

q_1 - Non-equilibrium stresses for one relaxation process

R - Radius of undeformed artery (Chapters 5 and 6), or radius of two-hinged anastomosis model (Chapter 9)

R_h - Radius of pin-loaded hole

R_a^o - Outer radius of undeformed host artery

R_g - Mean radius of undeformed graft

R_g^o - Outer radius of undeformed graft

R_p - Radius of isocompliant artery at pre-stressed state

R_{pa} - Radius of host artery at pre-stressed state

R_{pg} - Radius of graft at pre-stressed state

R_x - Far-field force along the x direction

R_z - Far-field force along the z direction

R_θ - Tensile far-field force along the graft axis

r - Radius of deformed artery

r_f - Radius of gyration

r_s - Radius of suture

S - Suture-line length

S_f - Parameter of frequency curves analysis

S_{in} - Incision length

S_θ^∞ - Second Piola-Kirchhoff circumferential strain

s - Distance between sequential stitches

T_n - Natural period of linear arterial model

T_z - Longitudinal Cauchy stress multiplied by current thickness

T_θ - Circumferential Cauchy stress multiplied by current thickness

t - Time

t_n - Time instant of step n

t_1 - Time instant corresponding to the maximum response of the diastolic phase

t_{cp} - Duration of cardiac pulse

t_s - Duration of systolic phase

t_H - Characteristic time of response of Hariton arterial model

t_{MR} - Characteristic time of response of Mooney-Rivlin arterial model

t_{Sk} - Characteristic time of response of Skalak et al. arterial model

t^i - Thickness of element i of the two-hinged anastomosis model ($i = \mathrm{I,II}$)

Δt - Time step duration

U^{II} - Normal function of u^{II}

u - Radial displacement, of isocompliant arterial segments, from pre-stress state

$u_0, \dot{u}_0, \ddot{u}_0$ - Initial radial displacement, velocity, and acceleration

u_a - Radial displacement, of arterial segment, from pre-stress state

u_g - Radial displacement, of graft segment, from pre-stress state

u_f - Response to free vibration (radial displacement)

u_p - Response to pulse loading (radial displacement)

u_{st} - Static radial displacement

$u_{\max}$ - Maximum radial displacement

u_r - Radial displacement from undeformed state

u^i - Radial displacement of element i of the two-hinged anastomosis model ($i = \mathrm{I,II}$)

u_x^i - Displacement of element i of the two-hinged anastomosis model along the *x*-axis ($i = \mathrm{I,II}$)

u_y^i - Displacement of element i of the two-hinged anastomosis model along the *y*-axis ($i = \mathrm{I,II}$)

Δu_r - Normalized radial displacement corrector

V_P - Phase velocity

V_i - Average flow velocity at cross-section i ($i = 1,\ 2,\ 3$)

$V_{(a)}$ - Volume of restrained arterial segment at-rest state

$V_{(b)}$ - Volume of unrestrained arterial segment at deformed state

$\mathbf{W}$ - Strain-energy density matrix

W - Strain-energy density

W^{II} - Normal function of w^{II}

w^i - Tangential displacement of element i of the two-hinged anastomosis model ($i = \mathrm{I}, \mathrm{II}$)

x - Longitudinal distance along the anastomosis (end-to-end anastomosis)

x_g - Distance between the edges of two anastomosed segments at unrestrained deformed state (end-to-end anastomosis)

x_{net} - Distance between the edges of two anastomosed segments at restrained deformed state (end-to-end anastomosis)

z_1, z_2 - State variables

Greek symbols

α - Stitching technique participation factor

β - Dimensionless material parameter of Mooney-Rivlin strain-energy function (Chapter 6), or graft-to-artery radii ratio $\beta = R_g^o / R_a^o$ (Chapter 8)

β_N - Constant of Newmark's constant-acceleration method, equal to 0.25

β_1^∞ - Dimensionless free-energy factor constant

Γ - Viscosity coefficient

γ - Ratio of artery radius to artery thickness $\gamma = R_a^o / H_a$

γ_N - Constant of Newmark's constant-acceleration method, equal to 0.5

ε_L - Arterial segment longitudinal strain

ε_s - Suture strain

ε_{sd} - Circumferential strain of the artery at systolic phase, in respect to the strain of the diastolic phase

ε^i - Strain of element i of the two-hinged anastomosis model ($i = \mathrm{I}, \mathrm{II}$)

η - Radial displacement as a function of the distance from the anastomotic interface

η_L - Far-field radial displacement of the artery

η_s - Modified radial displacement as a function of the distance from the anastomotic interface

η_0''' - Shear stress at the stitching region

θ - Angle along the arterial ring (Chapters 4 through 6), or anastomosis angle (Chapter 8)

θ_0 - Angle defining the stitches placement for the artery patch model

θ^i - Angle along the circular element i of the two-hinged anastomosis model ($i = \mathrm{I}, \mathrm{II}$)

κ - $\sqrt{12/(H_p R_p)^2}$

λ - Parameter of dynamic pinned circular arch model

λ_θ - Circumferential elongation

λ_r - Radial elongation

λ_z - Longitudinal elongation

λ_z^0 - Longitudinal pre-stretch

μ - Shear modulus material parameter of Mooney-Rivlin strain-energy function

μ_1, μ_2 - Stress-like material parameters of Holzapfel et al. strain-energy function

μ_3, μ_4 - Dimensionless material parameters of Holzapfel et al. strain-energy

function

ν , ν_{xy} - Poisson's ratio of the arterial tissue

ρ - Arterial-wall density at deformed state

ρ_0 - Arterial-wall density at undeformed state

ρ_b - Blood density

ρ^{II} - Density of element II of the two-hinged anastomosis model

σ_{22} - Tensile stress along the graft axis

$\sigma_{\theta\theta}$ - Circumferential Cauchy stress

σ_{rr} - Radial Cauchy stress

σ_{zz} - Longitudinal Cauchy stress

σ_s - Embedding stresses at the stitching hole

σ_s^{int} - Embedding stresses at the stitching hole of interrupted rigid suturing

σ_s^{cont} - Embedding stresses at the stitching hole of continuous stitching technique

$\sigma_{s,u}$ - Ultimate tensile strength of arterial tissue

$\sigma_{sa,u}$ - Ultimate tensile strength of arterial segment

$\sigma_{sg,u}$ - Ultimate tensile strength of graft segment

σ_a^{local} - Local stresses at the stitching zone of the artery side

σ_g^{local} - Local stresses at the stitching zone of the graft side

σ_{eff} - Misses effective stress

σ^i - Stress of element i of the two-hinged anastomosis model ($i = \mathrm{I}, \mathrm{II}$)

τ - Time of unit-impulse response function (Chapter 4), or graft-to-artery thicknesses ratio $\tau = H_g / H_a$ (Chapter 8)

τ_1 - Relaxation time

φ - Polar angle of intersection plane of an end-to-side anastomosis

φ_1 - Orientation angle of collagen fiber reinforcement

φ^i - Cross-section rotation of element i of the two-hinged anastomosis model ($i = \mathrm{I}, \mathrm{II}$)

Ω_f - Shear flexibility factor

ω_n - Circular frequency of linear arterial model

ω_0^{Sk} - Circular frequency of Skalak et al. "zero-order nonlinear" model

ω_0^{MR} - Circular frequency of Mooney-Rivlin equivalent linear arterial model

ω^{II} - Circular frequency of element I of the two-hinged anastomosis model

CHAPTER 1

Introduction

1.1 Motivation

Cardiovascular diseases continue to be the leading cause of mortality and premature death in the Western world. Vascular surgeries treat vascular diseases, such as atherosclerosis and aneurysms, and traffic or other serious injuries that lead to violent artery fractures.

Vascular surgeries potentially suffer from short-term and long-term post-surgery complications, related to the successful stitching of human arteries with themselves, or with grafts (venous or artificial). Short-term complications, involving the tearing of the arterial wall after the stitching is complete, suture-line bleeding, or failure of the suture or the knot that is tied by the surgeon, increase the total time of the operation. Long-term post-surgery complications, involving restenosis of the blood vessel due to the development of intimal hyperplasia, thrombosis due to blood leakage, or failure of the suture due to deterioration of the suture material, may lead to revision surgery if diagnosed in time. Evidently, stitching techniques and related suture and graft materials are of great importance for the short-term and long-term success of vascular surgeries.

In fact, little work has been published on the dynamic behavior of anastomosed arteries, and particularly on the stress concentration detail at the stitching holes. Related materials are characterized by large uncertainties and their material parameters depend on many factors. For example, the mechanical behavior of arterial tissues varies with topology, disease, age, and other physiological states of the blood vessel. Moreover, graft and suturing characteristics may change over time, as is the case of the mechanical properties of a Dacron-graft, which before use are different than those after five years in the human body. Thus, there is a need of investigating the general mechanical behavior of arterial anastomoses by taking into account all important parameters.

1.2 Objectives

The purpose of this research is to investigate the response of different arterial anastomosis techniques in a general manner and provide useful conclusions about the optimum graft properties and stitching details in order to avoid short-term or long-term post-surgery complications. To investigate the mechanics of the suture line, it is necessary to first examine the dynamic radial response of arteries with different material behaviors. Due to

the fact that arterial tissues and biological activities have a considerable complexity and their material parameters depend on many factors, we aim to develop basic models that are characterized by generality, and provide closed-form solutions (where it is feasible).

In particular, the following models are investigated in this thesis:

a. Linear arterial model under dynamic loading
b. Hyperelastic arterial model under dynamic loading
c. Viscoelastic arterial model under dynamic loading
d. End-to-end anastomosis model by using displacement-based analysis
e. End-to-side anastomosis model by using stress-based analysis
f. Two-hinged circular model identifying the role of elastic mismatch for end-to-side anastomosis, side-to-side anastomosis, and artery patching

The development of fundamental design-oriented methodologies can offer new and better-substantiated understanding of the mechanics of arterial stitching, and form the basis for the development of vascular anastomosis guidelines related to the prevention of post-surgery complications. We also expect through this research to interpret medical practices known to the medical society through patency rates but have not been justified by mathematical models.

Our investigation focuses on the analysis of the solid arterial part of the vascular system in terms of principal displacements, stresses, and/or energy density. The models are compared with experimental and finite-element studies available in the literature in order to evaluate the level of approximation of each approach. Constructive feedback and suggestions provided by cardiovascular surgeons are taken into account.

Note that, this thesis does not take place against the final medical decisions taken by the surgeons. Medical practice involves a larger amount of factors and higher complexity than those considered in the present study.

1.3 Outline

This thesis is organized into twelve chapters. Chapters 1 through 3 constitute an introduction on the topic of interest. Chapter 1 describes the motivation that led to this study and its objectives. Chapter 2 presents a comprehensive literature review on the analytical, computational, and experimental studies that examined the response of vascular anastomoses, as well as a review on theoretical studies concerning the elastic and viscoelastic arterial response. Furthermore, Chapter 3 reports important information

regarding topics of the cardiovascular engineering field, such as the induced blood pressures along the arterial tree, characteristics of the arterial system, vascular diseases, types of vascular anastomoses, etc.

Chapters 4 through 6 investigate the dynamic far-field response of the anastomotic region. In particular, Chapter 4 presents a review of a previous work regarding a recently proposed linear-elastic arterial model and its respective closed-form solution. Moreover, the response of the linear-elastic model under different pressure time-profile approximations is investigated for the first time. Chapter 5 examines the response of three hyperelastic arterial models, representing the hardening behavior of healthy arteries, the hardening behavior of atherosclerotic arteries, and the softening behavior of aneurysmatic arteries, respectively. Chapter 6 extents the model of the healthy hyperelastic artery, derived in Chapter 5, into a viscoelastic arterial model by adopting a generalized Maxwell model and the Bonet-Holzapfel approach.

The bulk of this thesis (Chapters 7 through 9) focuses on the suture-line response of different arterial anastomosis techniques. Numerical examples, and comparison against studies available in the literature are presented. In particular, Chapter 7 proposes a mathematical model governing the dynamic response of an end-to-end anastomosis. The proposed displacement-based methodology accounts for all the important problem parameters. In addition, a mathematical model describing the para-anastomotic hypercompliant zone (PHZ) phenomenon is introduced. Chapter 8 studies the response of the end-to-side anastomosis technique, by utilizing a stress-based analysis. The proposed methodology is based on the general stress-concentration-factor (SCF) results obtained from the analysis of pipe connections. Chapter 9 proposes a mathematical model aiming to investigate the effect of elastic mismatch on the response of side-to-side related anastomoses and artery patching. An idealized circular cylindrical anastomosis model consisting of two parts, interconnected by two hinges, is formulated. Finally, Chapter 10 elaborates on the complex topic of the stress concentration at the stitching hole.

The present thesis ends with a summary of all the important conclusions of this dissertation and with a discussion on the future work that may follow from this study, in Chapter 11.

CHAPTER 2

Literature Review

2.1 Previous work on the response of arterial anastomosis

Several studies have examined the response of vascular anastomoses by using analytical, computational, or experimental methods. However, related studies limit their research to specific arterial geometries or ignore the stress concentrations due to suture-artery interaction. For the problem solution, is often utilized finite-element analysis instead of analytical models. Moreover, little work has been published on the dynamic analysis of the stitched anastomotic region. In their review article, Migliavacca and Dubini [1], clearly point out the lack of such analyses.

Note that, many studies focus on the hemodynamic aspect of the problem, the induced wall shear stresses, and the fluid patterns. This study does not deal with the hemodynamic analysis of the problem. It focuses primarily on the arterial-wall mechanics and the suturing detail of different anastomosis techniques (end-to-end anastomosis, end-to-side anastomosis, side-to-side anastomosis).

Review articles on the computational [2, 1, 3, 4] and the experimental analysis of vascular anastomoses [2, 5] are available in the literature. The following sections describe the most representative published studies in the field of arterial suturing.

2.1.1 Analytical studies

Among the vascular anastomosis studies, analytical studies are the most limited. Representative analytical works are those of Paasche at al., Melbin and Ho, and Rachev et al. [6–8].

Paasche et al. [6] solved analytically a boundary-value problem describing the response of an end-to-end anastomosis. The graft behavior was assumed to be rigid. They calculated the radial displacements and the induced wall stresses, along the longitudinal axis of the host-artery, for different graft-to-artery radii ratios. They found that the optimum graft-to-artery radii ratio, minimizing the axial and shear stresses, is in the range of 1.4 to 1.5.

Melbin and Ho [7] investigated the effect of three different end-to-end anastomotic shapes (transverse sectioned, bias sectioned, graft with elliptic-end connected to a bias sectioned artery) on the peak stresses. The authors did not provide a complete solution of the

deformation at the anastomotic region. They assumed a range of peak circumferential elongation values in order to calculate the peak stresses.

Rachev et al. [8] proposed an analytical model to investigate the stress-induced thickening for the case of an artery/graft end-to-end anastomosis and for the case of an implanted stent. The mathematical model considered wall remodeling (thickening) and clamped conditions between the graft (or stent) and the host artery. The derived equations were solved numerically.

2.1.2 Computational studies

Most computational studies rely exclusively on finite-element analyses and their results concern the response of specific arterial geometries. The main advantage of using computational tools is that problems with complex geometries and irregular flow conditions can be analyzed.

In particular, in a finite-element study, Hofer et al. [9] investigated the case of end-to-side anastomosis, without modeling the response of individual stitches. They studied the effect of compliance mismatch on the anastomosis response and on the development of intimal hyperplasia. In order to correlate intimal hyperplasia to the calculated response, the computational results were compared to a pre-existing experimental study. The development of intimal hyperplasia at the suture line was found to be mainly affected by the induced stresses and strains at the blood-vessels wall.

Ballyk et al. [10] studied an end-to-end and an end-to-side anastomosis by use of finite-element analysis, aiming to examine if compliance mismatch promotes intimal hyperplasia. The sutures were modeled as discrete points along the suture line, resulting in excessive stress concentration values at the stitching area due to the point-like modeling approach as such. They concluded that elevated compliance mismatch increases the suture-line mechanical stresses and consequently the development of intimal hyperplasia.

Leuprecht et al. [11] and Perktold et al. [12] utilized three end-to-side anastomosis models, each one concerning a different technique (conventional anastomosis, Taylor-patch anastomosis, and Miller-cuff anastomosis). Their finite-element analysis yielded the wall shear stresses and maximum principal stresses for each case. In particular, the latter study modeled the stitches in detail using three-dimensional elements for the junction. They suggested that the Taylor-patch, and Miller-cuff anastomosis techniques may reduce the stress concentrations at the suture line, and therefore the generation of intimal hyperplasia.

In another finite-element study, Cacho et al. [13] investigated the effect of the insertion angle (insertion angles between 20° and 40°) and incision length of coronary arterial bypass models, though without modeling explicitly the response of individual stitches. Lower insertion angles require longer incisions, influencing the graft shape and the induced graft-wall stresses. They observed that with increasing insertion angles the peak stresses were slightly lower and more restricted.

Schiller et al. [14] studied an artery/vein-graft and an artery/synthetic-graft end-to-end anastomosis by using a fluid-structure coupling algorithm. The sutures were simulated as a two-dimensional anastomotic interface. The artery to vein-graft anastomosis (for which the artery was stiffer than the vein graft) caused increased stenosis at the stitching region, compared to the artery to synthetic-graft anastomosis (for which the artery was softer than the synthetic-graft).

More recently, Ngoepe et al. [15] examined the case of arterio-venous access grafts forming end-to-side anastomosis with intersecting angles of 45°, 90°, and 135°. Such anastomoses are performed in the case of patients undergoing hemodialysis. Ngoepe et al. used a fluid-structure interaction algorithm, coupling computational fluid dynamics with structural finite-elements models. They calculated, among others, the principal stresses and deformations of the blood-vessels walls, and found that the 90° end-to-side configuration shows slightly better performance than other configurations.

2.1.3 Experimental studies

Experimental studies carried out over the years have examined primarily the anastomosis compliance and the development of intimal hyperplasia at the anastomotic region.

Along with their computational studies, Ballyk et al. [10] and Leupretch et al. [11] carried out experimental investigations, aiming to correlate the development of intimal hyperplasia to the system's response (obtained from computational results). They both suggested that increased stress concentration at the suture line promotes the development of intimal hyperplasia.

In an end-to-end anastomosis study, Lyman et al. [16] implanted synthetic-grafts, with compliance approximately equal to that of the host artery, in dogs. They found that compliant vascular grafts exhibit better behavior than noncompliant grafts, and that compliance of synthetic grafts may decrease with time. Lyman et al. also observed that thin-walled grafts are more compliant, but easier to tear during the suturing process.

Hasson et al. [17] investigated an end-to-end anastomosis between isocompliant arterial grafts from dogs and found that a para-anastomotic hypercompliant zone (PHZ), which promotes subintimal hyperplasia (SIH), exists near the suturing region. The compliance at this region increases up to 50% compared to the compliance away from the stitching region. In a later study, Hasson et al. [18] suggested that the suture technique affects significantly the compliance of the anastomotic region. In particular, they showed that the PHZ phenomenon occurs more frequently for anastomosis of the continuous-stitching technique than that of the interrupted-stitching technique. In addition, they observed that increased longitudinal stress of the arterial vessel reduce the compliance. This phenomenon can be justified by the fact that longitudinal pre-stress affects the mechanical properties of dog arteries [19].

Abbott et al. [20] studied the response of end-to-end anastomosis by implanting compliant and stiff grafts in dogs. The longitudinal profiles of compliance differed considerably for the two cases, with the compliance values of the later case (stiff graft) being lower. A PHZ existed at the host artery side, either when using compliant or stiff grafts, whereas graft patency rates were significantly increased when using compliant instead of stiff grafts.

Moreover, Ulrich et al. [21] experimentally investigated an end-to-end anastomosis between pig aortic grafts and found that a PHZ does not exist in this case. They also suggested that the main factor affecting the anastomotic response is the suture line itself.

In a later end-to-end anastomosis study, Baguneid et al. [22] examined the effect of different suturing techniques on the para-anastomotic profile. They performed anastomoses between isocompliant goat arteries by using continuous polypropylene stitching, interrupted polypropylene stitching, and nonpenetrating clips. A PHZ existed for all cases. For the case of nonpenetrating clips, the PHZ phenomenon and the development of intimal hyperplasia were reduced.

In an end-to-side anastomosis study, Bassiouny et al. [23] found that the development of intimal hyperplasia at the suture line of conventional end-to-side anastomosis is promoted by healing mechanisms, compliance mismatch, and triangulation of the anastomotic junction that may result in complex hemodynamic patterns. They also suggested that intimal hyperplasia on the artery floor is developed due to low wall shear stresses and hemodynamic factors that generate stagnation points at that region.

Noberto et al. [24] experimentally investigated the effect of the expansibility of vein cuffs (end-to-side anastomosis technique) by jacketing the cuff with an artificial material. They

concluded that the good patency rates of Miller-cuff technique are not correlated to the mechanical properties of the cuffs.

Moreover, Noori et al. [25] studied the flow patterns of different end-to-side techniques and found that only the Miller-cuff technique appears to have better flow patterns due to its wider anastomotic cavity.

Limited investigations have been performed on side-to-side anastomoses. Clinical studies on side-to-side anastomoses showed that this technique has larger patency rates and better fluid dynamics [26–28].

2.2 Previous work on the elastic and viscoelastic response of arteries

An extensive part of this study deals with the dynamic response of the arterial model away from the anastomotic region. A number of elastic and viscoelastic arterial models have been investigated over the years. This section describes in brief the most representative elastic and viscoelastic theoretical studies available in the literature.

Previous analytical works on the dynamic radial response of elastic arterial models are quite limited. The most representative studies are the works of Demiray and Vito [29] and Humphrey and Na [30]. Demiray and Vito [29] investigated the dynamic response of arteries by assuming a simplified sinusoidal solution for the deformation field. They found that the dynamic loading increases the diastolic wall-pressures and decreases the systolic wall-pressures, compared to the static loading, and that under certain conditions negative wall-pressures may exist, implying artery collapse. Humphrey and Na [30] studied the arterial-wall stress and strain response of healthy and diseased arteries. In order to solve the problem they assumed that the motion (square of the inner radius) is described by a Fourier series. Their model constitutes an extension of the Demiray and Vito model.

Due to the fact that the viscoelastic response of arteries cannot be modeled adequately by a simple Maxwell or Voight element, several other models are proposed in the literature. Kalita and Schaefer indicate in their review article [31] the different kinds of mechanical systems that can simulate the viscoelastic behavior of arteries.

For example, Westerhof and Noordergaaf [32] proposed a five-parameter model consisting of two Maxwell elements and a spring placed in parallel. Cox [33] suggested a model consisting of a spring in series with a Voigt element, and Papageorgiou and Jones [34] proposed a mathematical model with a number of Voigt elements in series. Holzapfel and

Gasser [35] and Holzapfel et al. [36] adopted a generalized Maxwell model, i.e. a model that consists of a single spring on one end and a number of Maxwell devices set in parallel.

Haslach Jr [37] proposed a generalized model that describes the behavior of nonlinear thermoviscoelastic soft tissues, including all time-depended behavior types. The model consists of a system of evolution differential equations. He presented a number of numerical examples on the viscoelastic response of soft tissues, by adopting different constitutive laws, available in the literature, and their respective material data.

Moreover, Čanić et al. [38] developed a theoretical "reduced" model by considering axially-symmetric geometry of the artery, viscoelastic arterial walls, and axially-symmetric viscous blood flow. They calculated the viscoelastic response of arteries by conducting numerical simulations and verified their method by comparing the numerical values to experimental results.

CHAPTER 3

Background

3.1 Introduction

Predictive medicine and therapeutic decision-making necessitates comprehensive understanding of the human biological activities in order to develop a suitable mathematical model that describes the problem of interest and obtain the respective optimal solution. In the field of cardiovascular engineering, the researcher or the interested reader should be familiar with topics such as the histology and mechanical properties of biological tissues, the blood pressure profile, cardiovascular diseases, cardiovascular surgery techniques, etc.

This chapter provides a basic background regarding the cardiac cycle and the induced blood pressures along the arterial tree, the characteristics of the arterial system, vascular diseases that may lead to vascular operations, and types of vascular anastomoses. Moreover, related topics concerning large part of the literature, such as the compliance of blood-vessels and the phenomenon of intimal hyperplasia, are described.

3.2 The cardiac cycle and the induced blood pressure

The human heart constitutes the pumping station of the body. The heart vibrates due to electric pulses applied to its surface, inflating periodically the various heart chambers. In one single day, the heart beats about one hundred thousand times and it is able to pump about 10 000 liters of blood through the circulatory system.

The cardiac cycle consists of two major functional periods: systolic and diastolic. The systolic period occurs when the left and right ventricles contract, ejecting blood into the aorta and pulmonary artery. As a result, the aortic pressure increases and the arteries dilate. During the diastolic period, the aortic and pulmonary valves close, blocking further blood ejection into the arteries; the ventricles of the heart are relaxed, and the right and left atrium are filled with blood that passes to the ventricles.

Figure 3-1 shows the heart chambers, the adjacent blood vessels, and the direction of blood flow through them. The circulation from the right ventricle through the pulmonary artery, the lungs, and the pulmonary veins to the left atrium is called pulmonary circulation. It carries deoxygenated blood to the lungs and returns oxygenated blood to the heart. The circulation from the left ventricle through the aorta, to the entire body, back to the vena

cava veins, the right atrium, and the right ventricle is called systemic circulation. The systemic circulation carries oxygenated blood through the entire body and returns deoxygenated blood to the heart.

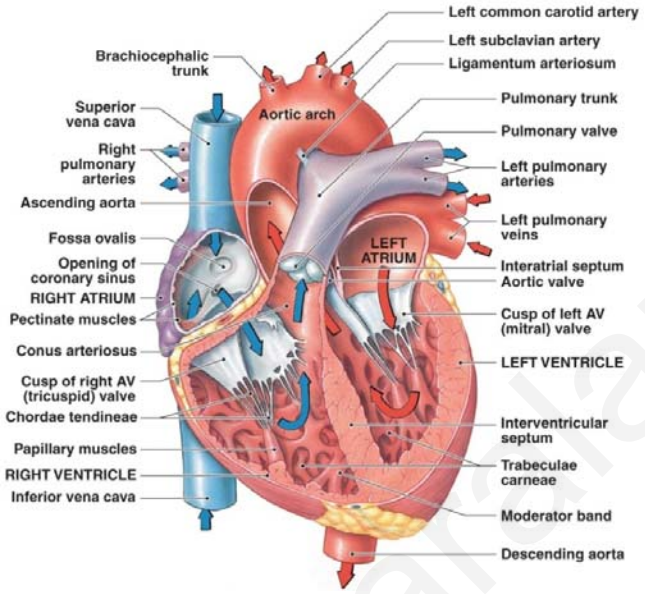

Figure 3-1: The human heart, adjacent blood vessels and blood flow circulation (from http://www.wyeriverupperschool.org/houserwrus/Anatomy%20Physiology/May52011/index.html).

During each cardiac cycle, the arterial system is subjected to intraluminal pressures (blood pressure) similar to the time-profile shown in Figure 3-2. Arterial blood pressure is the intraluminal pressure that the arterial walls have to sustain due to the action of the heart in pumbing blood to the entire body.

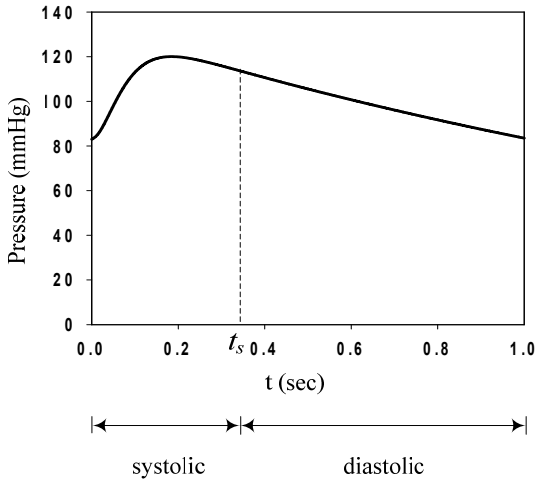

Figure 3-2: Aortic pressure-time profile (after Zhong et al. [39]).

Zhong et al. [39] presented an approximation of the aortic pressure-time profile, as a function of two exponential equations. Figure 3-2 shows a typical example of the aortic pressure-time profile approximation proposed by Zhong et al. The systolic-phase duration in this case is equal to $t_s = 0.35$ sec. The time interval $0 \le t \le t_s$ represents the systolic phase, during which the blood is pumped into the aorta and the aortic walls inflate due to the maximum overstress pressure, whereas the time interval $t_s < t < 1$ represents the diastolic phase, during which the aortic valve closes and the aortic blood pressure decreases. The pressure at the start of the systolic phase (and at the end of diastolic phase) is called diastolic pressure, while the maximum pressure during the systolic phase is called systolic pressure.

The pressure time-profile of Figure 3-2 corresponds to the case of an aorta under normal conditions. Blood pressure profiles may vary with topology along the human body or pathological conditions such as hypertension and hypotension. Figure 3-3 shows blood pressure profiles of different large-size arteries. It can be noticed that the descending aorta and the right subclavian artery exhibit the maximum systolic and diastolic pressures.

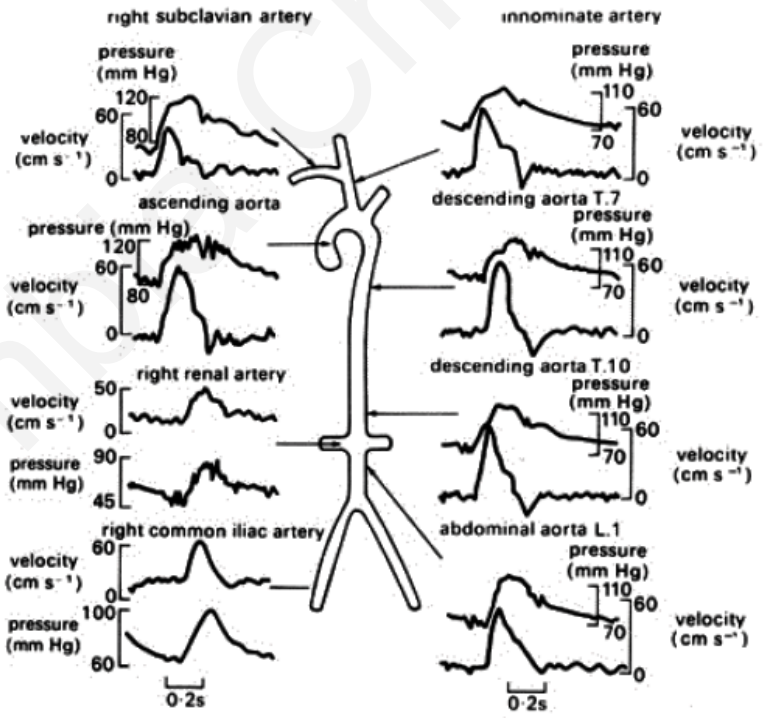

Figure 3-3: Blood pressure and velocity time-profiles of large-size arteries (after Mills et al. [40]).

Figure 3-4(a) reports the average blood pressure of veins and arteries along the human body. For regions located above the heart level (arms, neck, head), the mean arterial

pressure is decreased with increasing distance from the heart, whereas for the rest of the body the arterial or venous pressure is increased with increasing distance from the heart. The blood pressure profile is also affected by the position of the human body, as in the case of a person in the supine position. For a person in the supine position, the systolic pressure increases gradually along the arterial tree (Figure 3-4(b)).

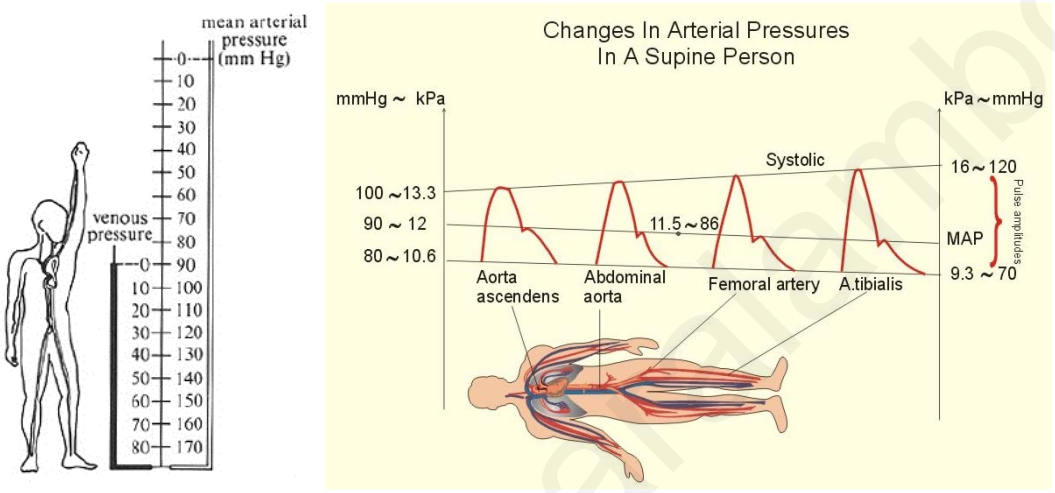

(a) (b)

Figure 3-4: (a) Average blood pressure along the human body (after Rushmer [41]), (b) Pressure time-profiles of a supine healthy person along the arterial tree (from http://www.zuniv.net/physiology/book/chapter9.html).

People that suffer from hypertension exhibit increased blood pressure values. According to the latest guidelines of the European Society of Hypertension (ESH) and of the European Society of Cardiology (ESC) for the management of arterial hypertension [42], the optimal values of the systolic and diastolic blood pressure is less than 120 mmHg and less than 80 mmHg, respectively. At optimal pressure values the cardiovascular system exhibits relatively low stresses and strains, delaying the aging and fatigue of the heart and the blood-vessels. Hypertension is categorized in three stages, namely Grade-1 hypertension, for systolic and diastolic pressure values 140-149 mmHg and 90-99 mmHg, respectively; Grade-2 hypertension, for systolic and diastolic pressure values 160-179 mmHg and 100-109 mmHg, respectively; and Grade-3 hypertension, for systolic and diastolic pressure values greater than 180 mmHg and 110 mmHg, respectively. Table 3-1 lists the blood pressure definitions and classifications for adults.

Note that, during the first critical hours after a major vascular operation (e.g. coronary artery bypass operation) the patient should not experience high blood pressures. Therefore,

the patient remains in repression ("sleep") for some hours following the operation. If the patient is already hypertensive, he takes the appropriate pharmaceutical treatment to maintain his blood pressure at optimal levels.

Observe that all pressure time-profiles can be approximated by the profile given in Figure 3-2 by varying the values of systolic pressure, diastolic pressure, systolic-phase duration, and cardiac cycle duration. A time-varying pressure profile (such as that of Figure 3-2) should be utilized in performing a dynamic analysis, as opposed to the (constant) systolic-pressure value utilized in performing a static analysis.

Table 3-1: Definitions and classification of blood pressure for adults (after [42]).

Category	Systolic (mmHg)		Diastolic (mmHg)
Optimal	<120	and	<80
Normal	120-129	and/or	80-84
High normal	130-139	and/or	85-89
Grade-1 hypertension	140-159	and/or	90-99
Grade-2 hypertension	160-179	and/or	100-109
Grade-3 hypertension	≥180	and/or	≥110
Isolated systolic hypertension	≥140	and	<90

3.3 The arterial system

3.3.1 Structure and histology

Arteries are characterized by complexity both at macroscopic and microscopic scale. They are inhomogeneous, anisotropic and their structure varies with age, topology along the arterial tree, and disease. Figure 3-5 shows a cross section of a typical artery. Macroscopically, the arterial wall is composed by three layers. Staring from the inside of the artery, these layers are the intimal, the media, and the adventitia.

The intimal consists of an endothelial and subendothelial layer and is separated from the media by the internal elastin lamina. In healthy arteries the intimal layer is very thin and has insignificant mechanical properties, whereas aged and atherosclerotic arteries have stiffer and thicker intimal, resulting in a significant contribution to the artery mechanical

behavior. The media consists of smooth muscle cells, elastin and collagen fibrils. At low blood pressures, the media has high strength compared to the other two layers and can resist circumferential and longitudinal loadings. The adventitia layer is separated from the media layer by the external elastin lamina. It consists mainly of fibroblasts, fibrocytes, and collagen fibrils. At high blood pressures, the adventitia stiffens and strengthens, behaving as a protective mechanism for the other layers. Furthermore, its thickness varies depending on the blood-vessel type, physiological function, and topology along the arterial tree.

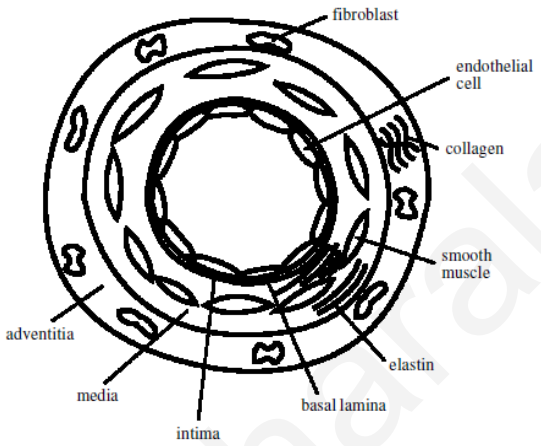

Figure 3-5: Cross section of a typical artery (after Humphrey [43]).

Arteries can be categorized in two types: elastic and muscular arteries. Elastic arteries are large-size arteries that are located close to the heart (e.g. aorta, iliac artery) and muscular arteries are medium-size arteries that consist mainly of muscular cells and are located at the peripheral circulation (e.g. cerebral arteries, femoral arteries) (Figure 3-6). Moreover, the media layer of medium- and small-size arteries is thicker than the adventitia layer and in some cases the adventitia is nonexistent (e.g. cerebral arteries). Figure 3-6 shows the diameter and histology of arteries and veins along the circulatory system.

Typical values of the radius of large- and medium-size arteries vary between 0.1 cm (e.g. coronary arteries) and 1.6 cm (aorta). Typical values of their wall thickness vary between 0.01 cm and 0.12 cm. Table 3-2 reports the geometric properties ranges of large- and medium-size arteries.

3.3.2 Mechanical behavior

The mechanical properties of arterial tissues depend on the artery location, age, disease, and other physiological states [44, 45]. In general, their mechanical behavior does not obey

Hooke's law [46, 47], exhibiting anisotropic nonlinear behavior for finite deformations. The arterial tissue is a hyperelastic material and its stress-strain relationship derives from a strain-energy function. Furthermore, it is an incompressible material, meaning that it does not change its volume under applied elongations [48].

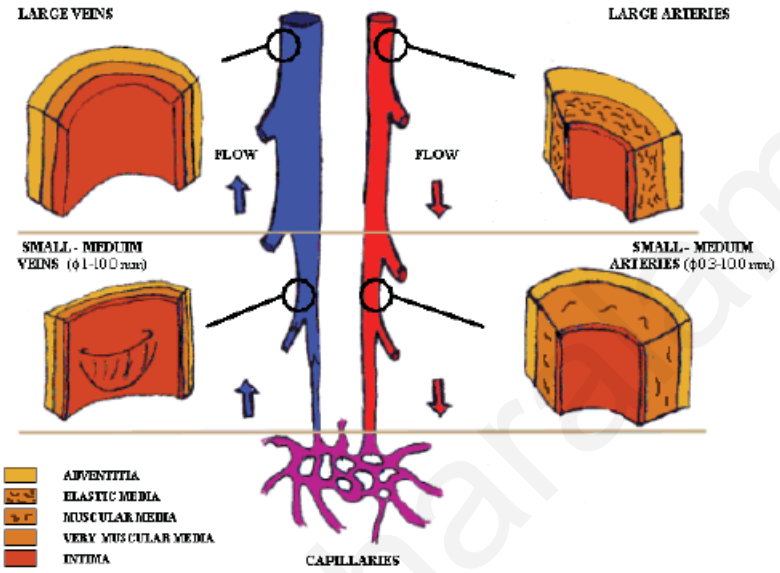

Figure 3-6: Variation of vessel diameter and histology along the circulatory system (after Rhodin [49]).

Table 3-2: Geometric properties of large- and medium-size arteries.

Parameter	Value
Radius	0.1-1.6 cm
Wall thickness	0.01-0.12 cm
Length	0.5-15 cm

Note that, muscular arteries often exhibit viscoelastic behavior, since they demonstrate hysteresis under cyclic loading, creep under constant loading, and stress relaxation under constant displacement. Their relatively low-energy loss in each cardiac cycle prevents reflected pressure waves from resonating in the arterial systems [50].

Typical hyperelastic constitutive laws that describe the mechanical behavior of biological tissues are the Mooney-Rivlin [51, 52], Fung [53], Gent [54], the strain-energy function of Skalak et al. [55], and the constitutive law proposed by Delfino et al. [56].

The stress-strain relationship of arterial tissues depends mainly on its elastin and collagen content (Figure 3-7(a)). At low blood pressures, the mechanical behavior depends on the elastin and smooth muscle content of the media. In this case, the elasticity modulus is relatively low. At higher blood pressures, the strength of the adventitia collagen fibers is activated, since the wavy collagen fibers are stretched and rearranged circumferentially. Thus, the elasticity modulus of the arterial tissue is increased and the stress-strain curve becomes steeper. Under physiological pressures (80-120 mmHg) the mechanical behavior of arterial tissues can be considered to be linear elastic.

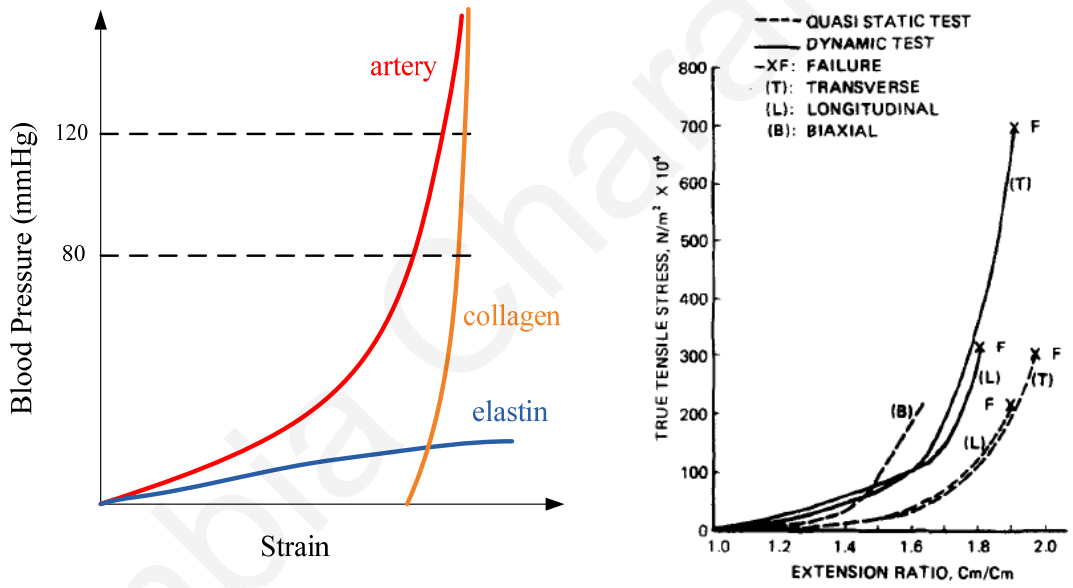

(a) (b)

Figure 3-7: (a) Induced blood pressure versus strain of the artery, collagen, and elastin; (b) Arterial tissue stress-strain relationship, of a 25 year old man, under dynamic and quasi-static loading (after Mohan and Melvin [47]).

Based on the biaxial dynamic tests of Mohan and Melbin [47], the ultimate strength of human arterial tissues varies between 1 and 3 MPa. Figure 3-7(b) shows the longitudinal and transverse stress-strain relationships of a human arterial tissue (conducted by Mohan and Melvin) under dynamic and quasi-static loading. Observe that the artery exhibits higher ultimate strength and lower ultimate elongations (point F) when subjected to dynamic loading, rather than quasi-static loading.

3.3.3 Residual stresses

The load-free configuration of an artery is not stress-free. Residual stresses pre-exist in the arterial tissue. These stresses exist due to delayed growth of arteries compared to the rest of the body, remodeling, injury, or viscoplastic strains, and have significant impact on the response of arteries to external loads [57]. Residual stresses are evident once an unloaded in vivo artery is cut transversally or longitudinally. When an artery is cut transversally it contracts along the longitudinal direction, releasing longitudinal stresses; and when an artery is cut longitudinally, the cylindrical sector opens, releasing circumferential stresses.

Consequently, residual stresses should be taken into account in the development of the arterial mathematical model. Longitudinal residual stresses are frequently accounted for by setting an initial pre-stretch to the artery [10], whereas circumferential residual stresses can be accounted for by the "opening-angle" method [57]. The "opening-angle" method assumes that the stress-free configuration of the artery is an open cylindrical sector. Thus, in order to obtain the initial cylindrical configuration, a bending moment is applied to the open sector. Once the axial pre-stretching and bending are applied to the model, the load-free (but not stress-free) initial configuration of the artery is obtained.

3.4 Vascular diseases

Among the vascular disorders, atherosclerosis and aneurysms are the most frequently encountered. Both diseases require surgical treatment when exhibiting critical characteristics, defined by medical regulations.

An aneurysm is a disorder of the arterial tissue, in which the wall of an artery section becomes weak and soft. While the blood pressure pushes outward this soft tissue, the artery dilates in a balloon-like shape, as shown in Figure 3-8(a). It most commonly occurs in people that are 60 years old or older. If the aneurysm is not diagnosed in time, it may rupture and uncontrolled bleeding will occur. In this case, the patient has low chances of survival (10-20%). On the other hand, if the aneurysm is diagnosed in time, the problem is treated by a vascular operation in which the diseased part is removed and a graft is sutured in that place (open repair), or by an endovascular repair [58, 59].

Atherosclerosis is the formation of a plaque on the inner surface of the artery, resulting in hardening of the arterial wall and narrowing of the arterial lumen. The plaque is formed by fatty substances, cellular waste products, fibrin cholesterol, calcium, and collagen fibers that are transferred by blood. Its development begins from an early age and is negatively

affected by high cholesterol and triglyceride levels, high blood pressure, and smoking. In early stages, only the inner layer (intimal) of the artery is affected, whereas in later stages the second layer (media) is also affected. When the arterial lumen is completely blocked by a blood clot or a smaller artery is blocked by a piece of the plaque that broke off, the affected area is not oxygenated and the adjacent tissue is destroyed. When arteries that oxygenate vital organs are blocked, as is the case of heart attack or stroke, the consequences may be fatal. Figure 3-8(b) shows the formation of an atherosclerotic plaque, the narrowing of the artery lumen, and the complete blocking by a blood clot. An artery with atherosclerotic stenosis is treated by bypass surgery or angioplasty [60, 61].

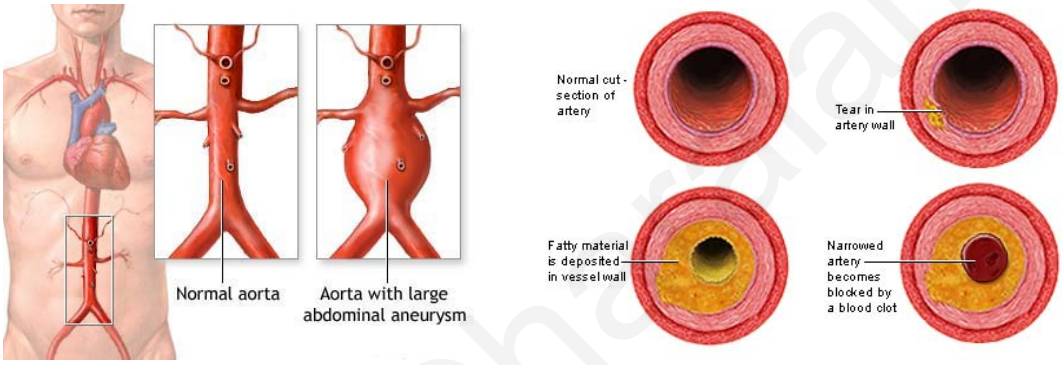

(a) (b)

Figure 3-8: (a) Aortic aneurysm (From http://www.ncbi.nlm.nih.gov/pubmedhealth /PMH0002109/), (b) Formation of atherosclerotic plaque (From http://www.nlm.nih.gov/ medlineplus/ency/imagepages/18020.htm).

3.5 Types of anastomosis

Vascular surgery operations treat vascular diseases, traffic-related and other serious injuries that lead to violent artery fracture. Arterial anastomosis may be categorized in three types: end-to-end anastomosis, end-to-side anastomosis, and side-to-side anastomosis (Figure 3-9).

An end-to-end anastomosis is performed when the diseased artery segment is removed, and the healthy segments are stitched together, either directly or through the insertion of an artificial graft. This technique is often applied in cases of aortic aneurysms, femoral aneurysms, etc. In addition, end-to-end anastomosis is applied when an artery is transversely cut after a violent incident.

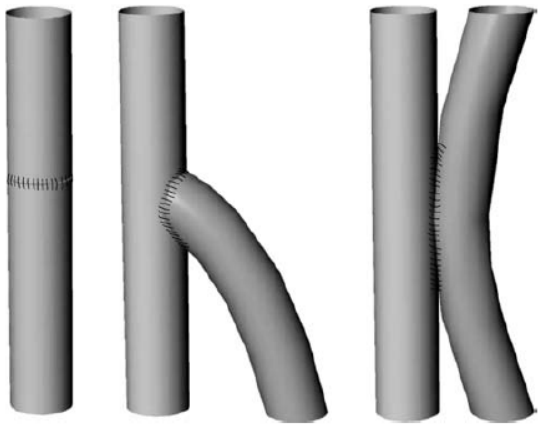

(a) (b) (c)

Figure 3-9: Different types of anastomosis (a) end-to-end anastomosis; (b) conventional end-to-side anastomosis; (c) side-to-side anastomosis (after Migliavacca and Dubini [1]).

The end-to-side and side-to-side techniques can bypass an arterial stenosis by utilizing an arterial, a vein, or an artificial graft. An end-to-side anastomosis uses a graft to bypass the diseased segment and provide oxygenated blood from the proximal to the distal anastomosis (e.g. coronary artery bypass), or uses an artery that was not removed from the blood circulation to provide oxygenated blood through a distal anastomosis (e.g. bypassing by using the internal mammary artery). In both, cases the graft is sutured laterally at a longitudinal incision of the host artery. On the other hand, for a side-to-side anastomosis, both the host artery and the graft are connected and stitched together through longitudinal incisions, as shown in Figure 3-9(c).

In the case of end-to-side anastomosis, several techniques have been proposed in an effort to reduce the development of intimal hyperplasia and increase graft patency rates of distal anastomoses. These techniques are relatively recent and are known mainly to the academic community rather than the medical community. Some of these conduits show promising patency rates. The most known techniques are the Miller-cuff (Figure 3-10(d)) and the Taylor-patch anastomosis (Figure 3-10(c)). Other end-to-side anastomosis techniques are the Linton-patch, the vein boot, and the arteriovenous fistula anastomosis (Figure 3-10(d,e,f)).

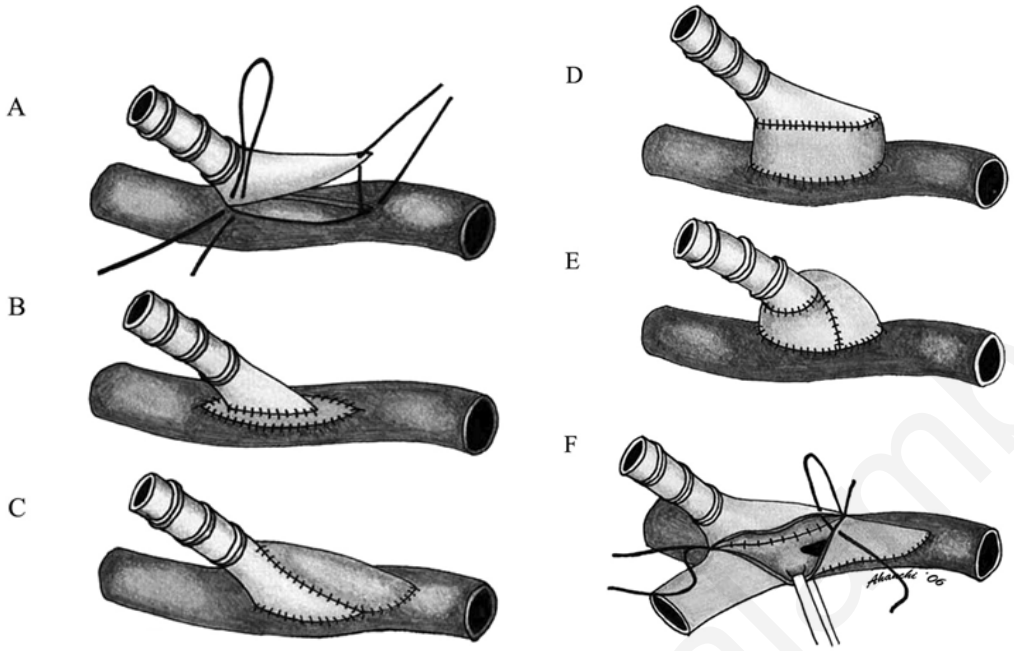

Figure 3-10: Different end-to-side techniques: (a) conventional technique; (b) Linton-patch; (c) Taylor-patch; (d) Miller-cuff; (e) vein boot; (f) arteriovenous fistula (after Kapadia et al. [62]).

3.6 Post-surgery complications

Vascular-operations suffer from short-term and long-term post-surgery complications. Short-term complications, including the tearing of the arterial wall after the stitching is complete, suture-line bleeding, or failure of the knot that is tied by the surgeon, increase the total time of the operation. Long-term complications involve restenosis of the blood vessel due to development of intimal hyperplasia, thrombosis due to blood leakage, or failure of the suture due to gradual deterioration of the suture material [63]. If a long-term post-surgery complication is diagnosed in time, it may lead to a revision surgery.

3.6.1 Intimal hyperplasia

Among the long-term post-surgery complications, the development of intimal hyperplasia (or neointimal hyperplasia) is the most widely-studied. It is considered to be the main cause of graft failure. Intimal hyperplasia is a physiologic healing response of the arterial-wall to injury. This response causes a decrease of the arterial lumen and re-stenosis of the blood vessel. If the stenosis is detected in time, the vascular operation is repeated and the graft is replaced.

Arterial-wall injury may be caused by a vascular anastomosis operation, angioplasty, stent insertion, or around long-term venous catheters. The injured endothelium releases inflammatory mediators that trigger platelet, fibrin, and leukocyte aggregation to the area. Smooth muscle cells migrate from the media to the intimal, where they multiply and deposit extracellular matrix. As a result, a neo-intima is formed and intimal hyperplasia (thickening) is developed.

All types of anastomosis suffer from intimal thickening at the suture line. Figure 3-11 shows that the development of intimal hyperplasia for the case of end-to-side anastomosis occurs at two characteristic regions: the suture line and the artery floor opposite of the distal anastomosis [23].

Several factors are identified to influence the problem, such as irregular flow conditions, low wall shear stresses, irregular mass transportation into the blood-vessel wall, compliance mismatch, increased mechanical stresses of the sutures and the blood-vessels, etc. Yet, it is not completely clear in what specific way and how important the influence of each factor is on the development of intimal hyperplasia.

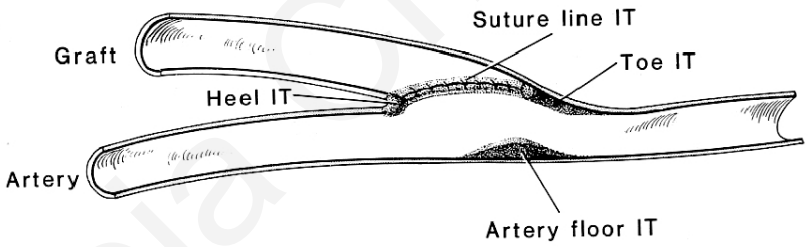

Figure 3-11: Development of intimal hyperplasia at an end-to-side anastomosis; IT: Intimal Thickening (after Bassiouny et al. [23]).

3.7 Compliance

The blood-vessels and anastomotic region response is frequently calculated in terms of compliance [17, 18, 20–22]. Compliance is the ability of a blood-vessel to distend and increase its diameter under applied intraluminal pressures. It is mathematically defined as the circumferential strain of the systolic phase in respect to the strain of the diastolic phase, ε_{sd} , divided by the pressure difference:

$$\text{Compliance} = \frac{D_s - D_d}{D_d (p_s - p_d)} = \frac{\varepsilon_{sd}}{(p_s - p_d)} \tag{3.1}$$

where D_s and D_d are the blood vessel diameters under systolic and diastolic pressure, respectively, and p_s and p_d are the systolic and diastolic pressures, respectively.

A graft that has equal compliance to that of the host artery is considered to be the optimal choice, to favor the decreased thickening of the intimal and the increased patency of the graft.

Researchers who studied the compliance of end-to-end anastomosis observed that, for some cases, a para-anastomotic hypercompliant zone (PHZ) exists. The PHZ phenomenon was observed for the first time by Hasson et al. [17]. Since then, several other researchers investigated the phenomenon [18, 20–22, 64].

A PHZ exists when the compliance of the host artery or the graft is increased to a maximum before falling to a minimum at the suture line. Figure 3-12 shows an experimental-response profile of an end-to-end anastomosis. The diameter profile along the anastomotic region (Figure 3-12(a)) does not reveal the PHZ phenomenon, whereas the compliance profile along the anastomotic region (Figure 3-12(b)) does reveal the PHZ existence close to the suture line (point 0 mm). Away from the suture line (6-10 mm) the compliance is constant.

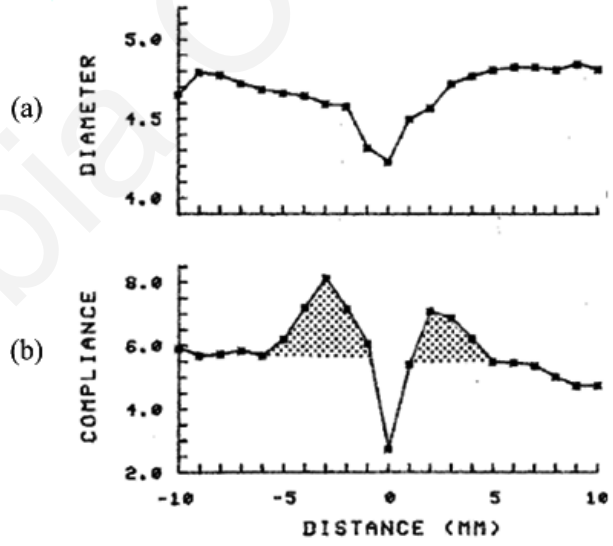

Figure 3-12: Response profiles of an end-to-end anastomosis along the anastomotic region: (a) Diameter of anastomosis measured by pulsed ultrasound instrument, (b) Compliance measured as % radial change/mmHg, $\times 10^{-2}$ (after Hasson et al. [17]).

CHAPTER 4

Arterial Dynamic Response: Linear Model

4.1 Introduction

From the mechanics point of view, the human arterial system can be idealized as a system of cylindrical elastic pipes that transport blood under pressure provided from the heart [65]. As discussed in Section 3.3, the arterial tissue is heterogeneous, consisting of three inhomogeneous layers. Its mechanical properties depend on the artery location, age, disease, and other physiological states [44, 45]. In general, the mechanical behavior of the arterial tissue does not obey Hooke's law [46, 47], exhibiting anisotropic nonlinear behavior for finite deformations. Moreover, the response of biological tissues is affected by the existence of residual stresses [57].

Herein the blood vessel is modeled as a cylindrical pipe which assumes that the elastic properties (elasticity modulus) of the model incorporate in an average sense the tangential stiffness, the anisotropy, the inhomogeneity, and the residual stresses of the artery walls. Therefore, the arterial wall is assumed to be homogeneous and the mechanical response linear elastic.

This chapter investigates the dynamic response of a linear-elastic artery in terms of the radial displacement away from the anastomotic region. The proposed linear arterial model and the derived closed-form solution described herein have been recently proposed by Demetriou [66]. The model is comprehensive, analytical and adopts the worst-case scenario of blood pressure loading (conservative case). Furthermore, this chapter studies the dynamic response of the linear-elastic artery under different pressure time-profile approximations, for the first time. Pressure time-profile approximations simulating the first loading cycle (after the blood flow is restored) and the long-term loading are considered.

The formulated linear arterial model is a single-degree-of-freedom system. By assuming a pulse-type loading approximation the system response can be analytically derived by means of Duhamel's integral. In this way, is obtained a general closed-form solution for the far-field response of the anastomosis. When considering more complex loading approximations, the response is derived through numerical methods.

Note that, the aforementioned model constitutes the basis of the hyperelastic and viscoelastic models proposed in Chapters 5 and 6 respectively. In addition, the derived maximum radial displacement is adopted by the displacement-based methodology

proposed in Chapter 7, in order to account for the arterial axial-circumferential deformation coupling and suture-artery interaction of end-to-end anastomosis.

4.2 Review of previous work

This section describes the dynamic response of the linear-elastic artery, away from the anastomotic region, based on the work of Demetriou [66]. Furthermore, the derived closed-form solution is presented.

4.2.1 Mathematical model

Figure 4-1(a) shows the configuration of the arterial model considered in this chapter. The artery is modeled as an elastic cylindrical pipe with wall thickness H_p and radius R_p. Note that, the thickness and radius are measured at zero blood pressure and in vivo length, implying that the artery is in its pre-stressed state. The mathematical formulation is based on the following assumptions: (a) the centerline of the ring in the undeformed state forms a full circle with radius R_p; (b) the arterial wall thickness is small compared to the radius of the centerline of the ring therefore the radial stresses are not considered; (c) the cross-section is axially symmetric and constant around the circle, implying that the arterial wall has constant thickness; (d) the arterial tissue consists of a single homogeneous layer; (e) the arterial tissue behaves as a simple orthotropic linear-elastic material (i.e. the mechanical properties in the radial and circumferential directions are the same and differ from those in the longitudinal direction, ignoring the Poisson effect in the orthotropy constitutive law); (f) no boundary constraints are applied on the ring; (g) the effects of rotary inertia and shear deformation are neglected; and (h) viscous effects are ignored. Note that, the simplified orthotropic model utilizes two elastic constants, E_θ and E_L, representing the plane-strain elastic moduli in the circumferential and the longitudinal directions respectively [64].

4.2.1.1 Response to general dynamic loading

The axially-symmetric arterial model undergoes in-plane extensional vibration due to a uniformly-distributed wall pressure $p(t)$. The flow-induced wall shear stresses are ignored. Their contribution to the response of the structural system is insignificant, since the flow-induced wall shear stresses values are very low (of the order of 100 Pa) compared to the principal stresses of the arterial walls (of the order of 100 kPa).

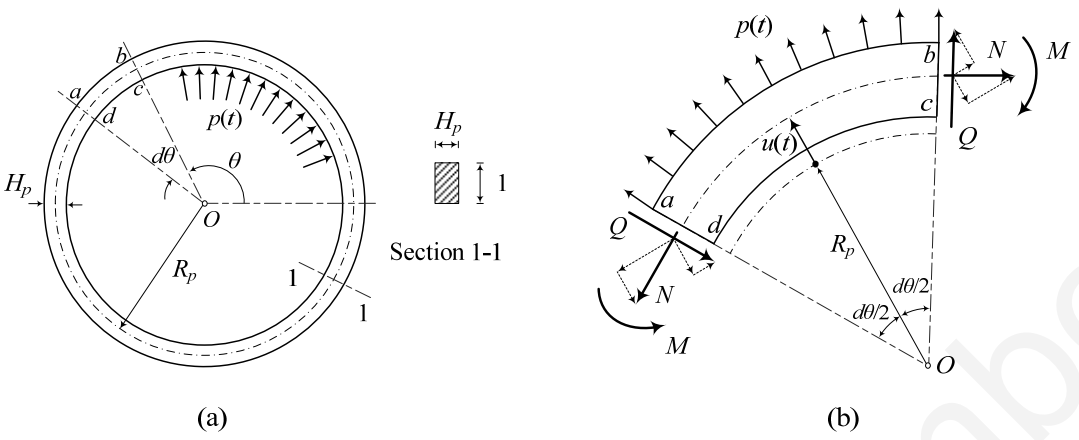

Figure 4-1: (a) Configuration of the linear arterial model considered in this chapter, (b) free-body diagram of a typical element of arterial ring.

The differential equation governing the radial displacement $u(t)$ of the vibrating arterial ring can be derived by considering the forces acting on the infinitesimal element of unit length shown in Figure 4-1(b). Equilibrium of forces in the radial direction requires that:

$$p(t)R_p d\theta - N(t)\sin\left(\frac{d\theta}{2}\right) - N(t)\sin\left(\frac{d\theta}{2}\right) = m\frac{d^2u(t)}{dt^2} \tag{4.1}$$

where $m = \rho_0 R_p H_p d\theta$ is the mass of the unit-length arterial element, ρ_0 is the density of the arterial tissue, and N is the unit-length axial force.

From Hooke's law, the axial force is given by

$$N(t) = E_\theta H_p \frac{u(t)}{R_p} \tag{4.2}$$

On substituting the above expression in Equation (4.1), and by assuming small angles (so that $\sin(d\theta/2) \approx d\theta/2$), we obtain

$$p(t)R_p d\theta - E_\theta H_p \frac{u(t)}{R_p} d\theta = \rho_0 R_p H_p d\theta \frac{d^2u(t)}{dt^2} \tag{4.3}$$

By dividing Equation (4.3) by $R_p d\theta$ we obtain the equation governing the radial displacement response as

$$\rho_0 H_p \frac{d^2u(t)}{dt} + \frac{E_\theta H_p}{R_p^{\,2}} u(t) = p(t) \tag{4.4}$$

This second-order differential equation is similar to the classical equation of motion of an undamped single-degree-of-freedom system to arbitrary excitation. The first term represents the radial inertia force acting on element *abcd* of the arterial ring, while the second term represents the circumferential tensile force developed on the element cross-section. The circular frequency of the system can be readily derived as

$$\omega_n = \frac{1}{R_p}\sqrt{\frac{E_\theta}{\rho_0}} \tag{4.5}$$

Equation (4.4) can be solved analytically by means of Duhamel's integral.

4.2.1.2 Response to pulse-type loading

Figure 4-2 shows a typical aortic blood pressure profile (left) along with the arterial pulse time-profile approximation adopted in the calculations (right). The time interval $0 \le t \le t_s$ represents the aortic systolic phase, whereas the time interval $t_s < t \le t_{cp}$ represents the aortic diastolic phase.

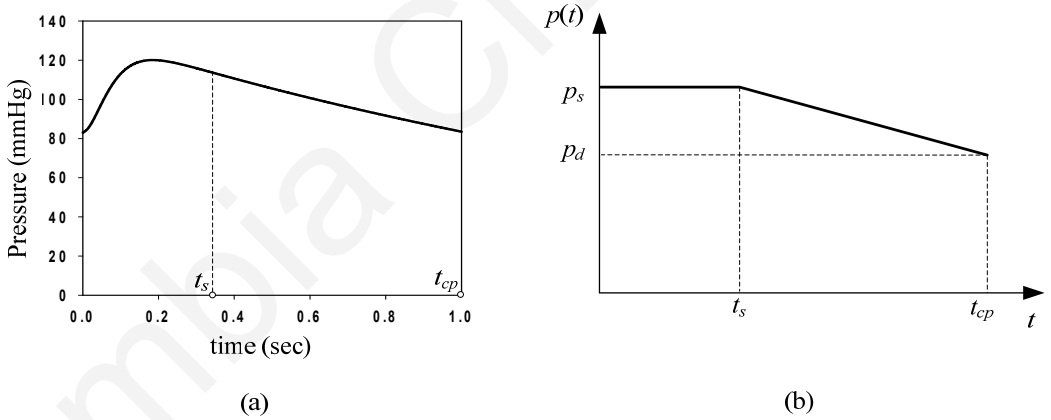

(a) (b)

Figure 4-2: (a) Typical aortic pressure-time profile following Zhong et al. [39], (b) arterial pulse time-profile approximation. (100mmHg=13.33kPa)

During a vascular surgery operation the blood flow is interrupted. The first loading cycle, immediately after the flow is restored, is approximated by the loading shown in Figure 4-2(b). This analysis adopts the worst-case scenario of blood pressure loading (conservative case) in which the internal pressure is abruptly increased from zero to the maximum systolic pressure. The assumed loading is expressed as

$$p(t) = \begin{cases} p_s & , \ 0 \le t \le t_s \\ p_s - \dfrac{p_s - p_d}{t_{cp} - t_s}\left(t - t_s\right) & , \ \mathrm{t}_s < t \le \mathrm{t}_{cp} \end{cases} \tag{4.6}$$

where p_s is the maximum systolic pressure, p_d the diastolic pressure, t_s the systolic-phase duration, and t_{cp} the total duration of the cardiac pulse.

The radius R_p is measured at zero blood pressure and in vivo length, implying the artery is in its pre-stressed state. During surgery the following procedure takes place: (a) the diseased blood vessel is cut transversely and longitudinal residual stresses are released, forcing the artery to decrease its length and increase its diameter; (b) When subsequently the stitching takes place, the arterial diameter and length return to their prior condition. The residual-stress effect is taken into account by considering an initial displacement $u(0) = u_0$, equal to the difference of the increased radius (relieved from axial residual stresses) and radius R_p, and initial velocity $\dot{u}(0) = 0$; and (c) The blood flow is restored and the anastomosis is subjected to dynamic blood pressure.

The total response of the system is the sum of the response to the pulse loading $u_p(t)$ $u_p(t)$ and the response to free vibration $u_f(t)$ due to initial conditions.

The response to free vibration with initial displacement $u_f(0) = u_0$ and initial velocity $\dot{u}_f(0) = 0$ is obtained by standard methods as

$$u_f(t) = u_0 \cos \omega_n t, \qquad 0 \le t \le t_{cp} \tag{4.7}$$

The dynamic response of a linear single-degree-of-freedom system to arbitrary external force $p(t)$ can be determined by means of the convolution (Duhamel) integral. A convolution integral is the sum of the all unit-impulse response functions $h(t-\tau)$ times the respective magnitude $p(\tau)d\tau$ up to time t, yielding

$$u_p(t) = \int_0^t p(\tau)h(t-\tau)d\tau = \frac{1}{m\omega_n}\int_0^t p(\tau)\sin\left[\omega_n(t-\tau)\right]d\tau \tag{4.8}$$

The systolic-phase response, in which the system is subjected to constant force $p(\tau) = p_s$, is obtained as

$$u_p{}^{I}(t)=\frac{1}{m\omega_n}\int_0^t p_s\sin\left[\omega_n(t-\tau)\right]d\tau=\frac{p_s R_p{}^2}{E_\theta H_p}\left(1-\cos\omega_n t\right),\qquad t\le t_s \tag{4.9}$$

whereas the diastolic-phase response, in which the system is subjected to force $p(\tau)=p_s-(p_s-p_d)\left(\tau-t_s\right)/(\,t_{cp}-t_s)$, is derived from

$$u_p{}^{II}(t)=\frac{1}{m\omega_n}\int_{t_s}^t\left[p_s-\frac{p_s-p_d}{t_{cp}-t_s}(\tau-t_s)\right]\sin\left[\omega_n(t-\tau)\right]d\tau+u_p{}^{I}(t_s)\cos\omega_n(t-t_s)$$
$$+\frac{\dot{u}_p{}^{I}(t_s)}{\omega_n}\sin\omega_n(t-t_s),\quad t_s<t\le t_{cp} \tag{4.10}$$

in which the first term represents the force-vibration response associated with the diastolic-phase loading, and the last two terms concern the free-vibration response due to initial conditions $u_p{}^{I}(t_s)$ and $\dot{u}_p{}^{I}(t_s)$ induced at the end of the systolic phase. On carrying out the calculations, Equation (4.10) reduces to

$$u_p{}^{II}(t)=\frac{p_s R_p{}^2}{E_\theta H_p}\left\{\frac{p_s-p_d}{t_{cp}-t_s}\left[t_s-t+\frac{\sin\omega_n\left(t-t_s\right)}{\omega_n}\right]+p_s\left(1-\cos\omega_n t\right)\right\},\quad t_s<t\le t_{cp} \tag{4.11}$$

The complete solution is equal to the sum of the pulse-loading response $u_p(t)$ and the free-vibration response $u_f(t)$. The total response of the system as a function of time is obtained as

$$u\left(t\right)=\begin{cases}u_0\cos\omega_n t+\dfrac{p_s R_p{}^2}{E_\theta H_p}\left(1-\cos\omega_n t\right), & 0\le t\le t_s\\[2ex] u_0\cos\omega_n t+\dfrac{p_s R_p{}^2}{E_\theta H_p}\left\{\dfrac{p_s-p_d}{t_{cp}-t_s}\left[t_s-t+\dfrac{\sin\omega_n\left(t-t_s\right)}{\omega_n}\right]+p_s\left(1-\cos\omega_n t\right)\right\} & \\ \qquad\qquad , t_s<t\le t_{cp}\end{cases} \tag{4.12}$$

The first term of Equation (4.12) (free-vibration response) is related with the residual-stress effect and the second term of Equation (4.12) is related with the response to the assumed pulse-type loading.

The static displacement of the system due to the maximum pressure p_s, is identified as

$$u_{st} = \frac{p_s R_p^{\,2}}{E_\theta H_p} \tag{4.13}$$

Of particular interest is the maximum arterial displacement, which is associated with the critical response of the anastomotic region. The maximum displacement of the arterial system may occur either during the systolic phase ($0 \le t \le t_s$) or during the diastolic phase ($t_s < t \le t_{cp}$), depending on the system circular frequency and the characteristics of the pulse loading.

The maximum displacement of the systolic phase (for $|u_0|/u_{st} < 1$) occurs for $\cos \omega_n t = -1$. Therefore, by substituting this expression into the first part of Equation (4.12) the maximum displacement of the systolic phase $u^I_{\max}$ is expressed as

$$u^I_{\max} = \frac{2 p_s R_p^{\,2}}{E_\theta H_p} - u_0 \tag{4.14}$$

To calculate the time instant t_1 corresponding to the maximum response of the diastolic phase, the derivative of the displacement with respect to time is set equal to zero:

$$\begin{aligned} \frac{du(t)}{dt} = {} & \frac{p_s R_p^{\,2}}{\omega_n E_\theta H_p}\left(\frac{p_s - p_d}{t_{cp} - t_s}\right) + \sin \omega_n t_1 \left[\frac{p_s R_p^{\,2}}{E_\theta H_p} + \frac{R_p^{\,2}}{E_\theta H_p}\frac{p_s - p_d}{t_{cp} - t_s}\frac{\sin \omega_n t_s}{\omega_n} - u_0\right] \\ & + \cos \omega_n t_1 \left[\frac{R_p^{\,2}}{E_\theta H_p}\frac{p_s - p_d}{t_{cp} - t_s}\frac{\sin \omega_n t_s}{\omega_n}\right] = 0 \end{aligned} \tag{4.15}$$

which can be recast in the following form

$$B_1 = \sqrt{B_2^{\,2} + B_3^{\,2}} \cos\left(\omega_n t_1 - \tan^{-1}\left|\frac{B_2}{B_3}\right|\right) \tag{4.16}$$

in which

$$B_1 = -\frac{p_s R_p^{\,2}}{\omega_n E_\theta H_p}\left(\frac{p_s - p_d}{t_{cp} - t_s}\right) \tag{4.17}$$

$$B_2 = \frac{p_s R_p^{\,2}}{E_\theta H_p} + \frac{R_p^{\,2}}{E_\theta H_p}\frac{p_s - p_d}{t_{cp} - t_s}\frac{\sin \omega_n t_s}{\omega_n} - u_0 \tag{4.18}$$

$$B_3 = \frac{R_p^{\,2}}{E_\theta H_p}\frac{p_s - p_d}{t_{cp} - t_s}\frac{\sin\omega_n t_s}{\omega_n} \tag{4.19}$$

On solving for t_1 we get

$$t_1 = \frac{1}{\omega_n}\left(\cos^{-1}\frac{B_1}{\sqrt{B_2^{\,2} + B_3^{\,2}}} + \tan^{-1}\left|\frac{B_2}{B_3}\right|\right) \tag{4.20}$$

The maximum displacement of the diastolic phase $u_{\max}^{II}$ is calculated at $t = t_1$ as

$$u_{\max}^{II} = u_0\cos\omega_n t_1 + \frac{R_p^{\,2}}{E_\theta H_p}\left[\frac{p_s - p_d}{t_{cp} - t_s}\left(t_s - t_1 + \frac{\sin\omega_n(t_1 - t_s)}{\omega_n}\right) + p_s\left(1 - \cos\omega_n t_1\right)\right] \tag{4.21}$$

The maximum response is then obtained through the overall maximum of expressions (4.14) and (4.21) as

$$u_{\max} = \max\left\{\begin{array}{l}\dfrac{2p_s R_p^{\,2}}{E_\theta H_p} - u_0, \\ u_0\cos\omega_n t_1 + \dfrac{R_p^{\,2}}{E_\theta H_p}\left[\dfrac{p_s - p_d}{t_{cp} - t_s}\left(t_s - t_1 + \dfrac{\sin\omega_n(t_1 - t_s)}{\omega_n}\right) + p_s\left(1 - \cos\omega_n t_1\right)\right]\end{array}\right\} \tag{4.22}$$

Figure 4-3 plots the normalized maximum deformation $u_{\max}/u_{st}$ as a function of the ratio t_s/T_n for different values of initial displacement, and for typical values of diastolic pressure ($p_d = 80$ mmHg), maximum systolic pressure ($p_s = 120$ mmHg), and cardiac pulse duration ($t_{cp} = 1$ sec). In particular, Figure 4-3(a) plots the normalized response for a typical cardiac pulse with fixed systolic-phase duration, $t_s = 0.35$ sec, and systems with different natural period $T_n = 2\pi/\omega_n$. In this case, the response exhibits an ascending curved profile for low values of t_s/T_n, reaching a plateau for high values of t_s/T_n. The threshold value of t_s/T_n that defines the boundary between the ascending part and the plateau depends on the loading characteristics. For the parameters used in Figure 4-3(a), the threshold value of t_s/T_n is approximately 0.4. Figure 4-3(b) plots the normalized response for a system with high value of natural period ($T_n = 0.9$ sec), implying that the system has severely damaged artery walls, with the artery elasticity modulus tending to zero, and different systolic-phase durations t_s. For high values of t_s/T_n the response is

equal to that of Figure 4-3(a), whereas for low values of t_s / T_n this case exhibits higher response values.

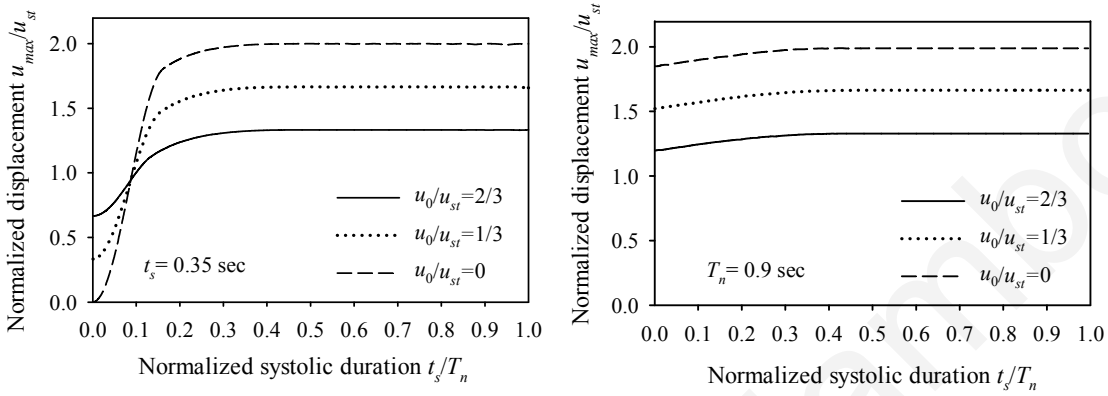

(a) (b)

Figure 4-3: Normalized maximum displacement as a function of the ratio t_s / T_n, for different values of the initial displacement u_0 / u_{st}, and for (a) $t_s = 0.35$ sec, (b) $T_n = 0.9$ sec.

4.3 Response to different loading approximations

The loading approximation used in the previous section concerns the first loading cycle, immediately after the flow is restored. The internal pressure was abruptly increased from zero to the maximum systolic pressure. To the best of our knowledge, there is no other study that simulates the first loading cycle immediately after the blood flow is restored. Other studies consider that the vascular anastomosis is already under diastolic pressure, and subjected dynamically only to the overpressure $p_s - p_d$.

In order to study the effect of different loading approximations on the maximum response, six different blood pressure profiles are considered. All profiles assume typical parameter values: $p_s \approx 120$ mmHg, $p_d \approx 80$ mmHg, $t_s = 0.35$ sec, $t_{cp} = 1$ sec. The pressure time-profiles of Figure 4-4(a)-(d) simulate the first loading cycle, immediately after the blood flow is restored, whereas the pressure time-profiles of Figure 4-4(e) and (f) simulate the long-term loading, implying that the artery was incrementally subjected to the diastolic pressure and then inflated due to the overpressure $p_s - p_d$. In particular, the six pressure time-profiles of Figure 4-4 stand for: (a) the aortic pressure proposed by Zhong et al. [39], simulating the first loading cycle; (b) constant-ramp pressure, simulating the first loading

cycle; (c) step pressure, simulating the first loading cycle; (d) smoothly increased pressure, simulating the first loading cycle; (e) long-term aortic pressure; and (f) long-term periodic aortic pressure.

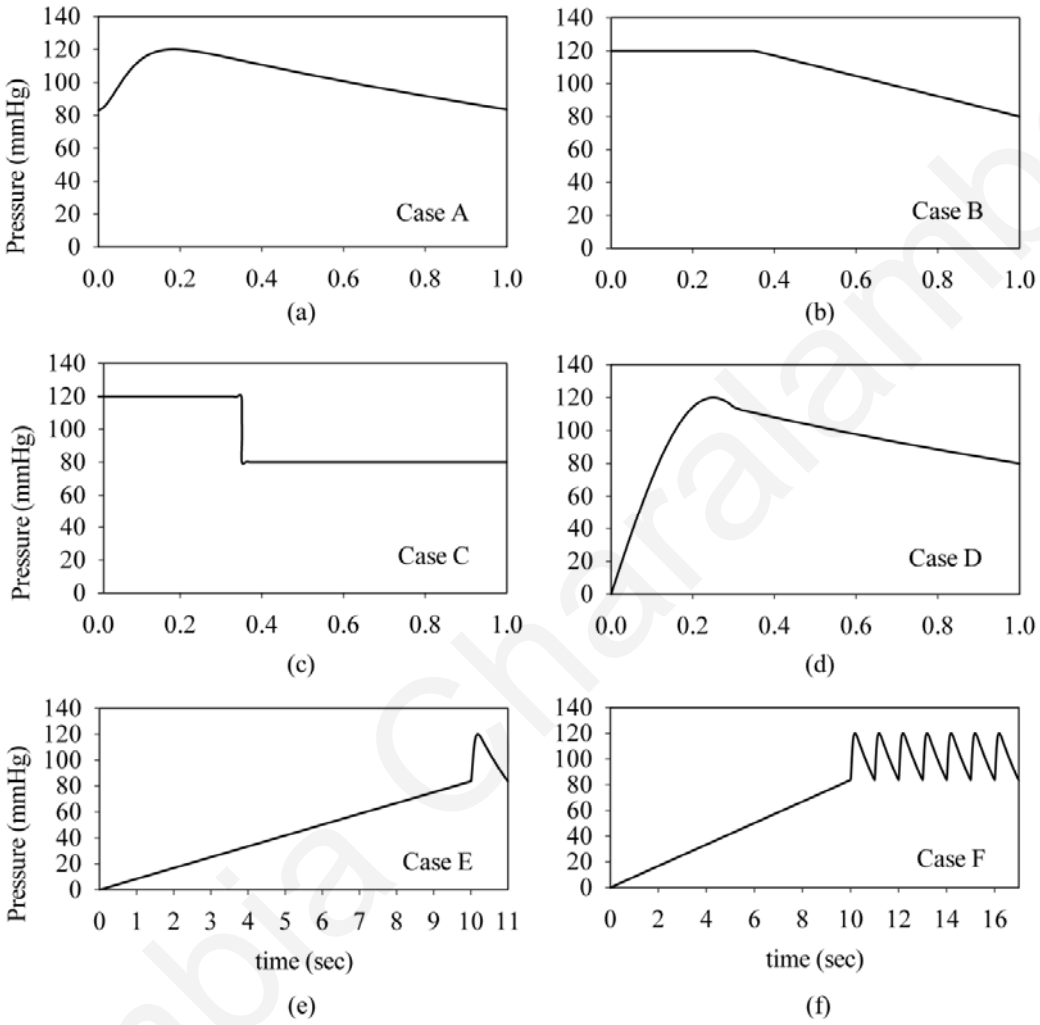

Figure 4-4: First loading cycle and long-term loading approximations. First loading cycle loadings: (a) Aortic pressure proposed by Zhong et al. [39]; (b) Constant-ramp pressure; (c) Step pressure; (d) Smoothly increased pressure. Long-term loadings: (e) Aortic pressure; (f) Periodic aortic pressure.

For typical values of the mechanical and geometrical characteristics of arteries the system natural period is in the range of 0.001-0.015 sec. The displacement spectrum of Figure 4-5 plots the normalized maximum radial displacement for arteries with natural periods 0-0.1 sec. All differential equations were solved numerically by using the ode23s function in MATLAB [67].

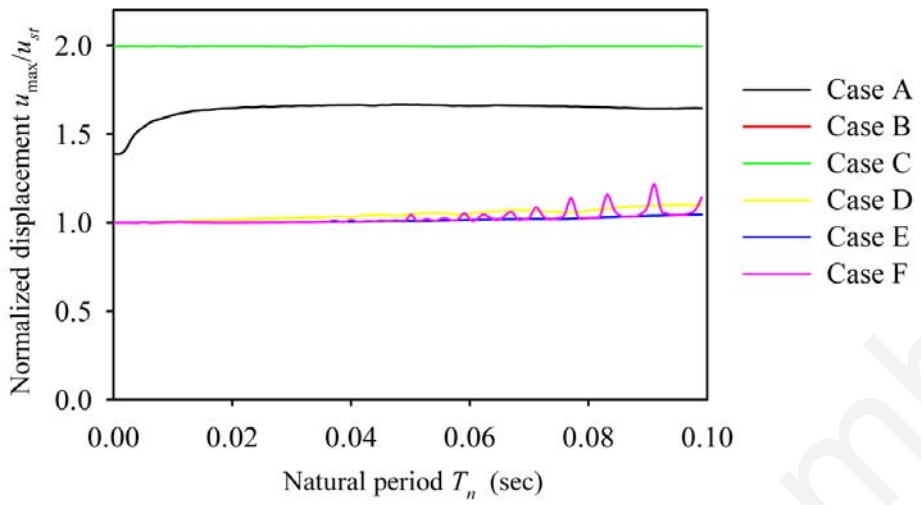

Figure 4-5: Spectrum of normalized maximum radial displacement for different blood pressure approximations ($u_0 = 0$).

As expected, cases simulating the first loading cycle exhibit higher normalized response values compared to the overpressure (long-term) loadings. In particular, cases B and C have equal response values and are the most conservative cases. Their maximum displacement is equal to two times the static displacement. The maximum displacement of case A is about 1.4-1.7 times the static displacement, whereas the maximum displacement of the smoothly increased pressure-profile of case D is about 1-1.1 times the static displacement. The maximum displacement under applied long-term loadings (case E and F) is approximately equal to the static displacement. Note that, under periodic loading (Case F of Figure 4-5) some systems with natural period values higher than 0.04 sec exhibit increased amplitude (spikes), indicating resonance and possible failure. As mentioned previously, typical arterial systems have natural period values lower than 0.04 sec, meaning that these systems may correspond to soft aneurysmatic arteries prone to rupture.

4.4 Concluding remarks

This Chapter investigates the response of the linear-elastic arterial model. An analytical time-dependent solution for the radial displacement of arteries (Equation (4.12)) is presented. For typical values of the geometric and mechanical properties of arteries the derived natural-frequency expression (Equation (4.5)) is of the order of 100-1000 Hz (natural period values of the order of 0.001-0.01 sec). We can say that under dynamic blood pressure the maximum response of a typical artery is equal to the maximum response

of the systolic phase (Equation (4.14)) and does not depend on the systolic-phase duration, the cardiac pulse duration, or the value of systolic pressure. It does depend on the systolic pressure value, the geometric and mechanical properties of the artery, and the initial displacement u_0.

By investigating different pressure time-profile approximations, it is observed that the worst-case scenario (first cardiac cycle) of the linear-elastic response is equal to two times the static (linear-elastic) response. The smoother the pressure increase from zero to the peak systolic pressure is, the lower the maximum displacement is (tending to become equal to the static displacement, Figure 4-4). In the case of long-term loading (case E and F of Figure 4-4), the maximum displacement is approximately equal to the static displacement, since the ratio of the cardiac pulse duration to the natural period of the artery is of the order of 100-1000.

The findings of this chapter constitute the basis of the hyperelastic and viscoelastic arterial models proposed in Chapters 5 and 6, respectively, and of the end-to-end anastomosis analysis presented in Chapter 7. Thus, these general closed-form expressions can form the basis for the development of vascular anastomosis guidelines, aiming to the prevention of post-surgery complications.

CHAPTER 5

Arterial Dynamic Response: Hyperelastic Model

5.1 Introduction

When human arteries are subjected to time-dependent arterial blood pressure they demonstrate large deformations, exhibiting mainly nonlinear hyperelastic type of response. Their stiffness depends on strain [68], since it is monotonically increasing with increasing strain. In this way, the artery is protected from aneurysms and other instabilities under increasing pressure. Typically, healthy arteries demonstrate convex strain hardening under tensile loading, atheromatic arteries demonstrate stiffer response, whereas aneurysmatic arteries demonstrate softening response.

The stress-strain relationship of hyperelastic materials derives from a strain-energy density function. The strain-energy density functions are usually expressed as a function of the principal invariants:

$$W = f\left(I_1, I_2, ..\right) \tag{5.1}$$

Several simple constitutive laws describing the mechanical behavior of biological tissues [51–56] exist in the literature. More sophisticated constitutive laws have been developed in recent years, such as the multi-parameter hyperelastic law proposed by Holzapfel et al. [69], which accounts for the material anisotropy and two families of collagen fibers arranged in symmetrical spirals. However, complex multi-parameter constitutive laws require many material parameters that cannot be easily obtained.

This chapter examines the effect of strain hardening in the dynamic response of human arteries, and compares the hyperelastic arterial response to the respective linear response. In particular, three material behaviors are investigated: (a) the hardening behavior of healthy arteries, (b) the hardening behavior of atherosclerotic arteries, and (c) the softening behavior of aneurysmatic arteries.

In general, arteries are anisotropic however, we are mainly concerned with the deformation of the artery cross-section and the hardening effect. Accordingly, the following isotropic hyperelastic models are adopted for each case respectively: (a) the constitutive law proposed by Skalak et al. [55], (b) the constitutive law of Delfino et al. [56], as modified by Hariton [70], and (c) the Mooney-Rivlin hyperelastic material [51, 52].

Figure 5-1 plots the stress-strain relationships of the linear and nonlinear constitutive laws for typical values of their material parameters, and in the absence of longitudinal pre-stretch ($\lambda_z^0 = 1$). By $\sigma_{\theta\theta}$ is denoted the circumferential Cauchy stress. We can observe that under increased strain the stress-strain relationship of Skalak et al. exhibits hardening, the Hariton model exhibits exponential hardening, and the Mooney-Rivlin model exhibits softening.

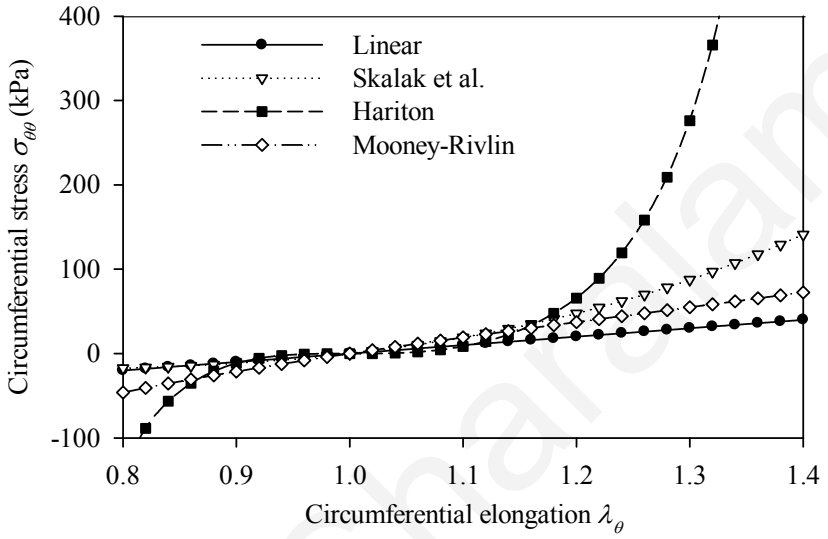

Figure 5-1: Circumferential stress-strain diagrams of hyperelastic incompressible models. No pre-stretch is applied to the models ($\lambda_z^0 = 1$).

The cross-section of the artery is modeled as a circular ring, consisting of a single homogenized layer. The arterial ring is subjected to dynamic intraluminal pressure, resulting in the formulation of a single-degree-of-freedom system. Note that, the worst-case loading approximation scenario (first loading cycle after the blood flow is restored) is considered.

By adopting the aforementioned hyperelastic strain-energy density functions the physical problem is described by nonlinear differential equations that require numerical methods to be solved. The results of the following analyses are characterized by generality and are presented in pictorial and tabular form.

5.2 Mathematical model

In formulating the mathematical model of the hyperelastic artery the following assumptions are considered: (a) the arterial wall thickness is small compared to the radius of the vessel; (b) the vessel cross-section in the undeformed state forms a full circle with

thickness-averaged radius R; (c) the arterial wall has constant thickness along the circle; (d) no boundary constraints are applied on the ring; (e) the effects of rotary inertia and shear deformation are neglected; (f) the arterial tissue consists of a single (homogeneous) layer; and (g) viscous effects are ignored. Note that arteries exhibit longitudinal and circumferential residual stresses. The longitudinal pre-stress will be accounted for by a constant longitudinal pre-stretch value, whereas other pre-stress effects will be assumed to be incorporated into the material constants of the constitutive law.

Herein, R, H, and L denote respectively the radius, thickness, and length of the initial configuration; and r, h, l denote respectively the radius, thickness, and length of the deformed configuration.

The deformed artery exhibits circumferential ($\sigma_{\theta\theta}$), longitudinal (σ_{zz}), and radial (σ_{rr}) Cauchy stresses as shown in Figure 5-1. Note that, based on the thin-wall assumption and in the absence of pressure on the outer wall, the radial stresses are almost zero.

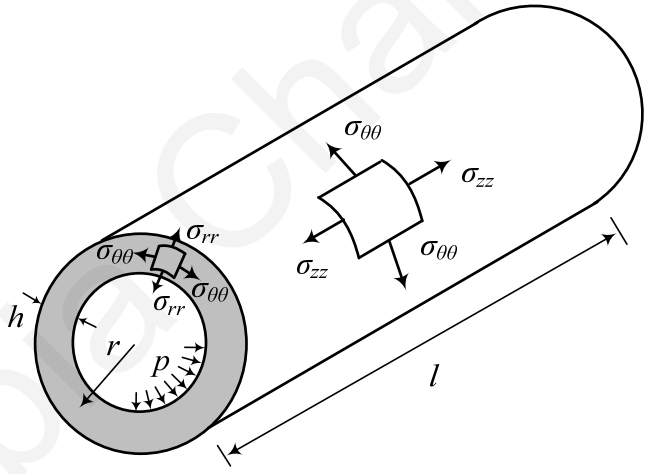

Figure 5-2: Stresses of thin-walled cylinder.

By considering the force equilibrium along the radial direction of the infinitesimal element shown in Figure 5-3(b), the equation of motion of the deformed model (Figure 5-3(a)) is obtained as

$$r(t)p(t) - N(t) = \rho_0 h(t) r(t) \frac{d^2 u_r(t)}{dt^2} \tag{5.2}$$

in which ρ_0 is the density of the arterial tissue, $p(t)$ is the uniform intraluminal pressure, $N(t)$ is the axial circumferential force that can be derived from a proper hyperelastic

constitutive law, and $u_r(t)$ is the radial displacement. Due to the mass conservation and incompressibility of the arterial tissue the initial density of the artery ρ_0 is equal to the density of the artery at the deformed state ρ. The deformed radius is expressed as

$$r(t) = R + u_r(t) \tag{5.3}$$

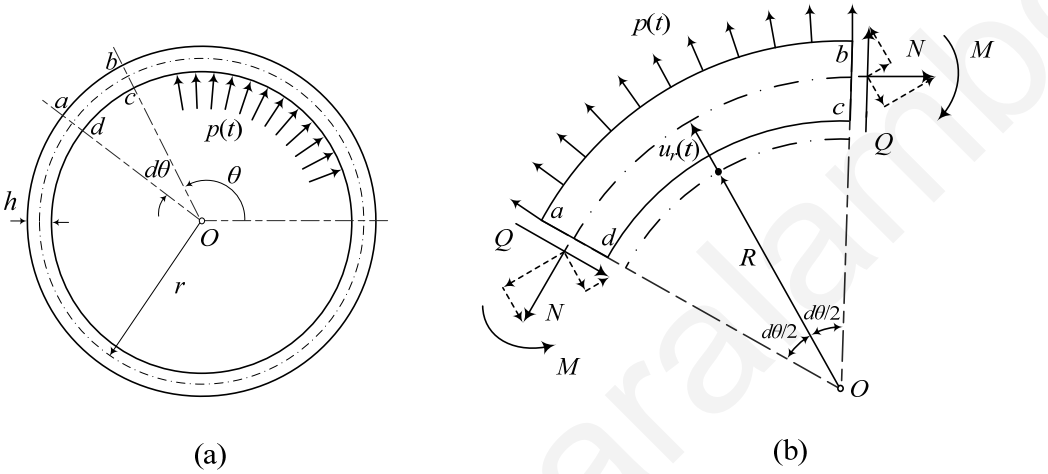

(a) (b)

Figure 5-3: (a) Hyperelastic arterial model at deformed state, (b) Typical element of arterial ring at deformed state.

For incompressible materials, such as the arterial walls and many artificial grafts, the determinant of the deformation gradient is equal to one and is expressed as

$$|\mathbf{F}| = J = \lambda_\theta(t)\lambda_r(t)\lambda_z = 1 \tag{5.4}$$

where $\lambda_\theta(t) = r(t)/R$ is the elongation in the circumferential direction, $\lambda_z = \lambda_z^0 = l/L$ is the elongation in the axial direction, and $\lambda_r(t) = h(t)/H$ is the elongation in the radial direction. On substituting these expressions in Equation (5.4), the deformed radius times the deformed thickness can be expressed as

$$r(t)h(t) = \frac{RH}{\lambda_z^0} \tag{5.5}$$

The general expressions of the strain and stress tensors can be found in Appendix A.

The following sections elaborate on the mathematical formulation of three arterial models, each one adopting one of the aforementioned hyperelastic constitutive laws.

5.2.1 Arterial model based on the strain-energy function of Skalak et al.

By adopting the isotropic, two-dimensional strain-energy function of Skalak et al. [55] we aim to investigate the response of healthy arteries or problematic arteries of which the deceased part was removed after surgery. This strain-energy function, originally developed for red blood cell membranes, demonstrates hardening behavior.

The strain-energy function proposed by Skalak et al. [55] is

$$W(t)=\frac{B}{4}\left(\frac{1}{2}(I(t))^2+I(t)-II(t)\right)+\frac{C}{8}(II(t))^2 \tag{5.6}$$

where B and C are the material parameters of the artery, having units of elastic modulus multiplied by artery thickness [N/m], and satisfying the condition $C\geq B\geq 0$. The alternative forms of the strain invariants $I(t)$ and $II(t)$ are expressed as

$$I(t)=2(e_{\theta\theta}(t)+e_{zz}(t))=(\lambda_\theta(t))^2+(\lambda_z^0(t))^2-2 \tag{5.7}$$

$$II(t)=4I_1(t)=4e_{\theta\theta}(t)e_{zz}(t)+2(e_{\theta\theta}(t)+e_{zz}(t))=(\lambda_\theta(t))^2(\lambda_z^0(t))^2-1 \tag{5.8}$$

in which $e_{\theta\theta}(t)$ and $e_{zz}(t)$ are the Green strain tensors given by

$$e_{\theta\theta}(t)=\frac{1}{2}\left((\lambda_\theta(t))^2-1\right) \tag{5.9}$$

$$e_{zz}(t)=\frac{1}{2}\left((\lambda_z^0(t))^2-1\right) \tag{5.10}$$

The circumferential and longitudinal Cauchy stress-strain relationships, multiplied by the current artery thickness, are expressed respectively as [55]

$$T_\theta(t)=\frac{\lambda_\theta(t)}{\lambda_z^0}\frac{\partial W}{\partial e_{\theta\theta}}=\frac{\lambda_\theta(t)}{\lambda_z^0}\left[\frac{B}{2}\left((\lambda_\theta(t))^2-1\right)+\frac{C}{2}(\lambda_z^0)^2\left((\lambda_\theta(t))^2(\lambda_z^0)^2-1\right)\right] \tag{5.11}$$

$$T_z=\frac{\lambda_z^0}{\lambda_\theta(t)}\frac{\partial W}{\partial e_{zz}}=\frac{\lambda_z^0}{\lambda_\theta(t)}\left[\frac{B}{2}\left((\lambda_z^0)^2-1\right)+\frac{C}{2}(\lambda_\theta(t))^2\left((\lambda_\theta(t))^2(\lambda_z^0)^2-1\right)\right] \tag{5.12}$$

Figure 5-4 shows the Cauchy stresses acting along the circumferential and longitudinal directions of the arterial model, and Figure 5-5 plots the Skalak et al. circumferential stress-strain relationship for different values of the ratio B/C. By increasing the ratio

B/C the hardening behavior of the material is increased, whereas for negative strains the model demonstrates softening. Note that, for $B/C=0$ the circumferential and longitudinal stresses are equal.

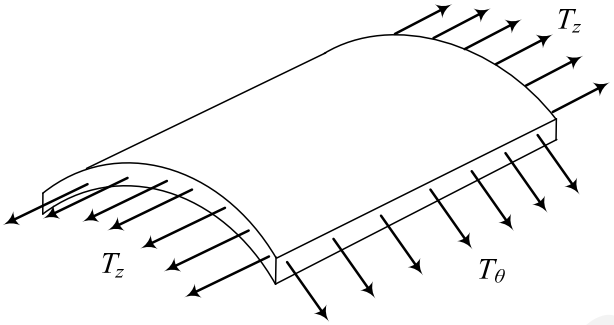

Figure 5-4: Circumferential stresses T_θ and axial stresses T_z multiplied by the current artery thickness.

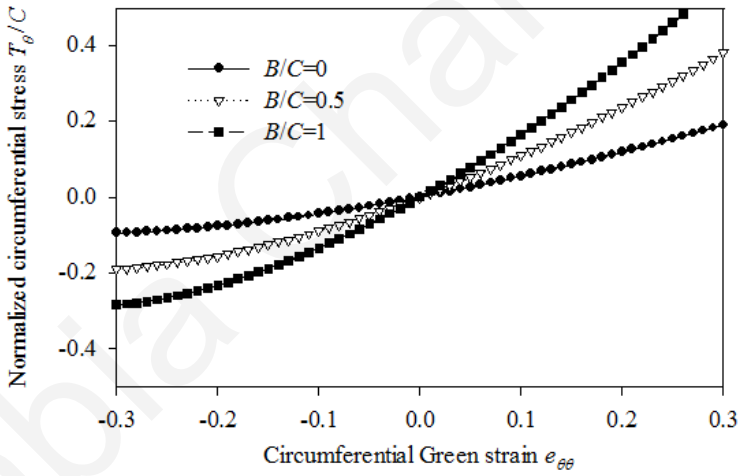

Figure 5-5: Normalized circumferential stress-strain diagram of Skalak et al. [55] hyperelastic model for different values of the ratio B/C, and for $\lambda_z^0=1$.

The circumferential stress, multiplied by the current artery thickness $T_\theta(t)$ is identical to the force acting along the circumferential direction $N(t)$. Thus, on substituting equations (5.3), (5.5), (5.11) in Equation (5.2) we obtain the normalized equation of motion of the arterial model as

$$-\left(1+\frac{u_r(t)}{R}\right)\left[\frac{B}{2C\lambda_z^0}\left(\frac{2u_r(t)}{R}+\frac{u_r(t)^2}{R^2}\right)+\frac{(\lambda_z^0)^3}{2}+\frac{u_r(t)}{R}(\lambda_z^0)^3+\frac{u_r(t)^2}{R^2}\frac{(\lambda_z^0)^3}{2}-\frac{\lambda_z^0}{2}\right]$$
$$+\left(1+\frac{u_r(t)}{R}\right)p(t)\frac{R}{C}=\frac{\rho_0 R^2 H}{C\lambda_z^0}\frac{\ddot{u}_r(t)}{R} \qquad (5.13)$$

The equation of motion can be expressed in polynomial form of the normalized radial displacement as

$$-\frac{u_r(t)}{R}\left[\frac{B}{C\lambda_z^0}+\frac{3(\lambda_z^0)^3}{2}-\frac{\lambda_z^0}{2}\right]-\left(\frac{u_r(t)}{R}\right)^2\left[\frac{3B}{2C\lambda_z^0}+\frac{3(\lambda_z^0)^3}{2}\right]-\left(\frac{u_r(t)}{R}\right)^3\left[\frac{B}{2C\lambda_z^0}+\frac{(\lambda_z^0)^3}{2}\right]+$$
$$\left[\left(1+\frac{u_r(t)}{R}\right)p(t)\frac{R}{C}-\frac{(\lambda_z^0)^3}{2}+\frac{\lambda_z^0}{2}\right]=\frac{\rho_0 R^2 H}{C\lambda_z^0}\frac{\ddot{u}_r(t)}{R} \qquad (5.14)$$

The physical problem is reduced to six dimensionless quantities: B/C, λ_z^0, $p(t)R/C$, $u_r(t)/R$, $t_{Sk}^2\ddot{u}_r(t)/R$, and t/t_{Sk}, where $t_{Sk}=\sqrt{\rho_0 R^2 H/C\lambda_z^0}$ is the characteristic time of the response. The initial tangent circumferential Young's modulus E_θ^0 can be expressed in terms of the material parameters B and C as

$$E_\theta^0=\left.\frac{d\sigma_{\theta\theta}}{d\lambda_\theta}\right|_{\lambda_\theta\to 1}=\left.\frac{d}{d\lambda_\theta}\left(\frac{T_\theta}{h}\right)\right|_{\lambda_\theta\to 1}=\left.\frac{d}{d\lambda_\theta}\left(\frac{\lambda_\theta\lambda_z^0 T_\theta}{H}\right)\right|_{\lambda_\theta\to 1}=\frac{B}{H}+2\frac{C}{H}(\lambda_z^0)^4-\frac{C}{H}(\lambda_z^0)^2 \qquad (5.15)$$

in which $\sigma_{\theta\theta}$ is the Cauchy stress in the circumferential direction. For known values of the circumferential Young's modulus E_θ^0 and ratio B/C, the two material parameters can be obtained respectively as

$$\frac{C}{H}=\frac{E_\theta^0}{(B/C)+2(\lambda_z^0)^4-(\lambda_z^0)^2},\qquad C\geq B\geq 0 \qquad (5.16)$$

$$\frac{B}{H}=\frac{B}{C}\frac{E_\theta^0}{(B/C)+2(\lambda_z^0)^4-(\lambda_z^0)^2} \qquad (5.17)$$

The polynomial equation of motion (Equation (5.14)) can be solved for four complexity levels, each one having a different order of nonlinearity (zero-, first-, second-, and third-order). To obtain the "zero-order nonlinear" equation we neglect the second- and third-power terms of radial displacement and the term $p(t)u_r(t)/R$ of Equation (5.14). The

resulting second-order linear non-homogeneous differential equation with constant coefficients equation is a expressed as

$$\left[p(t)\frac{R}{C}-\frac{(\lambda_z^0)^3}{2}+\frac{\lambda_z^0}{2}\right]-\frac{u_r(t)}{R}\left[\frac{B}{C\lambda_z^0}+\frac{3(\lambda_z^0)^3}{2}-\frac{\lambda_z^0}{2}\right]=\frac{\rho_0 R^2 H}{C\lambda_z^0}\frac{\ddot{u}_r(t)}{R} \tag{5.18}$$

For $\lambda_z^0=1$ this equation is identical to the equation of motion of the linear model. The equivalent circular frequency of the "zero-order nonlinear" model is given by

$$\omega_0^{Sk}=\frac{\sqrt{\dfrac{B}{C\lambda_z^0}+\dfrac{3}{2}(\lambda_z^0)^3-\dfrac{\lambda_z^0}{2}}}{t_{Sk}} \tag{5.19}$$

The "first-order nonlinear" equation is a second-order linear non-homogeneous differential equation with non-constant coefficients. It is obtained by neglecting the second- and third-power terms of the radial displacement in Equation (5.14) as

$$\left[\left(1+\frac{u_r(t)}{R}\right)p(t)\frac{R}{C}-\frac{(\lambda_z^0)^3}{2}+\frac{\lambda_z^0}{2}\right]-\frac{u_r(t)}{R}\left[\frac{B}{C\lambda_z^0}+\frac{3(\lambda_z^0)^3}{2}-\frac{\lambda_z^0}{2}\right]=\frac{\rho_0 R^2 H}{C\lambda_z^0}\frac{\ddot{u}_r(t)}{R} \tag{5.20}$$

The "second-order nonlinear" equation is a second-order nonlinear non-homogeneous differential equation with non-constant coefficients, and it is obtained by neglecting the third-power terms of the radial displacement in Equation (5.14) as

$$\begin{aligned}\left[\left(1+\frac{u_r(t)}{R}\right)p(t)\frac{R}{C}-\frac{(\lambda_z^0)^3}{2}+\frac{\lambda_z^0}{2}\right]-\frac{u_r(t)}{R}\left[\frac{B}{C\lambda_z^0}+\frac{3(\lambda_z^0)^3}{2}-\frac{\lambda_z^0}{2}\right]\\ -\left(\frac{u_r(t)}{R}\right)^2\left[\frac{3B}{2C\lambda_z^0}+\frac{3(\lambda_z^0)^3}{2}\right]=\frac{\rho_0 R^2 H}{C\lambda_z^0}\frac{\ddot{u}_r(t)}{R}\end{aligned} \tag{5.21}$$

Finally, the "third-order nonlinear" equation stands for the fully nonlinear problem described by Equation (5.14).

We are particularly interested in the response of the system in terms of circumferential elongation, variation of thickness, circumferential stresses, longitudinal stresses, and energy-density values. The normalized functions for these response quantities can be obtained respectively as

$$\lambda_\theta(t) = 1 + \frac{u_r(t)}{R} \tag{5.22}$$

$$\frac{h(t)}{H} = \frac{1}{\lambda_\theta(t)\lambda_z^0} \tag{5.23}$$

$$\frac{T_\theta(t)}{C} = \frac{\lambda_\theta(t)}{\lambda_z^0}\left[\frac{B}{2C}\left((\lambda_\theta(t))^2 - 1\right) + \frac{(\lambda_z^0)^2}{2}\left((\lambda_\theta(t))^2(\lambda_z^0)^2 - 1\right)\right] \tag{5.24}$$

$$\frac{T_z(t)}{C} = \frac{\lambda_z^0}{\lambda_\theta(t)}\left[\frac{B}{2C}\left((\lambda_z^0)^2 - 1\right) + \frac{(\lambda_\theta(t))^2}{2}\left((\lambda_\theta(t))^2(\lambda_z^0)^2 - 1\right)\right] \tag{5.25}$$

$$\frac{W(t)}{C} = \frac{B}{4C}\left(\frac{1}{2}(I(t))^2 + I(t) - II(t)\right) + \frac{(II(t))^2}{8} \tag{5.26}$$

Equation (5.23) is derived by solving Equation (5.4) for $h(t)/H$, and Equations (5.24) through (5.26) are derived by dividing Equations (5.11), (5.12), and (5.6) respectively, by the material parameter C.

5.2.2 Arterial model based on the strain-energy function of Hariton

Atheromatic arteries exhibit stiffer (exponential-like) behavior than healthy arteries. In order to study the response of atheromatic arteries we adopt the isotropic, three-dimensional strain-energy function proposed by Hariton [70], which is a modification of the strain-energy function proposed by Delfino et al. [56]. The strain-energy function proposed by Hariton is expressed as

$$W(t) = \frac{a}{b}\left\{\exp\left[\frac{b}{2}\left(I_1(t) - 3\right)^2\right] - 1\right\} \tag{5.27}$$

where $a > 0$ is a stress-like parameter, and $b > 0$ is a non-dimensional material parameter. Typical values of the material parameters are $a = 44.2$ kPa and $b = 16.7$ [56]. The first strain invariant I_1 is expressed as

$$I_1(t) = (\lambda_\theta(t))^2 + (\lambda_z^0)^2 + \frac{1}{(\lambda_z^0\lambda_\theta(t))^2} \tag{5.28}$$

By adopting the average theory for the composite arterial structure (i.e. the artery acts as a homogeneous-one layer model) and the thin-wall assumption, the hydrostatic pressure P

(from incompressibility) of a stress-free outer surface can be neglected ($P \approx 0$). Therefore, the Cauchy stress-strain relationships of the circumferential and longitudinal directions are equal to

$$\sigma_{\theta\theta}(t) = \lambda_\theta(t)\frac{\partial W}{\partial \lambda_\theta(t)} - P \approx 2\alpha\left[\left(\lambda_\theta(t)\right)^2 - \frac{1}{\left(\lambda_\theta(t)\lambda_z^0\right)^2}\right]\left(I_1(t)-3\right)\exp\left[\frac{b}{2}\left(I_1(t)-3\right)^2\right] \tag{5.29}$$

$$\sigma_{zz}(t) = \lambda_z^0\frac{\partial W}{\partial \lambda_z^0} - P \approx 2\alpha\left[\left(\lambda_z^0\right)^2 - \frac{1}{\left(\lambda_\theta(t)\lambda_z^0\right)^2}\right]\left(I_1(t)-3\right)\exp\left[\frac{b}{2}\left(I_1(t)-3\right)^2\right] \tag{5.30}$$

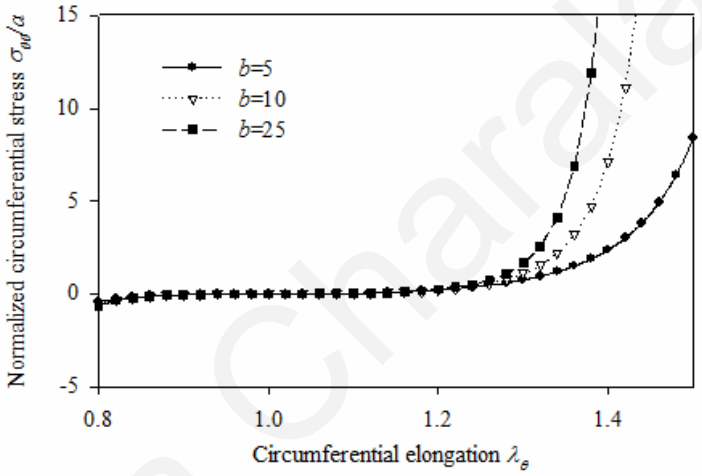

Figure 5-6: Normalized circumferential stress-strain diagram of Hariton [70] hyperelastic model for different values of the parameter b, and for λ_z^0 =1.

Figure 5-6 shows the normalized circumferential stress-strain diagram of the constitutive law proposed by Hariton, in the absence of longitudinal pre-stretch ($\lambda_z^0 = 1$). By increasing the material parameter b the hardening behavior of the material is increased.

The axial force acting along the circumferential direction is equal to $N(t) = \sigma_{\theta\theta}(t)h(t)$. The normalized equation of motion of the arterial model is obtained by substituting Equations (5.3), (5.5), (5.29) in Equation (5.2):

$$\frac{\rho_0 R^2}{a\lambda_z^0}\frac{\ddot{u}_r(t)}{R} = -\frac{2}{\lambda_z^0}\left[\left(1+\frac{u_r(t)}{R}\right)+\frac{1}{(\lambda_z^0)^2\left(1+\frac{u_r(t)}{R}\right)^3}\right]\left[\left(1+\frac{u_r(t)}{R}\right)^2+(\lambda_z^0)^2+\frac{1}{(\lambda_z^0)^2\left(1+\frac{u_r(t)}{R}\right)^2}-3\right] \tag{5.31}$$
$$\exp\left\{\frac{b}{2}\left[\left(1+\frac{u_r(t)}{R}\right)^2+(\lambda_z^0)^2+\frac{1}{(\lambda_z^0)^2\left(1+\frac{u_r(t)}{R}\right)^2}-3\right]^2\right\}+\left(1+\frac{u_r(t)}{R}\right)p(t)\frac{R}{aH}$$

In this case, the six dimensionless quantities of this model are b, λ_z^0, $p(t)R/(aH)$, $u_r(t)/R$, $t_H^2\ddot{u}_r(t)/R$, and t/t_H. The term $t_H=\sqrt{\rho_0 R^2/a\lambda_z^0}$ is the characteristic time of the response. The correlation between the initial circumferential Young's modulus E_θ^0 and the material parameters a and b is

$$E_\theta^0=\left.\frac{d\sigma_{\theta\theta}}{d\lambda_\theta}\right|_{\lambda_\theta\to 1}=4\alpha\left\{\left(\lambda_z^0\right)^2-\frac{3}{\left(\lambda_z^0\right)^2}+\frac{2}{\left(\lambda_z^0\right)^4}+b\left(1-\frac{1}{\left(\lambda_z^0\right)^2}\right)^2\left(\left(\lambda_z^0\right)^2+\frac{1}{\left(\lambda_z^0\right)^2}-2\right)^2\right\} \tag{5.32}$$
$$\exp\left[\frac{b}{2}\left(\left(\lambda_z^0\right)^2+\frac{1}{\left(\lambda_z^0\right)^2}-2\right)^2\right]$$

Finally, on normalizing Equations (5.29), (5.30), and (5.27) by the material parameter a the normalized functions of circumferential stress, longitudinal stress, and strain-energy are expressed respectively as

$$\frac{\sigma_{\theta\theta}(t)}{a}\approx 2\left[\left(\lambda_\theta(t)\right)^2-\frac{1}{\left(\lambda_\theta(t)\lambda_z^0\right)^2}\right]\left(I_1(t)-3\right)\exp\left[\frac{b}{2}\left(I_1(t)-3\right)^2\right] \tag{5.33}$$

$$\frac{\sigma_{zz}(t)}{a}\approx 2\left[\left(\lambda_z^0\right)^2-\frac{1}{\left(\lambda_\theta(t)\lambda_z^0\right)^2}\right]\left(I_1(t)-3\right)\exp\left[\frac{b}{2}\left(I_1(t)-3\right)^2\right] \tag{5.34}$$

$$\frac{W(t)}{a}=\frac{1}{b}\left\{\exp\left[\frac{b}{2}\left(I_1(t)-3\right)^2\right]-1\right\} \tag{5.35}$$

5.2.3 Arterial model based on the strain-energy function of Mooney-Rivlin

The third constitutive law adopted in this chapter is the isotropic three-dimensional strain-energy function of Mooney-Rivlin [51, 52]. The Mooney-Rivlin strain-energy function exhibits softening under applied elongations and can be parallelized with the behavior of aneurysmatic arteries. The strain-energy function suitable to incompressible materials is [52]

$$W(t)=\frac{1}{2}\mu\left[\left(\frac{1}{2}+\beta\right)\left(I_1(t)-3\right)+\left(\frac{1}{2}-\beta\right)\left(I_2(t)-3\right)\right],\qquad \mu>0,\qquad -\frac{1}{2}\le\beta\le\frac{1}{2} \quad (5.36)$$

in which μ is the shear modulus of the material under infinitesimal deformation of the initial undeformed configuration, β is a dimensionless material constant, and I_2 is the second strain invariant for incompressible materials expressed as

$$I_2(t)=(\lambda_\theta(t))^2(\lambda_z^0)^2+\frac{1}{(\lambda_z^0)^2}+\frac{1}{(\lambda_\theta(t))^2} \quad (5.37)$$

For $\beta=1/2$ the strain-energy function of Equation (5.36) corresponds to the Neo-Hookean model.

The Cauchy stress-strain relationships of the circumferential and longitudinal directions can be obtained by adopting the equations of Chadwick [52] (when setting the parameter x equal to 1). Based on the thin-wall assumption and in the absence of pressure on the outer wall, the radial stress is almost zero ($\sigma_{rr}\approx 0$). The stress-strain relations of the circumferential and longitudinal directions are respectively approximated by

$$\sigma_{\theta\theta}(t)\approx\mu\left(\frac{1}{2}+\beta\right)\left((\lambda_\theta(t))^2-\frac{1}{(\lambda_\theta(t))^2(\lambda_z^0)^2}\right)+\mu\left(\frac{1}{2}-\beta\right)\left((\lambda_\theta(t))^2(\lambda_z^0)^2-\frac{1}{(\lambda_\theta)^2}\right) \quad (5.38)$$

$$\sigma_{zz}(t)\approx\mu\left(\frac{1}{2}+\beta\right)\left((\lambda_z^0)^2-\frac{1}{(\lambda_\theta(t))^2(\lambda_z^0)^2}\right)+\mu\left(\frac{1}{2}-\beta\right)\left(\frac{1}{(\lambda_z^0)^2}-(\lambda_\theta(t))^2(\lambda_z^0)^2\right) \quad (5.39)$$

The Mooney-Rivlin circumferential stress-strain relationship exhibits increased softening for increasing values of the material parameter β (Figure 5-7). Note that, on the absence of longitudinal pre-stretch, the material parameter β has no effect on the stress-strain behavior.

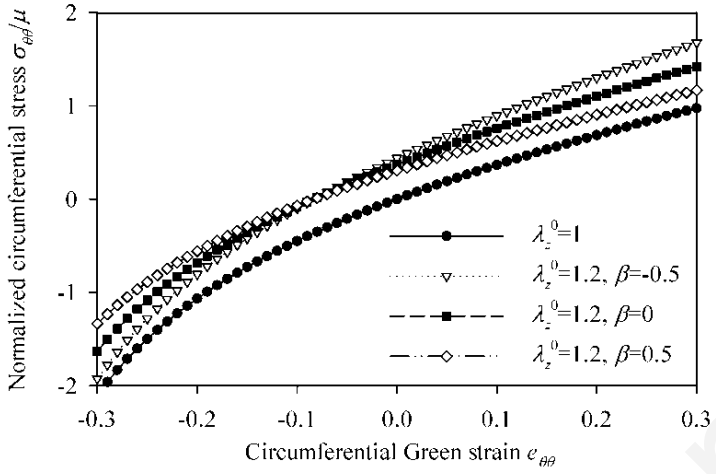

Figure 5-7: Normalized circumferential stress-strain diagram of Mooney-Rivlin [51, 52] hyperelastic model, for different values of the material parameter β, and longitudinal pre-stretch λ_z^0.

The normalized equation of motion of the artery, based on the Mooney-Rivlin [51, 52] material law, is obtained as

$$-\frac{1}{\lambda_z^0}\left\{\left(\frac{1}{2}+\beta\right)\left[\left(1+\frac{u_r(t)}{R}\right)-\frac{1}{(\lambda_z^0)^2\left(1+\frac{u_r(t)}{R}\right)^3}\right]+\left(\frac{1}{2}-\beta\right)\left[\left(1+\frac{u_r(t)}{R}\right)(\lambda_z^0)^2-\frac{1}{\left(1+\frac{u_r(t)}{R}\right)^3}\right]\right\} \quad (5.40)$$
$$+\left(1+\frac{u_r(t)}{R}\right)\frac{Rp(t)}{\mu H}=\frac{\rho_0 R^2}{\mu\lambda_z^0}\frac{\ddot{u}_r(t)}{R}$$

The six dimensionless quantities of this problem are β, λ_z^0, $p(t)R/(\mu H)$, $u_r(t)/R$, $t_{MR}^2\ddot{u}_r(t)/R$, and t/t_{MR}, where the term $t_{MR}=\sqrt{\rho_0 R^2/\mu\lambda_z^0}$ is the characteristic time of the response of the Mooney-Rivlin arterial model. The natural frequency of the equivalent linear equation is given by

$$\omega_0^{MR}=\frac{1}{t_{MR}}\sqrt{\frac{2}{\lambda_z^0}-\frac{2\beta}{\lambda_z^0}-\frac{3}{2(\lambda_z^0)^3}+\frac{3\beta}{(\lambda_z^0)^3}+\frac{\lambda_z^0}{2}-\beta\lambda_z^0} \quad (5.41)$$

The initial tangential circumferential Young's modulus E_θ^0 in terms of the material parameters μ and β, for the thin-wall model and $\sigma_{rr}\approx 0$, is expressed as

$$E_\theta^0 = \left.\frac{d\sigma_{\theta\theta}}{d\lambda_\theta}\right|_{\lambda_\theta \to 1} = 2\mu\left[\left(\frac{1}{2}+\beta\right)\left(1+\frac{1}{\left(\lambda_z^0\right)^2}\right)+\left(\frac{1}{2}-\beta\right)\left(1+\left(\lambda_z^0\right)^2\right)\right] \tag{5.42}$$

The normalized circumferential stress, normalized longitudinal stress, and normalized strain-energy functions are obtained by dividing Equations (5.38), (5.39), and (5.36) respectively by the material parameter μ yielding

$$\frac{\sigma_{\theta\theta}(t)}{\mu} \approx \left(\frac{1}{2}+\beta\right)\left((\lambda_\theta(t))^2 - \frac{1}{(\lambda_\theta(t))^2(\lambda_z^0)^2}\right)+\left(\frac{1}{2}-\beta\right)\left((\lambda_\theta(t))^2(\lambda_z^0)^2 - \frac{1}{(\lambda_\theta)^2}\right) \tag{5.43}$$

$$\frac{\sigma_{\theta\theta}(t)}{\mu} \approx \left(\frac{1}{2}+\beta\right)\left((\lambda_\theta(t))^2 - \frac{1}{(\lambda_\theta(t))^2(\lambda_z^0)^2}\right)+\left(\frac{1}{2}-\beta\right)\left((\lambda_\theta(t))^2(\lambda_z^0)^2 - \frac{1}{(\lambda_\theta(t))^2}\right) \tag{5.44}$$

$$\begin{aligned}\frac{W(t)}{\mu} \approx{}& \frac{1}{2}\left(\frac{1}{2}+\beta\right)\left((\lambda_\theta(t))^2 + (\lambda_z^0)^2 + \frac{1}{(\lambda_\theta(t))^2(\lambda_z^0)^2} - 3\right) \\ &+ \frac{1}{2}\left(\frac{1}{2}-\beta\right)\left((\lambda_\theta(t))^2(\lambda_z^0)^2 + \frac{1}{(\lambda_z^0)^2} + \frac{1}{(\lambda_\theta(t))^2} - 3\right)\end{aligned} \tag{5.45}$$

5.3 Numerical solution

The nonlinear dynamic equations that describe the physical problem can be characterized, from the numerical point of view, as "stiff", hence their solution demands special methods. An ordinary differential equation is "stiff", when there are computational efficiency issues (large computational time) and the numerical method must reduce the time step to obtain satisfactory results of the solution. In our case, the efficiency issues are caused due to the large differences in the orders of magnitude of the ordinary differential equation coefficients.

The formulated ordinary differential equations can be solved numerically through the appropriate ode solvers in MATLAB [67, 71]. In particular, the problem is solved by using the state-space analysis, according to which the second-order ordinary differential equation is transformed into two first-order ordinary differential equations [72].

In general, the state-space formulation of a second-order differential equation is derived by setting the displacement and velocity of the system equal to the state variables z_1 and z_2 respectively as

$$z_1 \equiv u_r \tag{5.46}$$

$$z_2 \equiv \dot{u}_r \tag{5.47}$$

The state variables describe the future response of a system, given the initial conditions, the excitation input, and the dynamic equation of motion.

The derivatives of the state variables are expressed as

$$\dot{z}_1 = \dot{u}_r = z_2 \tag{5.48}$$

$$\dot{z}_2 = \ddot{u}_r \tag{5.49}$$

The term $\dot{z}_2$, in Equation (5.49), is obtained by solving the second-order differential equation for $\ddot{u}_r$.

Finally, the state-input matrix consists of two first-order differential equations, representing the first derivative (Equation (5.48)) and the second derivative (Equation (5.49)) of the radial displacement:

$$\{\dot{z}\} = \begin{Bmatrix} \dot{z}_1 \\ \dot{z}_2 \end{Bmatrix} \tag{5.50}$$

The final solution is obtained through the following output matrix, which lists the radial displacements and the radial velocities of the system as

$$\begin{Bmatrix} z_1 \\ z_2 \end{Bmatrix}^{\mathrm{T}} = \begin{Bmatrix} u_r \\ \dot{u}_r \end{Bmatrix}^{\mathrm{T}} \tag{5.51}$$

In the following, the state-space formulation for each of the hyperelastic arterial models considered in this chapter, is presented. Note that, the problem has been investigated by proper normalization of the involved material parameters and of the pressure time-profile.

In the case of the Skalak et al. arterial model, the normalized pressure time-profile is obtained by multiplying the pressure values $p(t)$ by R/C and the time values by $1/t_{Sk}$. The normalized state-space formulation is derived by multiplying Equations (5.48) and (5.49) by $1/R$ and t_{Sk}/R respectively, yielding

$$\tilde{z}_1 \equiv \frac{u_r}{R} \tag{5.52}$$

$$\tilde{z}_2 \equiv \frac{\dot{u}_r t_{Sk}}{R} \tag{5.53}$$

Thus, the derivatives of the state variables can be expressed as

$$\dot{\tilde{z}}_1 = \frac{\dot{u}_r t_{Sk}}{R} = \tilde{z}_2 \tag{5.54}$$

$$\dot{\tilde{z}}_2 = \frac{\ddot{u}_r {t_{Sk}}^2}{R} \tag{5.55}$$

On substituting Equation (5.52) in Equation (5.14), and solving for the normalized radial acceleration $\ddot{u}_r {t_{Sk}}^2 / R$, we obtain the state term $\dot{\tilde{z}}_2$ as

$$\begin{aligned}\dot{\tilde{z}}_2 = -\tilde{z}_1\left[\frac{B}{C\lambda_z^0}+\frac{3(\lambda_z^0)^3}{2}-\frac{\lambda_z^0}{2}\right]-(\tilde{z}_1)^2\left[\frac{3B}{2C\lambda_z^0}+\frac{3(\lambda_z^0)^3}{2}\right]-(\tilde{z}_1)^3\left[\frac{B}{2C\lambda_z^0}+\frac{(\lambda_z^0)^3}{2}\right] \\ +\left[(1+\tilde{z}_1)\,p(t)\frac{R}{C}-\frac{(\lambda_z^0)^3}{2}+\frac{\lambda_z^0}{2}\right]\end{aligned} \tag{5.56}$$

The normalized state-input matrix consists of the two normalized first-order differential equations (5.54) and (5.56), resulting in the following expression:

$$\left\{\dot{\tilde{z}}\right\} = \begin{Bmatrix}\dot{\tilde{z}}_1 \\ \dot{\tilde{z}}_2\end{Bmatrix} = \left\{\begin{array}{c}\tilde{z}_2 \\ -\tilde{z}_1\left[\frac{B}{C\lambda_z^0}+\frac{3(\lambda_z^0)^3}{2}-\frac{\lambda_z^0}{2}\right]-(\tilde{z}_1)^2\left[\frac{3B}{2C\lambda_z^0}+\frac{3(\lambda_z^0)^3}{2}\right]-(\tilde{z}_1)^3\left[\frac{B}{2C\lambda_z^0}+\frac{(\lambda_z^0)^3}{2}\right] \\ +\left[(1+\tilde{z}_1)\,p(t)\frac{R}{C}-\frac{(\lambda_z^0)^3}{2}+\frac{\lambda_z^0}{2}\right]\end{array}\right\} \tag{5.57}$$

The derived output matrix lists the normalized radial displacements and the normalized radial velocities of the system as

$$\begin{Bmatrix}\tilde{z}_1 \\ \tilde{z}_2\end{Bmatrix}^{\mathrm{T}} = \begin{Bmatrix}\dfrac{u_r}{R} \\ \dfrac{\dot{u}_r t_{Sk}}{R}\end{Bmatrix}^{\mathrm{T}} \tag{5.58}$$

By following the same procedure, the normalized state variables of the arterial model based on the strain-energy function of Hariton et al. are obtained by letting

$$\tilde{z}_1 \equiv \frac{u_r}{R} \tag{5.59}$$

and

$$\tilde{z}_2 \equiv \frac{\dot{u}_r t_H}{R} \tag{5.60}$$

The derivatives of the state variables are expressed as

$$\dot{\tilde{z}}_1 = \frac{\dot{u}_r t_H}{R} = \tilde{z}_2 \tag{5.61}$$

$$\dot{\tilde{z}}_2 = \frac{\ddot{u}_r {t_H}^2}{R} \tag{5.62}$$

in which the state term $\dot{\tilde{z}}_2$ is obtained on substituting Equation (5.59) in Equation (5.32), and on solving for the normalized radial acceleration $\ddot{u}_r {t_H}^2 / R$:

$$\begin{aligned}\dot{\tilde{z}}_2 = -\frac{2}{\lambda_z^0}\left[\left(1+\tilde{z}_1\right)+\frac{1}{(\lambda_z^0)^2\left(1+\tilde{z}_1\right)^3}\right]\left[\left(1+\tilde{z}_1\right)^2+(\lambda_z^0)^2+\frac{1}{(\lambda_z^0)^2\left(1+\tilde{z}_1\right)^2}-3\right] \\ \exp\left\{\frac{b}{2}\left[\left(1+\tilde{z}_1\right)^2+(\lambda_z^0)^2+\frac{1}{(\lambda_z^0)^2\left(1+\tilde{z}_1\right)^2}-3\right]^2\right\}+\left(1+\tilde{z}_1\right)p(t)\frac{R}{aH}\end{aligned} \tag{5.63}$$

The resulting state-input matrix is formulated as

$$\left\{\dot{\tilde{z}}\right\} = \left\{\begin{array}{c} \tilde{z}_2 \\ -\frac{2}{\lambda_z^0}\left[\left(1+\tilde{z}_1\right)+\frac{1}{(\lambda_z^0)^2\left(1+\tilde{z}_1\right)^3}\right]\left[\left(1+\tilde{z}_1\right)^2+(\lambda_z^0)^2+\frac{1}{(\lambda_z^0)^2\left(1+\tilde{z}_1\right)^2}-3\right] \\ \exp\left\{\frac{b}{2}\left[\left(1+\tilde{z}_1\right)^2+(\lambda_z^0)^2+\frac{1}{(\lambda_z^0)^2\left(1+\tilde{z}_1\right)^2}-3\right]^2\right\}+\left(1+\tilde{z}_1\right)p(t)\frac{R}{aH} \end{array}\right\} \tag{5.64}$$

Similarly, for the Mooney-Rivlin arterial model (Equation (5.40)), the normalized state variables are obtained by multiplying Equations (5.48) and (5.49) by $1/R$ and t_{MR}/R respectively, yielding

$$\tilde{z}_1 \equiv \frac{u_r}{R} \tag{5.65}$$

$$\tilde{z}_2 \equiv \frac{\dot{u}_r t_{MR}}{R} \tag{5.66}$$

The derivatives of the state variables are expressed as

$$\dot{\tilde{z}}_1 = \frac{\dot{u}_r t_{MR}}{R} = \tilde{z}_2 \tag{5.67}$$

$$\dot{\tilde{z}}_2 = \frac{\ddot{u}_r t_{MR}{}^2}{R} \tag{5.68}$$

The state term $\dot{\tilde{z}}_2$ is obtained on substituting Equation (5.65) in Equation (5.40), and on solving for the normalized radial acceleration $\ddot{u}_r t_{MR}{}^2 / R$:

$$\dot{\tilde{z}}_2 = -\frac{1}{\lambda_z^0}\left\{\left(\frac{1}{2}+\beta\right)\left[\left(1+\tilde{z}_1\right)-\frac{1}{(\lambda_z^0)^2\left(1+\tilde{z}_1\right)^3}\right]+\left(\frac{1}{2}-\beta\right)\left[\left(1+\tilde{z}_1\right)(\lambda_z^0)^2-\frac{1}{\left(1+\tilde{z}_1\right)^3}\right]\right\} + \left(1+\tilde{z}_1\right)\frac{Rp(t)}{\mu H} \tag{5.69}$$

The state-input matrix of the Mooney-Rivlin arterial model is expressed as

$$\left\{\dot{\tilde{z}}\right\} = \left\{\begin{array}{c} \tilde{z}_2 \\ -\frac{1}{\lambda_z^0}\left\{\left(\frac{1}{2}+\beta\right)\left[\left(1+\tilde{z}_1\right)-\frac{1}{(\lambda_z^0)^2\left(1+\tilde{z}_1\right)^3}\right]+\left(\frac{1}{2}-\beta\right)\left[\left(1+\tilde{z}_1\right)(\lambda_z^0)^2-\frac{1}{\left(1+\tilde{z}_1\right)^3}\right]\right\} + \left(1+\tilde{z}_1\right)\frac{Rp(t)}{\mu H} \end{array}\right\} \tag{5.70}$$

Two ode solvers have been utilized in MATLAB to solve numerically the ordinary differential equations. The ordinary differential equations of the Skalak et al. case (Equations (5.14), (5.18), (5.20), and (5.21)) and of the Mooney-Rivlin case (Equation (5.40)) are solved numerically by using the ode23s function in MATLAB. This function uses a one-step solver based on the modified Rosenbrock method of order 2 [73, 74]. On the other hand, the "stiffer" ordinary differential equation of the Hariton case (Equation (5.32)) is solved numerically by using the ode23tb function in MATLAB. The ode23tb solver uses an implicit Runge-Kutta method [75], suitable for very stiff problems.

5.4 Results

This section presents response spectra for the three models adopted in this study. In particular, the maximum normalized radial displacement of the arterial model, and response spectra of the circumferential elongation, variation of thickness, circumferential stress, longitudinal stress, and strain-energy density are investigated by varying the problem parameters.

The hyperelastic models are compared to the equivalent linear arterial model. For each analysis, the Young's modulus of the linear model is taken to be equal to the initial tangent Young's modulus E_θ^0 of the hyperelastic model. The linear equation of motion is of the type of Equation (4.4) and is expressed as

$$\rho_0 H \ddot{u}_r(t) = p(t) - \frac{E_\theta^0 H}{R^2} u_r(t) \tag{5.71}$$

The aortic pressure-time profile adopted in this study is the first loading cycle approximation of Figure 4-2(b), having values of maximum systolic pressure p_s=120 mmHg=16 kPa , diastolic pressure p_d=80 mmHg=10.66 kPa , systolic-phase duration $t_s = 0.35$ sec , and total duration of the cardiac pulse $t_{cp} = 1$ sec .

The solution of the linear arterial model, subjected to this pulse-type loading, can be expressed in closed-form expressions (see Section 4.2). The longitudinal pre-tension of the linear model is taken into account through the initial displacement u_0. We assume that $u_0 = R\left(\lambda_z^0 - 1\right)$. For all cases the pre-stretch value is taken to be larger or equal to one ($\lambda_z^0 \geq 1$).

5.4.1 Response of healthy arteries

The nonlinear response of healthy arteries is calculated by solving the arterial model based on the strain-energy function of Skalak et al. (Equation (5.13)). The exact solution of this case is represented by the solution of the fully ("third-order") nonlinear model. Numerical examples of arterial systems are presented in order to demonstrate values of their maximum response and typical response time-histories. Furthermore, a comparison between the four models (zero-, first-, second-, and third-order nonlinear models) and the linear model is shown through radial-displacement spectra. Response spectra of other important response quantities are also plotted.

5.4.1.1 Examples of typical arterial systems

Table 5-1 reports the parameters for the three arterial systems investigated in this section and their calculated maximum normalized radial displacements and velocities.

Table 5-1: Parameters of each example, and calculated maximum normalized radial displacements and velocities.

	Example 1 (soft)	Example 2 (medium stiffness)	Example 3 (stiff)
Parameters			
B/C	0.5	0.5	1
λ_z^0	1.1	1	1
u_0	0.1	0	0
t_{cp}/t_{Sk}	166.67	1000	2000
$p_s R/C$	0.80	0.16	0.16
ω_0^{Sk} (1/sec)	230	1000	2828
Maximum normalized displacement $\lvert u_r(t)/R \rvert$ (%)			
Linear case	62.07	21.32	15.99
Zero-order	71.94	21.32	15.99
First-order	124.15	23.86	17.37
Second-order	62.00	19.58	14.95
Third-order	59.19	19.44	14.89
Maximum normalized velocity $\lvert \dot{u}_r(t) t_{Sk}/R \rvert$			
Linear case	0.3882	0.1305	0.1130
Zero-order	0.4960	0.1305	0.1130
First-order	0.6803	0.1380	0.1179
Second-order	0.5192	0.1305	0.1129
Third-order	0.5116	0.1304	0.1130

Example 1 represents a problematic (soft) artery, with a smaller circular frequency compared to other models. The normalized pressure profile used in this case is shown in Figure 5-8. The system exhibits large radial displacements. In particular, the "first-order nonlinear" case exhibits the largest radial displacements, whereas the fully nonlinear case ("third-order") exhibits the lower radial displacements. By observing the response

functions of the fully nonlinear problem shown in Figure 5-9, we can say that the envelope of the radial response vibrations is identical to the shape of the pressure time-profile.

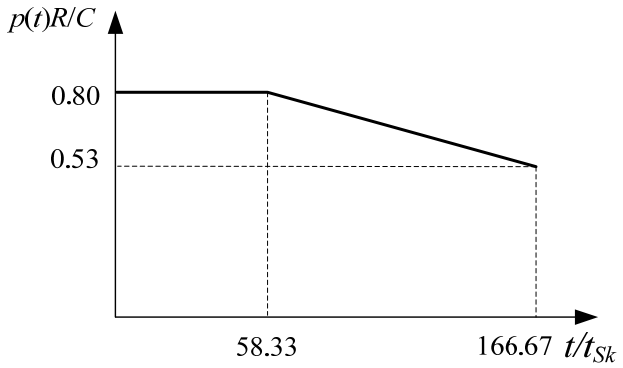

Figure 5-8: Normalized pressure time-profile used in Example 1.

Furthermore, the applied longitudinal pre-stretch $\lambda_z^0 = 1.1$ shifts the normalized displacements of the model towards the negative values of the u_r / R-axis.

Examples 2 and 3 represent stiff arterial systems. Their response values are relatively low, and the range of the calculated response values of the five models is limited, compared to the first example.

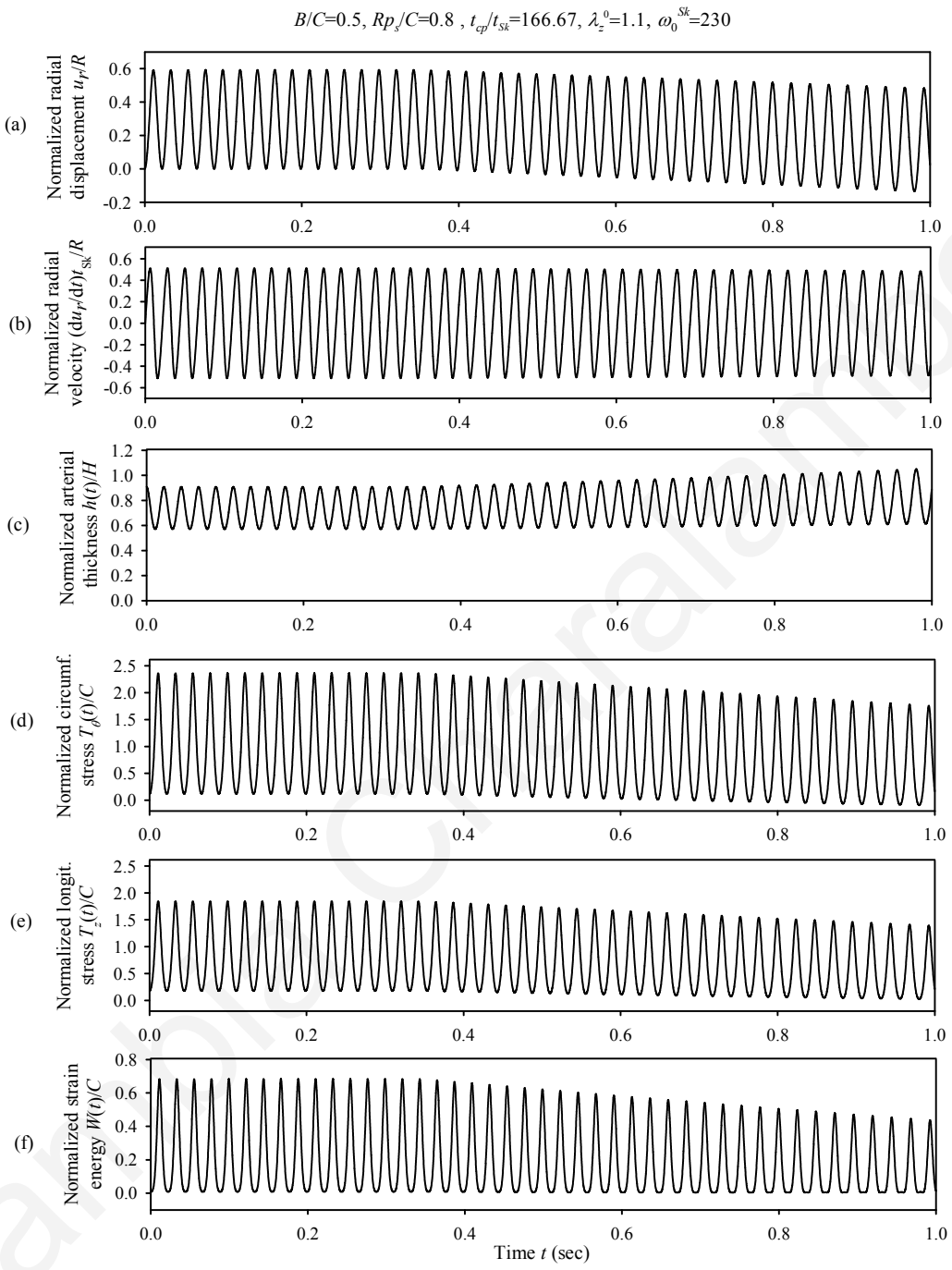

Figure 5-9: Normalized response of the "third-order nonlinear" model versus time: (a) radial displacement u_r / R, (b) radial velocity $\dot{u}_r t_{Sk} / R$, (c) arterial thickness h / H, (d) circumferential stress T_θ / C, (e) longitudinal stress T_z / C, and (f) strain-energy density W / C.

5.4.1.2 Maximum radial displacement

The response spectra of Figures 5-10 and 5-11 reveal the level of approximation of each arterial model (and order of nonlinearity) against the exact solution ("third-order" model). They also reveal how is the peak radial response affected when varying the problem parameters.

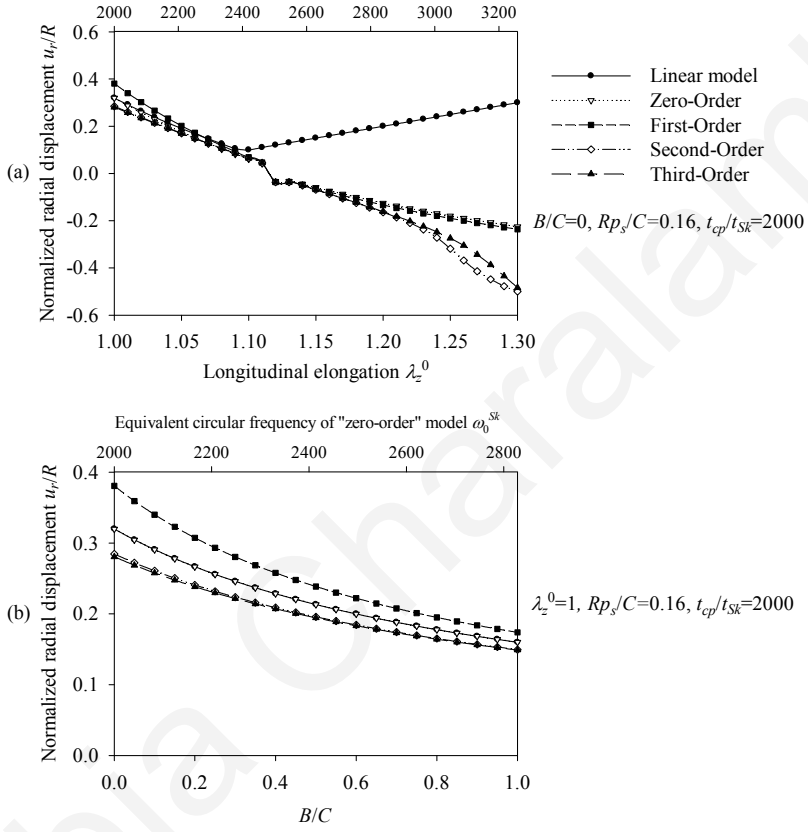

Figure 5-10: (a) Displacement spectrum for pre-stretch values $\lambda_z^0 = \{1 \div 1.3\}$ and $B/C = 0$, $p_s R/C = 0.16$, $t_{cp}/t_{Sk} = 2000$, (b) Displacement spectrum for ratios $B/C = \{0 \div 1\}$ and $\lambda_z^0 = 1$, $p_s R/C = 0.16$, $t_{cp}/t_{Sk} = 2000$.

In general, the "first-order nonlinear" model gives the largest response values, whereas the fully nonlinear model gives the lower response values. The "second-order nonlinear" model approximates well the fully nonlinear problem, meaning that the second-power term of radial displacement $(u_r/R)^2$ dominates. The peak response value of the linear model is always positive (due to the initial displacement $u_0 \geq 0$), making the linear model conservative under large pre-stretch values (Figure 5-10(a)). For $\lambda_z^0 = 1$ the linear and the "zero-order nonlinear" models have identical response.

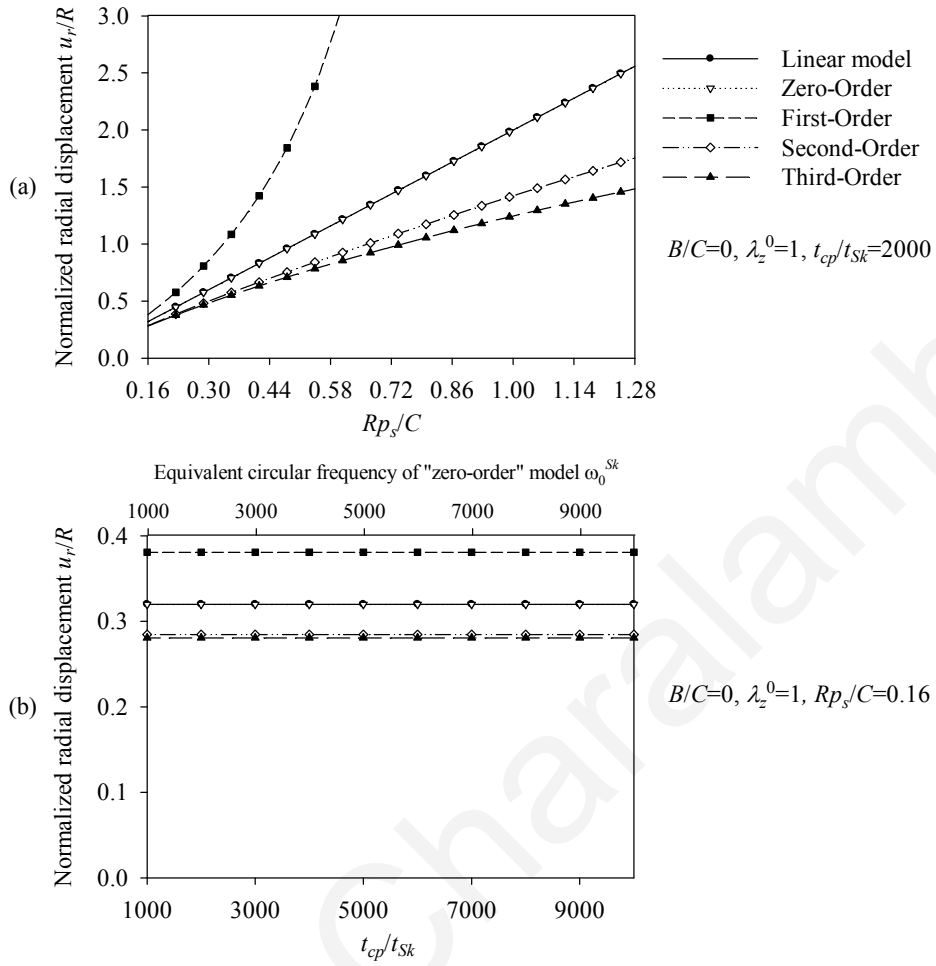

Figure 5-11: (a) Displacement spectrum for $p_sR/C=\{0.16\div1.28\}$ and $B/C=0$, $\lambda_z^0=1$, $t_{cp}/t_{Sk}=2000$. (b) Displacement spectrum for normalized characteristic time values $t_{cp}/t_{Sk}=\{1000\div10000\}$ and $B/C=0$, $p_sR/C=0.16$, $\lambda_z^0=1$.

Figure 5-10 shows that an increase of the longitudinal pre-stretch λ_z^0 or the ratio B/C, stiffens the system and decreases the radial displacement. For pre-stretch values between 1.1-1.15, the absolute value of the radial deformation is minimized (for $p_sR/C=0.16$).

On the other hand, Figure 5-11 shows that an increase in the normalized pressure p_sR/C, yields increased radial deformation response (Figure 5-11(a)), whereas the parameter t_{cp}/t_{Sk} do not affect the problem (Figure 5-11(b)).

An increase of the normalized pressure p_sR/C implies either an increase of the arterial pressure (hypertension) or a decrease of the elasticity modulus. In cases of hypertension, the systolic pressure p_s can be 5/3 times higher than the normal systolic pressure (120 mmHg). For example, according to Figure 5-11(a), if the normal value of normalized

systolic pressure is $p_s R/C = 0.16$, in case of hypertension it would reach a value of $p_s R/C = 0.27$ and the normalized radial displacement would increase from 28% to 42%. Similarly, in the case that the elasticity modulus ($E_\theta = (B + 2C(\lambda_z^0)^4 - C(\lambda_z^0)^2)/H$), and consequently the material parameter C/H of the artery are decreased, the normalized systolic pressure $p_s R/C$ is increased. The material parameter C/H has typical values between 0.1 and 1 MPa. Thus, the normalized systolic pressure $p_s R/C$ is potentially increased by a factor of 10 for soft arteries, resulting in a radial response over 100%, as shown in Figure 5-11(a).

5.4.1.3 Response spectra

Based on the results of the previous section, we can say that the most important parameters influencing the problem are the pre-stretch value λ_z^0, the ratio B/C, and the normalized pressure $p(t)R/C$. Accordingly, the spectra of the response quantities of Equations (5.22) through (5.26) are investigated for different values of these parameters.

Figure 5-12 present spectra for different longitudinal pre-stretch values, for three values of the ratio B/C, and for $p_s R/C = 0.16$. The circumferential elongation decreases with increasing values of the longitudinal pre-stretch λ_z^0, while the normalized strain-energy and normalized stresses exhibit an optimized minimum value for λ_z^0 between 1.1 and 1.15. When λ_z^0 is increased over this optimized value, the normalized strain-energy is increased rapidly, indicating possible failure for pre-stretch values close to 1.3. For increasing values of the ratio B/C, the response decreases for pre-stretch values up to 1.1-1.15, and increases for higher pre-stretch values.

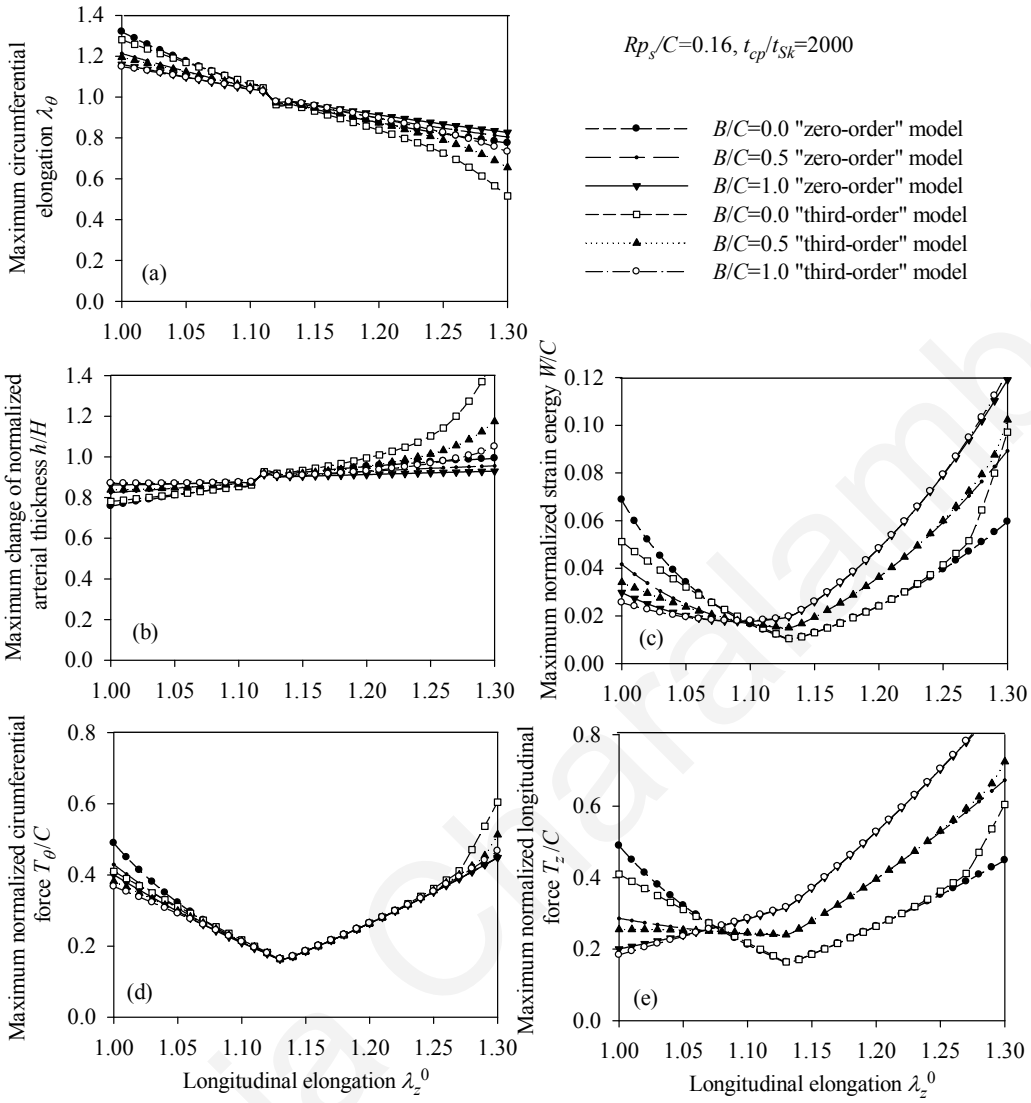

Figure 5-12: Response spectra for $\lambda_z^0 = \{1 \div 1.3\}$, $B/C = [0,\ 0.5,\ 1]$, $p_s R/C = 0.16$, $t_{cp}/t_{Sk} = 2000$: (a) circumferential elongation λ_θ, (b) normalized thickness h/H, (c) normalized strain energy W/C, (d) normalized circumferential stress T_θ/C, (e) normalized longitudinal stress T_z/C.

Figure 5-13 presents response spectra as a function of the ratio B/C and for three different values of parameter $p_s R/C$. It can be observed that the maximum response of the system is decreased with increasing values of B/C or with decreasing values of the normalized pressure $p_s R/C$. Moreover, the "zero-order nonlinear" model is conservative compared to the "third-order nonlinear" model.

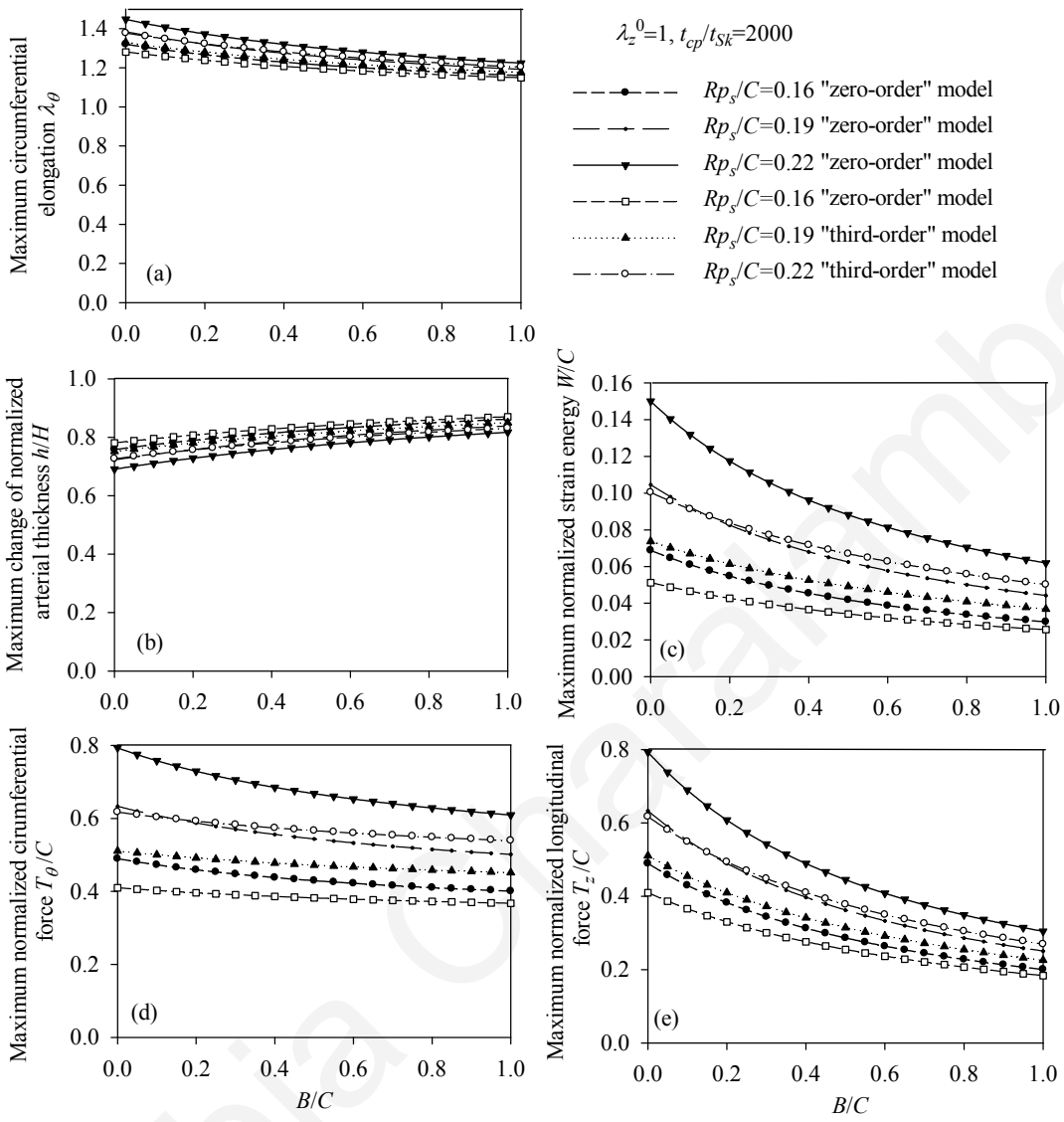

Figure 5-13: Response spectra for $B/C=\{0\div 1\}$, $p_sR/C=[0.16,\ 0.19,\ 0.22]$, $\lambda_z^0=1$, $t_{cp}/t_{Sk}=2000$: (a) circumferential elongation λ_θ, (b) normalized thickness h/H, (c) normalized strain-energy W/C, (d) normalized circumferential stress T_θ/C, (e) normalized longitudinal stress T_z/C.

Tables 5-2 and 5-3 list the peak value of normalized strain-energy W/C for the "third-order nonlinear" models of Figures 5-12 and 5-13 respectively, along with the time of its occurrence. In most cases, the peak strain-energy value occurs during the systolic phase.

Table 5-2: Maximum normalized strain-energy W/C and exact occurrence time for range of λ_z^0 and B/C values, and $p_s R/C = 0.16$ (case of Figure 5-12).

	B/C					
	0		0.5		1	
λ_z^0	Maximum W/C	Time (sec)	Maximum W/C	Time (sec)	Maximum W/C	Time (sec)
1	0.051184	0.001383	0.034112	0.001174	0.025579	0.00104
1.05	0.0321	0.001349	0.02378	0.001163	0.019512	0.001038
1.1	0.017248	0.001319	0.017016	0.001154	0.017996	0.001039
1.15	0.013001	0	0.019501	0	0.026002	0
1.2	0.0242	0	0.0363	0	0.0484	0
1.25	0.041494	0.35078	0.060049	0.35011	0.079324	0.34928
1.3	0.097124	0.99934	0.10226	0.99997	0.12222	0.35024

Table 5-3: Maximum normalized strain energy W/C and exact occurrence time for range of B/C and $p_s R/C$ values, and $\lambda_z^0 = 1$ (case of Figure 5-13).

	$p_s R/C$					
	0.16		0.19		0.22	
B/C	Maximum W/C	Time (sec)	Maximum W/C	Time (sec)	Maximum W/C	Time (sec)
0	0.0512	0.001383	0.0737	0.001359	0.1004	0.001337
0.2	0.0426	0.001286	0.0614	0.001265	0.0836	0.001247
0.4	0.0366	0.001207	0.0526	0.001189	0.0717	0.001173
0.6	0.032	0.001142	0.0461	0.001126	0.0627	0.001111
0.8	0.0284	0.001087	0.0409	0.001073	0.0557	0.001059
1	0.0256	0.00104	0.0368	0.001027	0.0501	0.001014

5.4.2 Response of atheromatic arteries

5.4.2.1 Maximum radial deformation

This section presents the peak normalized radial deformations of atheromatic arterial systems (arterial model based on the strain-energy function of Hariton) for different values of the non-dimensional parameters λ_z^0, b, $p_s R/(aH)$, and t_{cp}/t_H.

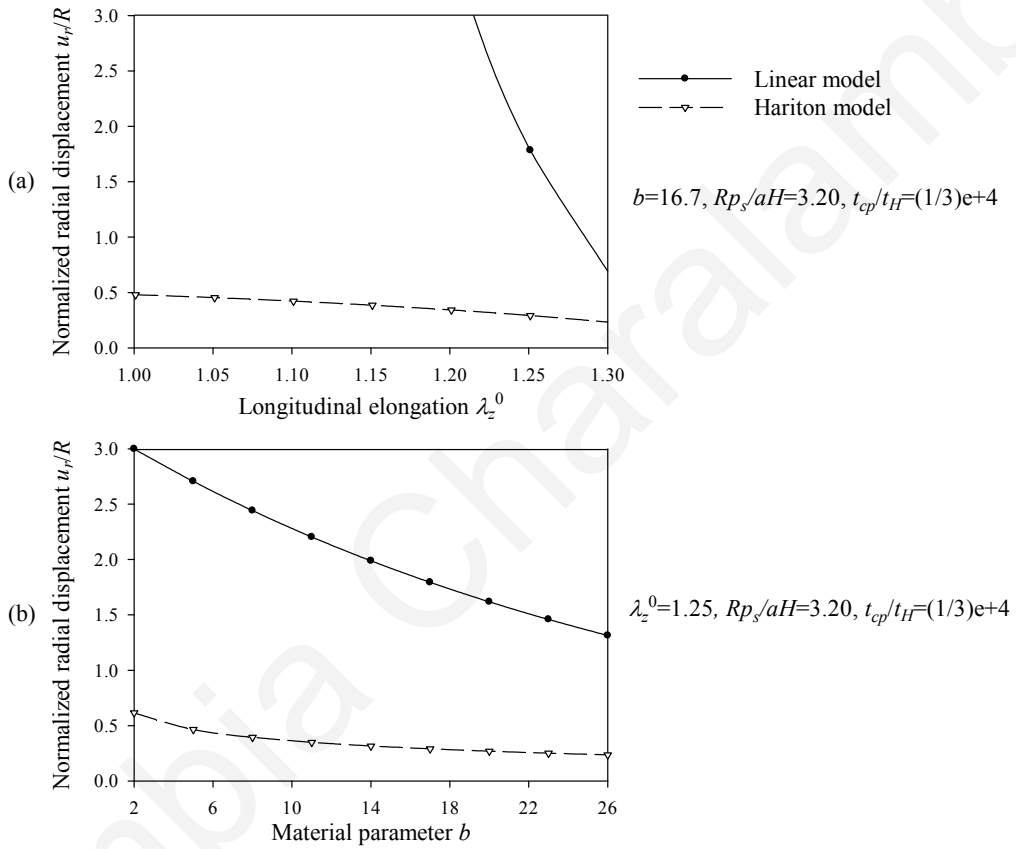

Figure 5-14: (a) Displacement spectrum for pre-stretch values $\lambda_z^0 = \{1 \div 1.3\}$ and $b = 16.7$, $p_s R/(aH) = 3.2$, $t_{cp}/t_H = 1/3\text{E}-4$, (b) Displacement spectrum for material parameter values $b = \{2 \div 26\}$ and $\lambda_z^0 = 1.25$, $p_s R/(aH) = 3.2$, $t_{cp}/t_H = 1/3\text{E}-4$.

As can be seen from Figure 5-14, the system becomes stiffer exhibiting reduced radial displacement as the longitudinal pre-stretch (Figure 5-14(a)) or the material parameter b (Figure 5-14(b)) is increased. Figure 5-15 shows that the normalized radial displacement increases slightly with increasing values of the normalized pressure $p_s R/(aH)$ (Figure 5-15(a)), whereas the characteristic time t_H seems to not affect the problem (Figure

5-15(b)). The linear case yields conservative values of the normalized radial displacement compared to the hyperelastic model, except for large pre-stretch values and low values of the normalized pressure. In addition, the maximum deformation occurs at the beginning of the loading while the system has not entered the exponential hardening region yet.

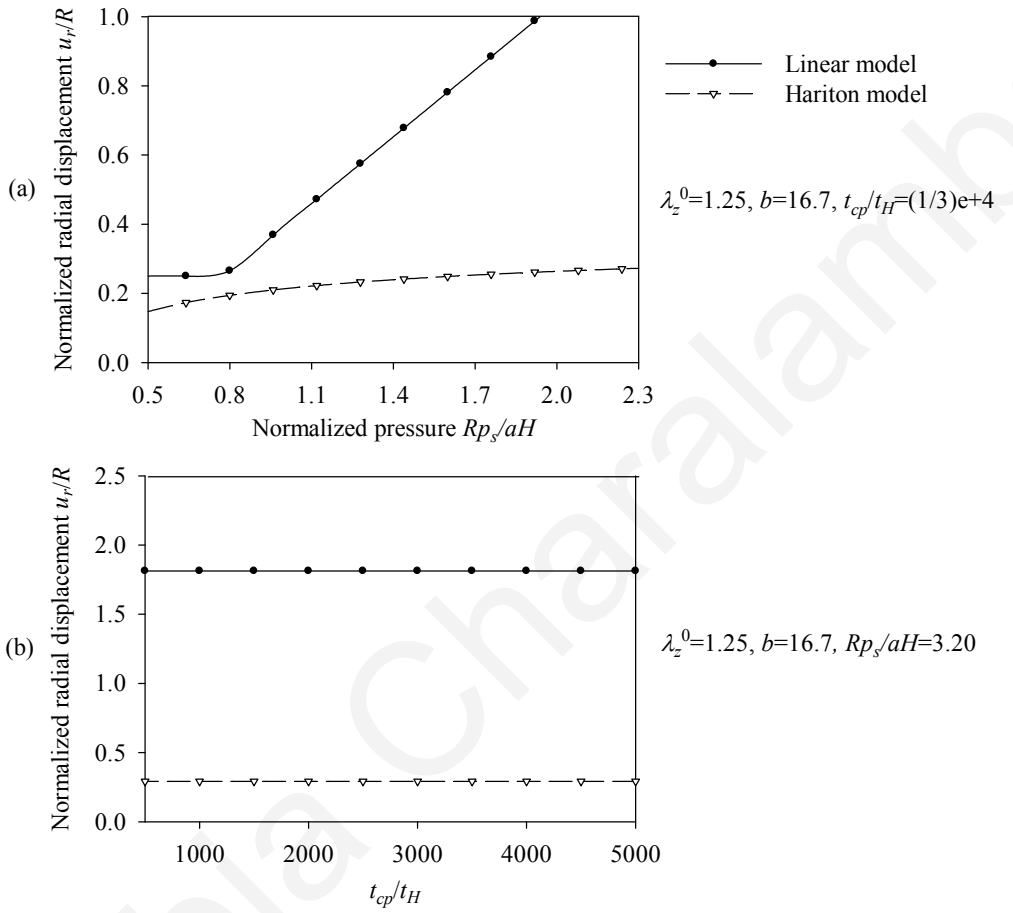

Figure 5-15: (a) Displacement spectrum for normalized pressure values $p_s R/aH = \{0.5 \div 2.3\}$ and $b = 16.7$, $\lambda_z^0 = 1.25$, $t_{cp}/t_H = 1/3\text{E}-4$, (b) Displacement spectrum for normalized characteristic time values $t_{cp}/t_H = \{500 \div 5000\}$ and $b = 16.7$, $p_s R/aH = 3.2$, $\lambda_z^0 = 1.25$.

5.4.2.2 Response spectra

Equations (5.33)-(5.35) are investigated by varying the pre-stretch value λ_z^0, the material parameter b and the normalized pressure $p_s R/aH$.

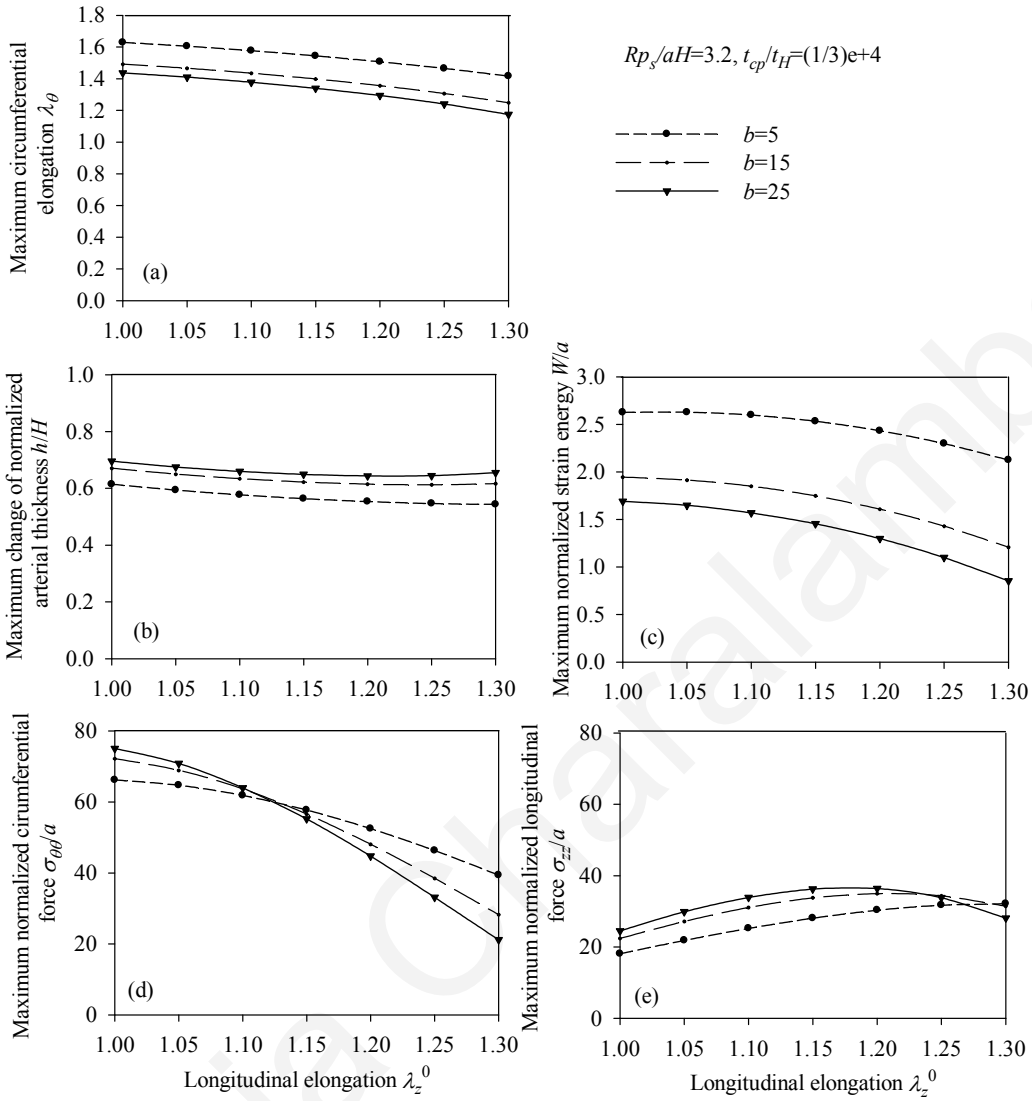

Figure 5-16: Response spectra for $\lambda_z^0 = \{1 \div 1.3\}$, $b = 5,\ 15,\ 25$, $p_s R/(aH) = 3.2$, $t_{cp}/t_H = 1/3\text{E}{-4}$: (a) circumferential elongation λ_θ, (b) normalized thickness h/H, (c) normalized strain energy W/a, (d) normalized circumferential stress $\sigma_{\theta\theta}/a$, (e) normalized longitudinal stress σ_{zz}/a.

Figure 5-16 plots response spectra as a function of the longitudinal pre-stretch, for three values of the material parameter b, and for $p_s R/aH = 3.2$. The normalized strain-energy W/a, the circumferential elongation λ_θ, and the normalized circumferential stress $\sigma_{\theta\theta}/a$ are decreased with increasing values of the longitudinal pre-stretch λ_z^0. We can observe that the normalized longitudinal stress exhibits peak values for pre-stretch values between 1.1-1.2. For increasing values of the material parameter b the circumferential elongation and the strain-energy are decreased, whereas for the different values of material parameter

b the calculated stresses present intersection points (Figure 5-16 (d,e)). Consequently, the hoop stress is not a representative criterion to obtain the response limits of different arterial systems. On the contrary, the strain-energy function and the displacements of different arterial systems appear distinctive.

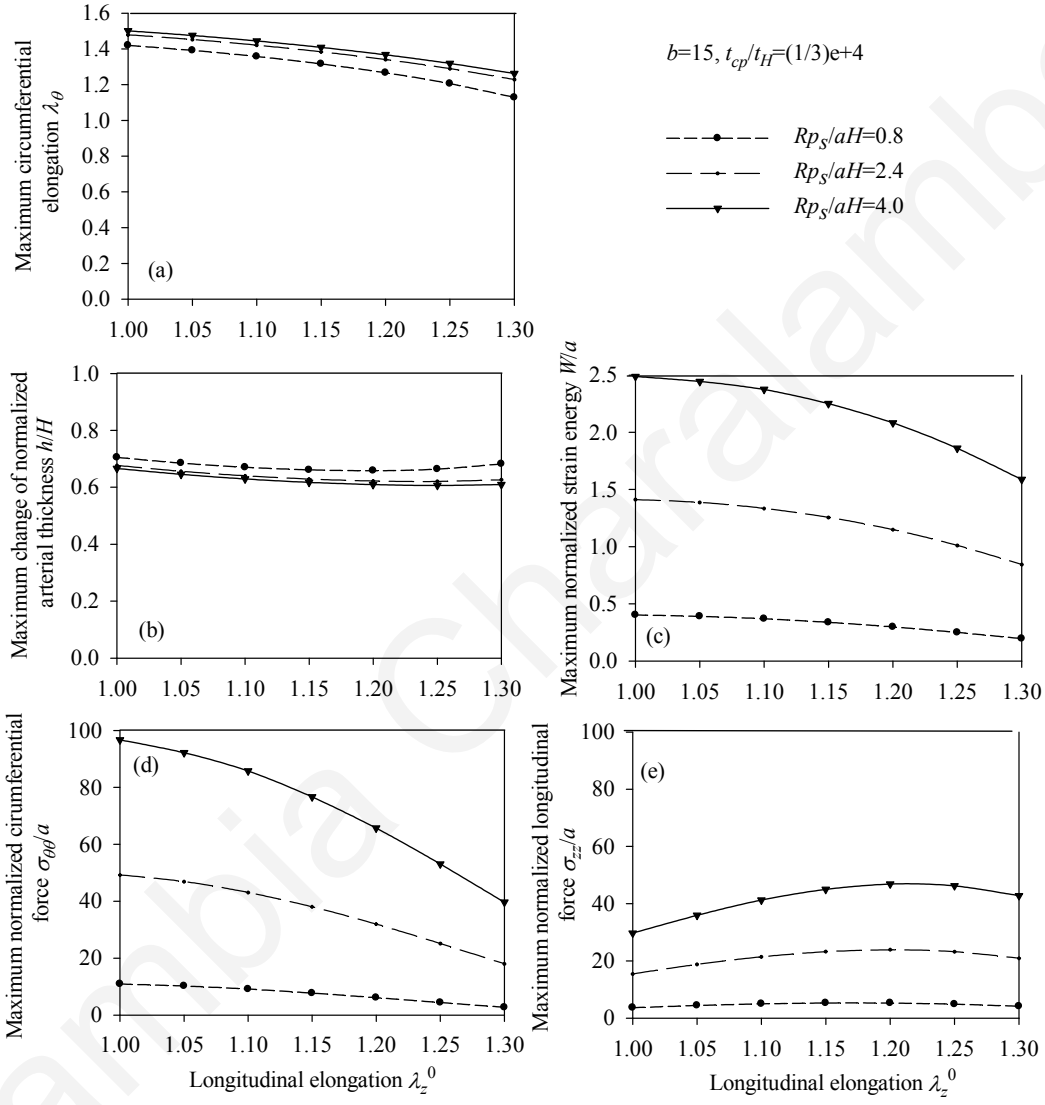

Figure 5-17: Response spectra for $\lambda_z^0 = \{1 \div 1.3\}$, $p_s R / aH = 0.8,\ 2.4,\ 4.0$, $b = 15$, $t_{cp} / t_H = 1/3\text{E}-4$: (a) circumferential elongation λ_θ, (b) normalized thickness h/H, (c) normalized strain energy W/a, (d) normalized circumferential stress $\sigma_{\theta\theta}/a$, (e) normalized longitudinal stress σ_{zz}/a.

The response spectra were investigated for different cases of longitudinal pre-stretch, three values of the normalized pressure Rp_s/aH, and $b = 15$ (Figure 5-17). The normalized strain-energy, the circumferential elongation, and the normalized circumferential stress are

decreased with increasing values of longitudinal pre-stretch λ_z^0. We can observe that, the normalized longitudinal curves exhibit peak values for pre-stretch values between 1.05-1.15. For increasing pressure values Rp_s / aH the response in increased.

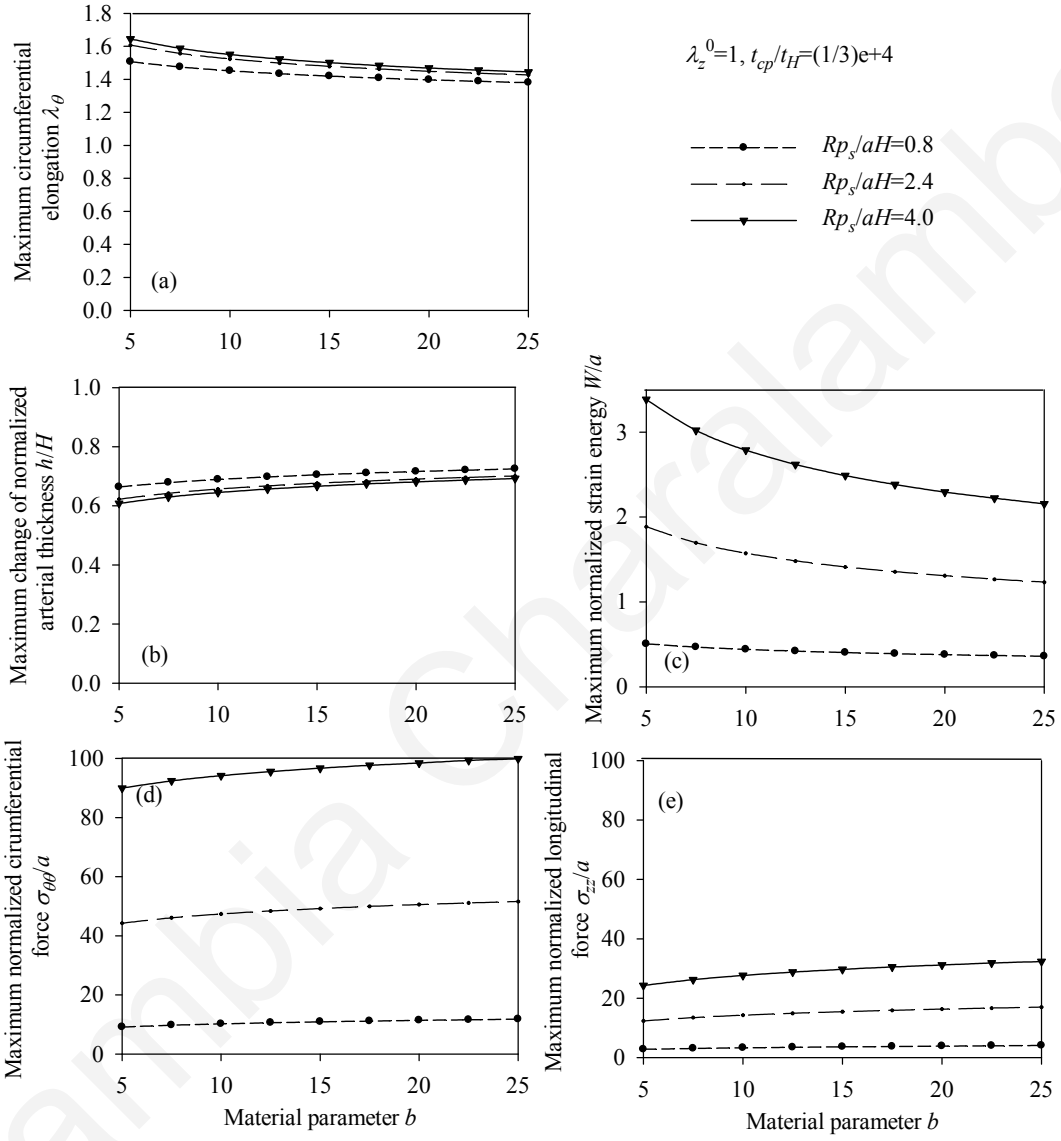

Figure 5-18: Response spectra for $b = \{5 \div 25\}$, $p_s R / aH = 0.8,\ 2.4,\ 4.0$, $\lambda_z^0 = 1$, $t_{cp} / t_H = 1/3\text{E}-4$: (a) circumferential elongation λ_θ, (b) normalized thickness h / H, (c) normalized strain-energy W / a, (d) normalized circumferential stress $\sigma_{\theta\theta} / a$, (e) normalized longitudinal stress σ_{zz} / a.

Figure 5-18 presents response spectra for different values of the material parameter b, for three different values of the normalized pressure Rp_s / aH, and $\lambda_z^0 = 1$. An increase of the material parameter b results in a decrease of the circumferential elongation and

normalized strain-energy, and an increase of the normalized circumferential and longitudinal stresses.

Table 5-4: Maximum normalized strain-energy W/a and exact occurrence time for range of λ_z^0 and b values, and for $Rp_s/aH = 3.2$ (case of Figure 5-16).

	b					
	5		15		25	
λ_z^0	Maximum W/a	Time (sec)	Maximum W/a	Time (sec)	Maximum W/a	Time (sec)
1	2.6255	0.00020	1.9443	0.00017	1.69	0.00016
1.05	2.6272	0.00019	1.913	0.00017	1.6495	0.00016
1.1	2.5968	0.00019	1.8488	0.00016	1.5688	0.00015
1.15	2.5317	0.00019	1.747	0.00016	1.4549	0.00015
1.2	2.4317	0.00019	1.6072	0.00016	1.2991	0.00014
1.25	2.2964	0.00018	1.4287	0.00015	1.0992	0.00014
1.3	2.1241	0.00018	1.2076	0.00015	0.85387	0.00013

Table 5-5: Maximum normalized strain-energy W/a and exact occurrence time for range of λ_z^0 and Rp_s/aH values, and for $b = 15$ (case of Figure 5-17).

	Rp_s/aH					
	0.8		2.4		4	
λ_z^0	Maximum W/a	Time (sec)	Maximum W/a	Time (sec)	Maximum W/a	Time (sec)
1	0.40285	0.00033	1.4107	0.00020	2.4879	0.00015
1.05	0.39027	0.00032	1.3863	0.00019	2.4441	0.00015
1.1	0.36872	0.00032	1.3341	0.00019	2.374	0.00019
1.15	0.33763	0.00031	1.2558	0.00018	2.2506	0.00014
1.2	0.29761	0.00030	1.1483	0.00018	2.0825	0.00014
1.25	0.2494	0.00030	1.0106	0.00017	1.8603	0.00013
1.3	0.19548	0.00029	0.84355	0.00017	1.5873	0.00013

Reported in Tables 5-4 through 5-6 are the peak values of normalized strain-energy and the time instant that it occurs. For all cases, the peak value occurs at the beginning of the loading.

Table 5-6: Maximum normalized strain-energy W / a and exact occurrence for range of Rp_s / aH and b values, and for $\lambda_z^0 = 1$ (case of Figure 5-18).

	Rp_s / aH					
	0.8		2.4		4	
b	Maximum W / a	Time (sec)	Maximum W / a	Time (sec)	Maximum W / a	Time (sec)
5	0.50448	0.000374	1.8847	0.000224	3.3855	0.000176
7.5	0.46631	0.000358	1.6958	0.000214	3.0219	0.000168
10	0.43967	0.000347	1.5721	0.000207	2.7875	0.000162
12.5	0.41922	0.000338	1.4818	0.000201	2.6183	0.000158
15	0.40285	0.000331	1.4107	0.000196	2.4879	0.000154
17.5	0.3893	0.000325	1.3548	0.000193	2.3827	0.000151
20	0.37778	0.00032	1.3074	0.00019	2.2938	0.000149
22.5	0.3678	0.000316	1.2669	0.000187	2.2218	0.000147
25	0.35903	0.000312	1.2317	0.000185	2.1548	0.000145

5.4.3 Response of aneurysmatic arteries

5.4.3.1 Maximum radial deformation

This section compares the radial displacement of the Mooney-Rivlin arterial model with that of the equivalent linear model. All models in the analysis assume the same initial tangent elasticity modulus E_θ^0. In particular, Figures 5-19 and 5-20 plot the peak radial displacement as a function of the longitudinal pre-stretch λ_z^0, the material parameter β, the normalized pressure $p(t)R/(\mu H)$, and the normalized characteristic time t_{cp} / t_{MR}.

It can be observed that an increase of the longitudinal pre-stretch λ_z^0, results in a decrease of the radial displacement and in stiffer arterial systems (Figure 5-19(a)). On the other hand, by increasing the material parameter β (Figure 5-19(b)), the normalized pressure $p(t)R/(\mu H)$ (Figure 5-20(a)) or the normalized characteristic time t_{cp} / t_{MR} (Figure

5-20(b)), the normalized radial displacement is increased. The linear model yields lower radial displacements than the Mooney-Rivlin arterial model, especially for low pre-stretch values or high normalized pressure values. Note that, when the material parameter β is increased the effect of the second invariant is reduced, resulting in softer systems, and that when $\lambda_z^0 = 1$ there is no effect of parameter β on the response of the system.

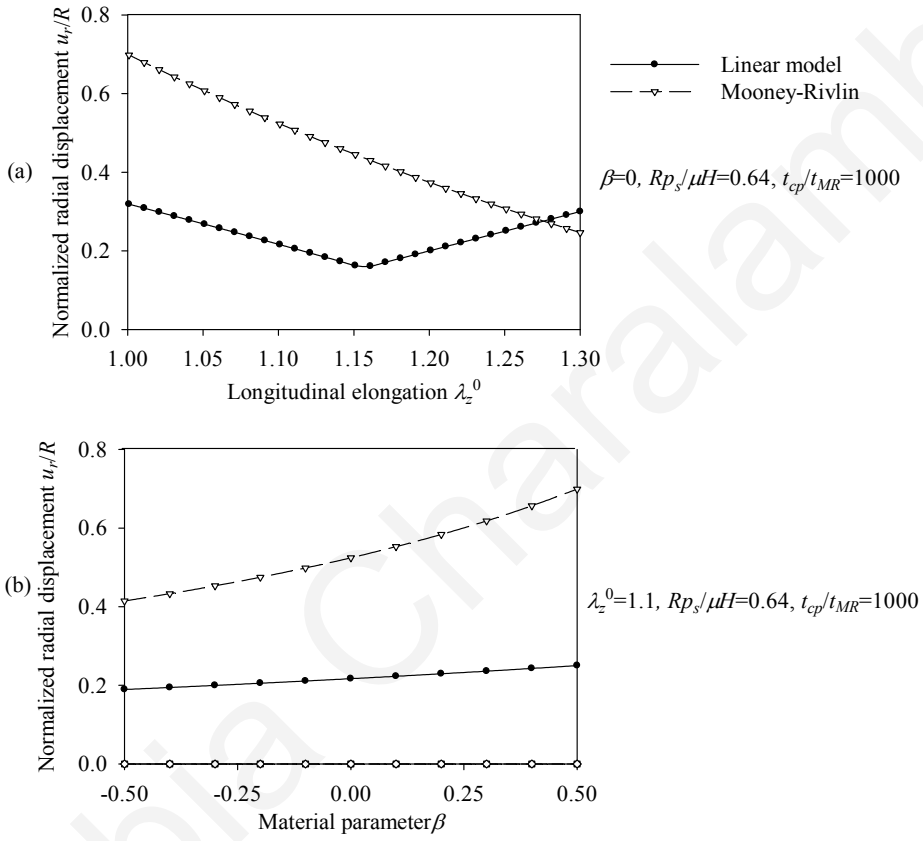

Figure 5-19: (a) Displacement spectrum for pre-stretch values $\lambda_z^0 = \{1 \div 1.3\}$ and $\beta = 0$, $p_s R/(\mu H) = 0.64$, $t_{cp}/t_{MR} = 1000$, (b) Displacement spectrum for material parameters $\beta = \{-0.5 \div 0.5\}$ and $\lambda_z^0 = 1.1$, $p_s R/(\mu H) = 0.64$, $t_{cp}/t_{MR} = 1000$.

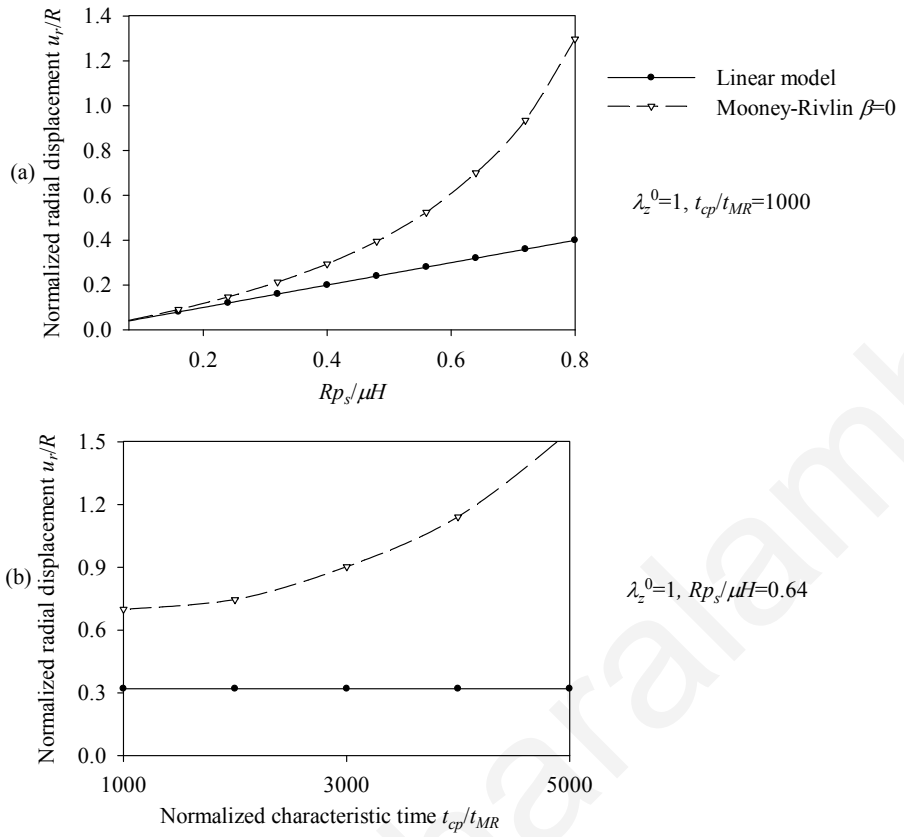

Figure 5-20: (a) Displacement spectrum for normalized pressure values $p_s R/(\mu H) = \{0.08 \div 0.8\}$ and $\lambda_z^0 = 1$, $\beta = 0$, $t_{cp}/t_{MR} = 1000$, (b) Displacement spectrum for characteristic time values $t_{cp}/t_{MR} = \{1000 \div 5000\}$ and $\lambda_z^0 = 1$, $\beta = 0$, $p_s R/(\mu H) = 0.64$.

5.4.3.2 Response spectra

Spectra of the response quantities (Equations (5.22), (5.23) and (5.43)-(5.45)) are plotted for different values of the non-dimensional parameters λ_z^0, β, and $p_s R/(\mu H)$.

Figure 5-21 plots response spectra for different values of longitudinal pre-stretch and for three values of the material parameter β. It can be observed that the circumferential elongation is reduced with increasing values of longitudinal pre-stretch λ_z^0, and that the normalized strain-energy has an optimized (minimum) point corresponding to a particular pre-stretch value. This is more noticeable for the case of normalized systolic pressure $p_s R/\mu H = 0.32$. On the other hand, the response quantities are increased with increasing values of the material parameter β.

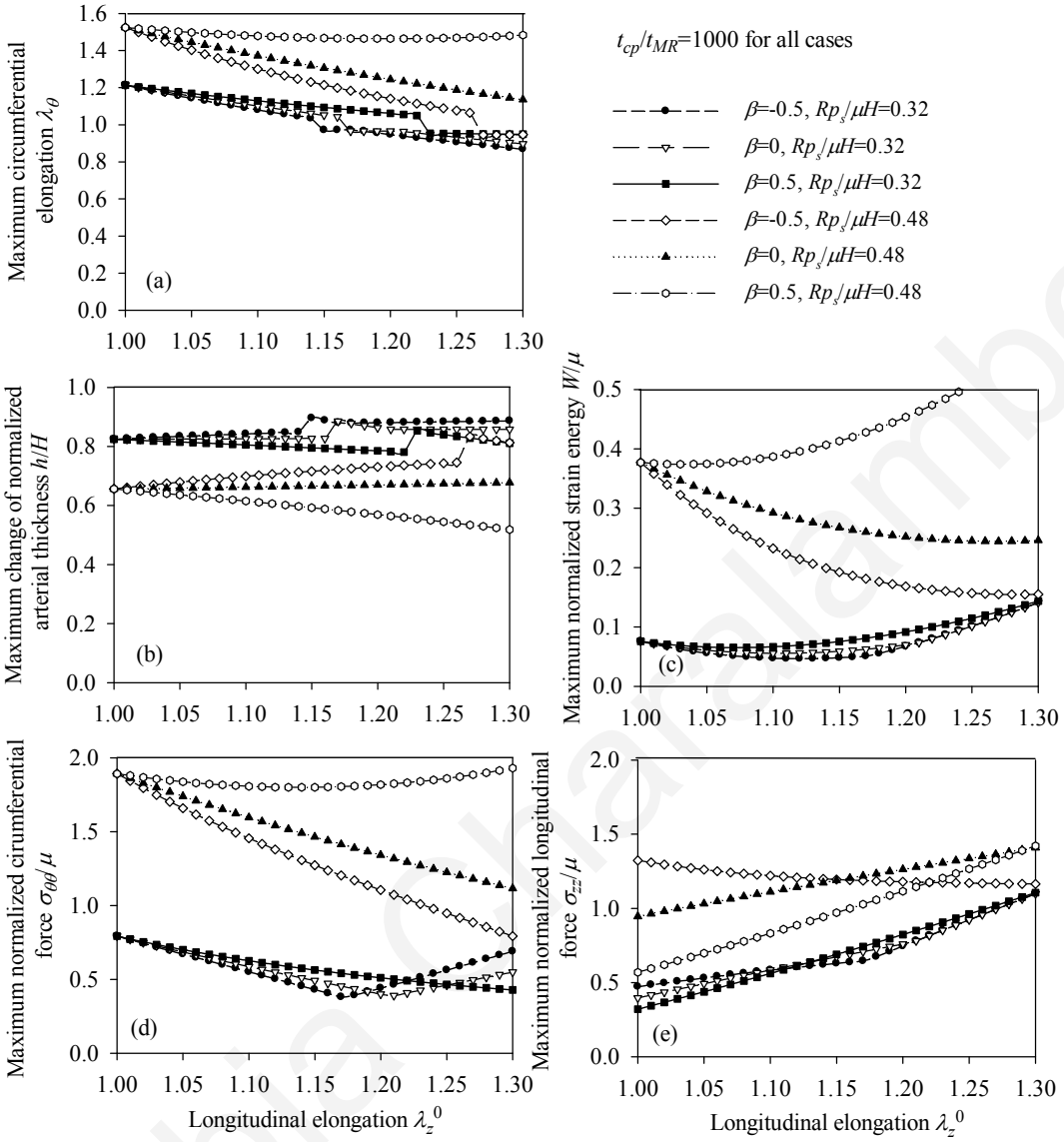

Figure 5-21: Response spectra for $\lambda_z^0 = \{1 \div 1.3\}$, for different values of the material parameter β and the normalized systolic pressure $p_s R/\mu H$, and $t_{cp}/t_{MR} = 1000$: (a) circumferential elongation λ_θ, (b) normalized thickness h/H, (c) normalized strain energy W/μ, (d) normalized circumferential stress $\sigma_{\theta\theta}/\mu$, (e) normalized longitudinal stress σ_{zz}/μ.

Response spectra were also investigated for different longitudinal pre-stretch values, for three values of normalized pressure $p_s R/\mu H$, and $\beta = 0$ (Figure 5-22). By increasing $p_s R/\mu H$ (case of hypertension or low elasticity modulus) the response is increased. Furthermore, for each case of normalized pressure, the normalized strain-energy exhibits an optimized (minimum) point for a particular pre-stretch value.

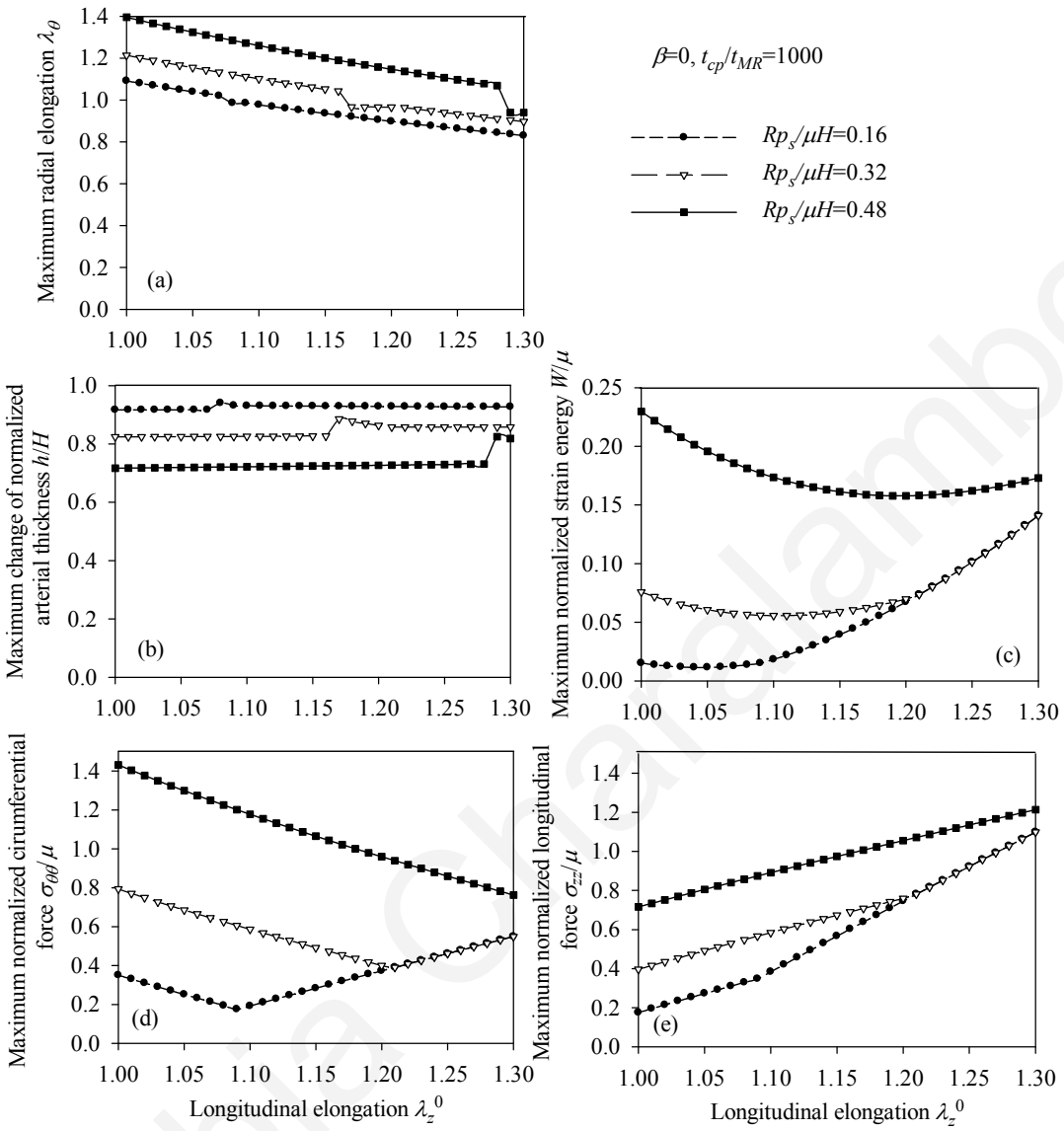

Figure 5-22: Response spectra for $\lambda_z^0 = \{1 \div 1.3\}$, three values of the normalized systolic pressure $p_s R/(\mu H)$, $\beta = 0$, and $t_{cp}/t_{MR} = 2000$: (a) circumferential elongation λ_θ, (b) normalized thickness h/H, (c) normalized strain energy W/μ, (d) normalized circumferential stress $\sigma_{\theta\theta}/\mu$, (e) normalized longitudinal stress σ_{zz}/μ.

Figure 5-23 presents response spectra as a function of the material parameter β, for three values of the parameter $p_s R/\mu H$ and for $\lambda_z^0 = 1.1$. The response parameters λ_θ, W/μ, and $\sigma_{\theta\theta}/\mu$ are increased for increasing values of the material parameter β, whereas all response quantities are increased for increasing values of the normalized pressure $p_s R/\mu H$.

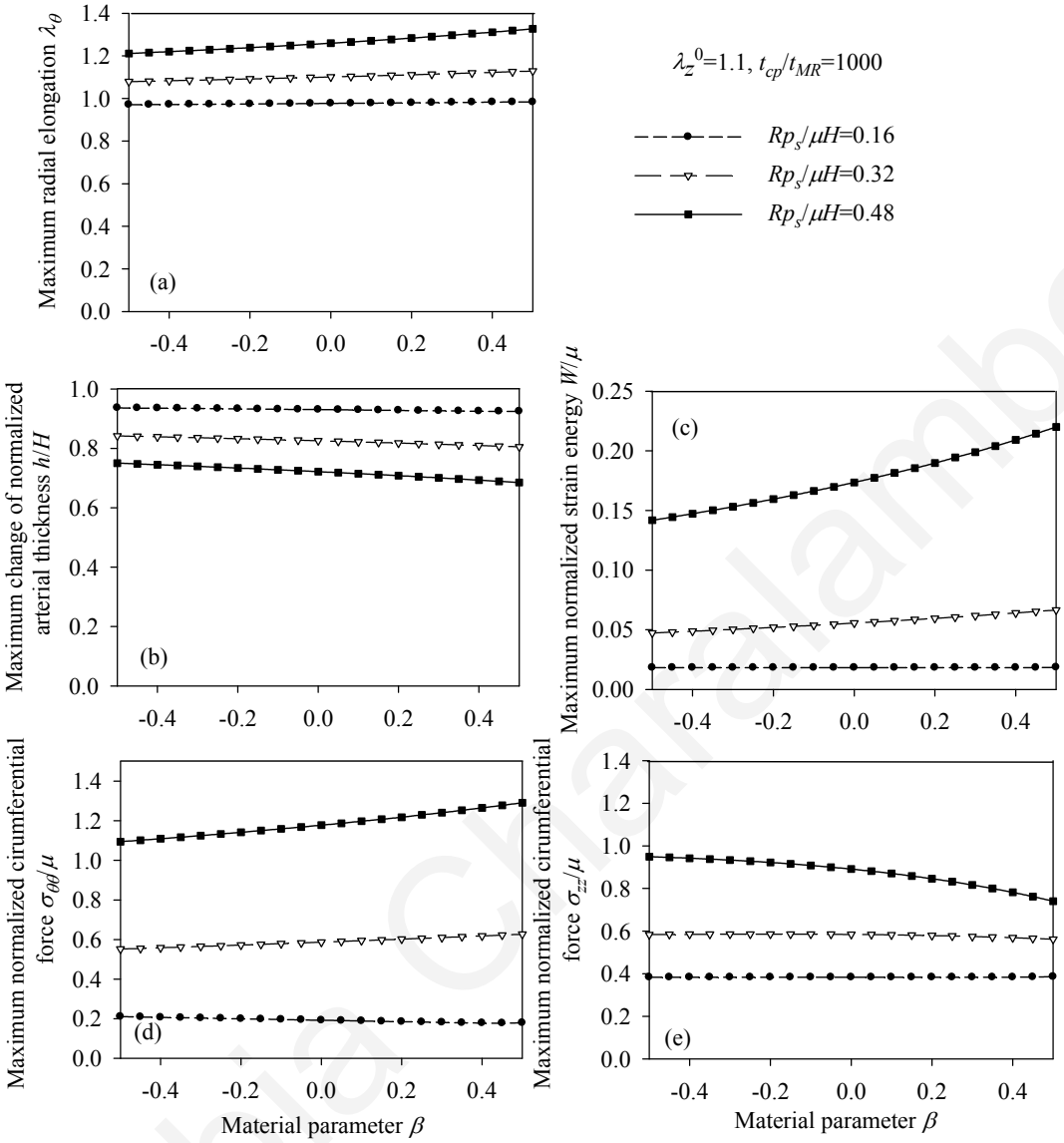

Figure 5-23: Response spectra for $\beta = \{-0.5 \div 0.5\}$, for three values of the normalized systolic pressure $p_s R/(\mu H)$ and for $\lambda_z^0 = 1.1$, $t_{cp}/t_{MR} = 1000$: (a) circumferential elongation λ_θ, (b) normalized thickness h/H, (c) normalized strain-energy W/μ, (d) normalized circumferential stress $\sigma_{\theta\theta}/\mu$, (e) normalized longitudinal stress σ_{zz}/μ.

Finally, Tables 5-7 through 5-9 report the time instant at which the peak value of normalized strain-energy occurs. In all cases, the peak value occurs during the systolic phase.

Table 5-7: Maximum normalized strain-energy W/μ and exact occurrence time for range of λ_z^0 and β values, and for $p_s R/\mu H = 0.32$ (case of Figure 5-21).

	β					
	-0.5		0		0.5	
λ_z^0	Maximum W/μ	Time (sec)	Maximum W/μ	Time (sec)	Maximum W/μ	Time (sec)
1	0.0757	0.34535	0.0757	0.34535	0.0757	0.34535
1.05	0.0558	0.001836	0.0606	0.001897	0.0662	0.31852
1.1	0.0473	0.001788	0.0556	0.001902	0.0666	0.002042
1.15	0.048	0.001739	0.0589	0.001902	0.0754	0.002115
1.2	0.0672	0	0.0697	0.005671	0.0916	0.002191
1.25	0.1013	0	0.1013	0	0.1145	0.002283
1.3	0.1409	0	0.1409	0	0.1435	0.002305

Table 5-8: Maximum normalized strain-energy W/μ and occurrence time for range of λ_z^0 and $p_s R/\mu H$ values, and for $\beta = 0$ (case of Figure 5-22).

	$p_s R/\mu H$					
	0.16		0.32		0.48	
λ_z^0	Maximum W/μ	Time (sec)	Maximum W/μ	Time (sec)	Maximum W/μ	Time (sec)
1	0.0152	0.001724	0.0757	0.34535	0.2298	0.35121
1.05	0.0114	0.005146	0.0606	0.001897	0.1958	0.35078
1.1	0.0182	0	0.0556	0.001902	0.1735	0.34967
1.15	0.0393	0	0.0589	0.001902	0.1612	0.34799
1.2	0.0672	0	0.0697	0.005671	0.1578	0.002133
1.25	0.1013	0	0.1013	0	0.1621	0.002123
1.3	0.1409	0	0.1409	0	0.173	0.002116

Table 5-9: Maximum normalized strain-energy W/μ and exact occurrence time for β and $p_s R/\mu H$ values, and for $\lambda_z^0 = 1.1$ (case of Figure 5-23).

	$p_s R/\mu H$					
	0.16		0.32		0.48	
β	maximum W/μ	Time (sec)	maximum W/μ	Time (sec)	maximum W/μ	Time (sec)
-0.5	0.0182	0	0.0473	0.001788	0.1418	0.34565
-0.4	0.0182	0	0.0488	0.001809	0.1473	0.34704
-0.3	0.0182	0	0.0503	0.001831	0.1531	0.34857
-0.2	0.0182	0	0.052	0.001854	0.1595	0.35023
-0.1	0.0182	0	0.0537	0.001877	0.1663	0.34776
0	0.0182	0	0.0556	0.001902	0.1735	0.34967
0.1	0.0182	0	0.0575	0.001928	0.1814	0.34737
0.2	0.0182	0	0.0596	0.001955	0.1897	0.34966
0.3	0.0182	0	0.0618	0.001983	0.1989	0.33365
0.4	0.0182	0	0.0641	0.002012	0.2091	0.35008
0.5	0.0185	0.009085	0.0666	0.002042	0.22	0.34816

5.4.4 Comparison of the proposed hyperelastic arterial models through response spectra

This section presents a comparison of the three proposed hyperelastic models. Each model is characterized by different material constants. Therefore, we choose to run two sets of analysis for the specific stress-strain curves shown in Figure 5-24. We can say that the models of Figure 5-24(a) correspond to arteries with large elasticity modulus (stiff models), whereas the models of Figure 5-24(b) correspond to arteries with low elasticity modulus (soft models). Note that, the models used in each analysis are not characterized by the same initial circumferential tangent modulus.

Figures 5-25 and 5-26 plot the response spectra of the three hyperelastic models as a function of the longitudinal pre-stretch. In addition, the circumferential elongation of the linear case is calculated. In the first case (stiff systems) the Hariton arterial model demonstrates large circumferential elongations compared to the other models. For low and medium pre-stretch values, it also demonstrates the higher strain-energy values and

stresses. On the other hand, the response of the Skalak et al. and the Mooney-Rivlin arterial models is similar. The linear case is conservative compared to the Skalak et al. and Mooney-Rivlin model, whereas for pre-stretch values up to 1.15 it demonstrates lower circumferential elongation than the Hariton case. The behavior of these models does not correspond to the strain hardening effect of each material, due to the fact that the models are stiff and the resulting strain is low (circumferential strains up to 30%). At low strains, the constitutive laws have not entered their hardening or softening regions yet.

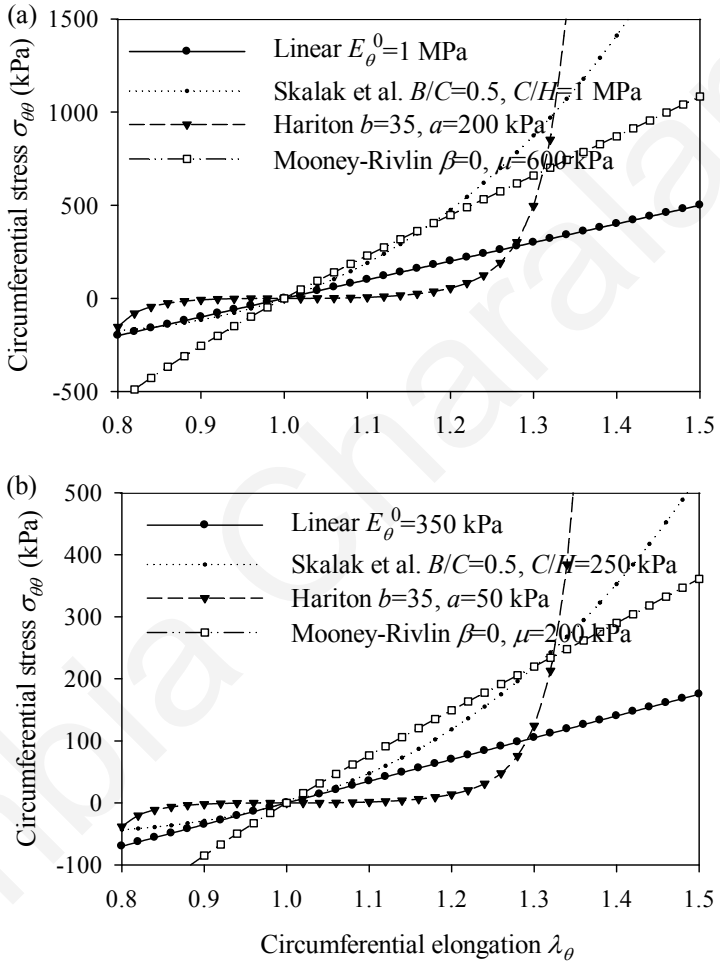

Figure 5-24: Selected stress-strain relationships of the hyperelastic models ($\lambda_z^0 = 1$): (a) systems with large elasticity modulus, (b) systems with low elasticity modulus.

In the second case (soft models) we can observe that the Mooney-Rivlin model demonstrates the largest elongations, it follows the linear model, the Skalak et al. model, and very last the Hariton arterial model. Furthermore, the Hariton case gives low strain-energy values and high stresses compared to the other two hyperelastic laws. These results clearly show the effect of material strain hardening on the dynamic arterial response, since

the models exhibited large strains (circumferential strains higher than 30%) and the constitutive laws have entered their characteristic hardening or softening regions.

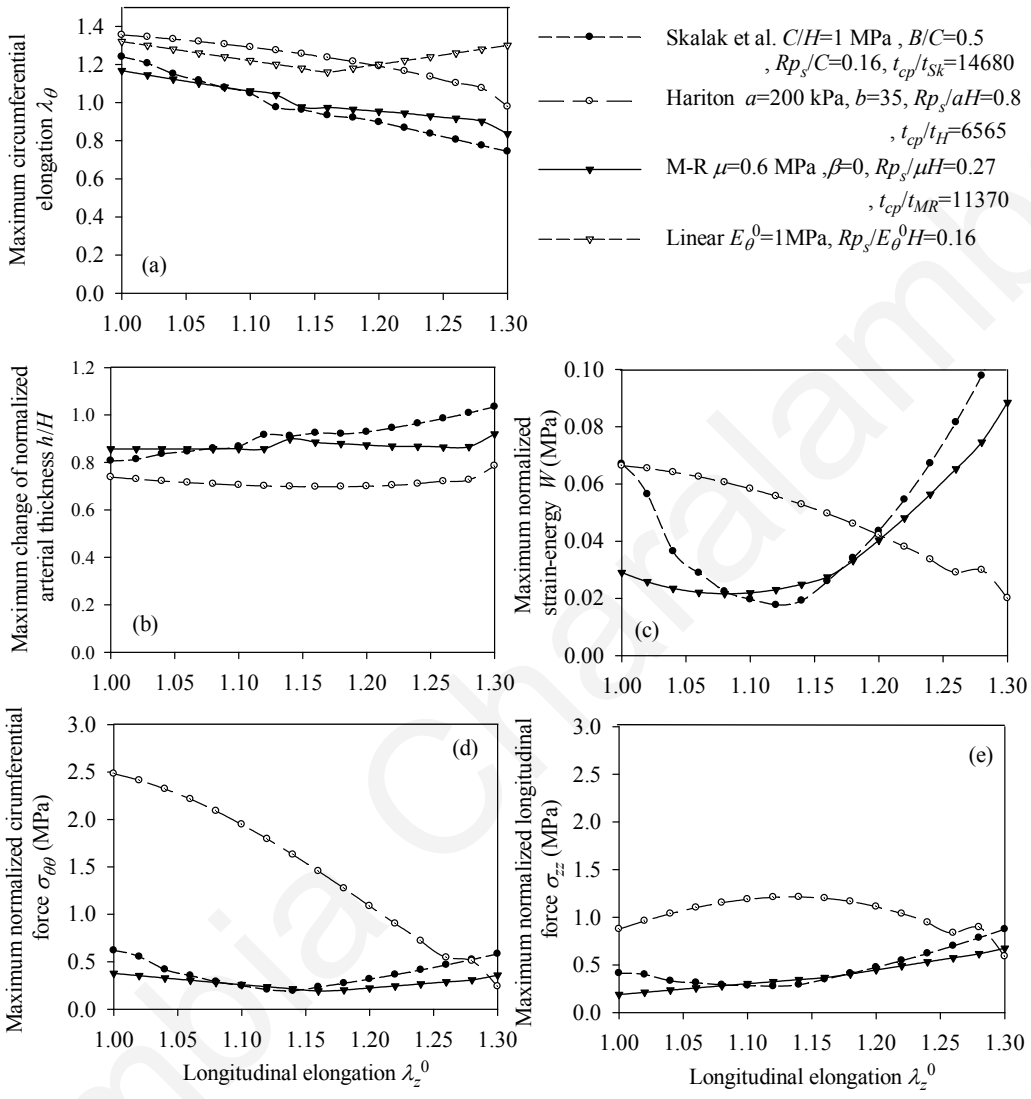

Figure 5-25: Response spectra of the three (stiff) hyperelastic arterial models for $\lambda_z^0 = \{1 \div 1.3\}$ and for the material laws shown in Figure 5-24(a): (a) circumferential elongation λ_θ, (b) normalized thickness h/H, (c) strain-energy density W, (d) circumferential stress $\sigma_{\theta\theta}$, (e) longitudinal stress σ_{zz}.

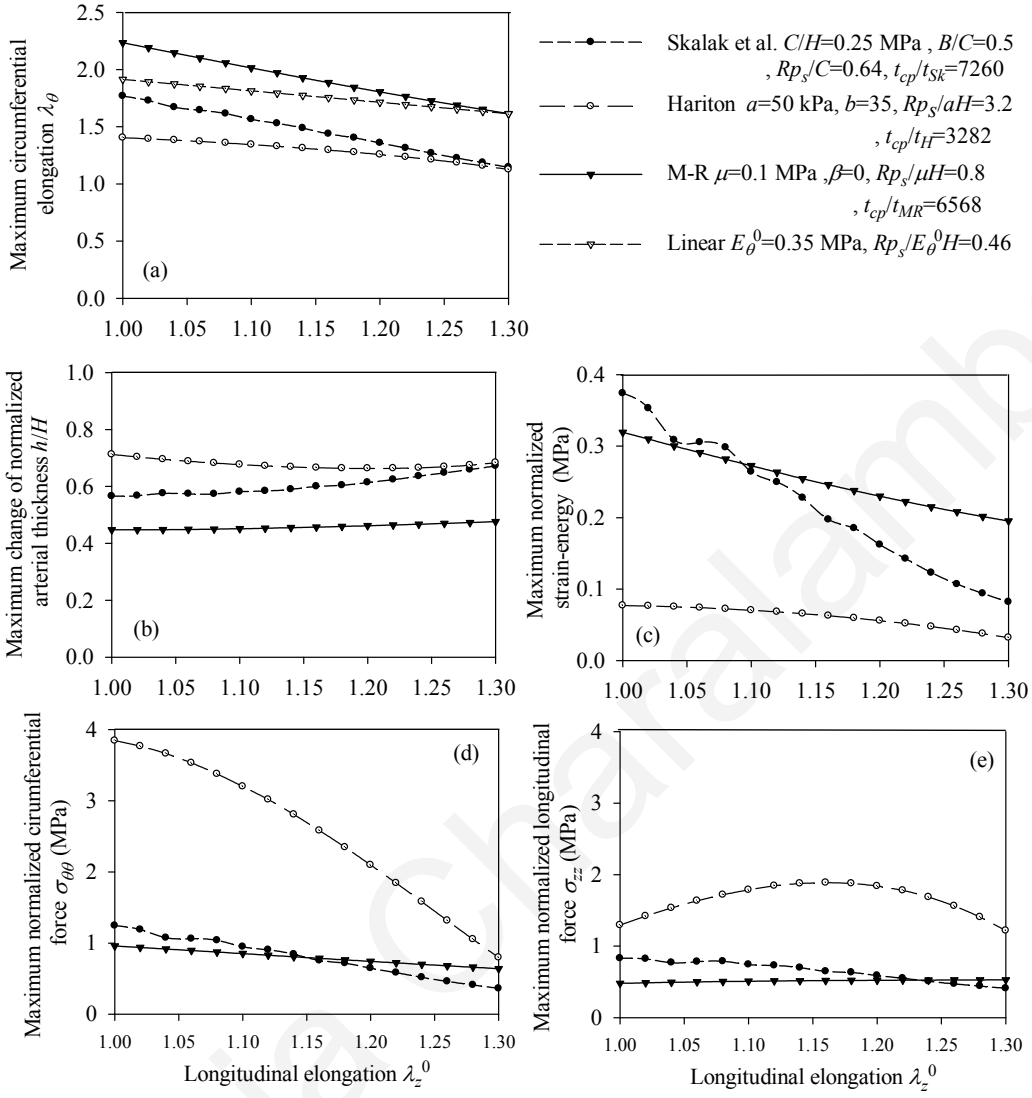

Figure 5-26: Response spectra of the three (soft) hyperelastic arterial models for $\lambda_z^0 = \{1 \div 1.3\}$ and for the material laws shown in Figure 5-24(b): (a) circumferential elongation λ_θ, (b) normalized thickness h/H, (c) strain-energy density W, (d) circumferential stress $\sigma_{\theta\theta}$, (e) longitudinal stress σ_{zz}.

5.5 Numerical examples

To illustrate the applicability of the proposed analytical models, numerical examples are presented and compared against analytical studies available in the literature. Such studies are the works of Demiray and Vito [29] and Humphrey and Na [30], which both investigated the case of an exponential hyperelastic constitutive law.

Demiray and Vito [29] studied the radial deformations of arteries subjected to dynamic inner pressure. Their model was assumed to be isotropic, homogeneous, and

incompressible. They presented a numerical example based on data corresponding to a dog's abdominal aorta, simulated by the exponential strain-energy density function of Blatz et al. [76]. The dog's abdominal aorta has inner radius 3.12 mm, outer radius 3.80 mm, and longitudinal pre-stretch equal to 1.53 and is subjected to dynamic loading with systolic and diastolic pressures 9.892 kPa and 3.466 kPa, respectively. The resulting circumferential stress at the artery centerline, at the beginning of the systolic phase, is calculated by Demiray and Vito as 395.7 kPa.

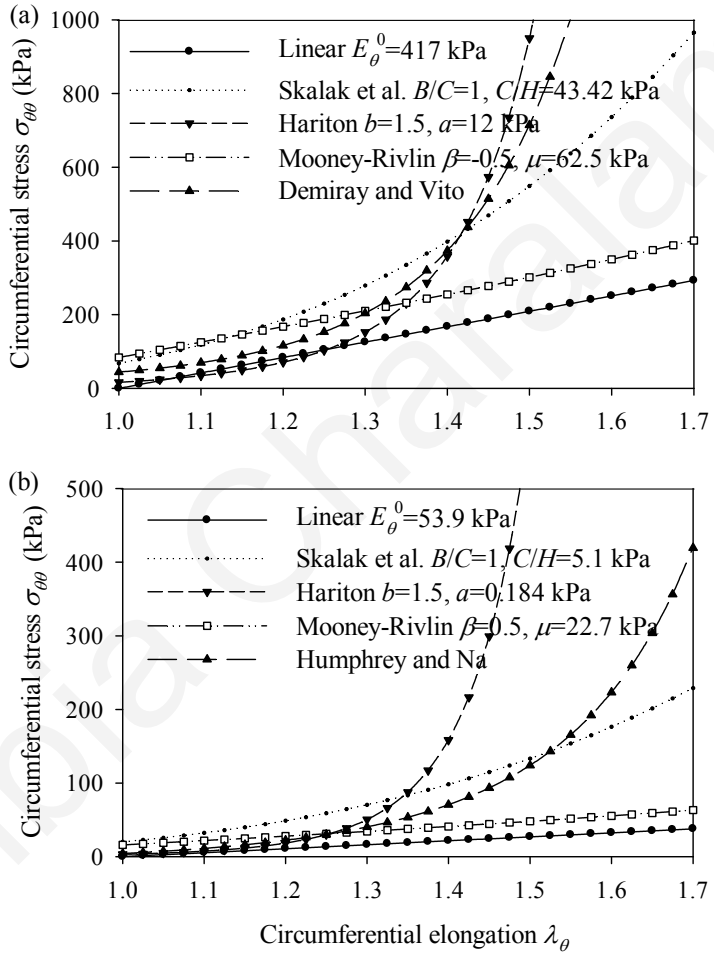

Figure 5-27: Circumferential stress-strain curves of the linear and hyperelastic constitutive laws used for the case of (a) Demiray and Vito [29], (b) Humphrey and Na [30].

The data used by Demiray and Vito [29] in their example, are utilized to calculate the arterial response for the proposed Skalak et al. and the Hariton arterial models (the Mooney-Rivlin arterial model is not suitable for the data of this example, due to the large pre-stretch value). The selected material parameters of each case have about the same initial tangent modulus and adequate curve fitting compared to the circumferential stress-

strain curve of the analysis of Demiray and Vito (Figure 5-27(a)). Table 5-10 reports the data used for each model and the corresponding response values. The case that approximates better the peak circumferential stress calculated by Demiray and Vito (395.7 kPa) is the arterial model that adopts the strain-energy function of Hariton (446.69 kPa). The linear model and the Skalak et al. arterial model yield lower values of circumferential stress. Note that, the peak strain-energy density value of the Skalak et al. and Hariton arterial model are comparable, whereas the linear arterial model yields larger strain-energy density values.

In another study, Humphrey and Na [30] investigated the dynamic response of an artery and the resultant wall stresses. They assumed that the artery is anisotropic, homogeneous, incompressible and obeys the exponential hyperelastic law of Chuong and Fung [77]. In a numerical example they investigated the passive response of an artery subjected to two cardiac cycles with systolic and diastolic pressures of 105 mmHg and 91 mmHg, respectively. The artery has inner radius 1.39 mm, outer radius 1.99 mm and longitudinal pre-stretch 1.832. The model also accounted for residual circumferential stresses by using the approximate "opened-up" stress-free configuration [77]. The peak circumferential and axial stresses of the inner surface were calculated by Humphrey and Na as 212.8 kPa and 177 kPa respectively (in general the inner surface has lower stress values than the outer surface). The maximum radial displacement of the outer surface was computed to be 0.72 mm (mean strain 42%).

We utilize the data used by Humphrey and Na [30] to investigated the arterial response for the hyperelastic functions considered in this study. Figure 5-27(b) shows the circumferential stress-strain curves of our analysis and of the analysis of Humphrey and Na. The material parameters of each case were selected to have about the same initial tangent modulus and adequate curve fitting to the Humphrey and Na model. To account for the residual circumferential stresses, we assume that a compressive pressure equal to 50 mmHg is applied to the arterial wall. Table 5-11 reports the data used for the linear, Skalak, and Hariton arterial model and the corresponding response values. The Mooney-Rivlin hyperelastic function is not suitable for the data (large pre-stretch value) of this example.

The calculated values of the arterial model of Skalak (strain 55% and circumferential stress 153.22 kPa) approach better the results of Humphrey and Na. Note that our calculations are based on the average stress assumption, whereas the values reported by Humphrey and Na

concern the stresses of the inner surface. In addition, we can observe that there is a variation of the peak values of strain-energy for the different material constitutive laws.

Table 5-10: Data used in the analysis (based on Demiray and Vito [29]) and response values for each case.

Data	
R (mm)	3.46
H (mm)	0.68
λ_z^0	1.53
ρ_0 (kg/m3)	1160
p_s (mmHg) /(Pa)	74.2/9892
p_d (mmHg) /(Pa)	26.0/3466
t_s (sec)	0.35
t_{cp} (sec)	1

Linear arterial model			
Parameters		Peak response values	
E_θ^0 (kPa)	417	u_r / R	0.53
u_0 (mm)	1.83	$\sigma_{\theta\theta}$ (kPa)	221
		σ_{zz} (kPa)	221
		W (kPa)	117

Skalak et al. arterial model			
Dimensionless parameters		Peak response values	
B/C	1	u_r / R	0.06
$p_s R / C$	1.16	$\sigma_{\theta\theta}$ (kPa)	96.68
t_{cp} / t_{Sk}	2187	σ_{zz} (kPa)	161.75
		W (kPa)	39.56

Hariton arterial model			
Dimensionless parameters		Peak response values	
b	1.5	u_r / R	0.42
$p_s R / aH$	4.19	$\sigma_{\theta\theta}$ (kPa)	446.69
t_{cp} / t_H	1143	σ_{zz} (kPa)	523.77

		W (kPa)	43.90

Table 5-11: Data used in the analysis (based on Humphrey and Na [30]) and response values for each case.

Data	
R (mm)	1.69
H (mm)	0.6
λ_z^0	1.832
ρ_0 (kg/m3)	1160
p_s (mmHg) /(Pa)	55/ 7.333
p_d (mmHg) /(Pa)	41/5.466
t_s (sec)	0.3
t_{cp} (sec)	0.8

Linear arterial model			
Parameters		Peak response values	
E_θ^0 (kPa)	53.9	u_r / R	0.83
u_0 (mm)	1.406	$\sigma_{\theta\theta}$ (kPa)	44.85
		σ_{zz} (kPa)	44.85
		W (kPa)	37.31

Skalak et al. arterial model			
Dimensionless parameters		Peak response values	
B/C	0.5	u_r / R	0.55
$p_s R/C$	4.04	$\sigma_{\theta\theta}$ (kPa)	153.22
t_{cp} / t_{Sk}	1679	σ_{zz} (kPa)	164.83
		W (kPa)	103.43

Hariton arterial model			
Dimensionless parameters		Peak response values	
b	1.5	u_r / R	0.46
$p_s R / aH$	111.9	$\sigma_{\theta\theta}$ (kPa)	354.27
t_{cp} / t_H	319	σ_{zz} (kPa)	569.67

		W (kPa)	22.28

5.6 Concluding remarks

This chapter investigates the macroscopic arterial dynamic response caused by three different material behaviors associated with arterial diseases. Each material behavior is described by a proper constitutive law. Important metrics that can be useful to vascular surgery were investigated, such as the radial deformation and the maximum energy density.

It should be noted that the study presented in this chapter is limited by the model assumptions (i.e. one homogenized layer, isotropic material). Indeed, several hyperelastic constitutive laws that consider more detailed and complex arterial structure are available in the literature. These models depend on many material parameters which cannot be easily obtained, nor are they available in the literature. The arterial material parameters are characterized by large uncertainties and vary with topology, age, gender, and disease of the artery. For this reason, at this point, it may not be useful to study detailed multi-parameter hyperelastic laws. Thus, we chose to investigate isotropic models which contained only two material parameters. If the material parameters of the complex/multi-parameter constitutive laws were definitely obtainable, the problem could be methodically solved by following the procedure presented in this chapter.

A good example of a more complex multi-parameter hyperelastic law is the constitutive model proposed by Holzapfel et al. [69]. This model accounts for the material anisotropy and two families of collagen fibers (arranged in symmetrical spirals) of non atherosclerotic thick-wall coronary arteries. Their proposed strain-energy function is a five-parameter equation expressed as

$$W = \mu_1 (I_1 - 3) + \frac{\mu_2}{\mu_3} \left\{ \exp\left[\mu_3 (1 - \mu_4)(I_1 - 3)^2 + \mu_3 \mu_4 (I_4 - 1)^2 \right] - 1 \right\} \tag{5.72}$$

where $\mu_1 > 0$ and $\mu_2 > 0$ are stress like parameters, $\mu_3 > 0$ and $\mu_4 = [0 \div 1]$ are dimensionless parameters, and $I_1 = \lambda_\theta^2 + \lambda_z^2 + (\lambda_\theta^2 \lambda_z^2)^{-2}$ and $I_4 = \lambda_\theta^2 \cos^2 \varphi_1 + \lambda_z^2 \sin^2 \varphi_1$ are the first and fourth invariants, respectively. By φ_1 is denoted the orientation angle of the collagen fiber reinforcement.

References in the literature suggest that the use of complex hyperelastic laws may not be very useful and could hide the generality of results or the most important aspects of the

problem. Humphrey and Na [30] observed that the more complex the arterial model, the less complex the stress field appears to be. Moreover, Hariton [70] modeled the realistic orientation of collagen fibers of the arterial tissue and observed that there is no significant difference between the macroscopic response of the simplified and the complex model.

Based on the finding of this chapter, we can conclude that the response of arterial models based on any other constitutive law (e.g. the constitutive laws proposed by Fung [53] or Gent [54]) depends on the increased hardening or softening behavior of the stress-strain relationship. For instance, the exponential strain-energy function of Hariton exhibits increased hardening compared to the strain-energy function of Skalak et al., implying that the radial deformation based on the Hariton arterial model is expected to be lower than what we calculated for the Skalak et al. arterial model.

The level of approximation of the linear-elastic model against the proposed hyperelastic models was investigated throught radial displacement spectra. For each analysis the models had the same initial tangent Young's modulus in the circumferential direction. It appears that for most cases the solution of the linear model constitutes a good approximation (conservative approximation) of the Skalak et al. solution (Figures 5-10 and 5-11). The Mooney-Rivlin case yields higher radial displacements compared to the linear case (Figures 5-19 and 5-20). On the other hand, for the Hariton model the approximation is not good, especially at low pre-stretch values, due to the fact that the initial tangent modulus approaches zero (the slope of the stress-strain curve becomes steeper at higher strains, Figures 5-14 and 5-15). The use of a tangent Young's modulus corresponding to circumferential elongations 10%-20% (instead of using the initial young modulus E_θ^0 corresponding to zero circumferential elongations) is expected to yield better approximations.

In general the most important factors influencing the peak response of the hyperelastic models are found to be the longitudinal pre-stretch λ_z^0 and the normalized pressure. The normalized radial displacement decreases with increasing values of pre-stretch. Figure 5-28 offers an explanation as to what this means for the human health along the years for the case that the material law is not significantly altered over the years. The longitudinal pre-stretch is caused due to the delayed growth of arteries compared to the rest of the body. Therefore, human arteries exhibit increasing longitudinal pre-stretch with aging. The gradual arterial stress softening, caused by aging, can be balanced by the longitudinal pre-stretch and the decreased radial response. On the other hand, at old age the human body exhibits small shrinkage causing the longitudinal pre-stretch to decrease. Combined with

the continuing loss of strength, the arterial response cannot be easily balanced, thus the human vascular system becomes vulnerable.

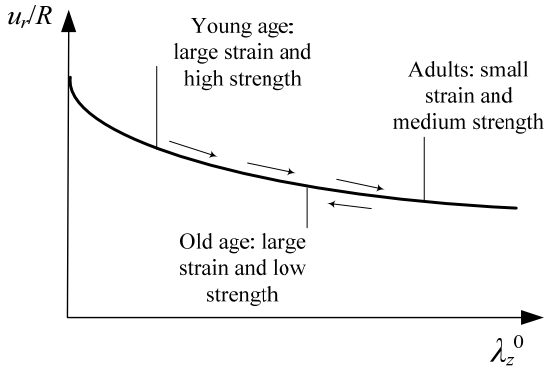

Figure 5-28: Explanatory diagram for the longitudinal pre-stretch and radial deformation the arterial response of different age groups. It is assumed that the material law is not significantly changed over the years.

An increase of the normalized pressure parameter implies increased intraluminal pressures (hypertension) and/or decrease of the elasticity modulus of the arterial tissue. The normalized pressure is increased by a factor of 5/3 or 10 in cases of hypertension or soft arterial tissue, respectively. Under the effect of large normalized pressures the system response is increased, especially for the Mooney-Rivlin case (Figure 5-20(a)).

The strain-energy density is an important metric for the response of arterial systems. The normalized strain-energy is increased with increasing values of the absolute normalized displacement $|u_r / R|$. In some cases, the stress value is not an appropriate criterion for distinguishing the limit values of different systems. On the contrary, the corresponding strain-energies and displacements are distinctive. Zafiropoulou [78] was the first to prove that the strain-energy density constitutes a trustworthy criterion for the arterial response. The energy criterion of the arterial tissue is consistent with the failure criterion, i.e. if the energy of the system reaches the limit value the system will fail. In contrast, in the case of artificial grafts the material properties are well known, thus a stress failure criterion would be more relevant.

In addition, numerical examples were demonstrated based on the data used in the analytical studies of Humphrey and Na [30] and Demiray and Vito [29]. The calculated response presented in these studies can be adequately approximated by the arterial models proposed herein, if the proposed circumferential stress-strain curves have sufficient curve fitting over the stress-strain curves used in the examples available in the literature.

In summary, this chapter proposes a theoretical method to investigate the effect of nonlinear hyperelastic constitutive laws and their strain-hardening characteristics on the dynamic behavior of human arteries. Important metrics, such as the radial deformation and the maximum energy density, are found to be influenced heavily by the strain-hardening characteristics of the model, as well as the longitudinal pre-stressing. The system response was calculated through numerical methods, and the results are presented through response spectra, revealing useful interrelations among the problem parameters.

CHAPTER 6

Arterial Dynamic Response: Viscoelastic Model

6.1 Introduction

Arterial tissue viscoelasticity is a characteristic of muscular arteries. Muscular arteries are medium-size arteries consisting mainly of muscular cells and located at the peripheral circulation (e.g. cerebral, celiac, and femoral arteries).They exhibit small hysteresis due to creep or relaxation process, which accounts for a relatively low-energy loss in each inflation-deflation cycle and prevents reflected pressure waves from resonating in the arterial systems [50]. Their viscosity is increased as the smooth muscle cells content, which exists mostly in the media layer, is increased. In addition, the viscoelastic characteristics of arterial tissues are affected by changes in temperature or by the presence of drugs [79]. Shah and Humphrey [80], who investigated the case of an elastic saccular aneurysm, noted that the elastic approach provides an upper bound on the dynamic response, and that the viscoelastic approach would probably describe a more stable system (i.e. provide a more refined solution to the problem).

Wall viscosity is a material characteristic and should be implemented in the constitutive law. Several studies investigated the viscoelastic behavior of arteries [32–34, 36]. It was concluded that a simple Maxwell or Voigt element cannot adequately model the viscoelastic response of such biological tissues. Kallita and Schaefer, in their review article [31], identify the different kinds of mechanical models that simulate the viscoelastic behavior of arteries. Westerhof and Noordergraaf [32] suggested a five-parametermodel consisting of two Maxwell elements and a spring, placed in parallel. In another study, Cox [33] proposed a spring in series with one or two Voigt elements, and Papageorgiou and Jones [34] proposed a model with a number of Voigt elements in series. Holzapfel et al. [36] adopted a model consisting of a single spring on one end and five Maxwell devices set in parallel (generalized Maxwell model).

Haslach Jr [37] recognized that the relatively recent approach proposed by Holzapfel et al. [36] adequately describes the viscoelastic behavior of arteries and that it requires many time-depended material constants. He proposed a nonlinear viscoelastic model that describes the long-term behavior of biological soft tissues, consisting of a system of evolution equations with time-independed material constants.

Herein, to simulate the viscoelastic behavior of arteries we adopt the sophisticated approach descriped by Holzapfel et al. [36] and the hyperelastic two-parameter constitutive

law proposed by Skalak et al. [55]. The proposed model is an extension of the hyperelastic arterial model developed in Chapter 5. The purpose of this investigation is to study the effect of each problem parameter on the macroscopic arterial response. Furthermore, it aims to examine if the proposed analytical model approximates well experimental and numerical data available in the literature.

The viscoelastic arterial model accounts explicitly for the longitudinal pre-stress, whereas other pre-stress effects are assumed to be incorporated in the constitutive law. Finally, although arteries are anisotropic, we are mainly concerned with the effect of viscosity in the dynamic response of the artery cross-section.

6.2 Mathematical model

The mathematical model developed (Figure 6-1(a)) is based on the following assumptions: (a) the arterial tissue consists of a single layer (homogenized media and adventitia); (b) the artery is a thin-walled structure (i.e. the arterial wall thickness is small compared to the internal radius of the vessel); (c) the vessel cross-section in the undeformed state forms a full circle with thickness-averaged radius R; (d) the arterial wall has constant thickness along the circle; (e) no boundary constrains are applied on the ring; and (f) the effects of rotary inertia and shear deformation are neglected.

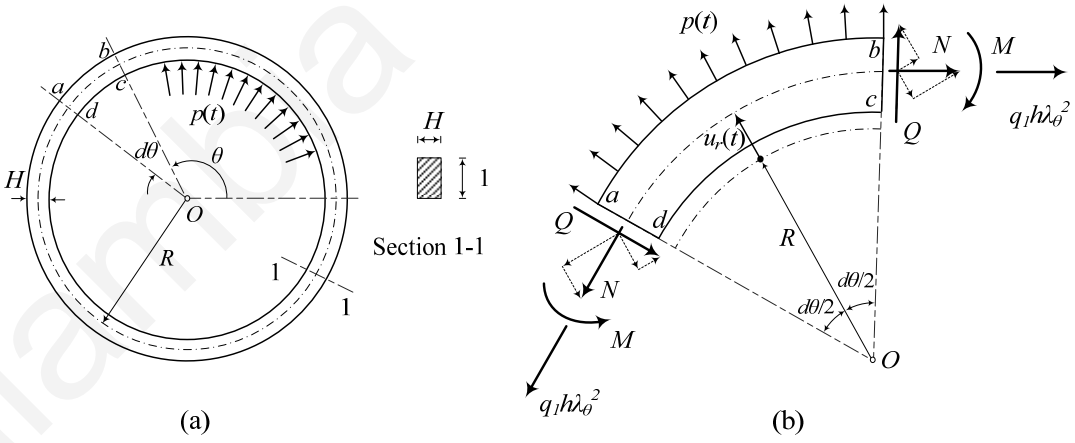

Figure 6-1: (a) Configuration of viscoelastic arterial model at undeformed state, (b) Free-body diagram of a typical element of viscoelastic arterial ring.

Note that, by R, H, and L are denoted the radius, thickness, and length of the initial configuration respectively; and by r, h, l are denoted the radius, thickness, and length of the deformed configuration respectively.

The arterial wall viscosity is simulated by adopting the generalized Maxwell model, which consists of a single spring on one end and a number of Maxwell devices set in parallel (Figure 6-2). Furthermore, the adopted model separates the total stresses to elastic long-term stress and viscoelastic stresses. This model was developed by Bonet [81] for the general case of large strain viscoelastic models. Holzapfel and Gasser [35] extended the Bonet approach to the case of fiber-reinforced composites, and in a later study Holzapfel et al. [36] extended the model to the case of arteries.

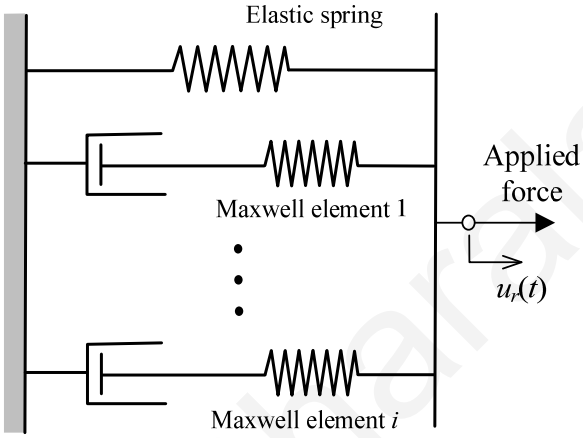

Figure 6-2: Generallized Maxwell model, consisting of a single spring and a number of i Maxwell elements set in parallel.

In terms of strains, the adopted model utilizes the total strain of the system (sum of elastic and viscoelastic strains) [82, 81, 35]. Note that, it would be more appropriate to use a model that separates the elastic from the viscoelastic strains, but the material parameters of such arterial models are not available in the existing literature.

The Bonet-Holzapfel viscoelastic model is based on the internal variable theory. The internal dissipation is described through the non-equilibrium stresses $q_i(t)$, which could be taken into account as body forces as shown in Figure 6-1(b). The non-equilibrium second Piola-Kirchhoff stresses, for one relaxation process, are expressed through the convolution integral [36]:

$$q_1(t) = \exp\left(\frac{-t}{\tau_1}\right) q_1(0^+) + \int_{0^+}^{t} \exp\left[-\frac{t-t_n}{\tau_1}\right] \beta_1^{\infty} \dot{S}_{\theta}^{\infty}(t_n) dt_n \qquad (6.1)$$

where β_1^∞ is a non-dimensional free-energy factor constant, τ_1 is the respective relaxation time, t_n is the time instant of step *n*, and $\dot{S}_\theta^\infty$ is the second Piola-Kirchhoff circumferential stress rate. The material parameters β_1^∞ and τ_1 can be obtained through experimental procedures. Typical values of these material parameters are $\beta_1^\infty = 0.2 - 0.4$ and $\tau_1 = 0.001 - 10$ sec [36].

The equation of motion of the arterial ring is formulated by considering the deformed state of the model. In particular, it is obtained by considering the force equilibrium along the radial direction of the infinitesimal element *abcd*, shown in Figure 6-1(b). Thus, the resulting equation of motion of the arterial segment, for one relaxation process, is expressed as

$$r(t)\,p(t) - N(t) - q_1(t)\left(\lambda_\theta(t)\right)^2 h(t) = \rho_0 h(t) r(t) \frac{d^2 u_r(t)}{dt^2} \tag{6.2}$$

Evidently, when the non-equilibrium stresses $q_1(t)$ are equal to zero, Equation (6.2) becomes identical to the equation of motion of the hyperelastic arterial model proposed in Chapter 5 (Equation (5.2)).

More relaxation processes can be taken into account, by adding to Equation (6.2) more time integrals $q_i(t)$, with different free-energy factor constants and corresponding relaxation times.

6.2.1 Viscoelastic arterial model based on the strain-energy function of Skalak et al.

The model requires a proper hyperelastic constitutive law to describe the elastic stresses of the problem. The strain-energy function of Skalak et al. [55], was originally developed for red blood cell membranes. It is an isotropic, two-dimensional strain-energy function, demonstrating hardening behavior similar to that of arteries. The strain-energy function proposed by Skalak et al. is expressed as

$$W(t) = \frac{B}{4}\left(\frac{1}{2}(I(t))^2 + I(t) - II(t)\right) + \frac{C}{8}(II(t))^2 \tag{6.3}$$

in which B and C are the material parameters of the artery, having units of elastic modulus multiplied by artery thickness [N/m], and satisfying the condition $C \geq B \geq 0$. The

alternative forms of the strain invariants $I(t)$ and $II(t)$ are expressed by Equations (5.7) and (5.8), respectively.

The axial force $N(t)$ acting along the circumferential direction of the arterial segment is identical to the distributed force $T_\theta(t)$ (Equation (5.11)). On substituting Equations (5.3), (5.5), and (5.11) in Equation (6.2) the equation of motion of the viscoelastic arterial model can be expressed in normalized polynomial form as

$$-\frac{u_r(t)}{R}\left[\frac{B}{C\lambda_z^0}+\frac{3(\lambda_z^0)^3}{2}-\frac{\lambda_z^0}{2}\right]-\left(\frac{u_r(t)}{R}\right)^2\left[\frac{3B}{2C\lambda_z^0}+\frac{3(\lambda_z^0)^3}{2}\right]-\left(\frac{u_r(t)}{R}\right)^3\left[\frac{B}{2C\lambda_z^0}+\frac{(\lambda_z^0)^3}{2}\right] \\ +\left[\left(1+\frac{u_r(t)}{R}\right)p(t)\frac{R}{C}-\frac{(\lambda_z^0)^3}{2}+\frac{\lambda_z^0}{2}\right]-\frac{q_1(t)h(t)}{C}\left(1+\frac{u_r(t)}{R}\right)^2=\frac{\rho_0 R^2 H}{C\lambda_z^0}\frac{\ddot{u}_r(t)}{R} \tag{6.4}$$

The problem description is reduced to seven dimensionless quantities: B/C, λ_z^0, pR/C, $q_1(t)h(t)/C$, $u_r(t)/R$, $t_{Sk}{}^2\ddot{u}_r(t)/R$, and t/t_{Sk}, in which the term $t_{Sk}=\sqrt{\rho_0 R^2 H/C\lambda_z^0}$ is the characteristic time of the response.

The tangent circumferential Young's modulus E_θ can be expressed as a function of the circumferential and radial elongations, as

$$E_\theta=\frac{d\sigma_{\theta\theta}}{d\lambda_\theta}=\frac{d}{d\lambda_\theta}\left(\frac{\lambda_\theta\lambda_z^0 T_\theta}{H}\right)=\frac{B}{H}\left(2\lambda_\theta{}^3-\lambda_\theta\right)+\frac{C}{H}\left(2\lambda_\theta{}^3(\lambda_z^0)^4-\lambda_\theta(\lambda_z^0)^2\right) \tag{6.5}$$

Furthermore, the normalized functions of the circumferential elongation, circumferential Cauchy stress, longitudinal Cauchy stress, and strain-energy density are expressed respectively as (Equations (5.22), (5.24), (5.25), and (5.26))

$$\lambda_\theta(t)=1+\frac{u_r(t)}{R} \tag{6.6}$$

$$\frac{T_\theta(t)}{C}=\frac{\lambda_\theta(t)}{\lambda_z^0}\left[\frac{B}{2C}\left((\lambda_\theta(t))^2-1\right)+\frac{(\lambda_z^0)^2}{2}\left((\lambda_\theta(t))^2(\lambda_z^0)^2-1\right)\right] \tag{6.7}$$

$$\frac{T_z(t)}{C}=\frac{\lambda_z^0}{\lambda_\theta(t)}\left[\frac{B}{2C}\left((\lambda_z^0)^2-1\right)+\frac{(\lambda_\theta(t))^2}{2}\left((\lambda_\theta(t))^2(\lambda_z^0)^2-1\right)\right] \tag{6.8}$$

$$\frac{W(t)}{C}=\frac{B}{4C}\left(\frac{1}{2}(I(t))^2+I(t)-II(t)\right)+\frac{(II(t))^2}{8} \tag{6.9}$$

The normalized kinetic-energy density E_K / C of the system and the normalized total-energy density E_t / C (equal to the sum of the kinetic-energy density E_K and the strain-energy density W) are expressed respectively as

$$\frac{E_K(t)}{C} = \frac{h(t)}{C}\frac{\rho_0 \left(\dot{u}_r\right)^2}{2} = \frac{1}{2\lambda_\theta}\left(\frac{\dot{u}_r t_{Sk}}{R}\right)^2 \tag{6.10}$$

$$\frac{E_t(t)}{C} = \frac{E_K(t)}{C} + \frac{W(t)}{C} \tag{6.11}$$

6.2.2 A simple Kelvin-Voigt model

The Kelvin-Voigt element is a common device in modeling viscous effects [31]. We aim to investigate if the sophisticated Bonet-Holzapfel model can be approximated by a simple Kelvin-Voigt element. The respective equation of motion of the arterial segment becomes

$$r(t)p(t) - N(t) - \frac{\Gamma}{R}\frac{du_r(t)}{dt} = \rho_0 h(t) r(t) \frac{d^2 u_r(t)}{dt^2} \tag{6.12}$$

where Γ / R is the viscosity coefficient of the arterial wall, having units of $\mathrm{Pa}\cdot\mathrm{s}$. The viscosity coefficient can be parallelized (however is different) to the relaxation time of the Bonet-Holzapfel model as $\Gamma = \tau_1^\infty C$. By adopting the hyperelastic function of Skalak et al., and by following the procedure described in Section 6.2.1, the normalized equation of motion of the viscoelastic arterial model in polynomial form is:

$$\begin{aligned} &-\frac{u_r(t)}{R}\left[\frac{B}{C\lambda_z^0} + \frac{3(\lambda_z^0)^3}{2} - \frac{\lambda_z^0}{2}\right] - \left(\frac{u_r(t)}{R}\right)^2\left[\frac{3B}{2C\lambda_z^0} + \frac{3(\lambda_z^0)^3}{2}\right] - \left(\frac{u_r(t)}{R}\right)^3\left[\frac{B}{2C\lambda_z^0} + \frac{(\lambda_z^0)^3}{2}\right] \\ &+ \left[\left(1 + \frac{u_r(t)}{R}\right)p(t)\frac{R}{C} - \frac{(\lambda_z^0)^3}{2} + \frac{\lambda_z^0}{2}\right] - \frac{\Gamma}{C}\frac{\dot{u}_r(t)}{R} = \frac{\rho_0 R^2 H}{C\lambda_z^0}\frac{\ddot{u}_r(t)}{R} \end{aligned} \tag{6.13}$$

The Kelvin-Voigt viscoelastic arterial model is described by seven dimensionless quantities: B/C, λ_z^0, pR/C, $\Gamma\dot{u}_r(t)/CR$, $u_r(t)/R$, $t_{Sk}{}^2\ddot{u}_r(t)/R$, and t/t_{Sk}.

6.3 Numerical solution

The problem is highly nonlinear and requires numerical methods to be solved. In addition, in order to calculate the non-equilibrium stresses an iterative method is required. Two different solution strategies are implemented: (a) an iterative algorithm that utilizes Newmark's constant-acceleration method [83, 84]; and (b) an iterative algorithm that

utilizes Rosenbrock's method [73, 74] through the ode23s function in MATLAB. Both algorithms are developed in the MATLAB environment [67].

The two algorithms have the same accuracy but different efficiency. The first algorithm is the most efficient, since it requires computational time up to twenty times lower than the second algorithm. This occurs due to the fact that the second algorithm utilizes the ode23s function in MATLAB in each time step. If Rosenbrock's method was originally programmed, in the same manner as Newmark's method, it would have about the same efficiency as the first algorithm.

In Chapter 5, the hyperelastic arterial response of three arterial models was investigated. The ode23s and ode23tb solvers in MATLAB were utilized. The solvers were efficient against the hyperelastic problem, for the reason that it was not required an iterative procedure for the calculation of the elastic stresses. Thus, for solving complex problems such as the viscoelastic response of systems, it is more correct to develop the proper solver.

In this chapter, the presented results are calculated by utilizing the first algorithm (Newmark's constant-acceleration method for nonlinear systems).

6.3.1 Based on Newmark's constant-acceleration method

The solution of the differential equation governing the system response (Equation (6.4)), and the numerical integration of the convolution integral of Equation (6.1) can be obtained by utilizing Newmark's constant-acceleration method for nonlinear systems [84] through the following iterative procedure:

1. A constant time step Δt is set, and the total time interval $[0, T]$ is divided into $n-1$ sub-intervals.
2. The initial displacement, initial velocity, and initial non-equilibrium stresses (at time t=0) are set equal to zero. The initial acceleration $\ddot{u}_0$ is obtained by solving Equation (6.4) for $\ddot{u}_r$.
3. The predictors of the radial response at time t_{n+1} are obtained by utilizing the formulas of Newmark's constant-acceleration method. The displacement, velocity, and acceleration predictors are expressed respectively, as

$$(u_r)_{n+1} = (u_r)_n + \Delta t(\dot{u}_r)_n + \frac{\Delta t^2}{2}(1-2\beta_N)(\ddot{u}_r)_n \tag{6.14}$$

$$(\dot{u}_r)_{n+1} = (\dot{u}_r)_n + (1-\gamma_N)\Delta t(\ddot{u}_r)_n \tag{6.15}$$

$$(\ddot{u}_r)_{n+1} = 0 \tag{6.16}$$

where β_N and γ_N are constants equal to 0.25 and 0.5, respectively.

The circumferential elongation and the current thickness are equal to

$$(\lambda_\theta)_{n+1} = 1 + \frac{(u_r)_{n+1}}{R} \tag{6.17}$$

$$h_{n+1} = \frac{H}{\lambda_z^0 (\lambda_\theta)_{n+1}} \tag{6.18}$$

4. The normalized distributed non-equilibrium force multiplied by the current thickness $(q_1 h)_{n+1} / C$ is calculated as [35]

$$\frac{(q_1 h)_{n+1}}{C} = \exp\left(\frac{-\Delta t}{2\tau_1}\right)\left[\exp\left(\frac{-\Delta t}{2\tau_1}\right)\frac{(q_1 h)_n}{C} - \beta_1^\infty \frac{\left(S_\theta^\infty h\right)_n}{C}\right] + \beta_1^\infty \exp\left(\frac{-\Delta t}{2\tau_1}\right)\frac{\left(S_\theta^\infty h\right)_{n+1}}{C} \tag{6.19}$$

in which S_θ^∞ denotes the second Piola-Kirchhoff circumferential stress. Note that, the normalized second Piola-Kirchhoff elastic stress (multiplied by the current thickness) at each time step is

$$\frac{\left(S_\theta^\infty h\right)_n}{C} = \frac{(T_\theta)_n}{C(\lambda_\theta)_n^{\,2}} = \frac{1}{(\lambda_\theta)_n \lambda_z^0}\left[\frac{B}{2C}\left((\lambda_\theta)_n^{\,2} - 1\right) + \frac{(\lambda_z^0)^2}{2}\left((\lambda_\theta)_n^{\,2}(\lambda_z^0)^2 - 1\right)\right] \tag{6.20}$$

5. The calculated values must satisfy the equilibrium of Equation (6.4). The residual value $(A_{res})_{n+1}$ is calculated as

$$(A_{res})_{n+1} = \left\{\begin{array}{c} -\frac{u_r}{R}\left[\frac{B}{C\lambda_z^0} + \frac{3(\lambda_z^0)^3}{2} - \frac{\lambda_z^0}{2}\right] - \left(\frac{u_r}{R}\right)^2\left[\frac{3B}{2C\lambda_z^0} + \frac{3(\lambda_z^0)^3}{2}\right] - \left(\frac{u_r}{R}\right)^3\left[\frac{B}{2C\lambda_z^0} + \frac{(\lambda_z^0)^3}{2}\right] \\ + \left[\left(1 + \frac{u_r}{R}\right)p\frac{R}{C} - \frac{(\lambda_z^0)^3}{2} + \frac{\lambda_z^0}{2}\right] - \frac{q_1 h}{C}\left(1 + \frac{u_r}{R}\right)^2 - \frac{\rho_0 R^2 H}{C\lambda_z^0}\frac{\ddot{u}_r}{R} \end{array}\right\}_{n+1} \tag{6.21}$$

6. If $\left|(A_{res})_{n+1}\right|$<tolerance the solution is acceptable. If not, then the normalized corrector Δu_r is calculated as

$$\Delta u_r = \frac{(A_{res})_{n+1}}{\left(\frac{(E_\theta)_{n+1} H}{C} + \frac{{t_{Sk}}^2}{\beta_N \Delta t^2} \right)} \tag{6.22}$$

where $(E_\theta)_{n+1}$ is the tangent elasticity modulus for $(\lambda_\theta)_{n+1}$ and λ_z^0 (Equation (6.5)). Note that, if the problem was not characterized by axisymmetric geometry and axisymmetric loading, the tangent elasticity term should be replaced by the tangent stiffness.

7. The corrected normalized response is obtained as

$$\frac{(u_r)_{n+1}}{R} = \frac{(u_r)_{n+1}}{R} + \Delta u_r \tag{6.23}$$

$$\frac{t_{Sk}(\dot{u}_r)_{n+1}}{R} = \frac{t_{Sk}(\dot{u}_r)_{n+1}}{R} + \frac{t_{Sk}\gamma_N}{\beta_N \Delta t} \Delta u_r \tag{6.24}$$

$$\frac{{t_{Sk}}^2(\ddot{u}_r)_{n+1}}{R} = \frac{{t_{Sk}}^2(\ddot{u}_r)_{n+1}}{R} + \frac{{t_{Sk}}^2}{\beta_N \Delta t^2} \Delta u_r \tag{6.25}$$

8. Steps (5) through (7) are repeated until the tolerance is satisfied.
9. Steps (3) through (8) are repeated for all time intervals.
10. The normalized time-profiles of the circumferential Cauchy stress $T_\theta(t)/C$, longitudinal Cauchy stress $T_z(t)/C$, strain-energy density $W(t)/C$, kinetic-energy density $E_K(t)/C$, and total-energy density $E_t(t)/C$ are calculated.

Figure 6-3 shows the flow diagram of the general algorithm, based on Newmark's constant-acceleration method for nonlinear systems, calculating the time-profiles of the radial displacement, radial velocity, and radial acceleration.

6.3.2 Based on the modified Rosenbrock method

A second algorithm was also implemented for solving the differential equation governing the response of the viscoelastic arterial model (Equation (6.4)). This algorithm utilizes the ode23s function in MATLAB [67, 71], a one-step solver based on the modified Rosenbrock method [73, 74]. The problem is solved in the following manner:

1. The total time interval $[0, T]$ is divided into $n-1$ sub-intervals, of constant time step Δt.

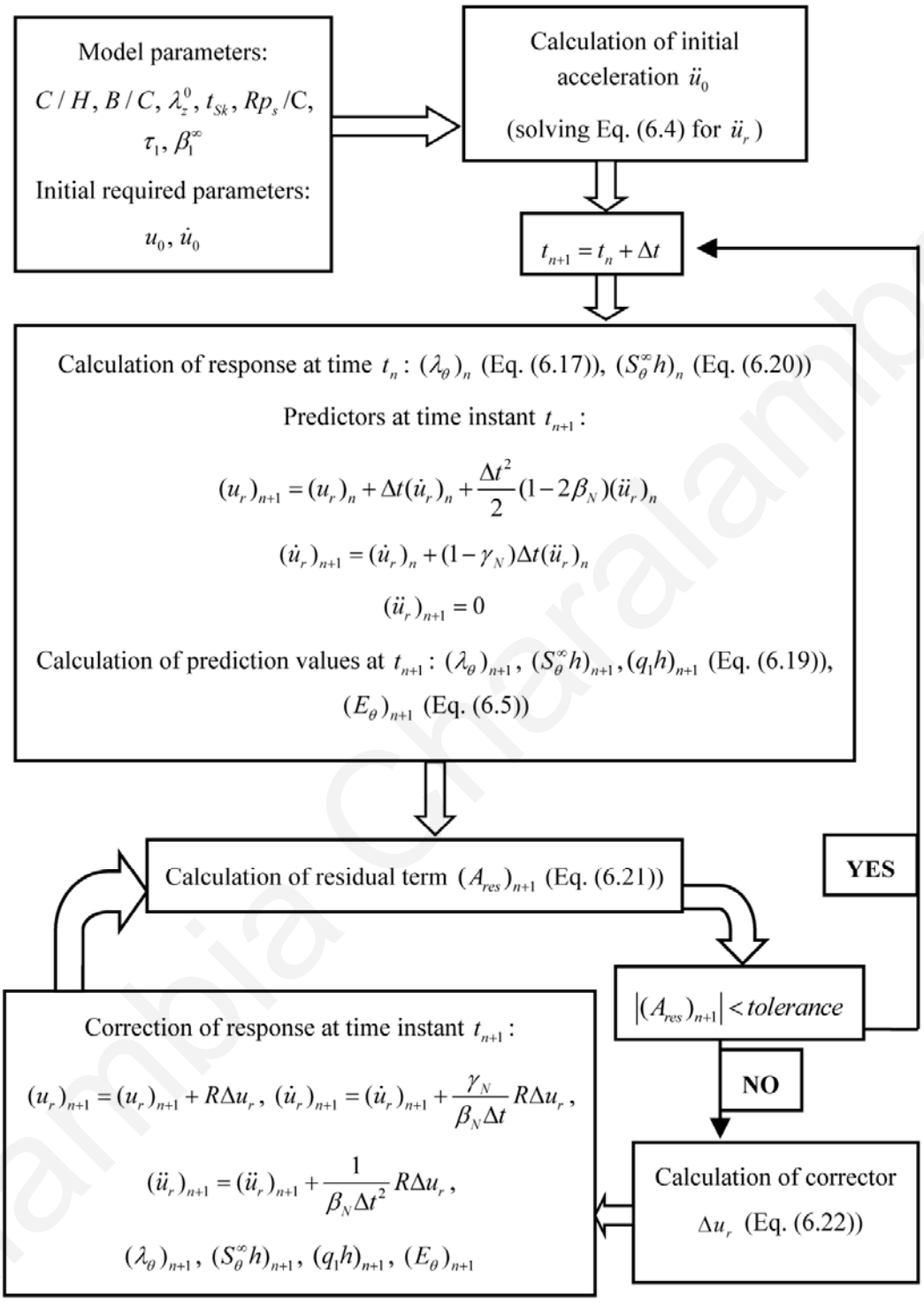

Figure 6-3: Flow diagram of Newmark's constant-acceleration method for nonlinear systems.

2. The initial displacement, initial velocity, and initial non-equilibrium stresses (at time t=0) are set equal to zero.

3. The radial displacement predictor at time t_{n+1} is obtained by using Newmark's constant-acceleration method for $\beta_N = 0.25$ and $\gamma_N = 0.5$, as

$$(\tilde{u}_r)_{n+1} = (u_r)_n + \Delta t(\dot{u}_r)_n + \frac{\Delta t^2}{2}(1-2\beta_N)(\ddot{u}_r)_n \tag{6.26}$$

where the acceleration $(\ddot{u}_r)_n$ is obtained by solving Equation (6.4) for $\ddot{u}_r$. The corrector of the displacement is

$$(u_r)_{n+1} = (\tilde{u}_r)_{n+1} + \beta_N \Delta t^2 (\ddot{u}_r)_{n+1} \tag{6.27}$$

in which the current acceleration $(\ddot{u}_r)_{n+1}$ is obtained by considering the predictor $(\tilde{u}_r)_{n+1}$ and the respective predictor of the non-equilibrium stress (Equation (6.19)).

4. The circumferential elongation $(\lambda_\theta)_{n+1}$ (Equation (6.17)), the normalized 2nd PK elastic stress $(S_\theta^\infty h)_{n+1}/C$ (Equation (6.20)), and the normalized distributed non-equilibrium force $(q_1 h)_{n+1}/C$ (Equation (6.19)) are calculated.

5. The radial displacement $(u_r)_{n+1}$ and radial velocity $(\dot{u}_r)_{n+1}$ are recalculated by solving the ordinary differential equation in the time interval $[t_n \; t_{n+1}]$, and for initial conditions $(u_r)_n$ and $(\dot{u}_r)_n$, by using the ode23s function in MATLAB. Based on these results, the response values $(\lambda_\theta)_{n+1}$, $(S_\theta^\infty h)_{n+1}/C$, and $(q_1 h)_{n+1}/C$ are also recalculated.

6. Steps (3) through (5) are repeated for all time intervals.

7. The normalized time-profiles of all the response values ($T_\theta(t)/C$, $T_z(t)/C$, $W(t)/C$, $E_K(t)/C$, $E_t(t)/C$) are obtained.

6.4 Results

The problem is characterized by high complexity, involving many parameters. In order to investigate the influence of each problem parameter on the response of the system, we conducted a large number of numerical investigations. In particular, the problem is investigated for different values of the dimensionless parameters B/C, λ_z^0, $p_s R/C$, t_{cp}/t_{Sk}, β_1^∞, and τ_1/t_{Sk} (where t_{cp} is the total duration of the cardiac pulse). The time step

of the iterative procedure is taken to be ten times lower than the characteristic time of the arterial model ($t_{Sk} / \Delta t = 10$).

The intraluminal pressure is approximated by two different pressure-time profiles. In the first case, the pressure is abruptly increased from zero to the maximum systolic pressure p_s=120 mmHg , as shown in Figure 6-4(a). The value of the diastolic pressure is p_d=80 mmHg , the systolic-phase duration is $t_s = 0.35$ sec , and the total duration of the cardiac pulse is $t_{cp} = 1$ sec . In the second case, the pressure is gradually increased (quasi-statically) from zero up to the initial diastolic pressure value of the dynamic pressure-time profile shown in Figure 6-4(b). Figure 6-4(b) shows the pressure-time profile of an aorta as proposed by Zhong et al. [39].

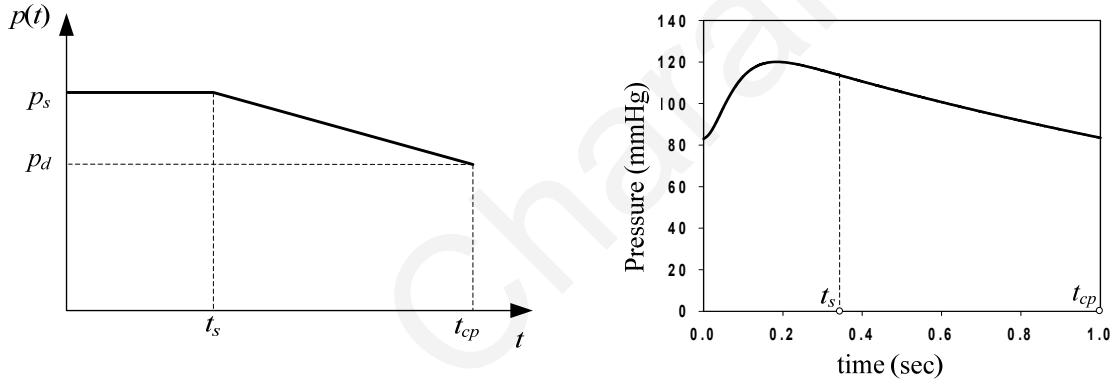

(a) (b)

Figure 6-4: (a) Arterial pulse time-profile approximation, (b) typical aortic pressure-time profile following Zhong et al. [39].

6.4.1 Response of the Bonet-Holzapfel model

After conducting a large number of numerical investigations the interrelation among the problem parameters is revealed. We can say that the viscoelastic problem is mainly affected by the normalized relaxation time τ_1 / t_{Sk} . An increase of the material parameter β_1^{∞} monotonically decreases the response of the system, whereas problem parameters λ_z^0 , B/C , and $p_s R/C$ affect the response of the viscoelastic model in the same manner that affect the response of the elastic model (see Section 5.4.1). In particular, an increase of the longitudinal pre-stretch λ_z^0 , or the material parameter B/C stiffens the system and decreases the radial displacement. An increase of the normalized pressure $p_s R/C$,

implying either an increase of the arterial pressure (hypertension) or a decrease of the elasticity modulus, increases the radial displacement.

Systems with increased normalized pulse duration t_{cp} / t_{Sk}, exhibit increased dissipation when subjected to the first loading approximation, whereas they exhibit decreased dissipation when subjected to the second loading approximation. In addition, systems with larger normalized pulse duration t_{cp} / t_{Sk} require longer computational time.

Since the problem is mainly affected by the relaxation time τ_1, we choose to present graphs for different values of the aforementioned material parameter. The presented results concern the case of a large artery (e.g. aorta) having radius 8 mm, wall thickness 1.2 mm, Young's modulus 1 MPa, and wall density 1160 Kg/m^3. Figures 6-5 through 6-9 show typical response time-histories of the elastic and viscoelastic models, by applying the pressure time-profile approximation of Figure 6-4(a), and for different values of the normalized relaxation time τ_1 / t_{Sk}. The response of the elastic model can be obtained either through the mathematical model proposed in this chapter (for $\beta_1^{\infty} = 0$), or through the mathematical model introduced in Section 5.2.1.

The normalized relaxation time values τ_1 / t_{Sk}, utilized in Figures 6-5 through 6-8, are equal to 1, 10, 100, and 1000, respectively. As follows from these figures, a decrease of the normalized relaxation time decreases the response time-history values, whereas slightly increases the peak circumferential elongation, which usually occurs at the beginning of the systolic phase. Moreover, it can be observed that the resulting circumferential elongation and the induced pressure time-profiles present the same morphology and are characterized by high-frequency vibrations. This is more evident in the case of the elastic model.

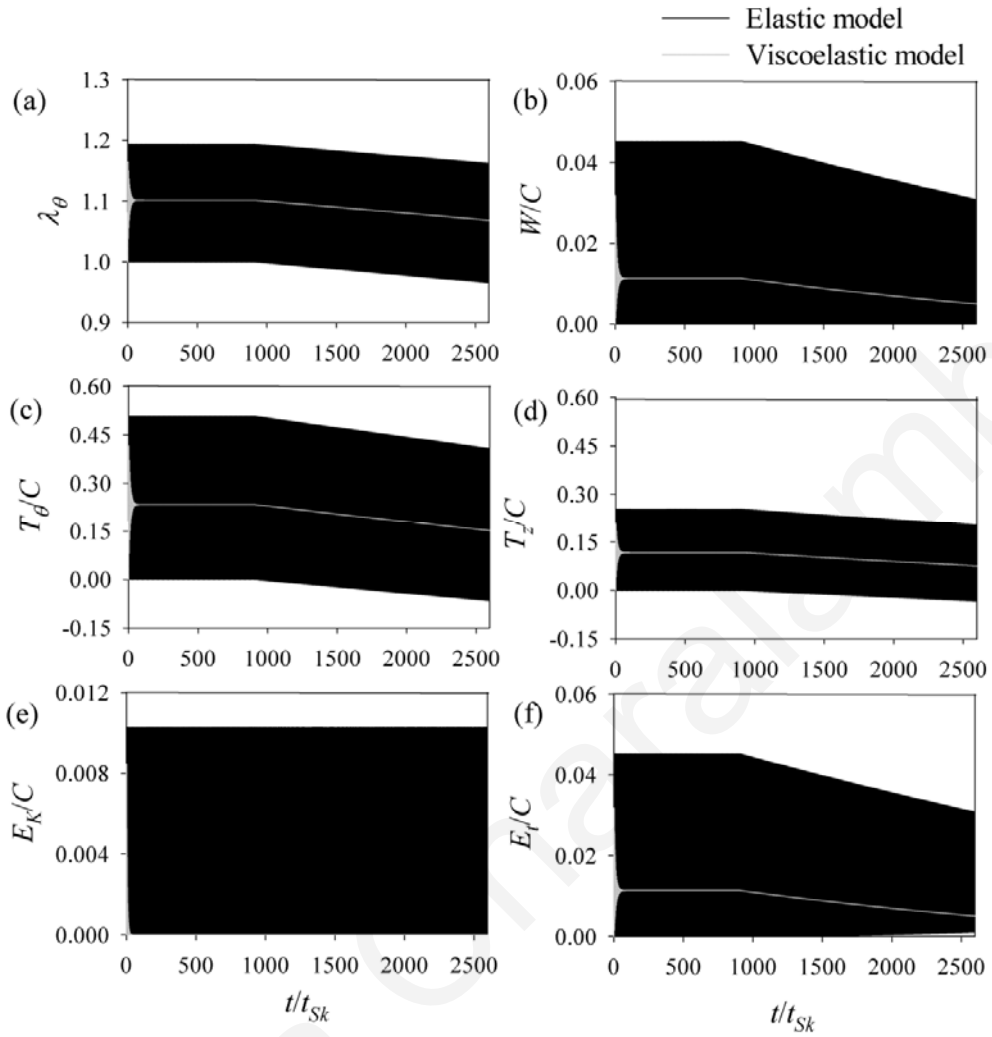

Figure 6-5: Response time-histories for $\tau_1 / t_{Sk} = 1$, $\beta_1^\infty = 0.3$, $\lambda_z^0 = 1$, $B/C = 1$, $p_s R/C = 0.21$, $t_{cp}/t_{Sk} = 2597$: (a) circumferential elongation λ_θ, (b) normalized strain-energy density W/C, (c) normalized circumferential stress T_θ/C, (d) normalized longitudinal stress T_z/C, (e) normalized kinetic-energy density E_K/C, (f) normalized total-energy density E_t/C.

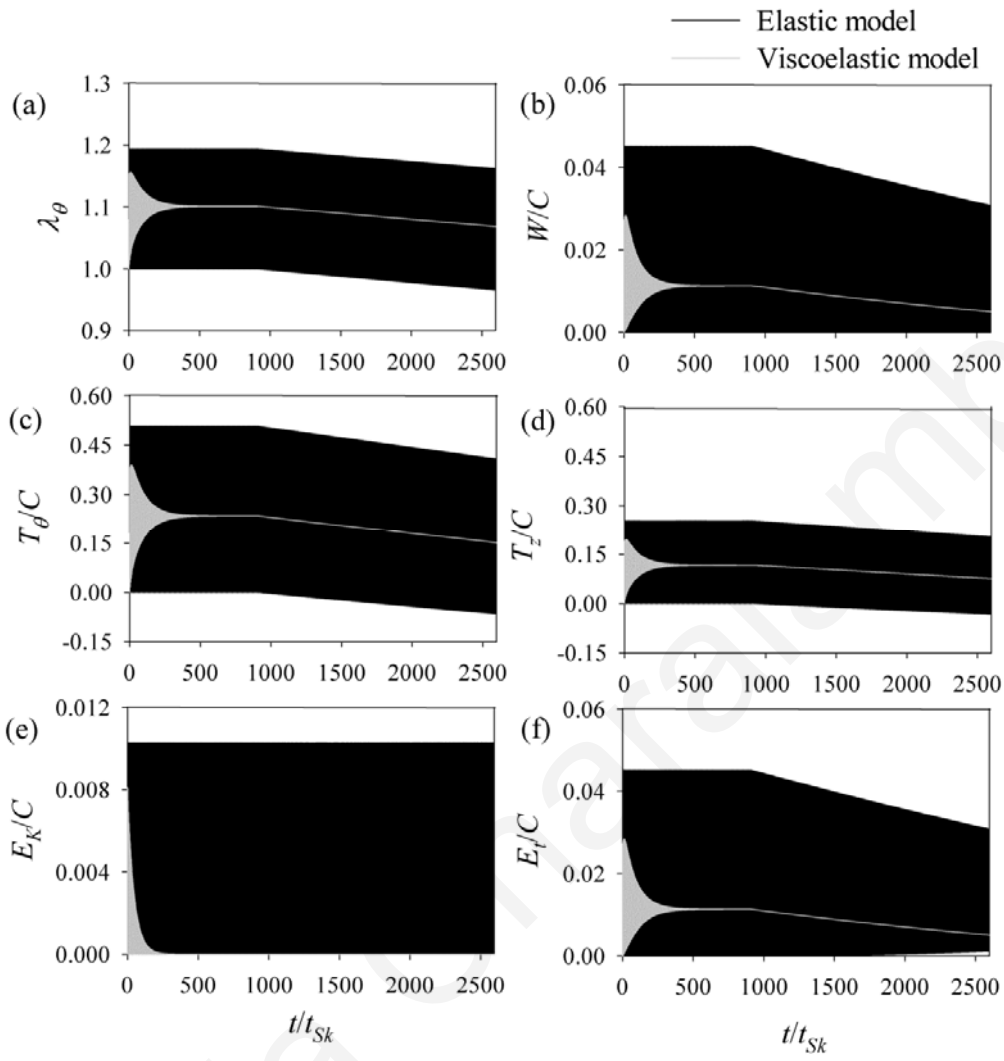

Figure 6-6: Response time-histories for $\tau_1 / t_{Sk} = 10$, $\beta_1^\infty = 0.3$, $\lambda_z^0 = 1$, $B/C = 1$, $p_s R/C = 0.21$, $t_{cp}/t_{Sk} = 2597$: (a) circumferential elongation λ_θ, (b) normalized strain-energy density W/C, (c) normalized circumferential stress T_θ/C, (d) normalized longitudinal stress T_z/C, (e) normalized kinetic-energy density E_K/C, (f) normalized total-energy density E_t/C.

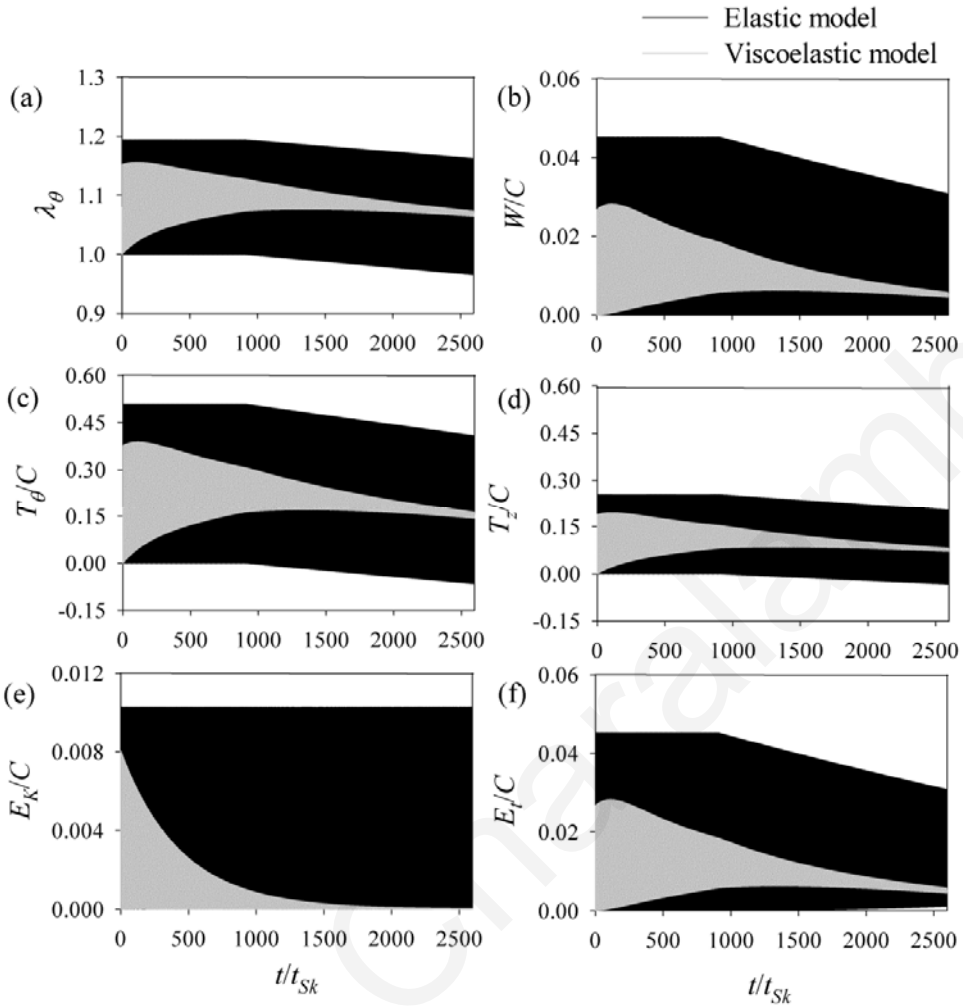

Figure 6-7: Response time-histories for $\tau_1 / t_{Sk} = 100$, $\beta_1^\infty = 0.3$, $\lambda_z^0 = 1$, $B/C = 1$, $p_s R/C = 0.21$, $t_{cp}/t_{Sk} = 2597$: (a) circumferential elongation λ_θ, (b) normalized strain-energy density W/C, (c) normalized circumferential stress T_θ/C, (d) normalized longitudinal stress T_z/C, (e) normalized kinetic-energy density E_K/C, (f) normalized total-energy density E_t/C.

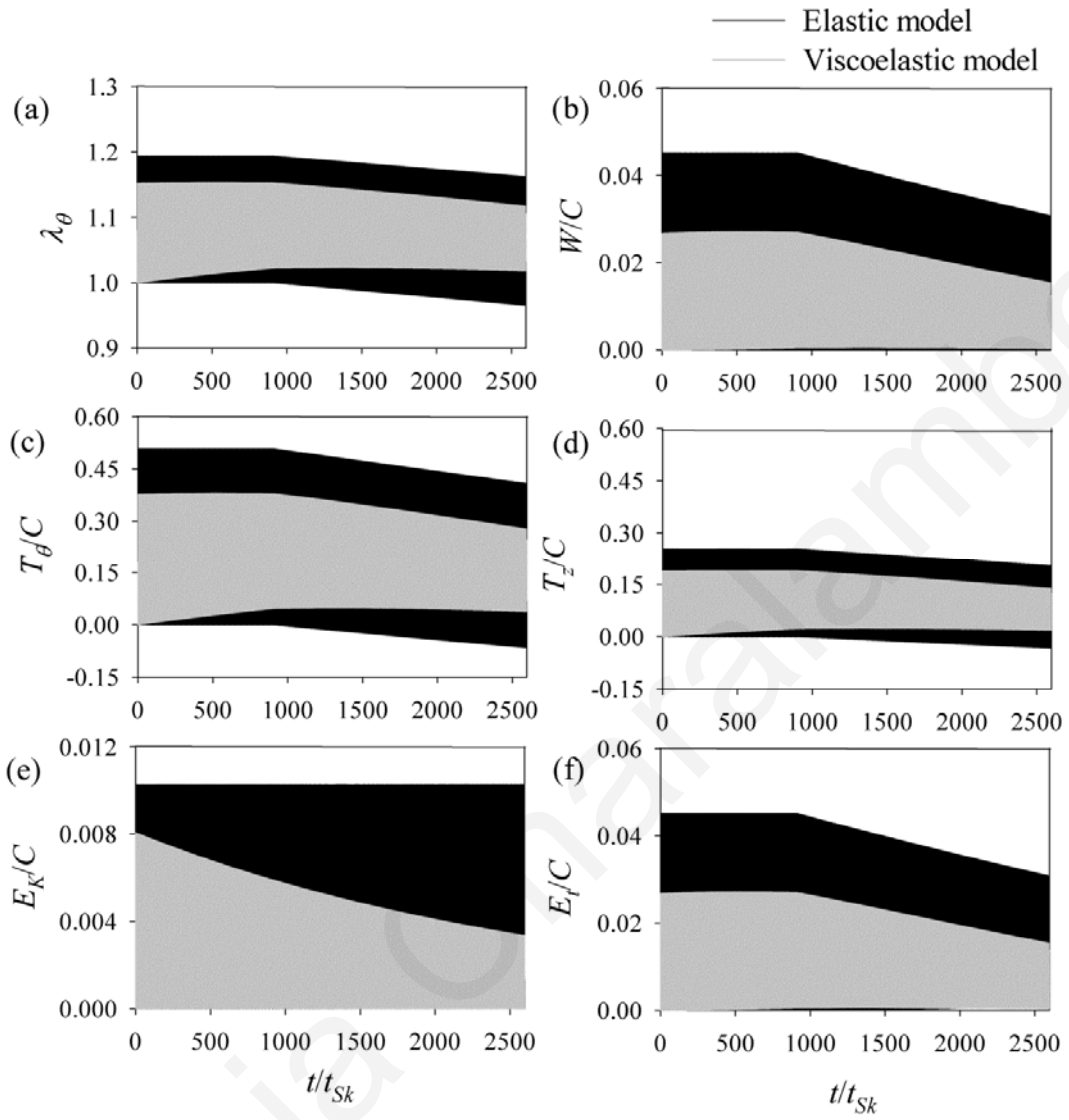

Figure 6-8: Response time-histories for $\tau_1 / t_{Sk} = 1000$, $\beta_1^\infty = 0.3$, $\lambda_z^0 = 1$, $B/C = 1$, $p_s R/C = 0.21$, $t_{cp}/t_{Sk} = 2597$: (a) circumferential elongation λ_θ, (b) normalized strain-energy density W/C, (c) normalized circumferential stress T_θ/C, (d) normalized longitudinal stress T_z/C, (e) normalized kinetic-energy density E_K/C, (f) normalized total-energy density E_t/C.

As follows from Figures 6-5 through 6-8, for increasing values of the normalized relaxation time, the loss of energy is decreased. The loss of total energy, by comparing the "response areas" of the elastic and viscoelastic models, is found to be about 98.5%, 96%, 72.8%, and 43.3%, for the cases of Figures 6-5 through 6-8 respectively. Figure 6-9 plots the respective normalized non-equilibrium stresses $q_1 h/C$. We can observe that, for low

values of the normalized relaxation time, the normalized non-equilibrium stresses exhibit lower values and nearly symmetric morphology along the time-axis.

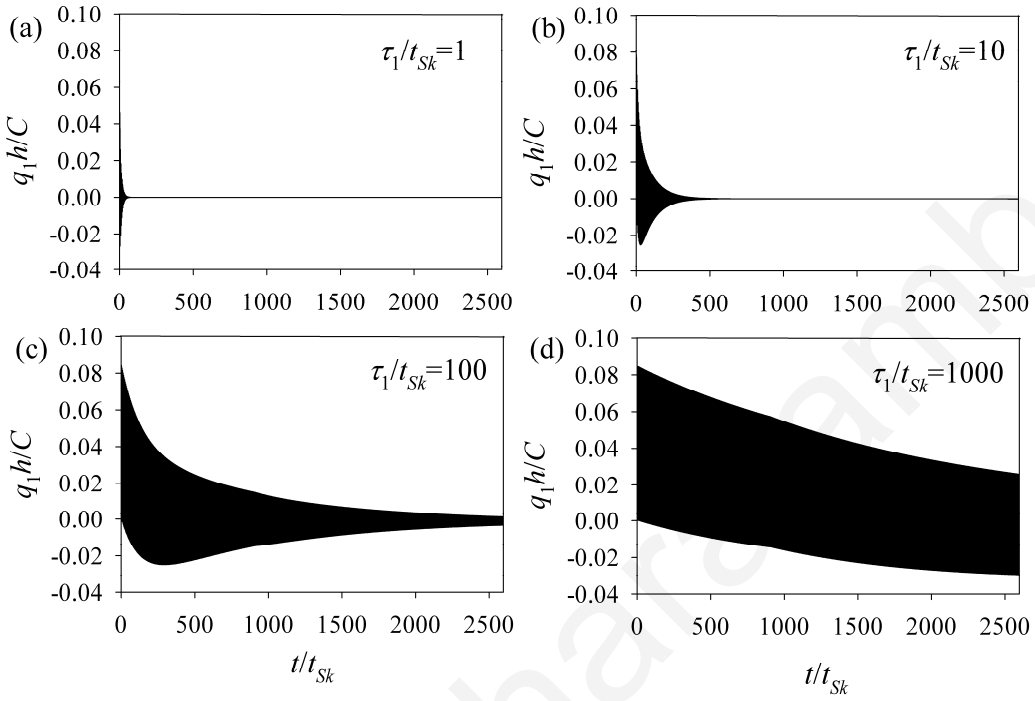

Figure 6-9: Normalized non-equilibrium stresses $q_1 h / C$ for (a) $\tau_1 / t_{Sk} = 1$, (b) $\tau_1 / t_{Sk} = 10$, (c) $\tau_1 / t_{Sk} = 100$, (d) $\tau_1 / t_{Sk} = 1000$ (cases of Figures 6-5 through 6-8, respectively).

In addition, we performed numerical analyses of arterial systems under periodic excitation, by repeating the profile of Figure 6-4(a). Figure 6-10 shows a typical time-profile of a system under periodic excitation. The conclusions obtained from this investigation are the same to that obtained by the non-periodic excitation. Furthermore, it is evident that the viscoelastic model has higher stability compared to the respective hyperelastic model.

In the case that the pressure is quasi-statically applied up to the diastolic pressure of the pressure time-profile shown in Figure 6-4(b), the viscoelastic system is not always characterized by high-frequency vibrations. Figure 6-11 shows the response of the elastic and viscoelastic models for different values of the normalized relaxation time, under this loading approximation. The model demonstrates viscous behavior, for normalized relaxation time values over 1000. In general, an increase of the normalized relaxation time or the free-energy parameter reduces the circumferential elongations.

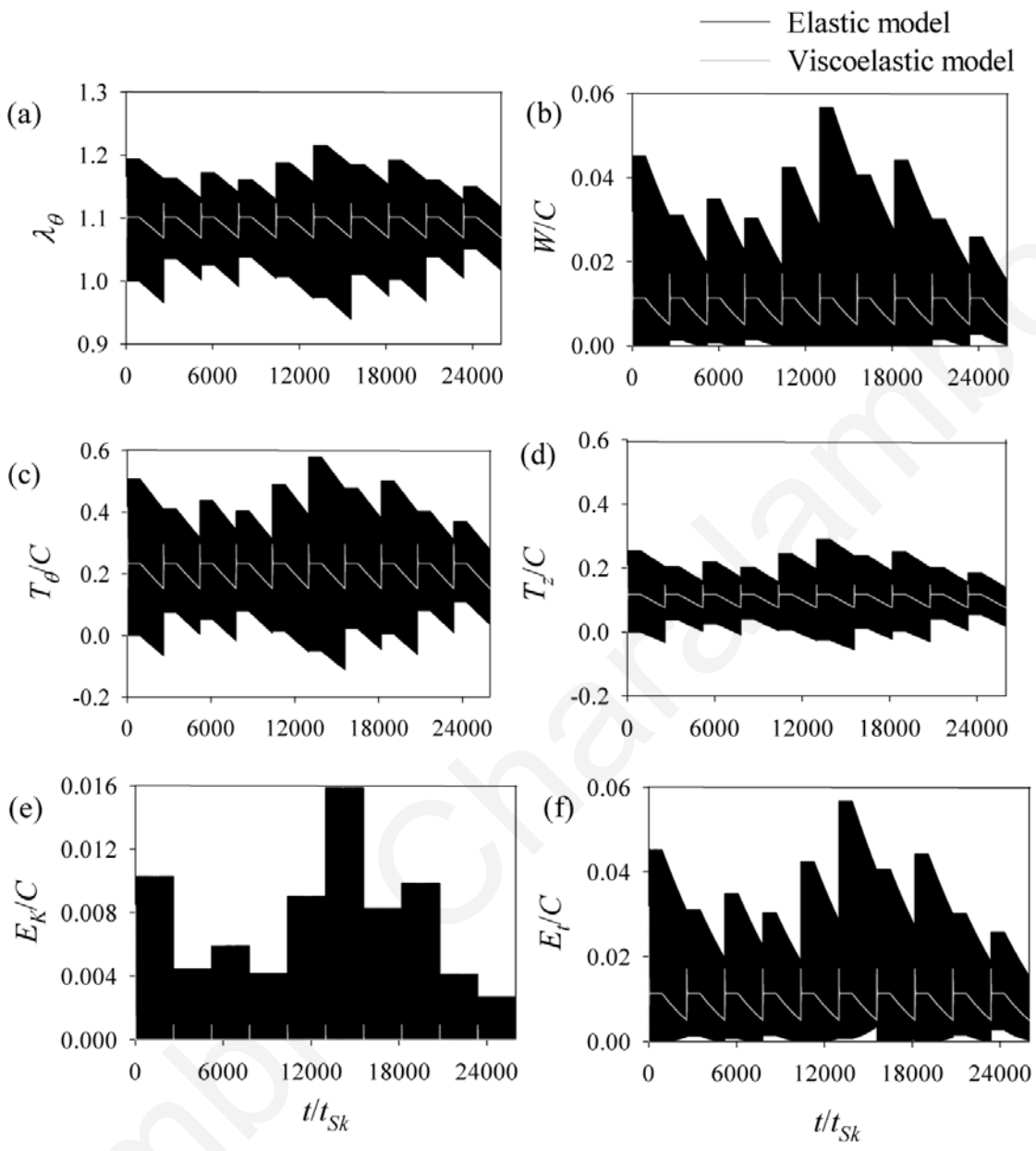

Figure 6-10: Arterial response under periodic loading for $\tau_1 / t_{Sk} = 1$, $\beta_1^\infty = 0.3$, $\lambda_z^0 = 1$, $B/C = 1$, $p_s R/C = 0.21$, $t_{cp}/t_{Sk} = 2597$: (a) circumferential elongation λ_θ, (b) normalized strain-energy density W/C, (c) normalized circumferential stress T_θ/C, (d) normalized longitudinal stress T_z/C, (e) normalized kinetic-energy density E_K/C, (f) normalized total-energy density E_t/C.

Finally, by adding two relaxation processes to the problem ($q_1 + q_2$ instead of q_1), we found that the arterial model responds differently to each loading scenario. For two relaxation processses, the non-equilibrium forces are calculated as

$$q_1(t)+q_2(t)=\exp\left(\frac{-t}{\tau_1}\right)q_1(0^+)+\int_{0^+}^{t}\exp\left[-\frac{t-t_n}{\tau_1}\right]\beta_1^{\infty}\dot{S}_{\theta}^{\infty}(t_n)dt_n$$
$$+\exp\left(\frac{-t}{\tau_2}\right)q_2(0^+)+\int_{0^+}^{t}\exp\left[-\frac{t-t_n}{\tau_2}\right]\beta_2^{\infty}\dot{S}_{\theta}^{\infty}(t_n)dt_n \qquad (6.28)$$

For the first loading approximation (Figure 6-4(a)), the response is dominated by the relaxation time that is closer to the characteristic time of the response. This occurs due to the fact that the problem is characterized by high-frequency vibrations and that there are not high loading frequencies involved in our problem (normal heart beat frequency of 1 Hz). For the second loading approximation (Figure 6-4(b)), the response is mainly affected by the higher relaxation time. In this case, by adding more relaxation processes to the problem the dissipation is increased (the arterial response is decreased).

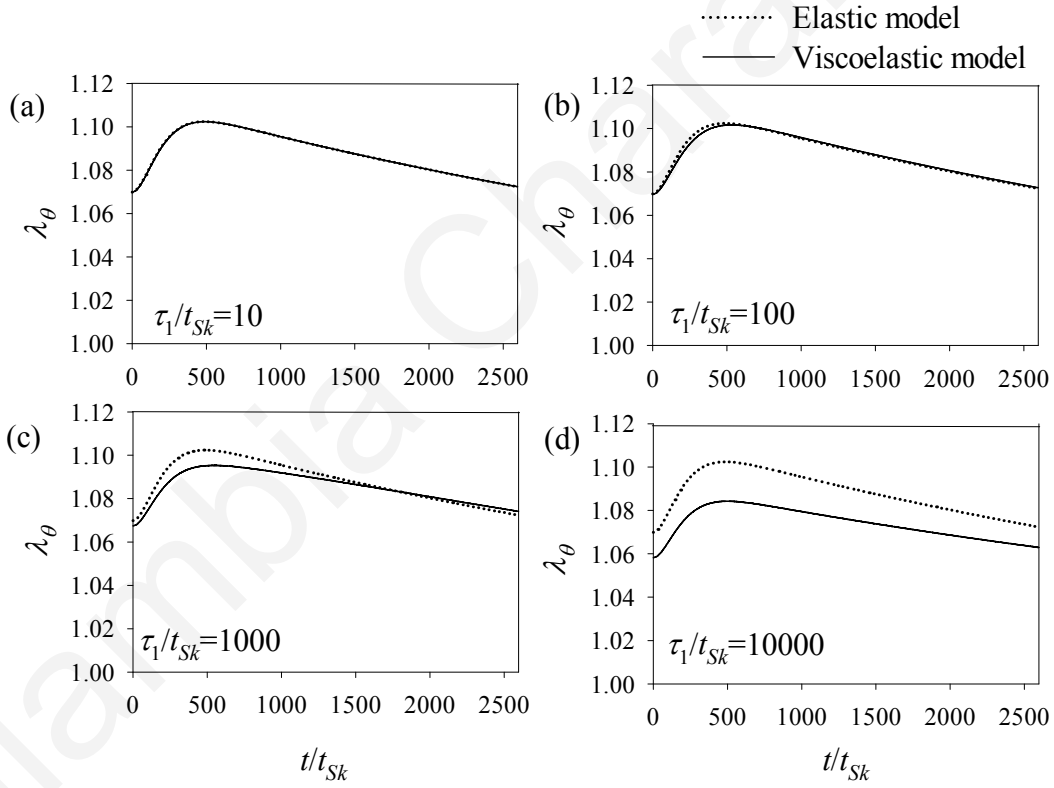

Figure 6-11: Circumferential elongation of elastic and viscoelastic arterial models by applying the second loading approximation (Figure 6-4(b)), and for $\beta_1^{\infty}=0.3$, $\lambda_z^0=1$, $B/C=1$, $p_sR/C=0.21$, $t_{cp}/t_{Sk}=2597$, and (a) $\tau_1/t_{Sk}=10$, (b) $\tau_1/t_{Sk}=100$, (c) $\tau_1/t_{Sk}=1000$, (d) $\tau_1/t_{Sk}=10000$.

6.4.2 Response of the Kelvin-Voigt model

After investigating typical arterial systems of the Kelvin-Voigt nonlinear model, for the pressure time-profile approximation of Figure 6-4(a), we can conclude that this model cannot adequately approximate the viscoelastic behavior of arteries. In particular, an increase of the viscosity term $\Gamma / C = \tau_1$ results in a decrease of the values of the response time-profile, in contrast to the generalized Maxwell model (Bonet-Holzapfel model) for which an increase of the relaxation time τ_1 increases the values of the response time-profile. In general the mean response values of the two models are comparable.

Under applied periodic excitation, the response showed similar behavior to that of the non-periodic excitation.

6.5 Numerical examples and comparison with existing studies

The applicability of the proposed theoretical model and the respective algorithm are demonstrated through characteristic numerical examples and comparison with existing studies. In particular, the inflation of a rubber tube, of a canine aorta, and of a porcine coronary artery are investigated.

6.5.1 Inflation of a rubber tube

Holzapfel and Gasser [35] presented a numerical example of an inflation of a three-dimensional fiber-reinforced rubber tube, under cyclic (sinusoidal) loading. The structure of the tube consists of three layers, has average radius 109 mm and thickness 18 mm. The sinusoidal loading has period 10 sec, peak value 10 MPa and minimum value 4 MPa. By utilizing finite-element analysis, they found that after five loading cycles the system reaches its steady state response, with the circumferential stretch of the rubber tube varying between 1.0547 and 1.1047, and the phase shift (time delay) with respect to the pressure time-profile being about 0.1 sec.

By utilizing the data used by Holzapfel and Gasser [35] in their example, we calculate the response of the rubber tube for the algorithm proposed in this chapter. We adopt the two-dimensional homogenized approximation of the walls. Their material constitutive law is expressed as

$$W = \frac{d_1}{2}\left(\left(\lambda_z^0\right)^2 + \lambda_\theta{}^2 + \frac{1}{\left(\lambda_z^0\right)^2 \lambda_\theta{}^2} - 3 \right) + \frac{d_2}{2}\left(\left(\lambda_z^0\right)^2 \lambda_\theta{}^2 + \frac{1}{\left(\lambda_z^0\right)^2} + \frac{1}{\lambda_\theta{}^2} - 3 \right) + \frac{d_3}{d_4}\left\{ \exp\left[d_4 \left(\lambda_\theta{}^2 \cos^2\varphi_1 + \left(\lambda_z^0\right)^2 \sin^2\varphi_1 - 1 \right)^2 \right] - 1 \right\} \tag{6.29}$$

in which d_1, d_2, and d_3 are positive stress-like material parameters, d_4 is a non-dimensional material parameter, and φ_1 is the angle of the fibers with respect to the circumferential direction. Table 6-1 reports the material parameters used in our analysis.

Note that, to properly approximate the viscoelastic response of the anisotropic, three layer model of Holzapfel and Gasser, the elasticity modulus must to be scaled in order to match the maximum steady state response (circumferential elongation) calculated by Holzapfel and Gasser to the steady state response calculated by this study. Thus, the material parameter d_3 is increased by a factor of ten, because we utilized a two-dimensional homogenization of the wall layers.

Table 6-1: Data used in the analysis of an inflation of a rubber tube.

Parameter	Value
R (mm)	109
H (mm)	18
λ_z^0	1
d_1 (kPa)	260.4
d_2 (kPa)	65.11
d_3 (MPa)	115 (scaled)
d_4	0.5
φ_1 (degrees)	33.1
τ_1 (sec)	3.5
β_1^∞	0.35
Δt (sec)	0.0001
Characteristic time (sec)	0.001

Figure 6-12 shows the input pressure profile and the resulting response of the viscoelastic and elastic models as calculated by this study. Note that, the tube is statically inflated up to the beginning of the sinusoidal loading. The response profile agrees with the profile given in the literature. The phase shift, caused by viscous and inertial effects, is 0.2 sec. The circumferential elongation varies between 1.109 and 1.063, at the steady state response. Moreover, the elastic model is characterized by high-frequency vibrations and increased response values, compared to the viscoelastic model.

Table 6-2 lists the results of the proposed methodology against the results calculated by Holzapfel and Gasser.

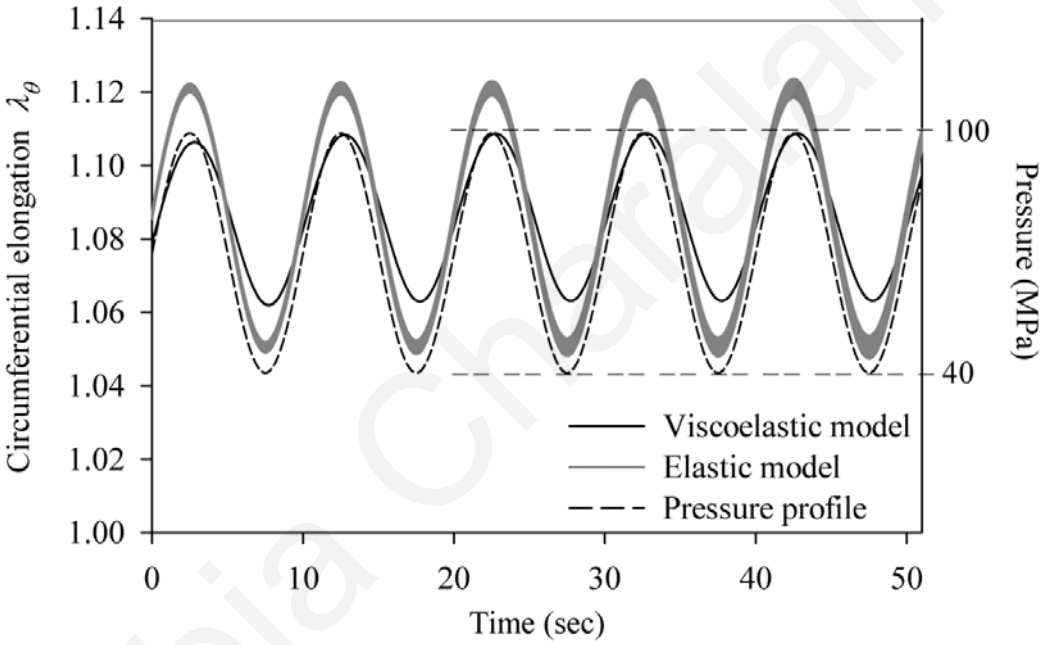

Figure 6-12: Circumferential elongation time-profile of rubber tube as calculated by this study. The dashed line represents the applied internal pressure time-profile.

Table 6-2: Comparison of our study to the study of Holzapfel and Gasser [35].

	Results	
	This study	Holzapfel and Gasser
Phase shift (sec)	0.2	0.1
Maximum λ_θ (steady state)	1.109	1.1046
Minimum λ_θ (steady state)	1.063	1.0547

6.5.2 Inflation of a canine aorta

Armentano et al. [85] experimentally investigated the inflation of a canine aorta. The induced blood pressure has systolic and diastolic values 87mmHg and 126mmHg respectively, and the radius of the aorta is 8 mm. Armentano et al. found that the maximum radial displacement of the canine aorta, under dynamic applied pressure, is 0.9 mm (strain 11.25%) and has a small phase shift compared to the pressure profile (0.02 sec). Čanić et al. [38] investigated the example of Armentano et al. for aortic wall thickness 1.4 mm. In particular, they developed a theoretical model to calculate the viscoelastic response of arteries loaded by viscous blood flow. Their calculations showed a response with similar time-profile to that of Armentano et al. and a phase shift equal to 0.05 sec.

Table 6-3: Data used in the analysis of an inflation of a canine aorta.

Data	
R (mm)	8
H (mm)	1.4
ρ_0 (kg/m^3)	1100
p_s (mmHg)	126
p_d (mmHg)	87
t_s (sec)	0.2
t_{cp} (sec)	0.6
E_θ (kPa)	1000
τ_1 (sec)	0.008
Dimensionless parameters	
B/C	1
$p_s R/C$	0.19
t_{cp}/t_{Sk}	2667
τ_1/t_{Sk}	21.4
β_1^∞	0.3
λ_z^0	1
$t_{Sk}/\Delta t$	10

Table 6-3 lists the problem parameters and the dimensionless parameters used in our analysis. Figure 6-13 shows the response of the canine aorta as calculated by this study, under dynamic overpressure excitation (i.e. the system is statically inflated up to the diastolic pressure and then dynamically inflated due to the overpressure). Our analysis resulted in maximum strain equal to 9.2%, for both the elastic and viscoelastic models, whereas there is not a phase shift of the circumferential elongation time-profile with respect to the pressure time-profile. Table 6-4 lists the results of our calculations as well as the results of the other studies.

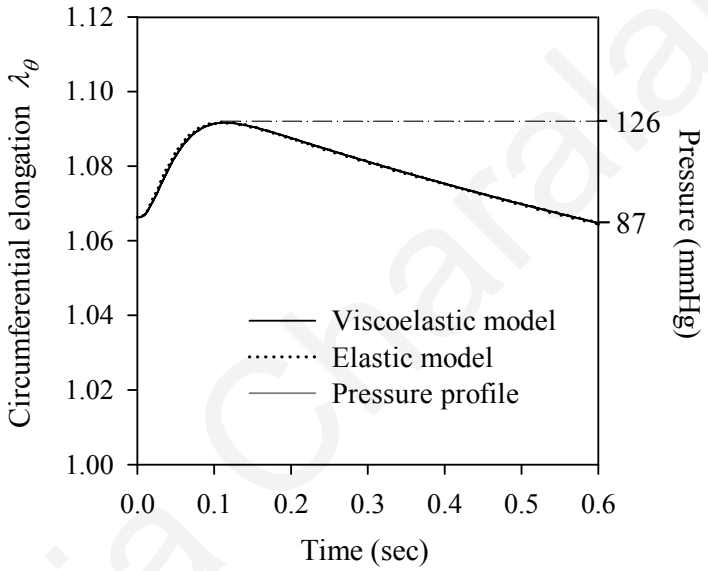

Figure 6-13: Circumferential elongation time-profile of canine aorta, and applied pressure time-profile.

Table 6-4: Comparison between our study, Armentano et al. study [85], and Čanić et al. study [38].

	Results		
	This study	Armentano et al.	Čanić et al.
Phase shift (sec)	0.0	0.02	0.05
Maximum strain (%)	9.2	11.25	(N/A)

6.5.3 Inflation of a porcine coronary artery

In another experimental study, Veress et al. [86] performed inflation creep tests on porcine left arterior descending coronary arteries and monitored their response. During the creep test the pressure was abruptly increased (over a time period of 0.15-0.25 sec) from 0 to 104-145 mmHg, and held for 15 sec. The time constant (relaxation time) was calculated to be 1.67 sec. The stress-strain relationship of the artery was experimentally obtained, revealing the hardening behavior of the porcine artery with increasing strain. As calculated by the analysis of Veress et al., the maximum circumferential strain is equal to 72%.

Table 6-5: Data used in the analysis of an inflation of a porcine coronary artery.

Data	
R (mm)	1.43
H (mm)	0.32
ρ_0 (kg/m^3)	1160
Applied pressure (mmHg)	145
E_θ (kPa)	112.5
τ_1 (sec)	1.67
t_{Sk} (sec)	0.0002
Dimensionless parameters	
B/C	1
$p_s R/C$	1.54
τ_1/t_{Sk}	8350
β_1^∞	0.3
λ_z^0	1
$t_{Sk}/\Delta t$	10

We performed an analysis based on the data provided by Veress et al. The mechanical behavior of the porcine artery is simulated by setting the material parameters of the Skalak et al. strain-energy function equal to $B/C=1$ and $C/H=56$ KPa (based on the tangent elasticity modulus value in the circumferential direction that is equal to 112.5 kPa, under applied circumferential strain about 0.3). The geometric data of the artery were not reported by Veress et al. Thus, we adopt typical values of porcine left arterior descending coronary arteries (R=1.43 mm, H=0.32 mm) [87]. Table 6-5 list the parameters used in

our analysis. The calculated circumferential strain time-profile approximates well the circumferential strain time-profile of the analysis of Veress et al. The maximum strain is calculated by this study to be 59% (Figure 6-14).

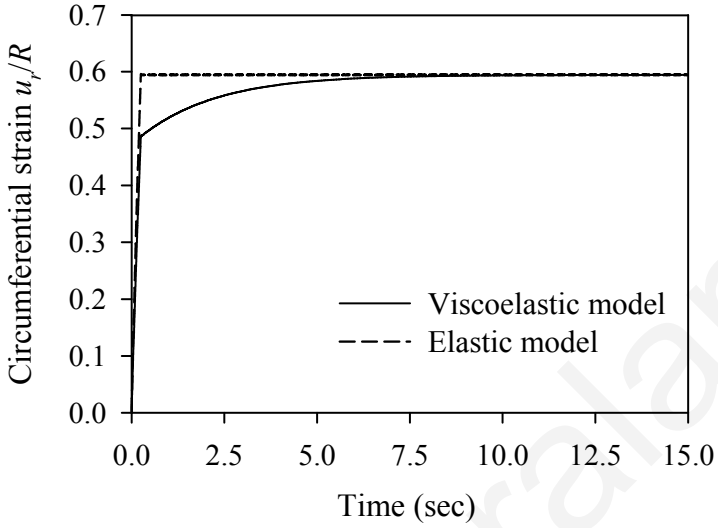

Figure 6-14: Circumferential strain time-profile of porcine coronary artery.

6.6 Concluding remarks

This chapter deals with the complex problem of the viscoelastic arterial behavior. The arterial wall viscosity is simulated by adopting a generalized Maxwell model and the internal variables approach, as suggested by Bonet [81] and Holzapfel et al. [36]. The proposed analytical model investigates the macroscopic response of viscoelastic arteries and the effect of each problem parameter on the macroscopic arterial response. An iterative algorithm, based on Newmark's constant-acceleration method for nonlinear systems, is developed, in order to obtain the numerical solution of the problem.

Two different loading approximations are considered. The first arterial pulse time-profile approximation adopted in this study (Figure 6-4(a)) constitutes a conservative scenario. The pressure is rapidly increased from zero to the maximum systolic pressure, as is the case of the restoration of the blood flow after a surgery. We can say that the resulting maximum radial displacements are two times higher than the respective radial displacements under a smoothly increased pressure time-profile. Furthermore, the problem is characterized by high-frequency vibrations, due to the pulse-type loading.

For the aforementioned loading scenario, the viscoelastic response is mainly affected by the relaxation time τ_1 and the material parameter β_1^∞. An increase of the relaxation time τ_1

increases the non-equilibrium stresses $q_1 h / C$ but may not increase the dissipation of the system over time. In particular, for extremely small relaxation time values τ_1, the exponential term of Equation (6.19) is zeroed and the system becomes completely elastic. For intermediate relaxation time values τ_1, the time-profile of the non-equilibrium stresses is almost symmetric about the time-axis and the response exhibits large dissipation (Figures 6-5 and 6-6). For higher relaxation time values, the non-equilibrium stresses exhibit higher values, that are non-symmetric about the time-axis and the response exhibits moderate dissipation (Figure 6-7), whereas for even higher values of the relaxation time, the exponential term of Equation (6.19) becomes equal to one and the dissipation of the response depends mainly on the material parameter β_1^∞ (Figure 6-8).

Rapid dissipation of the radial displacement time-response (and circumferential elongation) implies rapid dissipation of all the response quantities (circumferential stress, longitudinal stress, strain-energy density, kinetic-energy density, and total-energy density). Note that, the normalized strain-energy density dominates compared to the normalized kinetic-energy density of the system. The maximum strain-energy density occurs at the time instant that the respective kinetic-energy density is equal to zero. Therefore, the total-energy density has peak values equal to the peak values of the strain-energy density.

We are particularly interested in the maximum circumferential elongation of the conservative loading scenario. We can say that the elastic model adequately approximates the maximum response of the viscoelastic model, which frequently occurs at the beginning of the loading. The maximum circumferential elongation depends on the free-energy parameter β_1^∞, rather than the normalized relaxation time τ_1 / t_{Sk}.

In the case that the pressure is quasi-statically applied up to the diastolic pressure, the system is not always characterized by high-frequency vibrations. An increase of the normalized relaxation time τ_1 / t_{Sk} or the free-energy parameter β_1^∞ results in a decrease of the response.

Under both loading scenarios, most of the problem parameters affect the system response in the same manner. From Equation (6.1), we can observe that a decrease of the material parameter β_1^∞ decreases the non-equilibrium forces and subsequently increases the normalized radial displacement. Note that, for $\beta_1^\infty = 0$ the system is completely elastic. In addition, response parameters λ_z^0, B/C, $p_s R / C$ affect the viscoelastic artery in the same manner that affect the hyperelastic artery: an increase of the longitudinal pre-stretch λ_z^0,

the ratio B/C, or a decrease of the normalized pressure $p_s R/C$ yields a decrease of the radial displacement (and circumferential elongation).

By adding two relaxation processes to the problem, we found that for the first loading case the response is dominated by the relaxation time that is closer to the characteristic time of the response, whereas for the second loading case by adding more relaxation processes the dissipation is increased.

Of particular interest is the correlation of the arterial wall viscosity to the fatigue of the cardiovascular system. Increased viscoelastic arterial behavior corresponds to increased energy loss during each cardiac cycle, meaning that a large amount of blood will be accumulated in the heart. Thus, the heart is forced to work harder (to pump a larger amount of blood each time), causing the muscle content of the heart to increase, and its chambers volume to decrease, making the problem even worse.

In conclusion, this chapter proposes an analytical model describing the response of viscoelastic arteries. By choosing the proper viscoelastic material parameters the response of the system can be approximated with low computational cost. The present investigation revealed the strong influence of the ratio of relaxation time to characteristic time of the response, and of the pressure time-profile approximation on the response of viscoelastic arteries.

CHAPTER 7

Suture-line Response of End-to-end Anastomosis

7.1 Introduction

During a typical arterial reconstruction, the diseased artery segment is removed, and the healthy segments are stitched together, either directly or through the insertion of an artificial graft (end-to-end anastomosis). Modern grafts tend to exhibit similar geometric and stiffness characteristics with those of arteries. Thus, in any case, the mechanical behavior of the anastomotic region is comparable.

Limited investigations have been performed on the mathematical or computational modeling of end-to-end anastomosis [6, 10, 8, 14]. Moreover, most of the published studies rely solely on finite-element analyses rather than on analytical models, and often ignore the stress concentrations due to suture-artery interaction, or the axial-circumferential deformation coupling in the artery response.

A comprehensive (dynamic) analytical end-to-end anastomosis model between isocompliant arteries was recently proposed [66]. The model accounted for the geometric and mechanical properties of artery and sutures, the number of sutures, loading characteristics, and longitudinal residual stresses. The cross-section of the artery was assumed to be homogeneous and its mechanical response linear elastic, incorporating in an average sense the tangential stiffness, the anisotropy, the inhomogeneity and the residual stresses of the artery walls.

Herein, we propose an extension of the aforementioned model, to account for the suture pre-tensioning and the capability of the stitching on receiving forces along the axial direction of the end-to-end anastomosis model. A displacement-based method, considering the conservation of the blood volume and the suture-artery interaction, is utilized for the problem solution. Furthermore, a dynamic mathematical model of an artery/graft end-to-end anastomosis and a static mathematical model investigating the para-anastomotic hypercompliant zone (PHZ) phenomenon, are proposed in this chapter. The latter model is solved as a boundary value problem.

The present study aims to investigate the behavior of the stitched anastomotic region of end-to-end anastomosis through the development of analytical mathematical models, which account for all the important parameters. In addition, it aims to provide closed-form expressions for the problem solution, in order to extend current knowledge and offer useful

suggestions for the optimal selection of materials and improved functionality of the sutures in vascular surgery operations.

7.2 Mathematical model

Figure 7-1(a) shows a shematic of the end-to-end anastomosis model between isocompliant blood vessels. Note that, the artery cross-section is characterized by the assumptions described in Section 4.2.1. The arterial tissue is considered to be an orthotropic linear-elastic material, and the suture material is legitimately considered to be linear elastic for elongations up to 20% [88].

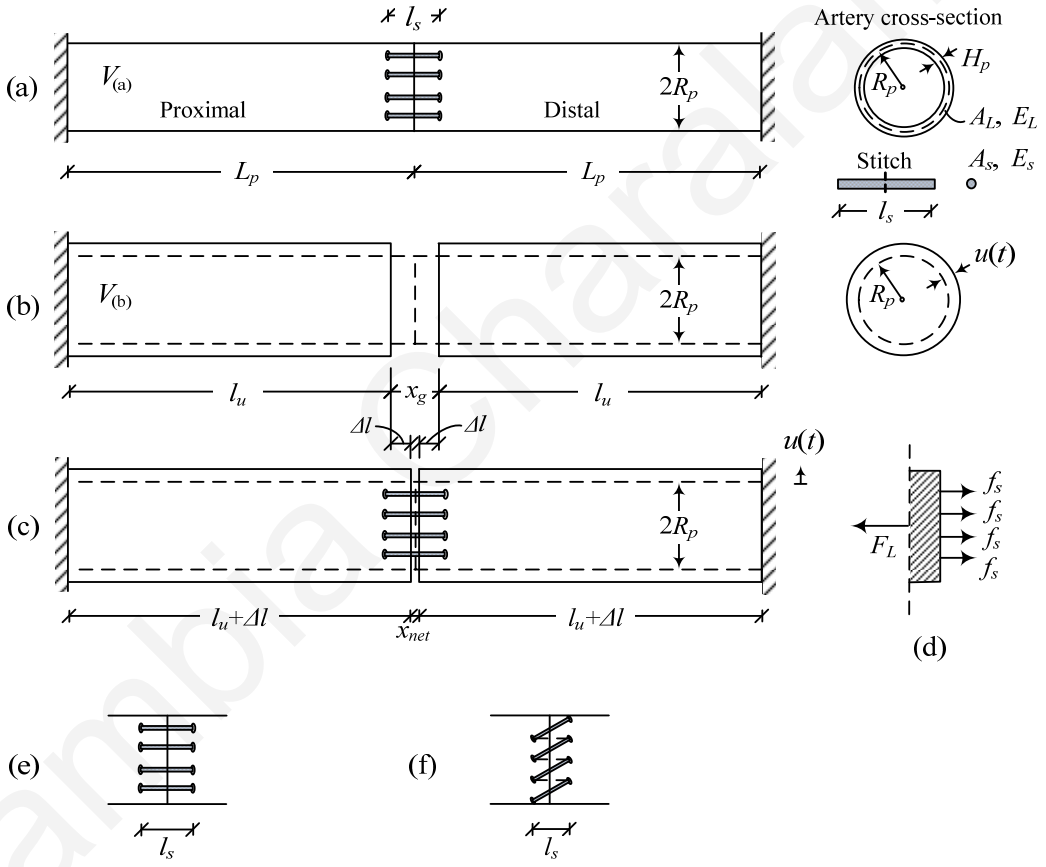

Figure 7-1: End-to-end anastomosis analysis between isocompliant blood vessels: (a) Anastomosis model (at-rest state), (b) unrestrained deformed state of artery (without sutures), (c) deformed state of anastomotic region due to dynamic loading, (d) forces acting on end-element of artery segment, (e) interrupted stitching scheme, (f) continuous stitching scheme.

The two blood vessels (proximal and distal) are connected together with a total of N_s stitches. Each blood vessel has length L_p, radius R_p (the initial configuration is

considered to be under zero blood pressure and in vivo length, implying that the blood vessel is in its pre-stressed state), and Young's modulus in the longitudinal direction E_L. The stitches have radius r_s, cross-sectional area $A_s = \pi r_s^2$, and Young's modulus E_s. The distance between stitching holes that are symmetrically located across the separation plane is denoted by l_s (with the assumption that $2L_p >> l_s$).

Two different stitching techniques are considered, resulting in different suture loading. Figure 7-1(e) shows the interrupted stitching technique, whereas Figure 7-1(f) shows the continuous (running) stitching technique. The particular loading condition associated with each stitching scheme is accounted for in the analysis by means of a participation factor α. The participation factor is derived from the local equilibrium of forces at the suture line that passes without friction through the stitch hole, indicating the alignment of the stitches along the longitudinal direction (the remaining part $(2-\alpha)$ indicates that the system is in torsion with limited relevance to the present problem). In particular, the interrupted stitching scheme corresponds to a maximum participation factor $\alpha = 2$, whereas the continuous stitching scheme (with diagonal at 45° angle), corresponds to participation factor $\alpha = 1.707$. Moreover, the stitching holes and the suture are considered to have almost equal diameters. Therefore, the suture segment penetrating the arterial wall is almost undeformable, due to friction forces developed between the arterial wall and the suture. Finally, the model also considers the pre-tensioning of stitches f_s^0 [89], that is the force exerted by the surgeon in tying the knot of the suture.

7.2.1 Objective functionalities

Vascular operations may exhibit post-surgery complications, caused by the interaction of sutures with the arterial tissue. The undesirable conditions can be described by three failure scenarios: (a) suture failure; (b) arterial-wall tearing; and (c) blood leaking at the suture line. Suture failure is caused when the maximum tensile force of the suture, f_s, exceeds the suture strength or leads to slip or relaxation of the knots that bind the stitches together [90]. Note that it is possible that suture failure may occur due to suture gradual deterioration with time [63]. Arterial-wall rupture or injury may be caused when the embedding stresses, σ_s, due to suture-artery contact interaction (at the stitching holes) exceed the limit value of artery-wall shear strength. Thrombosis may be caused if the distance between the edges of the two anastomosed artery segments, x_{net}, exceeds the typical size of a few red blood cells, leading to internal bleeding.

In order to avoid failure altogether, the following objective functionalities must be satisfied:

$$\max f_s < \text{ ultimate axial strength of suture/knot } \left(f_{s,u}\right) \tag{7.1}$$

$$\max \sigma_s < \text{ ultimate shear strength of arterial tissue } \left(\sigma_{s,u}/2\right) \tag{7.2}$$

$$\max\ x_{net} < 3 \text{ x red blood cell diameter } \left(3d_{rbc}\right) \tag{7.3}$$

In addition to the above objective functionalities, the following geometric constraint must be satisfied to assure adequate stitching spacing:

$$\pi R_p \geq 4N_s r_s \tag{7.4}$$

The case report of Seltmann et al. [91] on the development of post-surgery artery stenosis, due to a high number of utilized stitches, confirms the importance of adequate stitching spacing.

Furthermore, the mechanical and geometric properties of the blood vessels and the sutures may change over a time span of several weeks after surgery, implying that long-term complications may occur. In particular, the wall thickness of the sutured artery may decrease with time, as is the case of the inflammatory response after surgery. Moreover, the elastic properties and strength of the artery may change with time due to chemical change of the suture and its interaction with the arteries [63]. Such long-term complications lead to lower values of the elastic and strength properties of the arterial walls and suture materials.

7.2.2 Suture-line response

The proposed model accounts for the suture-artery interaction, and the axial-circumferential deformation coupling in the artery response. On account of the fact that blood is an incompressible fluid, the radial and longitudinal modes of arterial response are coupled. In particular, the solution is derived by first calculating the longitudinal displacement of the unrestrained model (Figure 7-1(b)), and secondly calculating the resulting longitudinal displacement of the restrained model (Figure 7-1(c)).

Under the applied blood pressure, the artery distends radially by $u(t)$, and, in order for the blood volume to be maintained, its axial length is decreased from L_p to l_u, resulting in the

formation of a gap x_g of the unrestrained model (Figure 7-1(b)). Conservation of the blood volume means that the cylindrical volume $V_{(a)} = V_{(b)}$ (Figure 7-1(a,b)). Then, the decreased anastomosis length at any time t is given by

$$l_u(t) = \frac{L_p {R_p}^2}{\left(R_p + u(t)\right)^2} \tag{7.5}$$

The decreased artery length $l_u(t)$ given by Equation (7.5) implies the following solid-fluid interaction procedure: (a) the blood volume fills the two parts of the anastomosis after completing the stitching, and (b) pressure is applied leading to contraction along the length of the initially emptied artery. Note that, the radial displacement $u(t)$ is the radial displacement of the linear-elastic arterial model introduced in Chapter 4.

By considering the unrestrained (without sutures) state of the artery (Figure 7-1(b)), the gap developed in this state can be determined as the difference between the initial length of the artery ($2L_p$) and the length of the unrestrained deformed state ($2l_u$):

$$x_g(t) = 2L_p\left[1 - \frac{{R_p}^2}{\left(R_p + u(t)\right)^2}\right] \tag{7.6}$$

The resulting net gap developed in the restrained (with sutures) anastomotic region (Figure 7-1(c)) can be derived from

$$x_{net}(t) = x_g(t) - 2\Delta l(t) \tag{7.7}$$

where Δl is the tensile deformation due to the stitching stiffness.

The tensile forces developed in the suture and arterial tissue (Figure 7-1(d)) are given respectively by

$$f_s(t) = A_s E_s \varepsilon_s(t) + f_s^0 = \frac{A_s E_s}{l_s} x_{net}(t) + f_s^0 \tag{7.8}$$

$$F_L(t) = E_L A_L(t) \varepsilon_L(t) = 2\pi H_p E_L \left(R_p + u(t)\right) \frac{\Delta l(t)}{l_u(t)} \tag{7.9}$$

where ε_s is the suture strain, ε_L is the strain of one artery segment, and A_L is the cross-sectional area of the artery. The tensile deformation Δl can be derived from equilibrium of forces in the axial direction, requiring that

$$F_L(t) = \alpha N_s f_s(t) \tag{7.10}$$

Substituting Equations (7.8) and (7.9) into Equation (7.10), the equilibrium of forces in the axial direction yields

$$2\pi H_p E_L \left(R_p + u(t)\right) \frac{\Delta l(t)}{l_u(t)} = \alpha N_s \left(\frac{A_s E_s}{l_s} x_{net}(t) + f_s^0 \right) \tag{7.11}$$

By combining Equations (7.6) and (7.7), the net gap between the anastomosed artery segments is derived as

$$x_{net}(t) = 2L_p \left[1 - \frac{R_p^{\,2}}{\left(R_p + u(t)\right)^2} \right] - 2\Delta l(t) \tag{7.12}$$

Substituting Equation (7.12) into Equation (7.11), the equilibrium equation is expressed in terms of $\Delta l(t)$ as

$$2\pi H_p E_L \left(R_p + u(t)\right) \frac{\Delta l(t)}{l_u(t)} = \alpha N_s \left\{ \frac{A_s E_s}{l_s} 2L_p \left[\left(1 - \frac{R_p^{\,2}}{\left(R_p + u(t)\right)^2} \right) - 2\Delta l(t) \right] + f_s^0 \right\} \tag{7.13}$$

which can be readily solved for the tensile deformation:

$$\Delta l(t) = \frac{\alpha N_s L_p R_p^{\,2} \left\{ A_s E_s L_p \left[1 - \dfrac{R_p^{\,2}}{\left(R_p + u(t)\right)^2} \right] + \dfrac{f_s^0}{2} l_s \right\}}{\pi E_L l_s H_p \left(R_p + u(t)\right)^3 + \alpha N_s A_s E_s L_p R_p^{\,2}} \tag{7.14}$$

Substituting Equations (7.6) and (7.14) into Equation (7.7), we obtain the net gap between the anastomosed artery segments as

$$x_{net}(t)=\begin{cases}\dfrac{2\pi L_p E_L l_s H_p\left(R_p+u(t)\right)\left[\left(R_p+u(t)\right)^2-{R_p}^2\right]-f_s^0\alpha N_s L_p {R_p}^2 l_s}{\pi E_L l_s H_p\left(R_p+u(t)\right)^3+\alpha N_s A_s E_s L_p {R_p}^2} & \text{, for } F_L(t)>\alpha N_s f_s^0 \\ 0 & \text{, for } F_L(t)\le\alpha N_s f_s^0\end{cases} \quad (7.15)$$

Note that a gap across the anastomotic interface will be formed only if the tension developed in the arterial tissue exceeds the total suture pre-tension.

Combining Equations (7.8) and (7.15), the total tensile force developed in a single suture is expressed as

$$f_s(t)=\begin{cases}2\pi E_L H_p\left(R_p+u(t)\right)\left\{\dfrac{L_p A_s E_s\left[\left(R_p+u(t)\right)^2-{R_p}^2\right]+\dfrac{f_s^0}{2}l_s\left(R_p+u(t)\right)^2}{\pi E_L l_s H_p\left(R_p+u(t)\right)^3+\alpha N_s A_s E_s L_p {R_p}^2}\right\} & \text{, for } F_L(t)>\alpha N_s f_s^0 \\ f_s^0 & \text{, for } F_L(t)\le\alpha N_s f_s^0\end{cases} \quad (7.16)$$

In addition, embedding stresses σ_s are developed because of suture-artery contact interaction at the stitching holes. The embedding stress induced on the arterial wall is approximated [92] by

$$\sigma_s(t)=\frac{\alpha f_s(t)}{2r_s H_p} \quad (7.17)$$

This is a well-known result used in the analysis of riveting of steel structures. Inserting Equation (7.15) into Equation (7.17) yields

$$\sigma_s(t)=\begin{cases}\dfrac{\alpha\pi E_L\left(R_p+u(t)\right)}{r_s}\left\{\dfrac{L_p A_s E_s\left[\left(R_p+u(t)\right)^2-{R_p}^2\right]+\dfrac{f_s^0}{2}l_s\left(R_p+u(t)\right)^2}{\pi E_L l_s H_p\left(R_p+u(t)\right)^3+\alpha N_s A_s E_s L_p {R_p}^2}\right\} & \text{, for } F_L(t)>\alpha N_s f_s^0 \\ \dfrac{\alpha f_s^0}{2r_s H_p} & \text{, for } F_L(t)\le\alpha N_s f_s^0\end{cases} \quad (7.18)$$

Although based on a linear-elastic model, the system response depends on a considerable number of parameters. In particular, the solution contains as many as seventeen input

parameters (L_p, R_p, N_s, H_p, E_θ, E_L, p_s, p_d, t_s, t_{cp}, ρ, u_o, l_s, E_s, r_s, α, f_s^0) related to the geometric and mechanical properties of sutures and arterial walls, the number of sutures, the loading characteristics, the longitudinal residual stresses, and suture pre-tensioning.

For completeness, the general solution of an artery/graft end-to-end anastomosis is presented in Appendix B.

7.3 Results

This section investigates the effect of each material parameter on the three response quantities of interest: the anastomotic gap x_{net}, the suture tensile force f_s, and the embedding stress σ_s. On normalizing by $2L_p$, $E_L H_p{}^2$ and E_L respectively, Equations (7.15), (7.16) and (7.18) become

$$\frac{x_{net}(t)}{2L_p} = \begin{cases} \dfrac{\left(1+\dfrac{u(t)}{R_p}\right)\left[\left(1+\dfrac{u(t)}{R_p}\right)^2-1\right]-\dfrac{\alpha f_s^0}{2\pi E_L r_s H_p}N_s\dfrac{r_s}{R_p}}{\left(1+\dfrac{u(t)}{R_p}\right)^3+\alpha\dfrac{E_s}{E_L}N_s\dfrac{A_s}{\pi R_p H_p}\dfrac{L_p}{l_s}}, & \text{for } F_L(t) > \alpha N_s f_s^0 \\ 0, & \text{for } F_L(t) \le \alpha N_s f_s^0 \end{cases} \tag{7.19}$$

$$\frac{f_s(t)}{E_L H_p{}^2} = \begin{cases} \dfrac{2\pi\alpha\dfrac{E_s}{E_L}\dfrac{r_s}{H_p}\left(1+\dfrac{u(t)}{R_p}\right)\left[\left(1+\dfrac{u(t)}{R_p}\right)^2-1\right]+\dfrac{\alpha f_s^0}{E_L r_s H_p}\dfrac{l_s}{L_p}\left(1+\dfrac{u(t)}{R_p}\right)^3}{\alpha\left[\left(1+\dfrac{u(t)}{R_p}\right)^3\dfrac{H_p}{r_s}\dfrac{l_s}{L_p}+\alpha\dfrac{E_s}{E_L}N_s\dfrac{r_s}{R_p}\right]} & \\ \qquad\qquad \text{, for } F_L(t) > \alpha N_s f_s^0 & \\ \left(\dfrac{\alpha f_s^0}{E_L H_p r_s}\right)\left(\dfrac{r_s}{\alpha H_p}\right) \qquad \text{, for } F_L(t) \le \alpha N_s f_s^0 & \end{cases} \tag{7.20}$$

$$\frac{\sigma_s(t)}{E_L}=\begin{cases}\dfrac{\pi\alpha\dfrac{E_s}{E_L}\left(1+\dfrac{u(t)}{R_p}\right)\left[\left(1+\dfrac{u(t)}{R_p}\right)^2-1\right]+\dfrac{\alpha f_s^0}{E_L r_s H_p}\dfrac{H_p}{r_s}\dfrac{l_s}{L_p}\left(1+\dfrac{u(t)}{R_p}\right)^3}{\left[\left(1+\dfrac{u(t)}{R_p}\right)^3\dfrac{H_p}{r_s}\dfrac{l_s}{L_p}+\alpha\dfrac{E_s}{E_L}N_s\dfrac{r_s}{R_p}\right]} & \text{, for } F_L(t)>\alpha N_s f_s^0 \\ \dfrac{\alpha f_s^0}{E_L H_p r_s} & \text{,for } F_L(t)\le\alpha N_s f_s^0\end{cases} \tag{7.21}$$

From Equations (7.19) to (7.21), we observe that the seventeen input parameters of the problem can be reduced into five dimensionless parameters, namely $\alpha E_s / E_L$, L_p / l_s, $N_s r_s / R_p$, r_s / H_p, $\alpha f_s^0 / r_s H_p E_L$. Figures 7-2 through 7-6 plot the normalized response quantities for parameter values varied within the physiological range.

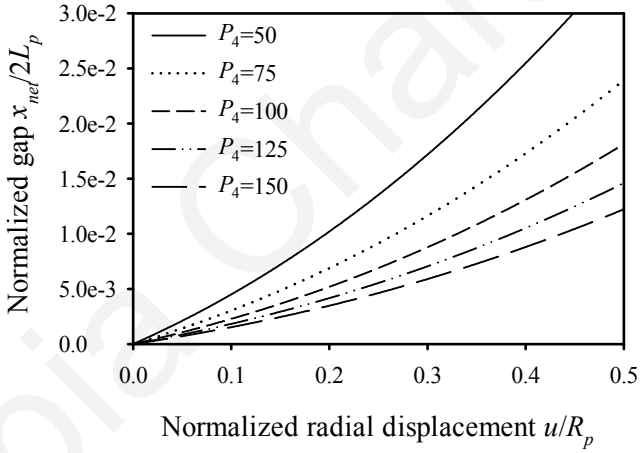

Figure 7-2: Normalized anastomotic gap versus normalized radial displacement for different values of product $P_4 = \alpha\dfrac{E_s}{E_L}N_s\dfrac{A_s}{\pi R_p H_p}\dfrac{L_p}{l_s}$ and for $f_s^0 = 0$.

From Equation (7.19) the normalized anastomotic gap $x_{net} / 2L_p$ depends on the product of four dimensionless parameters, namely $\alpha E_s / E_L$, L_p / l_s, $N_s r_s / R_p$, r_s / H_p, abbreviated herein as P_4, and suture pre-tension parameter $\alpha f_s^0 / r_s H_p E_L$. However, utilizing typical parameter values, we observe that the contribution of r_s / H_p is relatively small. Figure 7-2 plots the normalized gap as a function of the normalized radial displacement u / R_p, for different values of the product P_4, and for zero suture pre-tension.

Furthermore, Figures 7-3 and 7-4 plot the normalized gap as a function of the normalized radial displacement u / R_p, in a more elaborate manner, in terms of the design parameters $\alpha E_s / E_L$, L_p / l_s, $A_s / H_p R_p$, N_s, in order to provide simpler and useful graphs for the optimal selection of materials and improved functionality of sutures. In particular, Figures 7-3 and 7-4 highlight the influence of the variation of the suture stiffness (Figure 7-3(a,b)), the stitch length (Figure 7-3(c,d)), the suture cross-section area (Figure 7-4(a,b)), and the number of stitches (Figure 7-4(c,d)) on the anastomotic gap, for two different sets of parameters. The results suggest that increasing the value of any of the design parameters yields a decreased anastomotic gap. In particular, the most influential parameter in drastically reducing the anastomotic gap is the number of utilized stitches, N_s, as can be seen from Figure 7-4(c,d).

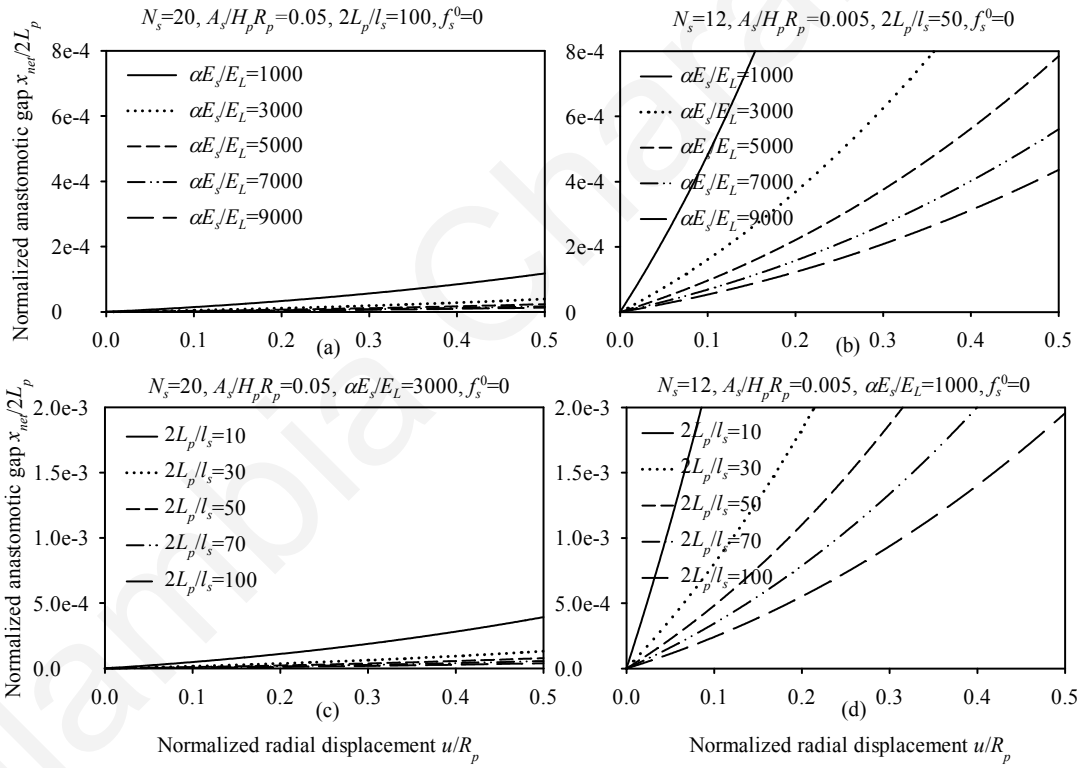

Figure 7-3: Normalized anastomotic gap versus normalized radial displacement for different values of parameters $\alpha E_s / E_L$ and $2L_p / l_s$.

The normalized tensile force in each stitch as a function of the normalized radial displacement for different values of parameters $2L_p / l_s$, $\alpha E_s / E_L$, N_s, and by assuming $f_s^0 = 0$ is presented graphically in Figure 7-5. It can be observed that the normalized

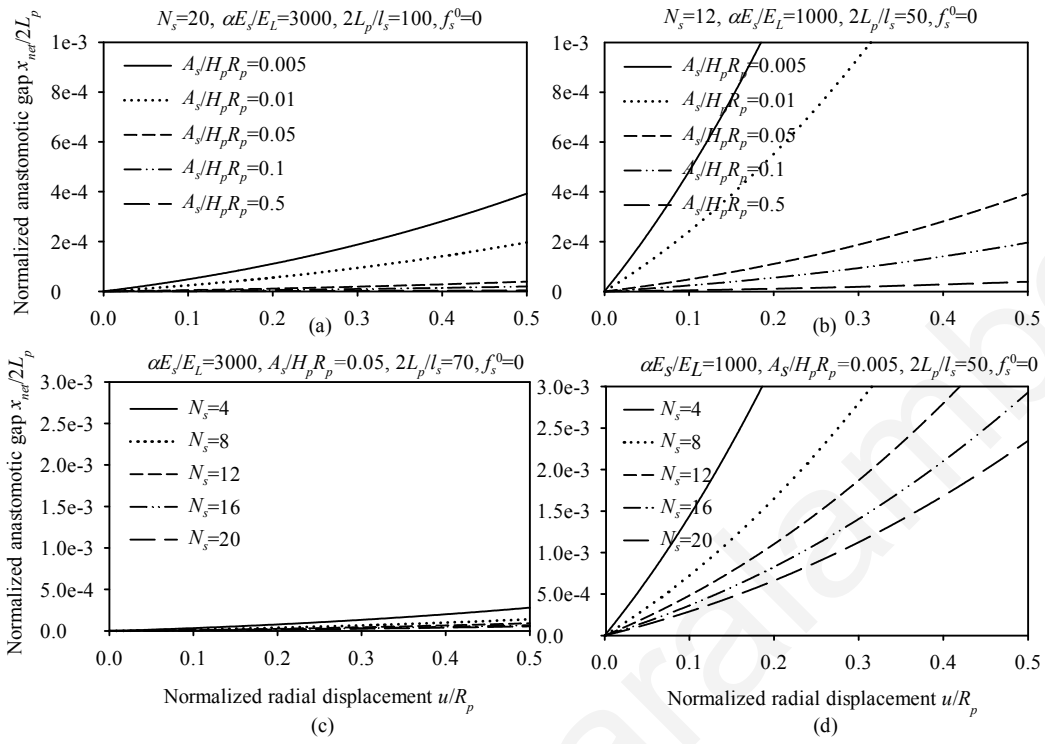

Figure 7-4: Normalized anastomotic gap versus normalized radial displacement for different values of parameters $A_s / H_p R_p$ and N_s.

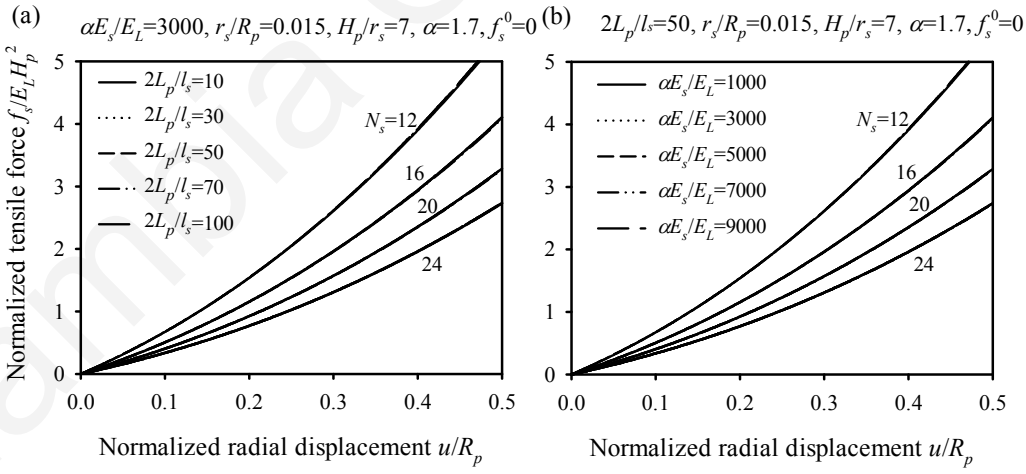

Figure 7-5: Normalized tensile force in each stitch versus normalized radial displacement for $f_s^0 = 0$, for different values of parameters N_s and (a) $2L_p / l_s$, (b) $\alpha E_s / E_L$.

suture tensile force is decreased as the number of stitches is increased, whereas the ratio of suture-to-artery elastic modulus and the normalized stitch length do not affect significantly

the tensile force developed in each stitch. The latter is also true for the suture radius as suggested by Equation (7.20).

Finally, Figure 7-6 plots the normalized embedding stress due to suture-artery contact interaction as a function of the normalized radial displacement, and for different values of parameters $\alpha E_s / E_L$ and N_s. It can be seen from Figure 7-6 that in order to reduce the embedding stress, the number of stitches must be increased, whereas the parameter $\alpha E_s / E_L$ plays an insignificant role. Moreover, the embedding stress becomes smaller with increasing suture radius, as can be seen from Equation (7.21).

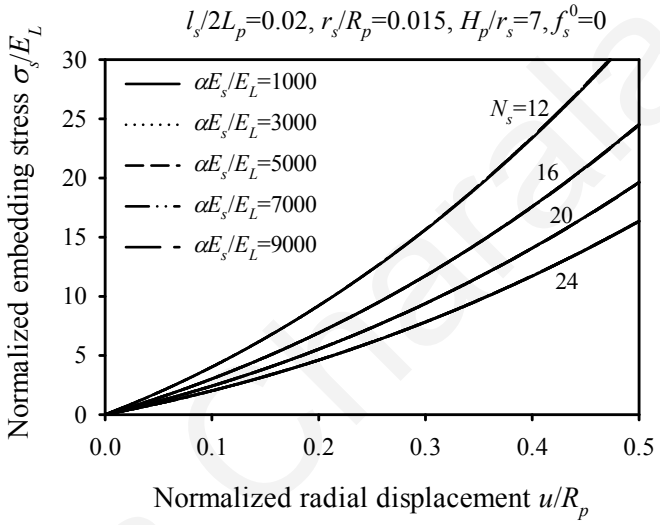

Figure 7-6: Normalized embedding stress versus normalized radial displacement for different values of parameter $\alpha E_s / E_L$, N_s and for $f_s^0 = 0$.

It should be noted that, for a typical anastomosis scheme (with parameters within the physiological range) and for $F_L(t) \le \alpha N_s f_s^0$, when the value of pre-tension f_s^0 exceeds a certain value (derived from $\alpha f_s^0 / 2 r_s H_p > \sigma_{s.u} / 2$) the arterial wall is likely to fail. On the other hand, for lower values of pre-tension and for $F_L(t) > \alpha N_s f_s^0$, the application of suture pre-tension can result in reducing the anastomotic gap (Equation (7.19)), while not affecting considerably the embedding stress (Equation (7.20)) and suture tensile force (Equation (7.21)).

7.4 Design considerations

For design purposes the maximum radial displacement of artery $u_{\max}$ (Equation (4.22)) is considered. The failure scenarios described by the inequalities (7.1), (7.2), (7.3), for the general case where $F_L(t) > \alpha N_s f_s^0$, can be prevented by calculating the minimum number of stitches required to prevent suture failure, arterial-wall tearing, and development of excessive gap, respectively as:

$$N_s > \frac{\pi E_L H_p (R_p + u_{\max})}{\alpha f_{s,u} L_p R_p^{\,2}} \left\{ 2L_p \left[\left(R_p + u_{\max} \right)^2 - R_p^{\,2} \right] - \frac{l_s \left(f_{s,u} - f_s^0 \right)}{A_s E_s} \left(R_p + u_{\max} \right)^2 \right\} \equiv N_1 \quad (7.22)$$

$$N_s > \frac{2\pi E_L (R_p + u_{\max})}{\alpha \sigma_{s,u} r_s L_p R_p^{\,2}} \left\{ \alpha L_p \left[\left(R_p + u_{\max} \right)^2 - R_p^{\,2} \right] - \frac{l_s \left(H_p \sigma_{s,u} - \dfrac{\alpha f_s^0}{r_s} \right)}{2\pi r_s E_s} \left(R_p + u_{\max} \right)^2 \right\} \equiv N_2 \quad (7.23)$$

$$N_s > \frac{\pi E_L H_p l_s (R + u_{\max}) \left\{ 2L_p \left[\left(R_p + u_{\max} \right)^2 - R_p^{\,2} \right] - 3 d_{rbc} \left(R_p + u_{\max} \right)^2 \right\}}{3 d_{rbc} \alpha A_s E_s L_p R_p^{\,2} + f_s^0 \alpha L_p R_p^{\,2} l_s} \equiv N_3 \quad (7.24)$$

in which d_{rbc} is the red blood cell diameter (approximately equal to 7 μm), and $f_{s,u}$, $\sigma_{s,u}$ are known from the suture strength and the tensile strength of the arterial wall, respectively. Obviously, the final selection will be the maximum of N_1, N_2, N_3.

The maximum number of utilized stitches is calculated by recasting the geometric constraint of Equation (7.4) in the form:

$$N_s \le \frac{\pi R_p}{4 r_s} \equiv N_4 \quad (7.25)$$

Therefore, the final selection of number of stitches should be bounded by

$$\max \{ N_1, N_2, N_3 \} < N_s \le N_4 \quad (7.26)$$

Failure to satisfy inequality (7.26) means that the material selection and geometric parameter must be rethought. Typical values related to suture materials indicate that $N_1 < N_2$ or N_3, although deteriorated stitches as well as the presence of sutures knots can change this.

Note that, for the case where $F_L(t) \le \alpha N_s f_s^0$, the derived inequalities (7.22) to (7.24) are not valid. In this case, the potential failure is not dependent on the number of sutures N_s, but rather on whether the pre-tension exceeds either the suture strength or artery strength.

When the suture strength is larger than the knot strength, the stitches will fail on the knot region, otherwise the failure will occur elsewhere. Experiments on the mechanical properties of different suture materials were performed by Brouwers et al. [90]. Table 7-1 reports values for the tensile strength of plain sutures, the tensile strength range for seven knots under dynamic loading, and the deteriorated tensile strength of plain sutures some weeks after the surgery. Moreover, the arterial longitudinal strength was found to be between 1-3 MPa, based on dynamic biaxial tension tests on human aortic tissues [47].

Table 7-1: Tensile strength of untied and tied fiber.

Suture Material	Diameter* (mm)	Tensile suture strength* (N)	Tensile knot strength* (N)	Tensile suture strength after n weeks (%/n)
Plain catgut	0.36	25.5	23.7-29.6	0%/1
Maxon 3-0	0.31	34.5	22.1-46.1	50%/3
PDS 3-0	0.3	27.2	12.4-36.5	50%/4
Prolene	0.26	16.7	6.2-26.7	(N/A)
Dexon 4-0	0.24	29.1	24.1-39.4	57%/2; 0%/4
Mersilene 4-0	0.26	28.3	20.5-37.8	(N/A)
Vicryl 3-0	0.29	34.6	14.1-38.8	55%/2

* Based on the results of Brouwers et al.[90]

7.5 Numerical example

A design example of the proposed model is presented, in which the minimum number of stitches required to prevent suture failure, arterial-wall tearing, and development of excessive anastomotic gap, is calculated.

We consider an arterial end-to-end anastomosis having length $L_p = 3$ cm, radius $R_p = 0.6$ cm, wall thickness $H_p = 0.11$ cm, arterial wall density $\rho_0 = 1160$ kg/m^3, and radial displacement due to residual stresses $u_0 = (2/3)u_{st} = 0.499$ mm. The circumferential and longitudinal Young's Modulus are $E_\theta = 700$ kN/m^2 and $E_L = 400$ kN/m^2,

respectively. More values for the mechanical properties of human ascending thoracic aorta can be found in the study of Gozna et al. [93]. Furthermore, we assume continuous suturing using a Prolene (polypropylene) suture having Young's Modulus $E_s = 1.5$ GPa, radius $r_s = 0.13$ mm, and stitch length $l_s = 0.2$ cm. Table 7-2 lists all the parameters used in this example.

Table 7-2: Parameters used in numerical example of end-to-end arterial anastomosis.

Parameter	Value
Artery	
Length, L_p (cm)	3
Radius, R_p (cm)	0.6
Thickness, H_p (cm)	0.11
Arterial tissue density, ρ_0 (kg m^{-3})	1160
Initial displacement, $u_0 = (2/3)u_{st}$ (mm)	0.499
Circumferential Young's modulus, E_θ (kPa)	700
Longitudinal Young's modulus, E_L (kPa)	400
Tissue strength, $\sigma_{s,u}$ (MPa)	3
Red blood cell diameter, d_{rbc} (μm)	7
Suturing (Continuous, Prolene)	
Length, l_s (cm)	0.2
Radius, r_s (mm)	0.13
Young's modulus, E_s (GPa)	1.5
Participation factor, a	1.7
Suture pre-tension, f_s^0 (N)	0
Suture strength, $f_{s,u}$ (N)	16.7
Loading	
Systolic pressure, p_s (mmHg)	120
Diastolic pressure, p_d (mmHg)	80
Systolic duration, t_s (sec)	0.35
Cardiac pulse duration, t_{cp} (sec)	1

Based on these parameter values, the maximum arterial response, occurring during the systolic phase, is calculated as $u_{\max} = 0.997$ mm. The maximum circumferential strain $u_{\max} / R_p = 16.6\%$ is within the validity range of the small-deformation assumption. Based on inequality (7.26), the optimal selection of the number of stitches for this example is $N_s = 17$. For the selected value of the design parameter N_s, the response quantities of interest are derived as: suture force $f_s = 0.24$ N (< 16.7 N $\equiv f_{s,u}$), embedding stress $\sigma_s = 1.43$ MPa (< 1.5 MPa $\equiv \sigma_{s,u}/2$), and anastomotic gap $x_{net} = 6.02$ μm (< 21 μm $\equiv 3d_{rbc}$). As expected, by virtue of satisfying simultaneously the objective functionalities given by Equations (7.1) through (7.3), all response quantities fall within the accepted range of values, preventing any of the aforementioned failure scenarios. Nevertheless, the calculated embedding stress is marginally acceptable, and the slightest increase of its value may lead to arterial-wall tearing. That is, despite the fact that the suture can withstand tensile force up to 16.7 N, any suture pre-tension $f_s^0 > H_p r_s \sigma_{s,u} / \alpha = 0.24$ N applied by the surgeon in tying the knot may cause arterial injury.

7.6 Validation of the model

The present model is fully analytic and has been conceived to be simple with minimum computational costs, and hence suitable for potential clinical application. The model incorporates a plethora of the most important-to-the-surgeon parameters for the first time, at the expense however of strong simplifying hypotheses. One main simplification is the linearization of the mechanical response of the anastomosis walls. Moreover, anisotropy in the circumferential and longitudinal direction has been retained also in an approximate way, ignoring Poisson effects. In addition, failure criteria based on octahedral equivalent stresses may not be completely appropriate for describing the strength of the arterial tissue. Finally, a limit-state analysis has been adopted for the failure mechanism of arterial tissues subject to the loading condition imposed by the stitches.

The aforementioned issues, important by themselves, do not change the holistic view of the study presented in this chapter. The linearization of all presented responses gives consistent strains of the order of 20%. The use of more elaborate hyperelastic constitutive laws does not appreciably change the central results of our work, since linear-elastic estimates can adequately simulate hyperelastic stress-strain relationships by adopting the appropriate tangent elastic moduli (see Figure 3-7(a)). Poisson effects can reduce the

stitching results by about 30%, thus ignoring the Poisson effects is not against safety. Failure of the arterial walls is still an uncharted topic. It is most probable that failure depends on energy criteria, and in this respect the shear stress used in this work corresponds to a critical deviatoric energy. Finally, the limit-state analysis based on a critical shear stress can be easily recast into a tearing criterion based on the almost-uniaxial state of stress on the sides of the stitches (the linear-elasticity local model predicts a stress-concentration factor of about two).

Although the literature contains several experimental studies dealing with the compliance of the anastomotic region [16–18, 20, 21], we found that many parameters that seem to affect the suture stressing are not reported (e.g. the number of stitches N_s). Our present work indicates that more details regarding the suture material and suturing technique should be reported, especially if the para-anastomotic hypercompliant zone (PHZ) phenomenon needs to be addressed. Previous experimental studies of end-to-end anastomosis between isocompliant arteries or grafts investigate the compliance of the anastomotic region, whereas the main response quantities calculated in this study (x_{net}, f_s, σ_s) are not reported in experimental studies. Nevertheless, it is shown that the present study provides a good estimation of the compliance value (Equation (3.1)) of the anastomotic region with respect to the published experimental results.

Hasson et al. [17, 18] calculated the compliance of dog arterial grafts under dynamic loading. The compliance away from the PHZ was 0.06% $mmHg^{-1}$ for the first study of Hasson et al. [17] and 0.05% $mmHg^{-1}$ for the later study of Hasson et al. [18]. Ulrich et al. [21] calculated the compliance of pig arterial grafts under dynamic loading as 0.075% $mmHg^{-1}$. The calculated compliance in our numerical example is 0.12% $mmHg^{-1}$. Given that the mechanical data and pressure time-profile data were not available for most of the experimental studies, and that our model is subjected to pulse loading of the first loading cycle (meaning that the calculated displacements may be up to two times larger than the static or long-term dynamic loading - see Section 4.3), our model constitutes a good approximation of the experimental results.

Of particular interest is the PHZ phenomenon. Hasson et al. [18] found that the PHZ phenomenon occurs more frequently for anastomosis of the continuous stitching technique than the interrupted stitching technique. Figure 7-7(a) shows the schematic compliance along the anastomotic region. The PHZ phenomenon (region 2) is pronounced in the case of continuous stitches, whereas away from the anastomosis zone the compliance is

constant (region 1). From our study, the net gap x_{net} is increased by 15% in the case of continuous stitching compared to the case of interrupted stitching. This may justify the decreased longitudinal stretch $\Delta l / L_p$ and lower tangent elastic modulus $E_{\theta 1} > E_{\theta 2}$ (Figure 7-7(b)) of the continuous stitching case. The decrease of tangent elastic modulus results to a higher compliance at the PHZ.

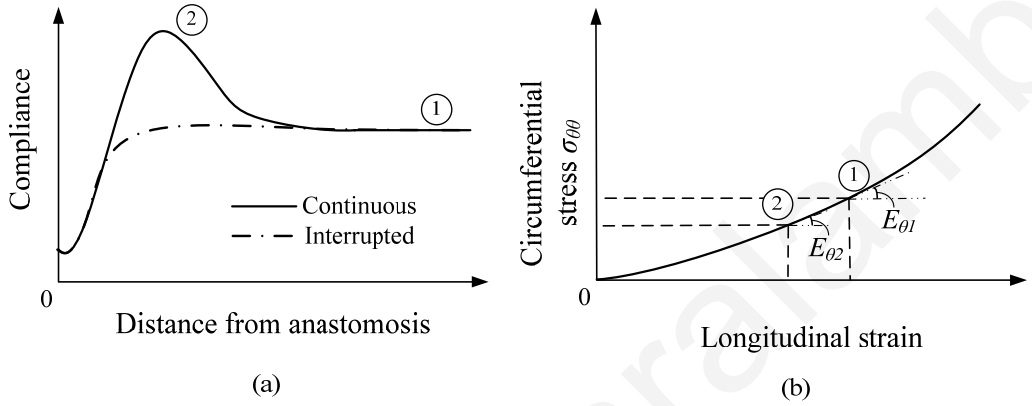

Figure 7-7: Schematic correlation of PHZ phenomenon to the stiffness of the arterial tissue (and the stitching technique): (a) Compliance of the anastomotic region for continuous and interrupted techniques, (b) Circumferential stress-longitudinal strain relationship of a nonlinear hyperelastic material.

The experimental results suggest a decrease of stiffness by about 29% (at the PHZ) for the continuous stitching technique [18]. From the numerical example presented in our study, the total longitudinal stretch away from the suture line is 1.36. The longitudinal stretch at the PHZ is reduced by 29% compared to the longitudinal stretch away from the anastomotic region. By considering a nonlinear stress-strain relationship according to Skalak et al. [55] (Equation (5.11)), the continuous stitching (stretch 1.27) decreases the tangent modulus by 24% in comparison to the interrupted stitching (stretch 1.36), indicating that the increase of compliance at the PHZ can be correlated to the decrease of stiffness, as Hasson et al. [18] suggest.

In conclusion, the present model, even though simple and approximate, captures adequately the essence of the phenomenon. More complex models can be important in refining the present results, but on the other hand will require more material data that may be difficult to obtain or assess their direct contribution.

7.7 An analytical investigation of the PHZ phenomenon

The para-anastomotic hypercompliant zone (PHZ) is a zone of increased compliance (and increased radial displacements) that occurs near the anastomotic region. To analytically investigate the PHZ phenomenon, a mathematical model considering that the radial displacement of the artery is a function of the distance along the longitudinal direction of the arterial anastomosis, is formulated. Paasche et al. [6] solved analytically the static boundary-value problem describing the response of an end-to-end anastomosis. Herein, we also investigate the static problem, by considering different boundary conditions than that adopted by Paasche et al. [6].

7.7.1 Mathematical model and static solution

Figure 7-8 shows the configuration of the proposed model. The mathematical model assumes that the radial displacement of the arterial wall η is a function of the axial distance x from the stitching region. The equation of motion of the cylindrical tube, under applied intraluminal pressure, is expressed as [6]:

$$\frac{\partial^4 \eta(x,t)}{\partial x^4} + \frac{12}{H_p{}^2 R_p{}^2}\eta(x,t) = \frac{12(1-\nu^2)}{E_\theta H_p{}^3} p(t) \tag{7.27}$$

where R_p denotes the radius of the artery, H_p the thickness of the arterial wall, E_θ the circumferential elasticity modulus of the artery, ν the Poisson's ratio of the arterial tissue (equal to 0.5 for incompressible materials), and $p(t)$ the internal pressure of the blood vessel.

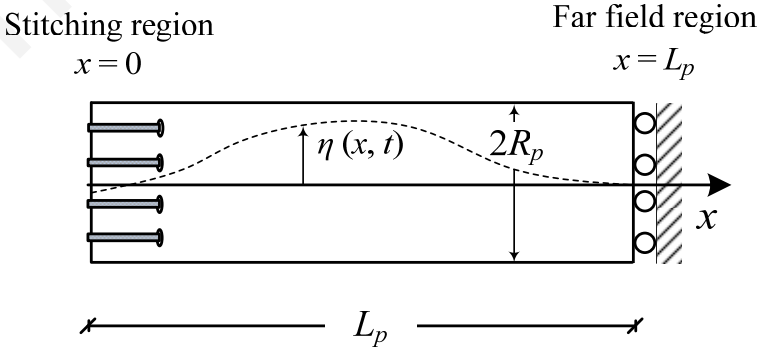

Figure 7-8: Configuration of the end-to-end anastomosis model for investigating the PHZ phenomenon.

On multiplying Equation (7.27) by $E_\theta / (12\,p(t)(1-v^2))$, the pressure term can be eliminated. In particular, Equation (7.27) reduces to

$$\frac{d^4\eta_s}{dx^4} + \frac{12}{H_p{}^2 R_p{}^2}\eta_s = \frac{1}{H_p{}^3} \tag{7.28}$$

where $\eta_s(x,t) = \eta(x,t)E_\theta / (12\,p(t)(1-v^2))$. The reduced problem of Equation (7.28) does not depend on time, describing the static response of the system. The derived differential equation is solved as a boundary-value problem. The four boundary conditions are

$$\eta_s(L_p) = \eta_L, \quad \frac{d\eta_s}{dx}(L_p) = 0, \quad \frac{d^2\eta_s}{dx^2}(0) = 0, \quad \frac{d^3\eta_s}{dx^3}(0) = \eta_0''' \tag{7.29}$$

in which $\eta_L = R_p{}^2 / (12H_p)$ is the far-field radial displacement of the artery, and η_0''' is the shear stress at the stitching region, caused by the sutures. The general solution of Equation (7.28) is of the following form

$$\begin{aligned}\eta_s(x) = \frac{1}{H_p{}^3\kappa^4} &+ G_1 e^{\frac{\kappa x}{\sqrt{2}}}\left[\cos\left(\frac{\kappa x}{\sqrt{2}}\right) + \sin\left(\frac{\kappa x}{\sqrt{2}}\right)\right] + G_2 e^{-\frac{\kappa x}{\sqrt{2}}}\left[\cos\left(\frac{\kappa x}{\sqrt{2}}\right) - \sin\left(\frac{\kappa x}{\sqrt{2}}\right)\right] \\ &+ G_3 e^{\frac{\kappa x}{\sqrt{2}}}\left[\cos\left(\frac{\kappa x}{\sqrt{2}}\right) - \sin\left(\frac{\kappa x}{\sqrt{2}}\right)\right] + G_4 e^{-\frac{\kappa x}{\sqrt{2}}}\left[\cos\left(\frac{\kappa x}{\sqrt{2}}\right) + \sin\left(\frac{\kappa x}{\sqrt{2}}\right)\right]\end{aligned} \tag{7.30}$$

where G_1, G_2, G_3, G_4 are constants that can be obtained by utilizing the boundary conditions, and $|\kappa| = \sqrt[4]{12/(H_p R_p)^2}$. By solving the boundary-value problem, the resulting radial displacement is analytically expressed as

$$\begin{aligned}\eta_s(x) = \frac{1}{H_p{}^3\kappa^4} &+ \mathrm{e}^{-\frac{\kappa x}{\sqrt{2}}}\left\{\mathrm{e}^{\frac{2\kappa x}{\sqrt{2}}} G_3\left[\cos\left(\frac{\kappa x}{\sqrt{2}}\right) - \sin\left(\frac{\kappa x}{\sqrt{2}}\right)\right] + \left(\frac{\sqrt{2}\eta_0'''}{2\kappa^3} + G_3\right)\left[\cos\left(\frac{\kappa x}{\sqrt{2}}\right) + \sin\left(\frac{\kappa x}{\sqrt{2}}\right)\right]\right. \\ &+ \frac{\mathrm{e}^{\frac{2\kappa x}{\sqrt{2}}}\left[\cos\left(\frac{\kappa x}{\sqrt{2}}\right) + \sin\left(\frac{\kappa x}{\sqrt{2}}\right)\right]}{1+\mathrm{e}^{\frac{2\kappa L_p}{\sqrt{2}}}}\left[\frac{\sqrt{2}\eta_0'''}{2\kappa^3} + 2G_3 + \left(\frac{\sqrt{2}\eta_0'''}{2\kappa^3} + G_3 + \mathrm{e}^{\frac{2\kappa L_p}{\sqrt{2}}} G_3\right)\tan\left(\frac{\kappa L_p}{\sqrt{2}}\right)\right] \\ &\left. + \left[\cos\left(\frac{\kappa x}{\sqrt{2}}\right) - \sin\left(\frac{\kappa x}{\sqrt{2}}\right)\right]\left[\frac{\sqrt{2}\eta_0'''}{2\kappa^3} + 2G_3 - \frac{\frac{\sqrt{2}\eta_0'''}{2\kappa^3} + 2G_3 + \left(\frac{\sqrt{2}\eta_0'''}{2\kappa^3} + G_3 + \mathrm{e}^{\frac{2\kappa L_p}{\sqrt{2}}} G_3\right)\tan\left(\frac{\kappa L_p}{\sqrt{2}}\right)}{1+\mathrm{e}^{\frac{2\kappa L_p}{\sqrt{2}}}}\right]\right\}\end{aligned} \tag{7.31}$$

in which the constant G_3 is equal to

$$G_3 = \frac{\dfrac{\sqrt{2}\eta_0'''}{2\kappa^3}\left\{-1-\mathrm{e}^{\frac{2\kappa L_p}{\sqrt{2}}}\left[2+\cos\left(\frac{2\kappa L_p}{\sqrt{2}}\right)+\sin\left(\frac{2\kappa L_p}{\sqrt{2}}\right)\right]\right\}}{1+\mathrm{e}^{\frac{4\kappa L_p}{\sqrt{2}}}+2\mathrm{e}^{\frac{2\kappa L_p}{\sqrt{2}}}\left[2+\cos\left(\frac{2\kappa L_p}{\sqrt{2}}\right)\right]} \tag{7.32}$$

The normalized response of the system is obtained by multiplying Equation (7.31) by $H_p{}^3\kappa^4$:

$$\begin{aligned}\eta_s(\kappa x)H_p{}^3\kappa^4 = 1+\mathrm{e}^{-\frac{\kappa x}{\sqrt{2}}}&\left\{\mathrm{e}^{\frac{2\kappa x}{\sqrt{2}}}G_3H_p{}^3\kappa^4\left[\cos\left(\frac{\kappa x}{\sqrt{2}}\right)-\sin\left(\frac{\kappa x}{\sqrt{2}}\right)\right]\right.\\
&+\left(\frac{\sqrt{2}\eta_0'''H_p{}^3\kappa}{2}+G_3H_p{}^3\kappa^4\right)\left[\cos\left(\frac{\kappa x}{\sqrt{2}}\right)+\sin\left(\frac{\kappa x}{\sqrt{2}}\right)\right]\\
&+\frac{\mathrm{e}^{\frac{2\kappa x}{\sqrt{2}}}\left[\cos\left(\frac{\kappa x}{\sqrt{2}}\right)+\sin\left(\frac{\kappa x}{\sqrt{2}}\right)\right]}{1+\mathrm{e}^{\frac{2\kappa L_p}{\sqrt{2}}}}\left[\begin{array}{l}\dfrac{\sqrt{2}\eta_0'''H_p{}^3\kappa}{2}+2G_3H_p{}^3\kappa^4\\ +\left(\dfrac{\sqrt{2}\eta_0'''H_p{}^3\kappa}{2}+G_3H_p{}^3\kappa^4+\mathrm{e}^{\frac{2\kappa L_p}{\sqrt{2}}}G_3H_p{}^3\kappa^4\right)\tan\left(\dfrac{\kappa L_p}{\sqrt{2}}\right)\end{array}\right]\\
&+\left[\cos\left(\frac{\kappa x}{\sqrt{2}}\right)-\sin\left(\frac{\kappa x}{\sqrt{2}}\right)\right]\left[\begin{array}{l}\dfrac{\sqrt{2}\eta_0'''H_p{}^3\kappa}{2}+2G_3H_p{}^3\kappa^4-\dfrac{\dfrac{\sqrt{2}\eta_0'''H_p{}^3\kappa}{2}+2G_3H_p{}^3\kappa^4}{1+\mathrm{e}^{\frac{2\kappa L_p}{\sqrt{2}}}}\\ -\dfrac{\left(\dfrac{\sqrt{2}\eta_0'''H_p{}^3\kappa}{2}+G_3H_p{}^3\kappa^4+\mathrm{e}^{\frac{2\kappa L_p}{\sqrt{2}}}G_3H_p{}^3\kappa^4\right)\tan\left(\dfrac{\kappa L_p}{\sqrt{2}}\right)}{1+\mathrm{e}^{\frac{2\kappa L_p}{\sqrt{2}}}}\end{array}\right]\left.\right\}\end{aligned} \tag{7.33}$$

Observe that, the normalized radial displacement $\eta_s(\kappa x)H_p{}^3\kappa^4$ depends on three dimensionless quantities: the normalized shear stress $\eta_0'''H_p{}^3\kappa$, the normalized length of the blood vessel κL_p, and the normalized distance from the anastomotic region κx. Note that, that the normalized radial displacement $\eta_s(\kappa x)H_p{}^3\kappa^4$ is equal to $\eta_s(\kappa x)/\eta_L$.

The radial displacement at the stitching region can be obtained by setting $\kappa x = 0$ in Equation (7.31), yielding

$$\eta_s(0)=\frac{1}{H_p{}^3\kappa^4}+\frac{\sqrt{2}\eta_0'''}{\kappa^3}+\frac{\dfrac{2\sqrt{2}\eta_0'''}{\kappa^3}\left\{-1-\mathrm{e}^{\frac{2\kappa L_p}{\sqrt{2}}}\left[2+\cos\left(\dfrac{2\kappa L_p}{\sqrt{2}}\right)+\sin\left(\dfrac{2\kappa L_p}{\sqrt{2}}\right)\right]\right\}}{1+\mathrm{e}^{\frac{4\kappa L_p}{\sqrt{2}}}+2\mathrm{e}^{\frac{2\kappa L_p}{\sqrt{2}}}\left[2+\cos\left(\dfrac{2\kappa L_p}{\sqrt{2}}\right)\right]} \tag{7.34}$$

Equation (7.34), reveals the linear dependency of the radial displacement $\eta_s(0)$ on the shear stress value.

The effect of the normalized artery length κL_p on the stitching-region response can be investigated by differentiating Equation (7.34) as

$$\frac{d\eta_s(0)}{d\left(\sqrt{2}\eta_0'''/\kappa^3\right)}=\frac{1+2\left\{-1-\mathrm{e}^{\frac{2\kappa L_p}{\sqrt{2}}}\left[2+\cos\left(\dfrac{2\kappa L_p}{\sqrt{2}}\right)+\sin\left(\dfrac{2\kappa L_p}{\sqrt{2}}\right)\right]\right\}}{1+\mathrm{e}^{\frac{4\kappa L_p}{\sqrt{2}}}+2\mathrm{e}^{\frac{2\kappa L_p}{\sqrt{2}}}\left[2+\cos\left(\dfrac{2\kappa L_p}{\sqrt{2}}\right)\right]} \tag{7.35}$$

7.7.2 Results

The radial displacement profile along the anastomosis length, for different values of normalized length κL_p and normalized shear stress $\eta_0'''H_p^3\kappa$, is investigated. As follows from Figures 7-9 and 7-10, the radial displacement profile strongly depends on the shear-stress value at the stitching region. In particular, a decrease of the normalized shear-stress $\eta_0'''H_p^3\kappa$ value decreases the lumen diameter at the anastomotic interface ($x=0$). The radial displacements are slightly larger than the far-filed displacement (normalized radial displacement larger than 1) at a region away from the anastomotic interface between $\kappa x=2.2$ and $\kappa x=5$ (PHZ region). The peak radial displacement occurs at a normalized distance about $\kappa x\approx 3$ away from the anastomotic interface. Note that, for zero shear-stress values η_0''' the artery is inflated uniformly, implying that the stitching perfectly simulates the behavior of the healthy arterial tissue. In regard to the normalized length of the anastomosis, it is observed that for $\kappa L_p=10$ (Figure 7-10), the system always reaches its far-field displacement value $\eta_L=R_p{}^2/(12H_p)$ away from the PHZ region (i.e. $\kappa x>5$ region).

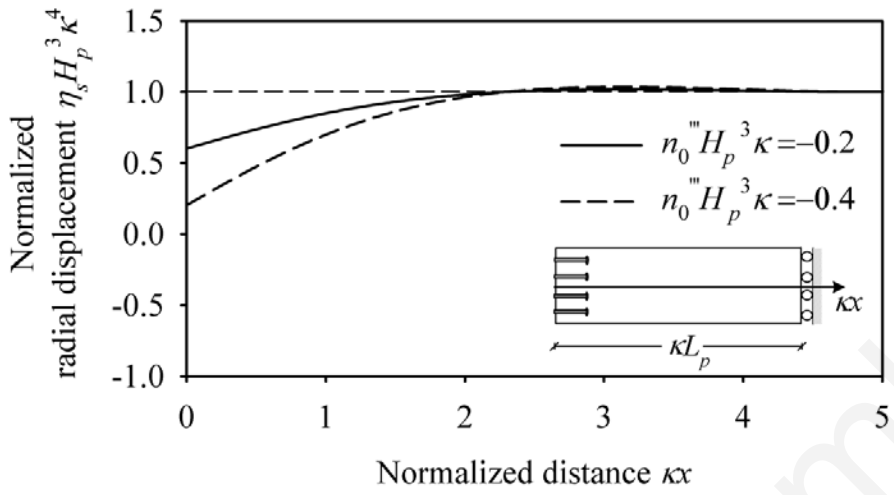

Figure 7-9: Normalized radial displacement of artery as a function of distance from the anastomotic interface, for normalized length $\kappa L_p = 5$ and normalized shear stress: (a) $\eta_0'''H_p^{\,3}\kappa = -0.2$, (b) $\eta_0'''H_p^{\,3}\kappa = -0.4$.

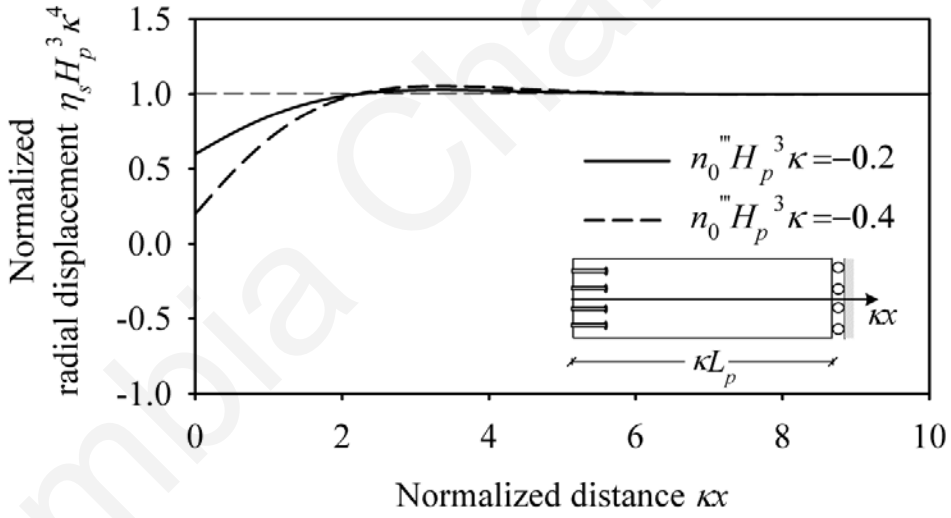

Figure 7-10: Normalized radial displacement of artery as a function of distance from the anastomotic interface, for normalized length $\kappa L_p = 10$ and normalized shear stress: (a) $\eta_0'''H_p^{\,3}\kappa = -0.2$, (b) $\eta_0'''H_p^{\,3}\kappa = -0.4$.

Figure 7-11 plots the response quantity $d\eta_s(0)/d\left(\sqrt{2}\eta_0'''/\kappa^3\right)$ (at the stitching region) as a function of the normalized artery length κL_p. For normalized length values lower than 5, an increase of the normalized length yields a decrease of the normalized length effect on the stitching-region response, whereas for normalized length values higher than 5 the response of the stitching region is not affected by the normalized length value.

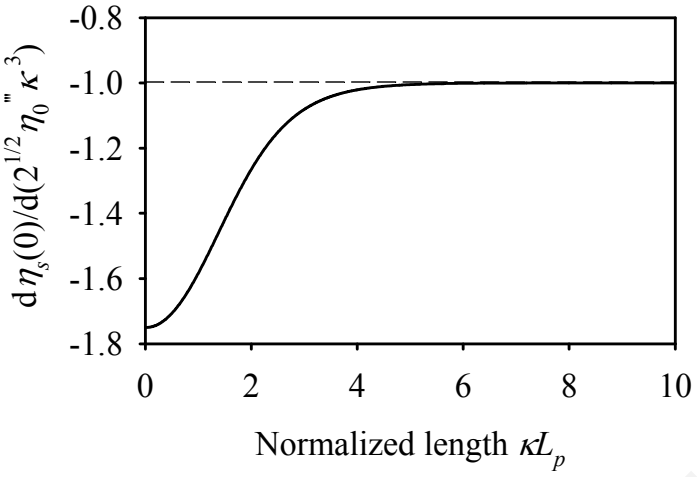

Figure 7-11: Response quantity $d\eta_s(0)/d\left(\sqrt{2}\eta_0'''/\kappa^3\right)$ as a function of the normalized artery length κL_p.

7.8 Concluding remarks

Proposed in this chapter are mathematical models governing the response of end-to-end arterial anastomoses. An extension of the model of Demetriou [66] that considers the suture pre-tensioning and the stitching technique participation factor, as well as a mathematical model investigating the para-anastomotic hypercompliant zone (PHZ) phenomenon, were formulated. The respective problem solutions were expressed by closed-form expressions.

In particular, for the dynamic end-to-end anastomosis model between isocompliant arteries, the time-depended response of the problem is derived in terms of the anastomotic gap (Equation (7.15)), the suture tensile force (Equation (7.8)), and the embedding stress due to suture-artery contact interaction (Equation (7.17)). The model, although linear elastic, is comprehensive in that it captures the effects of all pertinent parameters (geometric and mechanical properties of artery and sutures, number of sutures, loading characteristics, longitudinal residual stresses, suture pre-tensioning, and stitching technique participation factor). The resulting response is a function of seventeen input parameters. Nevertheless, on normalizing appropriately the response quantities, the problem can be described by only five dimensionless parameters ($\alpha E_s/E_L$, L_p/l_s, $N_s r_s/R_p$, L_p/l_s, $\alpha f_s^0/r_s H_p E_L$).

It is worth noting that end-to-end anastomoses with vertical-end cuts may exhibit stenosis (decreased diameter lumen) at the anastomotic interface. Thus, the interconnected blood vessels frequently have beveled ends, i.e. the edge of the blood vessel is inclined rather than vertical. In this way, the suture line is increased and allows a higher number of utilized stitches. Even though our model assumes a vertical incision at the anastomotic interface, the mathematical model and the results of this chapter are applicable in the case of a beveled incision. This modification only affects inequality (7.25), implying that it can be relaxed in order to allow a higher number of utilized stitches.

The suture-tissue interaction analysis reveals the nonlinear dependency of the system response on the radial extension of the artery and highlights useful interrelations among the problem parameters. In regard to the normalized anastomotic gap, the results suggest that increasing the value of any of the design parameters, excluding f_s^0, yields a decreased anastomotic gap. The most influential parameter in drastically reducing the anastomotic gap is the number of utilized stitches, N_s, as can be seen from Figure 7-4(c,d). The normalized suture tensile force is instead affected only by the number of stitches. A higher number of utilized stitches results in a smaller tensile force developed in each stitch (Figure 7-5). It has also been shown that the normalized embedding stress is decreased as the number of stitches is increased, whereas the influence of the ratio of suture-to-artery elastic modulus on the embedding stress is insignificant (Figure 7-6).

It should be noted that, among the failure modes discussed in Section 7.2.1, arterial wall failure is the most frequently encountered. For a typical anastomosis scheme and for $F_L(t) \le \alpha N_s f_s^0$, when the value of pre-tension f_s^0 exceeds a certain value (derived from $\alpha f_s^0 / 2 r_s H_p > \sigma_{s.u} / 2$) the arterial wall is likely to fail. On the other hand, for lower values of pre-tension and for $F_L(t) > \alpha N_s f_s^0$, the application of suture pre-tension can result in reducing the anastomotic gap (Equation (7.19)), while not affecting considerably the embedding stress (Equation (7.20)), which constitutes the critical response parameter, or the suture tensile force (Equation (7.21)).

In regard to the proposed mathematical model that investigates the PHZ phenomenon, a closed-form solution describing the static radial displacements as a function of the distance along the longitudinal direction of the arterial anastomosis is derived (Equation (7.33)). The solution adequately captures the PHZ phenomenon for normalized length values κL_p higher that 5 and normalized shear-stress values $\eta_o''' H_p{}^3 \kappa$ lower than -0.05.

In summary, the most important outcome of the study presented in this chapter is the development of a fundamental analytical model that predicts the dynamic behavior of end-to-end arterial anastomosis and the establishment of failure criteria that can ultimately form the basis for the development of vascular anastomosis guidelines pertaining to the prevention of post-surgery complications. The mathematical formulation reveals useful interrelations among the problem parameters, thus making the proposed model a valuable tool for the optimal selection of materials and improved functionality of sutures.

CHAPTER 8

Suture-line Response of End-to-side Anastomosis

8.1 Introduction

End-to-side vascular anastomosis has a considerable complexity concerning the suturing of the juncture line between the artery and the graft. The problem is influenced by a number of parameters: the blood vessels and the suturing geometrical and mechanical properties, the intersecting angle between the artery and the graft, the blood flow rate, and the blood pressure. Note that, this type of vascular anastomosis is utilized extensively in bypassing arterial diseases and restoring normal blood supply to arteries through a vein or artificial graft.

There are several studies carried out in this field driven by the need to assess and prevent post-surgery complications. Marble et al. [94] calculated analytically the tensile force in the direction of the graft, away from the anastomosis junction. In their work, the suture-blood vessels interaction was ignored, as well as the stress concentration at different locations of the intersection area. Although studies that utilize numerical methods can simulate asymmetrical geometries, dynamically-applied blood flow and biological activities, they inevitably sacrifice generality due to the limited number of investigated models [9, 10, 12, 13, 15].

The main objective of this chapter is to derive an analytical model and provide closed-form expressions for the response of end-to-side anastomosis, in order to improve the end-to-side anastomosis technique through improved functionality of the sutures and optimal selection of materials and anastomosis angle.

The two blood vessels are assumed to have comparable elastic properties, and their cross-sections are modeled as axis-symmetric cylinders, consisting by a single homogeneous layer. The proposed methodology is based on general results obtained from the analysis of pipe connections, a topic that has been investigated in recent years in the field of offshore structural engineering [95, 96]. A key aspect for implementing the stress-concentration-factor (SCF) approach is the recognition that the axial load due to pressure and flow dynamics exerted along the graft axis controls the “hot spots” on the juncture line, which in turn affects the mechanical response of the sutures. The analysis accounts explicitly for three possible failure modes directly associated with the suture-blood vessels interaction: suture failure, blood-vessel tearing, and suture-line blood leaking.

8.2 Model configuration

The human arterial system can be idealized as a system of interconnected cylindrical pipes that transport blood. An end-to-side anastomosis configuration can be parallelized with pipe junctions, called K- or Y-joints. The analysis of stress concentration at the junction line of the cylindrical pipes is a well-known and well-studied subject in the field of offshore structural engineering.

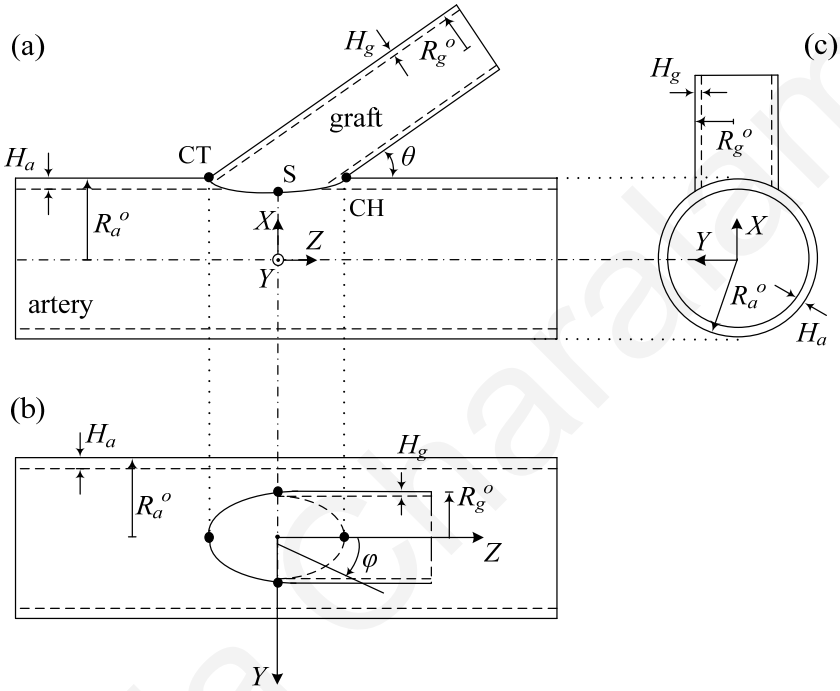

Figure 8-1: Configuration of the three-dimensional end-to-side anastomosis model: (a) *X*-*Z* view, (b) *Y*-*Z* view, (c) *X*-*Y* view (CT: crown toe, CH: crown heel, S: saddle).

Figure 8-1 shows the three-dimensional configuration of the proposed end-to-side vascular anastomosis model. The host-artery has outer radius R_a^o and wall thickness H_a, while the vein or artificial graft that is connected to the artery side has outer radius R_g^o and wall thickness H_g. In Figure 8-1, angle φ denotes the polar angle of the intersection plane, measured from the crown heel (CH), and θ denotes the angle of the graft axis with respect to the artery axis. The intersecting angle assumes values in the range $0° \le \theta \le 90°$. Note that, the origin of the *X*-*Y*-*Z* coordinate system lies on the artery axis, beneath the intersection point between the artery surface and the graft axis.

The mathematical model developed herein is based on the following assumptions: (a) the cross-sectional dimensions of the artery and graft are circular and small compared to the

radius of their centerline; (b) the vessels wall thicknesses are constant along the centerline; (c) the arterial tissue and the graft consist of a single (homogeneous) layer; (d) the artery and the graft have comparable elastic properties; and (e) viscous effects are ignored. According to the study of Thubrikar et al. [97], increased thickness of the junction line and nonlinear elastic properties of the blood vessels have secondary effect on the induced stresses. In particular, they proved that the local stress concentration of an arterial branch is primarily affected by the geometry of the end-to-side junction and is secondarily affected by factors like the elastic properties of the blood vessel or thickening of the junction line.

The three-dimensional curve of the intersection of the two blood-vessels can be expressed parametrically (with parameter $\varphi \in [0, 2\pi]$) in the *X*-*Y*-*Z* coordinate system by the normalized equations [98]:

$$\frac{X}{R_a^o} = \cos\left[\sin^{-1}\left(\frac{R_g^o}{R_a^o}\sin\varphi\right)\right], \quad 0 \le \varphi \le 2\pi \tag{8.1}$$

$$\frac{Y}{R_a^o} = \frac{R_g^o}{R_a^o}\sin\varphi, \quad 0 \le \varphi \le 2\pi \tag{8.2}$$

$$\frac{Z}{R_a^o} = \left\{\frac{R_g^o}{R_a^o}\cos\varphi - \left[1 - \cos\left(\sin^{-1}\left(\frac{R_g^o}{R_a^o}\sin\varphi\right)\right)\right]\cos\theta\right\}\frac{1}{\sin\theta}, \quad 0 \le \varphi \le 2\pi \tag{8.3}$$

Figures 8-2 and 8-3 plot the normalized intersection curve of the artery-graft junction on the *Y*-*Z* and *X*-*Z* plane respectively (Equations (8.1) and (8.2)), for different values of the intersecting angle θ and radii ratio R_g^o / R_a^o. It can be observed that the length of the intersection curve is increased as the intersecting angle θ between the artery and the graft is decreased and/or the ratio R_g^o / R_a^o is increased. Thus, the intersection curve becomes longer as R_g^o / R_a^o approaches 1 and as θ approaches zero, leading to longer suture lines. For $R_g^o / R_a^o = 1$, the intersection curve becomes largest and sharp-edged with two corner-like points (*A*, *B* in Figure 8-2). On the other hand, for $R_g^o / R_a^o < 1$ the curves become smooth.

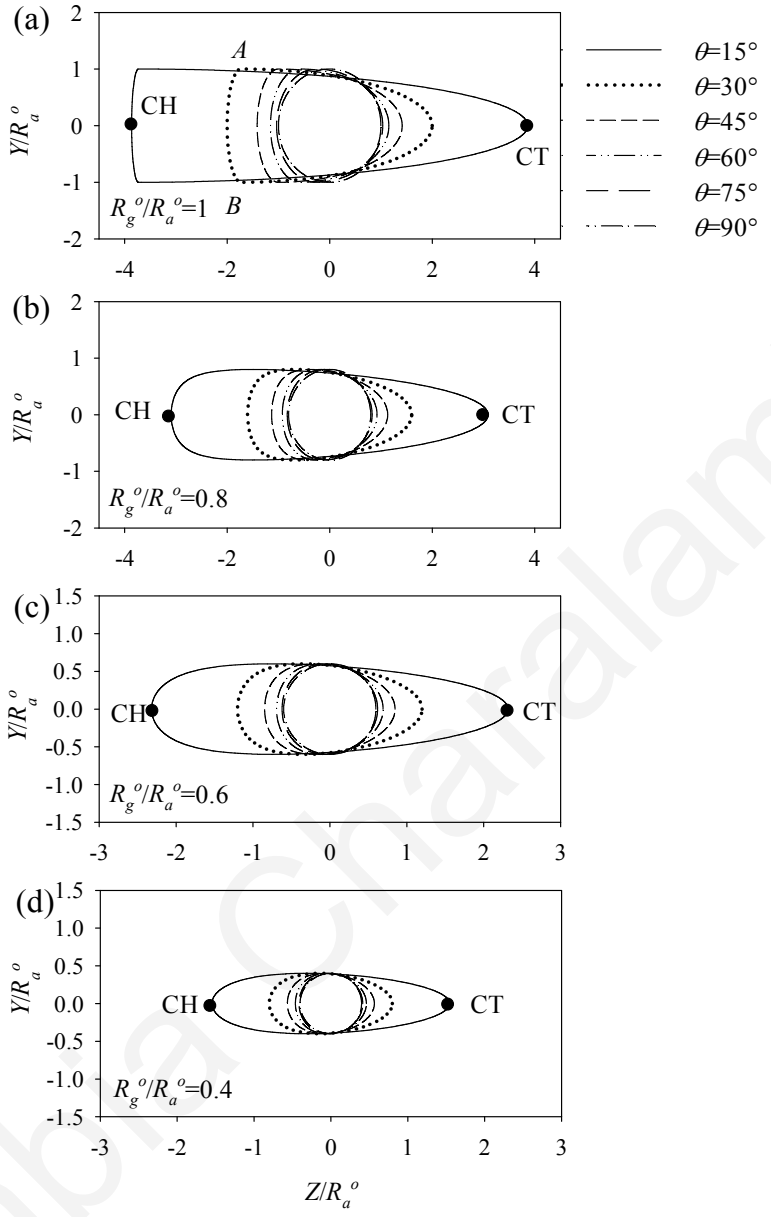

Figure 8-2: Normalized intersection curve of the artery-graft junction on the *Y-Z* plane for different values of the intersecting angle θ and for (a) $R_g^o / R_a^o = 1$, (b) $R_g^o / R_a^o = 0.8$ (c) $R_g^o / R_a^o = 0.6$, (d) $R_g^o / R_a^o = 0.4$ (CT: crown toe, CH: crown heel).

The normalized length of the suture line is equal to the normalized length of the intersection curve, calculated as

$$\frac{S}{R_a^o} = \int_0^{2\pi} \sqrt{\left(\frac{X}{R_a^o}\right)^2 + \left(\frac{Y}{R_a^o}\right)^2 + \left(\frac{Z}{R_a^o}\right)^2}\, d\varphi \qquad (8.4)$$

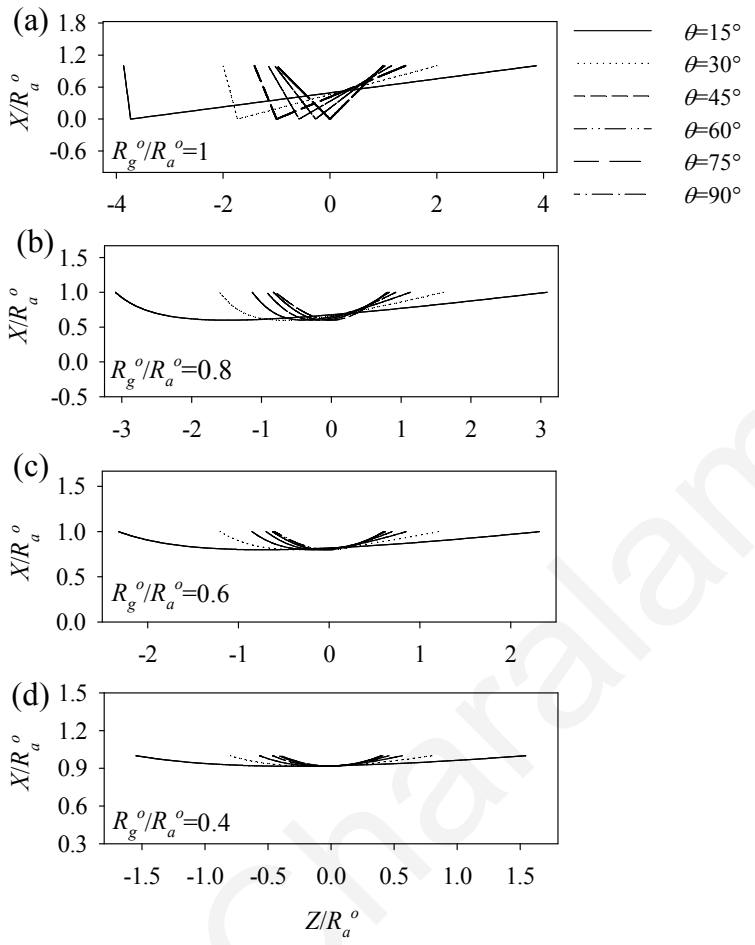

Figure 8-3: Normalized intersection curve of the artery-graft junction on the *X*-*Z* plane for different values of the intersecting angle θ and for (a) $R_g^o / R_a^o = 1$, (b) $R_g^o / R_a^o = 0.8$, (c) $R_g^o / R_a^o = 0.6$, (d) $R_g^o / R_a^o = 0.4$.

Table 8-1 lists the values of the normalized length S / R_a^o for different intersecting angles θ and radii ratios R_g^o / R_a^o. The total suture length has low bound the value $2S / R_a^o$ (interrupted stitching case with stitch length equal to the distance between two sequential stitches). For the case of running stitching with diagonal at 45° angle the normalized suture length is $\left(S / R_a^o\right)\left(\sqrt{2}+1\right)$.

In vascular surgery the incision length is frequently equal to two times the graft diameter. The normalized incision length (length of the line connecting the crown heel to the crown toe) can be calculated as

$$\frac{S_{in}}{R_a^o} = \frac{Z\left(\varphi = 0\right)}{R_a^o} - \frac{Z\left(\varphi = \pi\right)}{R_a^o} = \frac{2R_g^o}{R_a^o \sin\theta} \tag{8.5}$$

Table 8-1: Values of normalized suture length S / R_a^o for different values of the intersecting angle θ and radii ratios R_g^o / R_a^o.

R_g^o / R_a^o \ θ	15^0	30^0	45^0	60^0	75^0	90^0
1	20.50	11.78	9.25	8.22	7.77	7.64
0.8	15.35	9.63	8.10	7.51	7.26	7.19
0.6	11.94	8.25	7.33	7.00	6.85	6.18
0.4	9.20	7.21	6.77	6.61	6.54	6.53

On multiplying Equation (8.5) by R_a^o / R_g^o, the normalized incision length can be expressed as

$$\frac{S_{in}}{R_g^o} = \frac{2}{\sin\theta} \tag{8.6}$$

To perform an incision length equal to two times the graft diameter, the normalized incision length S_{in} / R_g^o must be equal to 4. Thus, in vascular surgery, the intersection angle θ is frequently equal to 30° (Equation (8.6)).

8.3 Far-field forces of the anastomosis model

The blood flow and the longitudinal pre-stress of the artery result in far-field forces on the artery-graft junction. In particular, the blood flow induces global forces along the *z* and *x* directions of the flow domain, as shown in Figure 8-4. The three cross-sections of Figure 8-4(a) have average flow rates Q_1, Q_2, Q_3 corresponding to the cross-sections A_1, A_2, A_3. The average flow velocities are V_1, V_2, V_3 (derived from $Q_i = A_i V_i$) and the blood pressures are p_1, p_2, p_3, respectively. It is assumed that the artery cross-section is constant along the artery axis ($A_1 = A_3$). The far-field forces acting along the *x*-axis, *y*-axis, and the graft axis are expressed as [94]:

$$R_x = -p_1 A_1 + p_2 A_2 \cos\theta + p_3 A_3 - \rho_b V_1^2 A_1 + \rho_b V_2^2 A_2 \cos\theta + \rho_b V_3^2 A_3 \tag{8.7}$$

$$R_y = p_2 A_2 \sin\theta + \rho_b V_2^2 A_2 \cos\theta \tag{8.8}$$

$$R_\theta = R_x \cos\theta + R_y \sin\theta \tag{8.9}$$

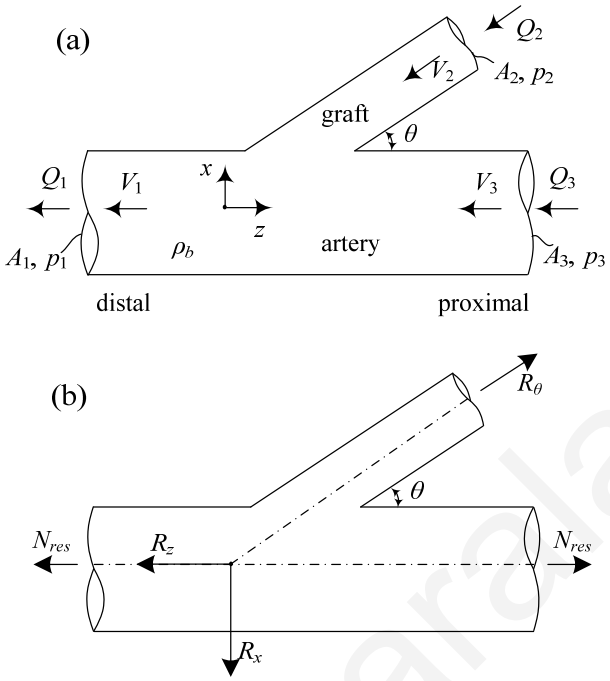

Figure 8-4: (a) Flow domain of an end-to side anastomosis. (b) Forces acting on the anastomosis junction.

By utilizing Bernoulli's momentum and continuity equation ($Q_1 = Q_2 + Q_3$), the far-field forces along the *z* and *x* directions may be simplified as follows [94]:

$$R_z = \cos\theta\left[\frac{\rho_b Q_1^2}{2A_1}\left(\frac{k_1^2}{k_2}+k_2\right)+k_2 A_1 p_1\right]+\frac{\rho_b Q_1^2}{2A_1}k_1\left(k_1-2\right) \tag{8.10}$$

$$R_x = \sin\theta\left[\frac{\rho_b Q_1^2}{2A_1}\left(\frac{k_1^2}{k_2}+k_2\right)+k_2 A_1 p_1\right] \tag{8.11}$$

in which $k_1 = Q_2 / Q_1$, $k_2 = A_2 / A_1$, and ρ_b is the density of the blood. The tensile far-field force in the direction of the graft is

$$R_\theta = \frac{\rho_b Q_1^2}{2A_1}\left(\frac{k_1^2}{k_2}+k_2\right)+k_2 A_1 p_1+\frac{\rho_b Q_1^2}{2A_1}k_1\left(k_1-2\right)\cos\theta \tag{8.12}$$

On normalizing the tensile far-field force in the direction of the graft by $\rho_b Q_1^2 / 2A_1$, Equation (8.12) takes the form

$$\frac{R_\theta}{\frac{\rho_b Q_1^2}{2A_1}} = \frac{k_1^2}{k_2} + k_2 + k_2 \frac{2A_1^2 p_1}{\rho_b Q_1^2} + k_1 (k_1 - 2)\cos\theta \tag{8.13}$$

The dimensionless ratio k_1 typically varies between 0 and 1, and the dimensionless ratio k_2 varies between 0.2 and 1. For large- and medium-size arteries under pressure, the expression $2A_1^2 p_1 / \rho_b Q_1^2$ typically varies between 340 and 3400. Therefore, R_θ can be approximated by

$$R_\theta \approx A_2 p_1 \tag{8.14}$$

In the case of veins, in which the blood pressure is low, R_θ may be approximated by

$$R_\theta \approx \frac{\rho_b Q_1^2}{2A_1}\left[\frac{k_1^2}{k_2} + k_2 + k_1 (k_1 - 2)\cos\theta\right] \tag{8.15}$$

In addition, longitudinal residual stresses may exist along the host-artery. The longitudinal residual force N_{res} (Figure 8-4(b)) is usually taken into account as a strain percentage, which is about 10-30% of the unstressed artery length. In this chapter, the effect of the residual force N_{res} is ignored, since it does not affect considerably the suture-line response of an end-to-side anastomosis and has not been taken into consideration in relatively recent investigations [12].

8.4 Stress-concentration factors (SCF)

The local stresses of the junction can be obtained from the stress-concentration methodology, utilized in the analysis of K- and Y-joints of circular hollow pipe sections. Specifically, the local stress acting at any point of the artery-graft intersection zone is calculated from the axial tensile stress (of the applied load R_θ) and the SCF. The SCF applies on the tensile force (due to pressure and hydrodynamic effects) in the direction of the graft, which in turn affects the loading of the sutures. The axial tensile stress along the graft is

$$\sigma_{22} = \frac{R_\theta}{2\pi R_g H_g} \tag{8.16}$$

in which R_g is the mean radius of the graft. Therefore, the local stresses at the stitching zone of the artery and graft side are expressed respectively as

$$\sigma_a^{local} = \mathrm{SCF}_a \sigma_{22} \tag{8.17}$$

$$\sigma_g^{local} = \mathrm{SCF}_g \sigma_{22} \tag{8.18}$$

where SCF_a and SCF_g are the stress-concentration factors corresponding to the artery and graft side, respectively.

The most representative SCF prediction studies in the literature are: (1) the method adopted by the American Welding Society [96] and American Petroleum Institute [95]; (2) the work of Shao et al. [99]; and (3) the work of Karamanos et al. [100]. The SCF equations were obtained from parametric investigations based on a large number of finite-element analyses and experiments, for specific ranges of the normalized geometric parameters

$$\beta = R_g^o / R_a^o,\ \gamma = R_a^o / H_a,\ \tau = H_g / H_a \tag{8.19}$$

Herein, we adopt the parametric SCF equations of the first two methodologies. The American Welding Society and the American Petroleum Institute SCFs for the artery and graft are expressed respectively as

$$\mathrm{SCF}_a^{(1)} = 2.16\tau \sin\theta \sqrt{\gamma} \tag{8.20}$$

$$\mathrm{SCF}_g^{(1)} = 1.375 + 0.375\sqrt{\tau/\beta}\,\mathrm{SCF}_a^{(1)} \tag{8.21}$$

Shao et al. proposed a SCF solution for all values of $\varphi \in [0, 2\pi]$ along the juncture line (Figure 8-1(b)). According to their solution, the general parametric SCF equations for the artery and graft are expressed respectively as

$$\mathrm{SCF}_a^{(2)} = C_0 + C_1 \cos\varphi + C_2 \cos(2\varphi), \quad 0 \le \varphi \le 2\pi \tag{8.22}$$

$$\mathrm{SCF}_g^{(2)} = C_0 + C_1 \cos\varphi + C_2 \cos(2\varphi) + C_3 \cos(3\varphi) + C_4 \cos(4\varphi),\ 0 \le \varphi \le 2\pi \tag{8.23}$$

in which the coefficients C_i are functions of parameters τ, β, γ, θ. The reader is referred to the original paper of Shao et al. [99] for the complete forms of C_i's. To obtain

the SCF value for the crown toe (CT in Figure 8-1), φ must be set equal to π, and for the crown heel (CH in Figure 8-1), φ must be set equal to zero. Shao et al. found that the maximum SCFs, for axial loading in the direction of the graft are usually located at the crown toe.

Figures 8-5 through 8-7 plot the SCF curves according to Equations (8.20) through (8.23), for $\varphi = \pi$ (crown toe) and for different values of the dimensionless ratios τ, β, γ. Observe that the SCFs for the artery side are frequently higher than the SCFs for the graft side. Furthermore, for low values of anastomosis angle ($\theta < 20^\circ$) the SCF is always lower than 2.7, whereas for large anastomosis angles ($\theta > 60^\circ$) the SCF is larger than 3, regardless of the adopted prediction. The points marked by dots in Figures 8-5 through 8-7 indicate the intersecting angle θ for which the artery and graft SCFs are equal, for the pair of equations of the American Welding Society and the pair of equations of Shao et al. The artery and graft SCFs are equal for intersecting angle θ in the range 10° to 30°. This result implies equal stress amplifications for the graft and the artery side, which could lead to evenly-distributed hyperplasia.

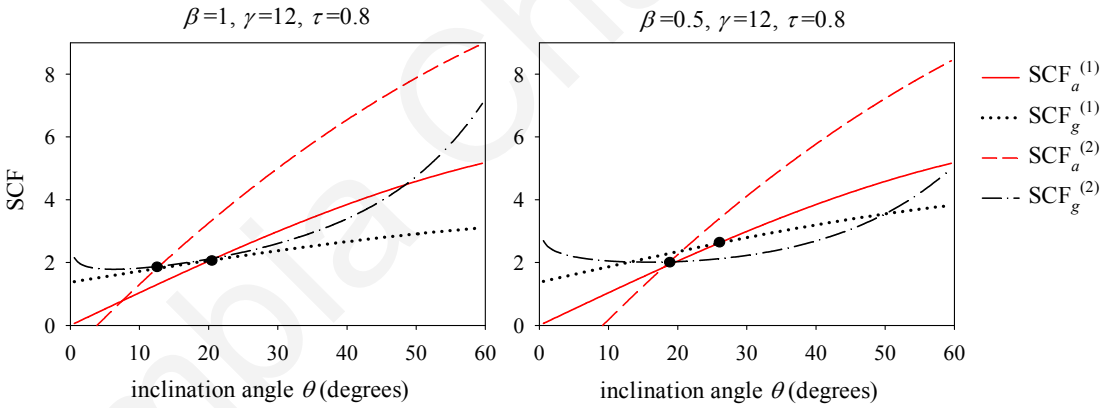

Figure 8-5: Stress-concentration factors for the artery and graft for different values of the graft-to-artery radii ratio: (a) $\beta = 1$, (b) $\beta = 0.5$.

8.5 Suture-line response

As discussed in Section 7.2.1, for the case of end-to-end anastomosis, the interaction of sutures with the blood vessels may lead to post-surgery complications in a number of ways. Correspondingly, post-surgery complications may occur in the case of end-to side anastomosis. The suture may fail when its maximum tensile force f_s exceeds its tensile strength, or lead to slip or relaxation of the knots that bind the stitches together. Note that,

sutures may creep and gradually deteriorate with time and potentially fail some weeks after the operation. Furthermore, the blood vessel wall may rupture and injury may be caused when the embedding stresses σ_s due to suture-wall contact interaction (at the stitching holes) exceed the limit value of wall shear strength. High-stress values is one of many factors that promote the generation of intimal hyperplasia and cause the arterial wall to increase its cross-section [10]. Yet another complication may be caused due to large deformations at the suture line, which in turn may cause blood leak or reduction of the artery-graft intersecting angle at the anastomosis area.

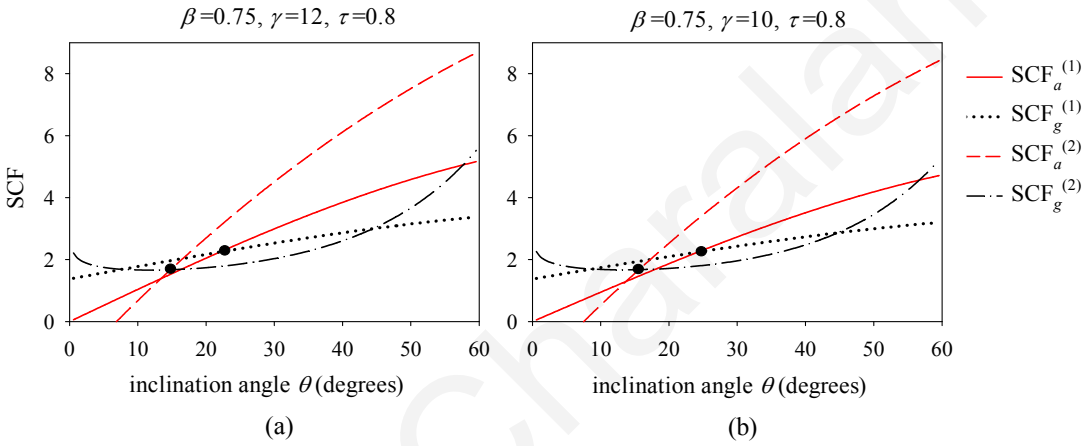

Figure 8-6: Stress-concentration factors for the artery and graft for different values of the artery radius to artery thickness ratio: (a) $\gamma = 12$, (b) $\gamma = 10$.

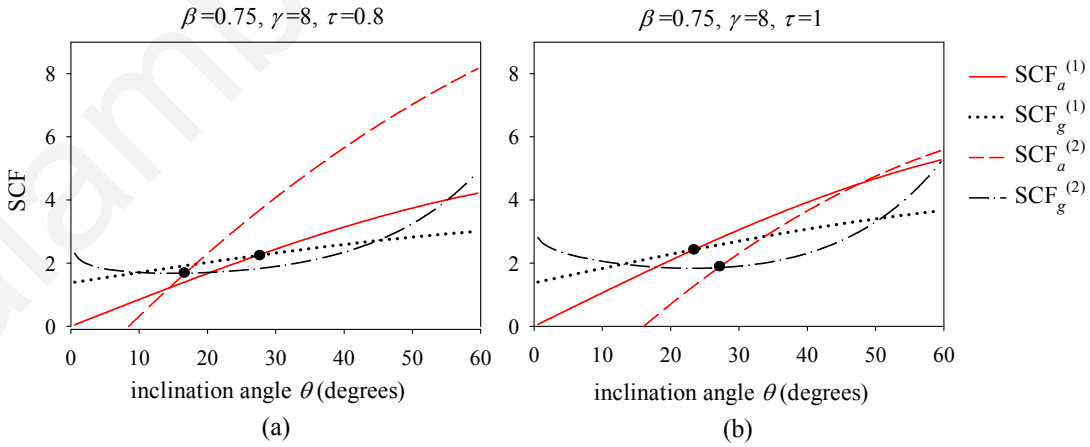

Figure 8-7: Stress-concentration factors for the artery and graft for different values of graft-to-artery thicknesses ratio: (a) $\tau = 0.8$, (b) $\tau = 1$.

For the suture-line analysis we consider two different models. The interrupted stitching or interrupted vascular clips model (Figure 8-8(a)), and the continuous (running) stitching with diagonal at 45° angle model (Figure 8-8(b)).

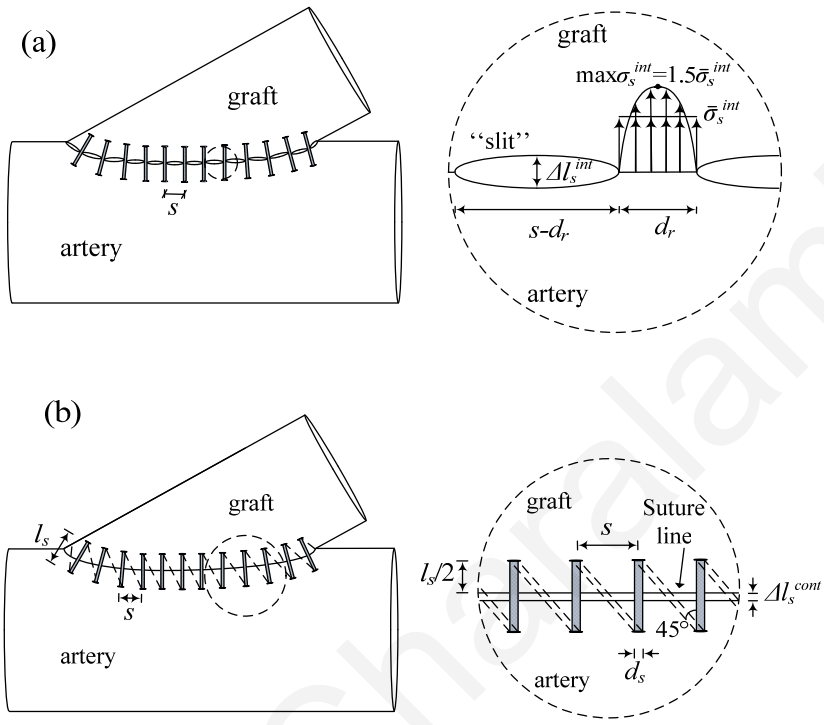

Figure 8-8: (a) Interrupted stitching or clips model of an end-to-side anastomosis. The insert on the right shows a detail of the suture-line opening, Δl_s^{int}, and stress distribution, σ_s^{int}; (b) Continuous stitching model of end-to-side anastomosis. The insert on the right shows a detail of the suture-line opening, Δl_s^{cont}.

In the case of interrupted stitches or clips, the suture is assumed to be rigid and the suture line can be approximated as a solid surface with cracks (microslits). The cracks are located between the sutures or clips. Figure 8-8(a) shows the approximate stress distribution of σ_s^{int} along the clip thickness, which is distributed parabolically according to the smooth contact solution of Hertz [101], with the maximum embedding stress obtained as

$$\max \sigma_s^{int} = 1.5\bar{\sigma}_s^{int} \tag{8.24}$$

in which $\bar{\sigma}_s^{int}$ is the peak average embedding stress at the stitching hole of an interrupted stitch or vascular clip. The peak average embedding stress is calculated as

$$\bar{\sigma}_s^{int} = \max\left\{ \frac{\sigma_a^{local} s H_a}{d_r \min\{H_a, H_g\}},\ \frac{\sigma_g^{local} s H_g}{d_r \min\{H_a, H_g\}} \right\} \tag{8.25}$$

where d_r denotes the suture diameter or the clip thickness and s denotes the distance between two sequential stitches. When dividing with the artery thickness H_a we get the average embedding stress at the artery, whereas by dividing with the graft thickness H_g we get the average embedding stress at the graft.

For systems with considerable stiffness (i.e. artery-artificial graft anastomosis), the fracture mechanics theory [102] can be applied to calculate the maximum opening of the anastomosis interface as a crack opening problem, leading to the approximation

$$\Delta l_s^{int} \approx \max\left\{ \sigma_a^{local}(s - d_r)\left(\frac{1}{E_a} + \frac{1}{E_g}\right),\ \sigma_g^{local}(s - d_r)\left(\frac{1}{E_a} + \frac{1}{E_g}\right) \right\} \tag{8.26}$$

in which E_a and E_g are the Young's modulus of the artery and graft, respectively.

In the case of continuous stitching with diagonal at 45° angle (Figure 8-8(b)), the uniform tensile force of the suture depends on the maximum local stress of the artery or graft side:

$$f_s^{cont} = \max\left\{ \frac{\sigma_a^{local} s H_a}{1.7} + f_s^0,\ \frac{\sigma_g^{local} s H_g}{1.7} + f_s^0 \right\} \tag{8.27}$$

where *s* is the distance between two sequential stitches, and f_s^0 is the suture pre-tensioning exerted by the surgeon in tying the suture knot. The peak embedding stress, due to suture-wall contact interaction at the stitching holes, takes the form

$$\sigma_s^{cont} = \max\left\{ \frac{\sigma_a^{local} s H_a + 1.7 f_s^0}{d_s \min\{H_a, H_g\}},\ \frac{\sigma_g^{local} s H_g + 1.7 f_s^0}{d_s \min\{H_a, H_g\}} \right\} \tag{8.28}$$

in which d_s is the suture diameter. By dividing with the artery thickness H_a we obtain the peak embedding stress at the artery, whereas by dividing with the graft thickness H_g we obtain the peak embedding stress at the graft. The gap created between the two blood vessels, according to Hooke's law, is obtained as

$$\Delta l_s^{cont} = \begin{cases} \dfrac{4l_s}{\pi d_s^2 E_s} \max\left\{ \dfrac{\sigma_a^{local} sH_a}{1.7} - f_s^0,\ \dfrac{\sigma_g^{local} sH_g}{1.7} - f_s^0 \right\} \\ \qquad\qquad , \text{for } \max\left\{ \dfrac{\sigma_a^{local} sH_a}{1.7},\ \dfrac{\sigma_g^{local} sH_g}{1.7} \right\} > f_s^0 \\ 0 \qquad\qquad , \text{for } \max\left\{ \dfrac{\sigma_a^{local} sH_a}{1.7},\ \dfrac{\sigma_g^{local} sH_g}{1.7} \right\} \le f_s^0 \end{cases} \quad (8.29)$$

in which l_s denotes the stitch length and E_s denotes the Young's modulus of the suture. A gap between the two blood vessels will be formed only if the suture tensile force caused by the blood pressure exceeds the pre-tension value.

Note that, this analysis investigates the conservative scenario of the typical stitches/clips technique. Parameters that may decrease the suture-line response are ignored. For example, days, weeks, and months after the anastomosis is carried out, tissue is formed around the suture line, resulting in increased local curvature/intersecting angle of the junction (Figure 8-9). The decrease of the sharpness of the suture line results to smaller stress concentration and increased strength of the anastomosis. In addition, reinforcement of the suture line by pledgeted sutures or other techniques decreases the risk of post-surgery complications because the tearing stresses from the tension of the sutures are decreased.

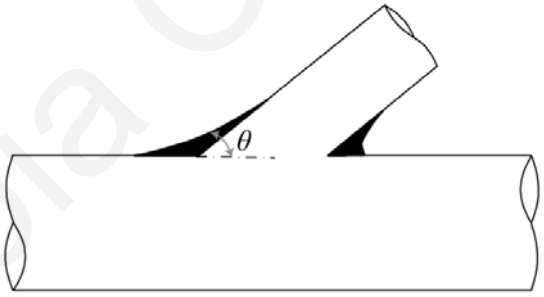

Figure 8-9: The formation of tissue around the suture line (black areas), weeks and months after the anastomosis is carried out, results in increased local curvature/intersecting angle θ of the junction.

8.6 Comparison with finite-element studies

The proposed methodology is compared against the finite-element studies of Ballyk et al. [10], Perktold et al. [12] and Thubrikar et al. [97]. In order to obtain comparable response values for the first two studies, we calculated the normalized mean stress and the principal stress concentration based on the proposed SCFs, respectively.

Ballyk et al. [10] simulated an end-to-side artery-Dacron graft anastomosis with identical geometric properties (Table 8-2). Their model clearly shows that the three-dimensional line formed by the intersection of the two blood vessels has sharp edges, as indicated also in Figures 8-2 and 8-3 (for $H_g / H_a = 1$). The sutures were modeled as points along the intersection curve resulting in excessive stress concentrations. The hoop stress at the graft, derived from Laplace's law, is $\sigma_{\theta\theta} = p_1 R_g / H_g$. In their work, Ballyk et al. calculated the normalized mean stress as $(\sigma_{local} + \sigma_{\theta\theta}) / (2p_1)$, and found that the maximum mean stresses for the artery and graft, just away from the suture, are 8 and 6 respectively. Table 8-3 reports values for the far-field stress and the SCF based on the model proposed in this chapter, and compares the calculated normalized mean stress with that reported in Ballyk et al. Our calculations of the normalized mean stress are in good agreement with their results.

Table 8-2: Parameters of end-to-side model of Ballyk et al.

Parameter	Value
p_1 (kPa)	13.3
θ (degrees)	45
R_a^o (mm)	2.75
R_g^o (mm)	2.75
H_a (mm)	0.5
H_g (mm)	0.5
$\beta = R_g^o / R_a^o$	1
$\gamma = R_a^o / H_a$	5.5
$\tau = H_g / H_a$	1
E_a / E_g	3.14-1.33
N_{res} (N)	0.19

Table 8-3: Results of the proposed methodology against the Ballyk et al. analysis.

Results		
	This study	Ballyk et al.
$R_\theta = A_2 p_1$ (N)	0.26	(NA)
σ_{22} (kPa)	33.32	(NA)
$\sigma_{\theta\theta}$ (kPa)	66.65	(NA)
$SCF_\alpha^{(1)}$	3.58	(NA)
$SCF_g^{(1)}$	2.72	(NA)
$SCF_\alpha^{(2)}$	4.23	(NA)
$SCF_g^{(2)}$	3.50	(NA)
Normalized mean stress		
$(SCF_a^{(1)}\sigma_{22} + \sigma_{\theta\theta}) / (2p_1)$	6.97	8
$(SCF_g^{(1)}\sigma_{22} + \sigma_{\theta\theta}) / (2p_1)$	5.90	6
$(SCF_a^{(2)}\sigma_{22} + \sigma_{\theta\theta}) / (2p_1)$	7.79	8
$(SCF_g^{(2)}\sigma_{22} + \sigma_{\theta\theta}) / (2p_1)$	6.87	6

In another finite-element study, Perktold et al. [12] modeled an end-to-side artery/ePTFE conventional anastomosis and a Taylor-patch anastomosis with the parameters reported in Table 8-4. Perktold et al. calculated the principal stress concentration normalized by the average principal stress of the artery as $\sigma^{local} / \sigma_{ave} = \sigma^{local} 2H_a / p_1(R_\alpha^o - \mathrm{H}_a / 2)$. For the conventional and the Taylor-patch anastomosis, the normalized maximum and minimum principal stress concentration were calculated as 4.7 and 0.7, respectively. Table 8-5 presents the far-field stress and the SCFs as proposed by this study, the principal stress-concentration calculations, as well as the suture-line response. By using the SCF of Shao et al., we obtain a realistic maximum response corresponding to the principal stress concentration of the artery equal to 4.55, which compares well with the respective result of Perktold et al. ($=4.7$). The minimum SCF for the artery, according to the plots presented by Shao et al., occurs at the crown heel and can be found by scaling the maximum SCF by a factor of 1/6. Therefore, the scaled principal stress concentration is 0.76, which is a good approximation of the finite-element result ($=0.7$). It should be noted that Perktold et al. found that the stress concentration of these models does not occur at the toe, due to the

irregular geometries of the blood vessels. However, the SCFs as proposed by this study constitute a good approximation of the maximum and minimum values.

Table 8-4: Parameters of end-to-side model of Perktold et al.

Parameter	Value	Parameter	Value
Artery/graft		*Interrupted clips*	
p_1 (kPa)	13.3	d_r (mm)	0.34
θ (degrees)	25	s (mm)	1.02
R_a^o (mm)	2.15-2.25	*Continuous stitches*	
R_g^o (mm)	2.075-2.175	d_s (mm)	0.093
H_a (mm)	0.5	s (mm)	1
H_g (mm)	0.35	l_s (mm)	1
$\beta = R_g^o / R_a^o$	0.97	E_s (GPa)	1.44
$\gamma = R_a^o / H_a$	4.5		
$\tau = H_g / H_a$	0.7		
E_a (kPa)	410		
E_g (kPa)	7500		
N_{res} (N)	0		

Perktold et al. [12] also studied the individual suture response of two different models: a model with interrupted vascular clips and a model with continuous stitching. The clips/stitch properties are reported in Table 8-4, and the suture-line response of the proposed methodology against the Perktold et al. analysis is listed in Table 8-5. In the case of the interrupted-clips model, the maximum embedding stress is calculated by the present study as 760 kPa (Equation (8.24)) and the opening created between the two vessels is calculated as 206 μm (Equation (8.26)). The opening is considered to be excessive and blood leakage is induced (the opening is larger than the sum of diameters of three red blood cells: 206 μm > 21 μm). In the case of the continuous-stitching model, the suture tensile force, by assuming zero suture pre-tension, is derived from the maximum SCF of Shao et al. as 0.034 N (Equation (8.27)). As expected, this value does not compare well with the corresponding value obtained in the work of Perktold et al. since they modeled the stitching of the saddle region only. In order to obtain a better approximation against their work, we calculated a hypothetical value of the tensile force by using the SCF for the

saddle. The hypothetical tensile force is 0.005 N. Additionally, the gap between the two blood vessels, for the continuous stitching case, is calculated as 3.51 μm in the present study (Equation (8.29)). According to these calculations, we can conclude that the finite-element results (related to the interrupted-model embedding stress and the continuous-model suture force) compare well with the formulas suggested in this chapter based on the SCFs (Table 8-5).

Table 8-5: Results of the proposed methodology against the Perktold et al. analysis.

	This study	Perktold et al.
$R_\theta = A_2 p_1$ (N)	0.16	(NA)
σ_{22} (kPa)	37.31	(NA)
$\sigma_{\theta\theta}$ (kPa)	26.00	(NA)
$\mathrm{SCF}_\alpha^{(1)}$	1.35	(NA)
$\mathrm{SCF}_g^{(1)}$	1.81	(NA)
$\mathrm{SCF}_\alpha^{(2)}$	3.17	(NA)
$\mathrm{SCF}_g^{(2)}$	2.11	(NA)
Principal stress concentration		
$\mathrm{SCF}_a^{(1)}\sigma_{22} / \sigma_{ave}$	1.94	4.7
$\mathrm{SCF}_g^{(1)}\sigma_{22} / \sigma_{ave}$	2.60	(NA)
$\mathrm{SCF}_a^{(2)}\sigma_{22} / \sigma_{ave}$	4.55	4.7
$\mathrm{SCF}_g^{(2)}\sigma_{22} / \sigma_{ave}$	3.03	(NA)
Suture-line response (Interrupted clips)		
$\max \sigma_s^{\mathrm{int}}$ (kPa)	760	700
$\Delta l_s^{\mathrm{int}}$ (μm)	206	(NA)
Suture-line response (Continuous stitches)		
f_s^{cont} (N)	0.034 (realistic), 0.005 (hypothetical)	0.008-0.017 (saddle)
Δl_s^{cont} (μm)	3.51	(NA)

The proposed stress-concentration methodology can be as well utilized to easily obtain the maximum stress of arterial branches. Thubrikar et al. [97] studied the stress concentrations of a bovine coronary arterial branch with inclination angle 70°. The parameters of the arterial branch are reported in Table 8-6.

Table 8-7 lists the stress-concentration results of our study and of the study of Thubricar et al. The SCFs, as calculated by this study, are 5.36 and 3.78 for the main artery and branch, respectively, resulting in maximum stresses $\sigma_a^{local} = 116$ kPa and $\sigma_g^{local} = 82$ kPa at the artery and branch side, respectively. Our stress-concentration results compare well with the finite-element results of Thubrikar et al. (113 kPa and 90 kPa for the artery and branch side, respectively).

Table 8-6: Parameters of arterial branch model of Thubrikar et al.

Parameter	Value
p_1 (kPa)	5.33
θ (degrees)	70
R_a^o (mm)	4.46
R_g^o (mm)	2.33
H_a (mm)	0.36
H_g (mm)	0.27
$\beta = R_g^o / R_a^o$	0.5224
$\gamma = R_a^o / H_a$	12.39
$\tau = H_g / H_a$	0.75
N_{res} (N)	0

Table 8-7: Results of the proposed methodology against the Thubrikar et al. analysis.

	Results	
	This study	Thubrikar et al.
σ_{22} (kPa)	21.67	(NA)
$SCF_a^{(1)}$	5.36	(NA)
$SCF_g^{(1)}$	3.78	(NA)
σ_a^{local} (kPa)	82	90
σ_g^{local} (kPa)	116	113

8.7 Numerical example related to PTFE venous access graft

Ngoepe et al. [15] studied the case of arterio-venous access grafts, by utilizing finite-element analysis. Such anastomoses are performed in the case of patients undergoing hemodialysis. Herein, we investigate the response of vein/PTFE access grafts, forming end-to-side anastomosis configurations with 45° and 90° intersection angles. Ngoepe et al. found that the maximum structural wall stress at the junction of the venous anastomosis is equal to 3.36 kPa, and that the 90° configuration shows slightly better performance than the 45° configuration.

The parameters used in our analysis are listed in Table 8-8. For the calculation of the far-field forces Equations (8.7) through (8.9) are utilized. Note that, the inertia terms (flow velocity terms) are insignificant compared to the pressure terms, and therefore are neglected.

Table 8-8: Parameters of Vein/PTFE access graft models of Ngoepe et al.

Parameter	Value	
	$\theta = 90^{\circ}$	$\theta = 45^{\circ}$
p_1 (kPa)	24.2	14.4
p_2 (kPa)	21.8	6.48
p_3 (kPa)	1.21	0.72
V_1 (m/s)	0.06	0.07
V_2 (m/s)	0.02	0.025
V_3 (m/s)	0.0886	0.0847
R_a^o (mm)	3	3
R_g^o (mm)	3	3
H_a (mm)	1	1
H_g (mm)	1	1
ρ_b (Kg/m^3)	1050	1050
$\beta = R_g^o / R_a^o$	1	1
$\gamma = R_a^o / H_a$	1	1
$\tau = H_g / H_a$	2	2

Table 8-9: Results of the proposed methodology for the access graft models of Ngoepe et al.

	Value	
	$\theta = 90^\circ$	$\theta = 45^\circ$
R_x (N)	-0.180	-0.325
R_y (N)	0.357	0.154
R_θ (N)	0.125	0.154
$\sigma_{\theta\theta 1}$ (kPa)	66.55	39.6
$\sigma_{\theta\theta 2}$ (kPa)	59.95	17.82
$\sigma_{\theta\theta 3}$ (kPa)	3.33	1.98
σ_{22} (kPa)	7.27	8.91
$\mathrm{SCF}_a^{(1)}$	2.64	3.74
$\mathrm{SCF}_g^{(1)}$	2.37	2.78
σ_a^{local} (kPa)	19.18	33.32
σ_g^{local} (kPa)	17.22	24.77

8.8 Concluding Remarks

This chapter proposes a systematic stress-concentration methodology for the prediction of the stress distribution at the junction line of the end-to-side anastomosis and end-to-side arterial branches. Closed-form expressions were derived for calculating the embedding stress (Equations (8.24) and (8.28)), the gap formed between the two blood vessels (Equations (8.26) and (8.29)), and the suture tensile force for the continuous stitching model (Equation (8.27)). Furthermore, expressions for the calculation of the suture-line length S (Equation (8.4)) and the approximate suture length ($S\left(\sqrt{2}+1\right)$) are introduced.

Although the proposed model constitutes an idealized approach of the end-to-side anastomosis problem, the results of the proposed methodology are a good approximation of the response of more complex models. For example, the results of finite-element studies with geometrical asymmetries and irregular flow conditions, such as the study of Perktold et al. [12], are approximated well by our model (which assumes that the cross-sectional dimensions of the artery and graft are circular and that the blood flow is steady). On the

other hand, the elastic modulus of the graft must not be much lower than the elastic modulus of the artery. The reason is that the less stiff graft will be excessively deformed at the junction, rendering the proposed model invalid. This has been shown by Hofer et al. [9]. For the case of a stiff graft (10 times stiffer than the artery), their finite-element solution close to the artery-graft junction shows a maximum stress of 300 kPa at the artery side. Our model predicts a maximum local stress of 282 kPa. However, for a graft that is less stiff than the artery, the stress is significantly reduced to 80 kPa.

The problem is mainly affected by the intersecting angle between the artery and the graft, the radii and thicknesses of the artery and graft, the blood pressure, and the suturing characteristics. The SCF investigation demonstrated that lower values of the graft-to-artery radii ratio R_g^o / R_a^o, the graft-to-artery thicknesses ratio H_g / H_a, and the ratio of artery radius to artery thickness R_a^o / H_a frequently decrease the SCFs (Figures 8-5 through 8-7). Moreover, the range of anastomosis angle θ for which the artery and graft SCFs are equal lies between 10° and 30°. Although low values of anastomosis angle θ typically reduce the SCF (and consequently reduce the suture-line opening, the embedding stress, and the suture force), they require longer suture lines and larger number of stitches, which is a potential source of fluid disturbance [103].

The suture-line response is calculated by Equations (8.24) through (8.29). These expressions highlight the influence of the suturing parameters on the suture-line response. For a given end-to-side anastomosis configuration, when the distance between two sequential stitches is decreased (meaning that the number of stitches is increased) or the stitch diameter/thickness is increased, the embedding stress and the gap created between the two blood vessels are decreased, regardless of the adopted stitching technique. In the case of the continuous stitching technique, it can be observed that when stronger sutures are used the gap developed between the two blood vessels is decreased. In regard to the suture tensile force, it can be shown that it is increased as the distance between two sequential stitches is increased. Furthermore, the interrupted-stitching technique is more compliant at the anastomosis than the continuous-stitching technique, as suggested by the literature [104].

In the case that pre-tension is applied to the suture, the knot strength, the suture tensile force, and the embedding stress are increased. Note that a gap between the two blood vessels will be formed only if the suture tensile force due to blood pressure exceeds the pre-tension value.

Accordingly, this chapter suggests the following practical techniques to minimize the risk of post-surgery complications: (a) longer suture lines (low values of anastomosis angle θ); (b) suture/clip thickness as large as possible; (c) number of stitches as high as possible (i.e. distance between sequential stitches as low as possible); (d) graft radius smaller than the artery radius; and (e) pre-tension of the suture as low as possible (merely to secure the strength of the knot).

The proposed methodology, as a design-oriented approach, can be synopsized in the following steps:

a) The tensile far-field force in the direction of the graft R_θ and the axial tensile stress along the graft σ_{22} are calculated from Equations (8.14) and (8.16), respectively.
b) The local stresses at the stitching zone of the artery and graft side (Equations (8.17) and (8.18)) are obtained by using the parametric SCF Equations of Shao et al. for $\varphi=\pi$ (Equations (8.22) and (8.23)).
c) The individual suture response in terms of embedding stress, the gap created between the two blood vessels and the suture tensile force, is calculated from Equations (8.24) through (8.29).
d) The individual suture response results must be compared to the respective limit values as specified in Section 7.2.1. In the case that the limit values are exceeded, the intersecting angle θ and/or the stitching parameters must be reconsidered and steps (a) through (d) must be repeated.

Note that, in order to predict the stress concentration of arterial branches only steps (a) and (b) are required.

By utilizing the aforementioned design-oriented approach, the optimum suturing parameters and anastomosis angle can be selected.

CHAPTER 9

Response of Side-to-side Related Anastomosis and Artery Patching

9.1 Introduction

The long-term complications of side-to-side related anastomoses (i.e. end-to-side and side-to-side anastomosis) and artery patching, primarily involve the development of intimal hyperplasia that results in stenosis of the blood-vessel lumen. Several factors, such as arterial wall mechanics, hemodynamics effects, biological activities and compliance between the host artery and the graft are identified to influence the problem. Yet, it is not completely clear which are the factors that influence most the long-term complications and in what specific way.

Special attention has been given to the effect of elastic (compliance) mismatch between the graft and the host artery. Better compliance may be obtained by using grafts with similar mechanical properties to the host artery or by anastomosis techniques that utilize vein patches and cuffs. Recent end-to-side anastomosis techniques that use "compliant" patches or cuffs, are the Taylor-patch anastomosis and Miller-cuff anastomosis. Studies suggest that these techniques may reduce the stress concentrations at the suture line, and therefore the generation of intimal hyperplasia [11, 12].

An end-to-side anastomosis develops intimal hyperplasia at two regions of the anastomosis: the suture line and the artery floor opposite of the distal anastomosis [10, 23]. Bassiouny et al. [23] found that the development of intimal hyperplasia at the suture line of conventional end-to-side anastomosis is promoted by healing mechanisms, compliance mismatch and triangulation of the anastomotic junction that may result in complex hemodynamic patterns. They also suggested that intimal hyperplasia on the artery floor is developed due to low wall shear stresses and hemodynamic factors that generate stagnation points at that region. Note that, our study does not deal with the hemodynamic analysis and flow patterns of side-to-side related anastomosis. It focuses on the suture-line behavior in terms of displacements, strains, and stress concentration.

To identify the problem of side-to-side related anastomosis by means of stress concentration, it must be noted that the local stress concentration of an arterial branch (referring to a branch that was not surgically formed) is primarily affected by the geometry of the junction [97]. In the case of anastomosis, the junction is additionally stressed due to the suture-arterial tissue contact at the stitching holes. As concluded in Chapter 8, the average embedding stresses, at the stitching holes, increase when the distance between

sequential stitches is increased and/or the suture diameter is decreased. The study presented in this chapter aims to investigate if the elastic mismatch constitutes a third factor for further stress concentration at the suture line, thus influencing the development of intimal hyperplasia.

An idealized circular cylindrical anastomosis model consisting of two semi-cylinders, interconnected by two hinges is considered, in order to study the influence of elastic mismatch on the problem. The solution is obtained by solving a boundary value problem. The resulting system response is described in terms of internal forces, radial and tangential displacements, strains of the blood vessels, and the rotation angle of each cross-section. The dynamic response of the model is also examined in order to evaluate if the effect of the dynamic component is significant and must be taken into consideration.

9.2 Mathematical model

Figure 9-1 shows the three end-to-side anastomoses and the side-to-side anastomosis techniques that can be analyzed by the proposed method. End-to-side anastomosis techniques include the conventional anastomosis, the Taylor-patch anastomosis, and the Miller-cuff anastomosis [12, 11, 23, 10, 24, 25, 105].

By considering a vertical plane section in the end-to-side or side-to-side anastomosis of Figure 9-1, the resulting system can be approximated by a two-hinged circular model, consisting of two semicircles with different elasticity modulus, cross-sectional areas and moments of inertia. The proposed mathematical model consists of element I representing the graft that is connected to the artery side, and element II representing the host artery (Figure 9-2(a)). Element I has thickness t^{I}, cross-sectional area A^{I} (per unit-length), Young's modulus E^{I}, and moment of inertia I^{I} (per unit-length), whereas element II has thickness t^{II}, cross-sectional area A^{II} (per unit-length), Young's modulus E^{II}, and moment of inertia I^{II} (per unit-length). The unloaded centerline of the two elements is assumed to form a circle with radius *R*, and the sutures are modeled by two hinges that separate the centerline into two semicircles. The origin of the varying angles of each element are shown in Figure 9-2(a). The varying angles fall in the range $0 \le \theta^{\mathrm{I}} \le \pi$ and $-\pi/2 \le \theta^{\mathrm{II}} \le \pi/2$ for the graft and artery, respectively. When subjected to uniform internal pressure p, the system is deformed in the radial direction by $u^i(\theta^i)$ and in the tangential direction by $w^i(\theta^i)$. Note that, notation i takes the form I or II when referring to elements I and II respectively.

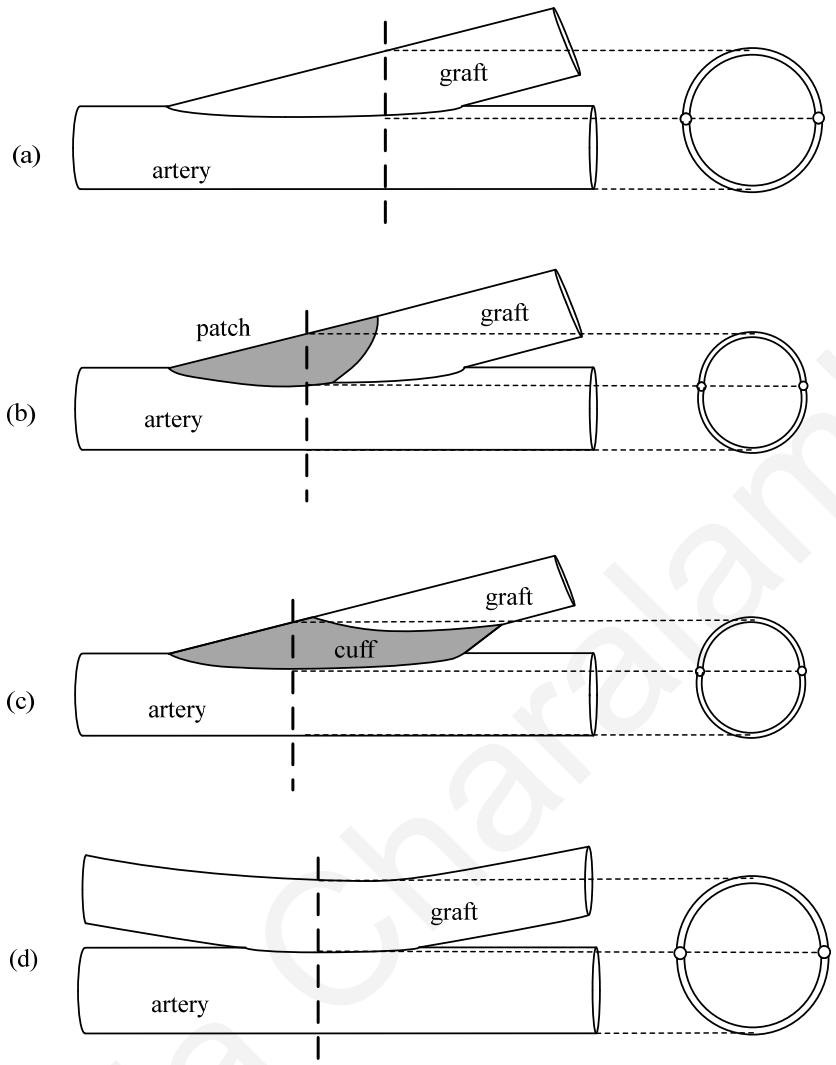

Figure 9-1: Vertical plane sections of different anastomosis techniques that can be modeled as two-hinged circular systems: (a) conventional end-to-side anastomosis; (b) Taylor-patch anastomosis; (c) Miller-cuff anastomosis; (d) side-to-side anastomosis.

9.2.1 Response to static loading

The problem can be solved as a boundary-value problem of continuous curved beams [106, 107]. The differential equations governing the static response of the system are derived by considering the equilibrium of forces acting on an infinitesimal element of the circular ring shown in Figure 9-2(b), where $N^i(\theta^i)$ is the unit-length tangential tensile force, $Q^i(\theta^i)$ is the unit-length shear force, and $M^i(\theta^i)$ is the unit-length in-plane bending moment. The equilibrium of forces along the radial and tangential directions result in the following expressions, respectively

$$\frac{dQ^i(\theta^i)}{d\theta^i} - N^i(\theta^i) = -pR \tag{9.1}$$

$$\frac{dN^i(\theta^i)}{d\theta^i} + Q^i(\theta^i) = 0 \tag{9.2}$$

Moreover, the moment equilibrium of the infinitesimal element of Figure 9-2(b) requires that:

$$\frac{dM^i(\theta^i)}{d\theta^i} - RQ^i(\theta^i) = 0 \tag{9.3}$$

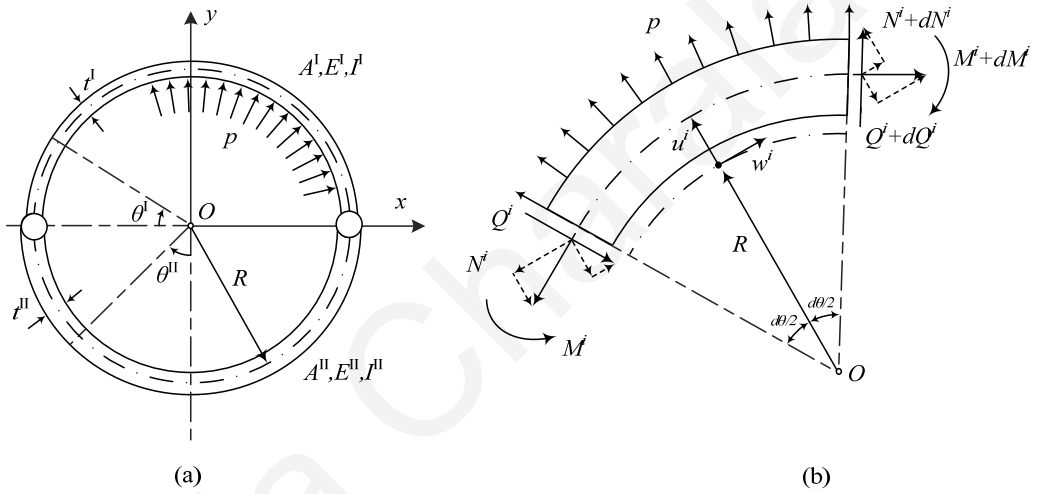

Figure 9-2: (a) Two-hinged anastomosis model, (b) Free-body diagram of a typical element of circular sector under static loading.

By assuming extensibility of the centerline, the tangential force $N^i(\theta^i)$ and moment $M^i(\theta^i)$ can be expressed in terms of displacements as

$$M^i(\theta^i) = \frac{E^i I^i}{R^2}\left(\frac{dw^i(\theta^i)}{d\theta^i} - \frac{d^2u^i(\theta^i)}{d\theta^{i2}}\right) \tag{9.4}$$

$$N^i(\theta^i) = \frac{E^i A^i}{R}\left(u^i(\theta^i) + \frac{dw^i(\theta^i)}{d\theta^i}\right) \tag{9.5}$$

The symmetric boundary conditions of elements I and II are respectively

$$M^{\mathrm{I}}(0)=0,\ w^{\mathrm{I}}(0)=0,\ w^{\mathrm{I}}\left(\frac{\pi}{2}\right)=0,\ \frac{du^{\mathrm{I}}}{d\theta}\left(\frac{\pi}{2}\right)=0,\ Q^{\mathrm{I}}\left(\frac{\pi}{2}\right)=0 \tag{9.6}$$

$$M^{\mathrm{II}}\left(\frac{\pi}{2}\right)=0,\ w^{\mathrm{II}}\left(\frac{\pi}{2}\right)=0,\ w^{\mathrm{II}}(0)=0,\ \frac{du^{\mathrm{II}}}{d\theta}(0)=0,\ Q^{\mathrm{II}}(0)=0 \tag{9.7}$$

and the continuity equations between the two elements are expressed as

$$N^{\mathrm{I}}(0)=N^{\mathrm{II}}\left(\frac{\pi}{2}\right),\ Q^{\mathrm{I}}(0)=Q^{\mathrm{II}}\left(\frac{\pi}{2}\right),\ u^{\mathrm{I}}(0)=u^{\mathrm{II}}\left(\frac{\pi}{2}\right) \tag{9.8}$$

By combining Equations (9.1) through (9.8), the response of the two elements in terms of axial forces, shear forces, moments, radial and tangential displacements can be derived. For element I ($0\le\theta^{\mathrm{I}}\le\pi$) the normalized response is given by

$$\frac{N^{\mathrm{I}}(\theta^{\mathrm{I}})}{pR}=A\sin\theta^{\mathrm{I}}+1 \tag{9.9}$$

$$\frac{Q^{\mathrm{I}}(\theta^{\mathrm{I}})}{pR}=-A\cos\theta^{\mathrm{I}} \tag{9.10}$$

$$\frac{M^{\mathrm{I}}(\theta^{\mathrm{I}})}{pR^2}=-A\sin\theta^{\mathrm{I}} \tag{9.11}$$

$$\frac{u^{\mathrm{I}}(\theta^{\mathrm{I}})}{R}=B^{I}ApR\cos\theta^{\mathrm{I}}+\left(\frac{1}{2A^{\mathrm{I}}E^{\mathrm{I}}}-\frac{R^2}{2E^{\mathrm{I}}I^{\mathrm{I}}}\right)ApR\sin\theta^{\mathrm{I}}-\frac{2B^{\mathrm{I}}}{\pi}ApR\theta^{\mathrm{I}}\cos\theta^{\mathrm{I}}+C^{\mathrm{I}}pR \tag{9.12}$$

$$\frac{w^{\mathrm{I}}(\theta^{\mathrm{I}})}{R}=-B^{\mathrm{I}}ApR\sin\theta^{\mathrm{I}}+\frac{2B^{\mathrm{I}}}{\pi}ApR\theta^{\mathrm{I}}\sin\theta^{\mathrm{I}} \tag{9.13}$$

in which

$$A=\frac{C^{\mathrm{II}}-C^{\mathrm{I}}}{B^{\mathrm{II}}+B^{\mathrm{I}}} \tag{9.14}$$

$$B^{\mathrm{I}}=\frac{\pi}{4}\left(\frac{1}{A^{\mathrm{I}}E^{\mathrm{I}}}+\frac{R^2}{E^{\mathrm{I}}I^{\mathrm{I}}}\right) \tag{9.15}$$

$$B^{\mathrm{II}}=\frac{\pi}{4}\left(\frac{1}{A^{\mathrm{II}}E^{\mathrm{II}}}+\frac{R^2}{E^{\mathrm{II}}I^{\mathrm{II}}}\right) \tag{9.16}$$

$$C^{\mathrm{I}} = \frac{1}{A^{\mathrm{I}} E^{\mathrm{I}}} \tag{9.17}$$

$$C^{\mathrm{II}} = \frac{1}{A^{\mathrm{II}} E^{\mathrm{II}}} \tag{9.18}$$

Parameter A indicates the elastic and geometric mismatch between the host artery and the graft.

Moreover, the strain of the middle-wall surface and the rotation of the cross-section at any point along the circular arch are given respectively by

$$\varepsilon^{\mathrm{I}}(\theta) = \frac{u^{\mathrm{I}}(\theta^{\mathrm{I}})}{R} + \frac{1}{R}\frac{dw^{\mathrm{I}}(\theta^{\mathrm{I}})}{d\theta^{\mathrm{I}}} = pRC^{\mathrm{I}}\left(A\sin\theta^{\mathrm{I}} + 1\right) \tag{9.19}$$

$$\varphi^{\mathrm{I}}(\theta^{\mathrm{I}}) = \frac{1}{R}\left(\frac{du^{\mathrm{I}}(\theta^{\mathrm{I}})}{d\theta^{\mathrm{I}}} - w^{\mathrm{I}}(\theta^{\mathrm{I}})\right) \tag{9.20}$$

The response of the artery (element II) can be easily obtained from Equations (9.9) through (9.18) by assuming that the artery represents element I and the graft represents element II.

We are particularly interested in calculating the response of the suture line in terms of suture force f_s, displacements, strains, and rotation of the cross-section at the junction. The suture force is the resultant force of the tangential and radial forces at the junction ($\theta^{\mathrm{I}} = 0$). The normalized suture tensile force f_s / pR constitutes a stress-concentration factor due to the artery/graft compliance mismatch and is calculated from

$$\frac{f_s}{pR} = \sqrt{\left(\frac{N^{\mathrm{I}}(0)}{pR}\right)^2 + \left(\frac{Q^{\mathrm{I}}(0)}{pR}\right)^2} = \sqrt{1 + A^2} \tag{9.21}$$

The normalized radial displacement at the junction ($\theta^{\mathrm{I}} = 0$) is obtained from Equation (9.12) and expressed as

$$\frac{u^{\mathrm{I}}(0)}{pR^2 C^{\mathrm{I}}} = \frac{\left(B^{\mathrm{II}} / B^{\mathrm{I}}\right) + \left(C^{\mathrm{II}} / C^{\mathrm{I}}\right)}{1 + B^{\mathrm{II}} / B^{\mathrm{I}}} \tag{9.22}$$

Furthermore, the normalized rotation of the cross-section at the junction, for $C^{\mathrm{I}} \ll B^{\mathrm{I}}$, can be derived from Equation (9.20) as

$$\frac{\varphi^{\mathrm{I}}(0)}{pRC^{\mathrm{I}}} \approx \frac{4}{\pi}\frac{1-C^{\mathrm{II}}/C^{\mathrm{I}}}{1+B^{\mathrm{II}}/B^{\mathrm{I}}} \tag{9.23}$$

For typical values of geometric and mechanical properties of the two blood vessels, parameter A ranges from 0 to ± 0.01. Thus, the stress concentration at the suture is insignificant. Furthermore, as can be seen from Equations (9.9) through (9.11), for low values of parameter A, the solution is dominated by almost uniform axial hoop stress $N = pR$, and the moments and shear forces acting along the blood vessel wall are almost zero. Upon this, the strain of a blood vessel is approximated by $\varepsilon^i(\theta^i) \approx pRC^i$, depending mainly on the elasticity modulus of that blood vessel.

Figure 9-3 plots the normalized radial displacement and approximate normalized rotation at the junction for a range of the ratios $B^{\mathrm{II}}/B^{\mathrm{I}}$ and $C^{\mathrm{II}}/C^{\mathrm{I}}$. From Equation (9.22) and Figure 9-3(a), the radial displacement at the junction is minimized for values $B^{\mathrm{II}}/B^{\mathrm{I}}$ lower than 1. The radial displacement will never be equal to zero, due to the fact that $B^{\mathrm{II}}/B^{\mathrm{I}}$ will always have nonzero positive values. Equation (9.23) and Figure 9-3(b) indicate that the rotation of the cross-section is minimized for large values of the ratio $B^{\mathrm{II}}/B^{\mathrm{I}}$, and is equal to zero when $C^{\mathrm{II}}/C^{\mathrm{I}}$ is equal to unity, meaning that the term $A^{\mathrm{I}}E^{\mathrm{I}}$ is equal to $A^{\mathrm{II}}E^{\mathrm{II}}$.

The maximum rotation of the artery is developed when the graft is rigid (applies when $A^{\mathrm{II}}E^{\mathrm{II}} \to \infty$ and $E^{\mathrm{II}}I^{\mathrm{II}} \to \infty$). In this case, the cross-section of the graft will not rotate, whereas the cross-section of the artery will undergo large rotation approximated by

$$\varphi^{\mathrm{II}}(\pi/2) \approx \frac{4pR}{\pi A^{\mathrm{II}}E^{\mathrm{II}}} \tag{9.24}$$

For typical values of anastomosis properties the resultant maximum value of rotation (derived from Equation (9.24)) is about 10°.

9.3 The case of artery patching

The problem of patching with longitudinal graft materials can be solved by developing a similar model in which the graft occupies a smaller part of the model. Longitudinal patches are frequently used for carotid endarterectomies [108]. The main post-surgery complications of this technique are the development of intimal hyperplasia, suture-line bleeding, and patch infection.

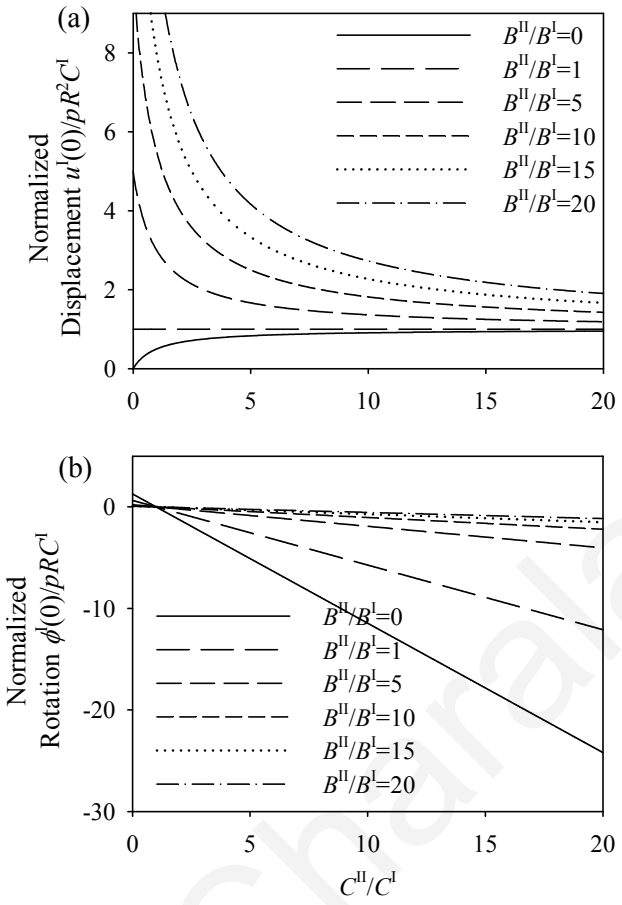

Figure 9-3: Normalized response as a function of the ratio C^{II}/C^{I}, and for different values of the ratio B^{II}/B^{I}: (a) Normalized displacement at the junction, (b) Normalized rotation of the cross-section at the junction.

Figure 9-4(a) shows a patched carotid artery and the vertical plane section that can be approximated by two circular parts connected by two hinges (Figure 9-4(b)). The hinge locations correspond to the suturing position. To appropriately model this system we solved the general problem in which the hinges can be placed at the edges of any chord of the centerline. The origin of the varying angles of each part are shown in Figure 9-4(b). The varying angles have range $0 \le \theta^{I} \le \pi - 2\theta_0$ and $-\pi/2 - \theta_0 \le \theta^{II} \le \pi/2 + \theta_0$, for the patch and artery, respectively.

The differential equations governing the static response of the system are expressed by Equations (9.1) through (9.5), with the symmetric boundary conditions of parts I and II given respectively

$$M^{I}(0) = 0,\ u_y^{I}(0) = 0,\ u_x^{I}\left(\frac{\pi}{2} - \theta_0\right) = 0,\ \frac{du_y^{I}}{d\theta}\left(\frac{\pi}{2} - \theta_0\right) = 0,\ Q^{I}\left(\frac{\pi}{2} - \theta_0\right) = 0 \qquad (9.25)$$

$$M^{\mathrm{II}}\left(\frac{\pi}{2}+\theta_0\right)=0,\ u_y^{\mathrm{II}}\left(\frac{\pi}{2}+\theta_0\right)=0,\ u_x^{\mathrm{II}}(0)=0,\ \frac{du_y^{\mathrm{II}}}{d\theta}(0)=0,\ Q^{\mathrm{II}}(0)=0 \tag{9.26}$$

where u_x^i and u_y^i are the global horizontal and vertical displacements, respectively ($i=\mathrm{I}$ for patch and $i=\mathrm{II}$ for artery).

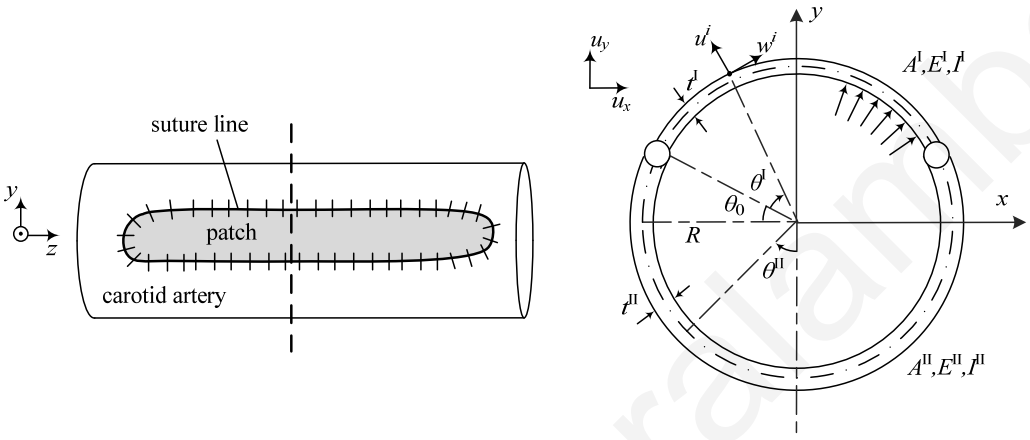

(a) (b)

Figure 9-4: (a) Carotid endrarterectomy with longitudinal patch, (b) Two-hinged anastomosis model with the hinges placed at the ends of any chord of the centerline. (I: patch, II: artery)

The continuity equations between the two parts are

$$N^{\mathrm{I}}(0)=N^{\mathrm{II}}\left(\frac{\pi}{2}+\theta_0\right),\ Q^{\mathrm{I}}(0)=Q^{\mathrm{II}}\left(\frac{\pi}{2}+\theta_0\right),\ u_x^{\mathrm{I}}(0)=u_x^{\mathrm{II}}\left(\frac{\pi}{2}+\theta_0\right) \tag{9.27}$$

The global displacements $u_x^i(\theta)$ and $u_y^i(\theta)$ can be expressed as

$$u_x^{\mathrm{I}}(\theta)=w^{\mathrm{I}}\sin(\theta^{\mathrm{I}})-u^{\mathrm{I}}\cos(\theta^{\mathrm{I}}) \tag{9.28}$$

$$u_y^{\mathrm{I}}(\theta)=w^{\mathrm{I}}\cos(\theta^{\mathrm{I}})+u^{\mathrm{I}}\sin(\theta^{\mathrm{I}}) \tag{9.29}$$

$$u_x^{\mathrm{II}}(\theta)=-w^{\mathrm{II}}\cos(\theta^{\mathrm{II}})-u^{\mathrm{II}}\sin(\theta^{\mathrm{II}}) \tag{9.30}$$

$$u_y^{\mathrm{II}}(\theta)=w^{\mathrm{II}}\sin(\theta^{\mathrm{II}})-u^{\mathrm{II}}\cos(\theta^{\mathrm{II}}) \tag{9.31}$$

By combining Equations (9.1) through (9.5) and Equations (9.25) through (9.27) the response of the two elements in terms of axial forces, shear forces, moments, radial and tangential displacements of the artery/element II ($-\pi/2-\theta_0 \le \theta^{II} \le \pi/2+\theta_0$) are obtained respectively as

$$N^{II}(\theta^{II}) = D_1^{II}\cos\theta^{II} + pR \tag{9.32}$$

$$Q^{II}(\theta^{II}) = D_1^{II}\sin\theta^{II} \tag{9.33}$$

$$M^{II}(\theta^{II}) = -RD_1^{II}\left(\sin\theta_0 + \cos\theta^{II}\right) \tag{9.34}$$

$$u^{II}(\theta^{II}) = D_2^{II}\cos\theta^{II} + D_1^{II}\left[\frac{\theta^{II}}{2}\sin\theta^{II}\left(\frac{R}{A^{II}E^{II}}+\frac{R^3}{E^{II}I^{II}}\right)+\frac{R^3}{E^{II}I^{II}}\sin\theta_0\right]+\frac{pR^2}{A^{II}E^{II}} \tag{9.35}$$

$$w^{II}(\theta^{II}) = -D_2^{II}\sin\theta^{II} + D_1^{II}\left[\begin{array}{l}\left(\dfrac{R}{2A^{II}E^{II}}-\dfrac{R^3}{2E^{II}I^{II}}\right)\sin\theta^{II} \\ +\dfrac{\theta^{II}}{2}\cos\theta^{II}\left(\dfrac{R}{A^{II}E^{II}}+\dfrac{R^3}{E^{II}I^{II}}\right)-\dfrac{R^3}{E^{II}I^{II}}\theta^{II}\sin\theta_0\end{array}\right] \tag{9.36}$$

in which

$$D_1^{II} = \frac{pR^2\cos\theta_0\left(\dfrac{1}{A^{I}E^{I}}-\dfrac{1}{A^{II}E^{II}}\right)}{\begin{array}{l}\dfrac{\sin\theta_0\cos\theta_0}{2}\left(\dfrac{R}{A^{I}E^{I}}-\dfrac{R^3}{E^{I}I^{I}}-\dfrac{R}{A^{II}E^{II}}+\dfrac{R^3}{E^{II}I^{II}}\right)+\left(\dfrac{\pi}{4}-\dfrac{\theta_0}{2}\right)\left(\dfrac{R}{A^{I}E^{I}}+\dfrac{R^3}{E^{I}I^{I}}\right)+\left(\dfrac{\pi}{4}+\dfrac{\theta_0}{2}\right)\left(\dfrac{R}{A^{II}E^{II}}+\dfrac{R^3}{E^{II}I^{II}}\right)\cdots \\ \cdots+\sin\theta_0\left\{\dfrac{R^3}{E^{I}I^{I}}\left[\sin\theta_0\left(\dfrac{\pi}{2}-\theta_0\right)-\cos\theta_0\right]+\dfrac{R^3}{E^{II}I^{II}}\left[\sin\theta_0\left(\dfrac{\pi}{2}+\theta_0\right)+\cos\theta_0\right]\right\}\end{array}} \tag{9.37}$$

and

$$D_2^{II} = \frac{pR^2\sin\theta_0}{A^{II}E^{II}} + D_1^{II}\left\{\cos^2\theta_0\left[\frac{R}{2A^{II}E^{II}}-\frac{R^3}{2E^{II}I^{II}}\right]+\sin\theta_0\frac{R^3}{E^{II}I^{II}}\left[\sin\theta_0-\cos\theta_0\left(\frac{\pi}{2}+\theta_0\right)\right]\right\} \tag{9.38}$$

Furthermore, the strain of the middle wall surface and the rotation of the cross-section at any point along the circular arch are respectively

$$\varepsilon^{II}(\theta^{II}) = \frac{u^{II}(\theta^{II})}{R}+\frac{1}{R}\frac{dw^{II}(\theta^{II})}{d\theta^{II}} = \frac{pR}{A^{II}E^{II}}+\frac{D_1^{II}\cos\theta^{II}}{A^{II}E^{II}} \tag{9.39}$$

$$\varphi^{\mathrm{II}}(\theta^{\mathrm{II}}) = \frac{D_1^{\mathrm{II}} R^2}{E^{\mathrm{II}} I^{\mathrm{II}}} \left(\sin\theta^{\mathrm{II}} + \theta^{\mathrm{II}} \sin\theta_0 \right) \tag{9.40}$$

The resulting strain and rotation at the junction ($\theta^{\mathrm{II}} = \pi / 2 + \theta_0$) are

$$\varepsilon^{\mathrm{II}} \left(\frac{\pi}{2} + \theta_0 \right) = \frac{pR}{A^{\mathrm{II}} E^{\mathrm{II}}} - \frac{D_1^{\mathrm{II}} \sin\theta_0}{A^{\mathrm{II}} E^{\mathrm{II}}} \tag{9.41}$$

$$\varphi^{\mathrm{II}} \left(\frac{\pi}{2} + \theta_0 \right) = \frac{D_1^{\mathrm{II}} R^2}{E^{\mathrm{II}} I^{\mathrm{II}}} \left[\cos\theta_0 + \sin\theta_0 \left(\frac{\pi}{2} + \theta_0 \right) \right] \tag{9.42}$$

The response of the graft (element I) can be easily obtained from Equations (9.32) through (9.42), by assuming that element II represents the graft and element I represents the artery.

The normalized suture tensile force f_s / pR, which constitutes a stress-concentration factor due to the artery/graft compliance mismatch, can be calculated as

$$\frac{f_s}{pR} = \sqrt{\left(\frac{N^{\mathrm{II}}(\frac{\pi}{2} + \theta_0)}{pR} \right)^2 + \left(\frac{Q^{\mathrm{II}}(\frac{\pi}{2} + \theta_0)}{pR} \right)^2} = \sqrt{\left(D_1^{\mathrm{II}} \right)^2 - 2 D_1^{\mathrm{II}} pR \sin\theta_0 + \left(pR \right)^2} \tag{9.43}$$

9.4 Effect of dynamic excitation

The static response of the two-hinged circular model was derived in Sections 9.2 and 9.3. To answer the question if the dynamic vibration of the artery is significant and must be taken into consideration, the long-term dynamic response of element II has to be evaluated. The graft is assumed to be rigid and the artery is modeled as a pinned circular arch (Figure 9-5(a)). This model constitutes the most unfavorable case of elevated elastic mismatch. The evaluation is performed in terms of dispersion graphs and the frequency coefficient.

The analysis assumes extensibility of the centerline of the arch and rotary inertia, whereas shear deformations are ignored. The dynamic equations of motion of the system are obtained by considering the equilibrium of forces acting on the infinitesimal element of Figure 9-5(b). The resulting in-plane dynamic response is described by the following equations

$$\frac{\partial Q^{\mathrm{II}}(\theta^{\mathrm{II}},\, t)}{\partial \theta^{\mathrm{II}}} - N^{\mathrm{II}}(\theta^{\mathrm{II}},\, t) = \rho^{\mathrm{II}} A^{\mathrm{II}} R \frac{\partial^2 u^{\mathrm{II}}(\theta^{\mathrm{II}},\, t)}{\partial t^2} - p(\theta^{\mathrm{II}},\, t) R \tag{9.44}$$

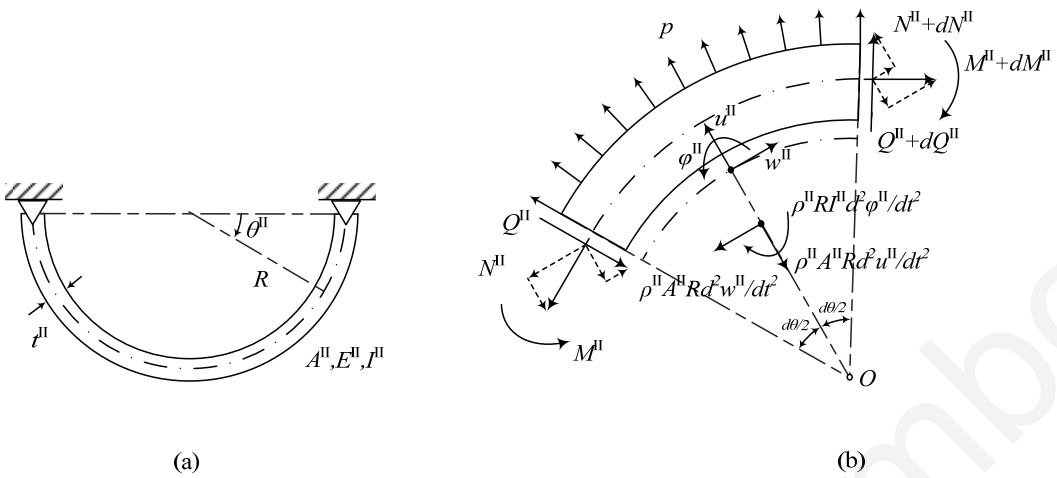

Figure 9-5: (a) Two-hinged artery segment under the assumption of rigid graft, (b) Free-body diagram of a typical element of arterial sector under dynamic loading.

$$\frac{\partial N^{\mathrm{II}}(\theta^{\mathrm{II}},\ t)}{\partial \theta^{\mathrm{II}}}+Q^{\mathrm{II}}(\theta^{\mathrm{II}},\ t)=\rho^{\mathrm{II}}A^{\mathrm{II}}R\frac{\partial^2 w^{\mathrm{II}}(\theta^{\mathrm{II}},\ t)}{\partial t^2} \tag{9.45}$$

$$\frac{\partial M^{\mathrm{II}}(\theta^{\mathrm{II}},\ t)}{\partial \theta^{\mathrm{II}}}-RQ^{\mathrm{II}}(\theta^{\mathrm{II}},\ t)=\rho^{\mathrm{II}}RI^{\mathrm{II}}\frac{\partial^2 \varphi^{\mathrm{II}}(\theta^{\mathrm{II}},\ t)}{\partial t^2} \tag{9.46}$$

where ρ^{II} is the artery density and $\varphi^{\mathrm{II}}(\theta^{\mathrm{II}},\ t)$ is the rotation of the artery cross-section. The rotation is expressed in terms of displacements as

$$\varphi^{\mathrm{II}}(\theta^{\mathrm{II}},\ t)=\frac{1}{R}\left(\frac{\partial u^{\mathrm{II}}(\theta^{\mathrm{II}},\ t)}{\partial \theta^{\mathrm{II}}}-w^{\mathrm{II}}(\theta^{\mathrm{II}},\ t)\right) \tag{9.47}$$

The moment $M^{\mathrm{II}}(\theta^{\mathrm{II}},\ t)$ and tangential force $N^{\mathrm{II}}(\theta^{\mathrm{II}},\ t)$ are expressed in terms of displacements as

$$M^{\mathrm{II}}(\theta^{\mathrm{II}},\ t)=\frac{E^{\mathrm{II}}I^{\mathrm{II}}}{R^2}\left(\frac{\partial w^{\mathrm{II}}(\theta^{\mathrm{II}},\ t)}{\partial \theta^{\mathrm{II}}}-\frac{\partial^2 u^{\mathrm{II}}(\theta^{\mathrm{II}},\ t)}{\partial \theta^{\mathrm{II}2}}\right) \tag{9.48}$$

$$N^{\mathrm{II}}(\theta^{\mathrm{II}},\ t)=\frac{E^{\mathrm{II}}A^{\mathrm{II}}}{R}\left(u^{\mathrm{II}}(\theta^{\mathrm{II}},\ t)+\frac{\partial w^{\mathrm{II}}(\theta^{\mathrm{II}},\ t)}{\partial \theta^{\mathrm{II}}}\right) \tag{9.49}$$

By solving Equation (9.46) for $Q^{\mathrm{II}}(\theta^{\mathrm{II}},\ t)$ and using Equations (9.47) and (9.48), the resulting shear force is obtained as

$$Q^{\mathrm{II}}(\theta^{\mathrm{II}},\ t)=\frac{E^{\mathrm{II}}I^{\mathrm{II}}}{R^3}\left(\frac{\partial^2 w^{\mathrm{II}}(\theta^{\mathrm{II}},\ t)}{\partial\theta^{\mathrm{II}2}}-\frac{\partial^3 u^{\mathrm{II}}(\theta^{\mathrm{II}},\ t)}{\partial\theta^{\mathrm{II}3}}\right)+\frac{\rho^{\mathrm{II}}I^{\mathrm{II}}}{R}\frac{\partial^2}{\partial t^2}\left(\frac{\partial u^{\mathrm{II}}(\theta^{\mathrm{II}},t)}{\partial\theta^{\mathrm{II}}}-w^{\mathrm{II}}(\theta^{\mathrm{II}},\ t)\right) \tag{9.50}$$

By substituting Equations (9.48) through (9.50) into Equations (9.44) and (9.45), and by assuming free-vibration conditions ($p(\theta^{\mathrm{II}},t)=0$), we obtain two equations that include only displacements terms:

$$\frac{E^{\mathrm{II}}I^{\mathrm{II}}}{R^3}\left(\frac{\partial^3 w^{\mathrm{II}}(\theta^{\mathrm{II}},\ t)}{\partial\theta^{\mathrm{II}3}}-\frac{\partial^4 u^{\mathrm{II}}(\theta^{\mathrm{II}},\ t)}{\partial\theta^{\mathrm{II}4}}\right)+\frac{\rho^{\mathrm{II}}I^{\mathrm{II}}}{R}\frac{\partial^2}{\partial t^2}\left(\frac{\partial^2 u^{\mathrm{II}}(\theta^{\mathrm{II}},\ t)}{\partial\theta^{\mathrm{II}2}}-\frac{\partial w^{\mathrm{II}}(\theta^{\mathrm{II}},\ t)}{\partial\theta^{\mathrm{II}}}\right)-\frac{E^{\mathrm{II}}A^{\mathrm{II}}}{R}\left(u^{\mathrm{II}}(\theta^{\mathrm{II}},\ t)+\frac{\partial w^{\mathrm{II}}(\theta^{\mathrm{II}},\ t)}{\partial\theta^{\mathrm{II}}}\right)-\rho^{\mathrm{II}}A^{\mathrm{II}}R\frac{\partial^2 u^{\mathrm{II}}(\theta^{\mathrm{II}},\ t)}{\partial t^2}=0 \tag{9.51}$$

$$\frac{E^{\mathrm{II}}A^{\mathrm{II}}}{R}\left(\frac{\partial u^{\mathrm{II}}(\theta^{\mathrm{II}},\ t)}{\partial\theta^{\mathrm{II}}}+\frac{\partial^2 w^{\mathrm{II}}(\theta^{\mathrm{II}},\ t)}{\partial\theta^{\mathrm{II}2}}\right)+\frac{E^{\mathrm{II}}I^{\mathrm{II}}}{R^3}\left(\frac{\partial^2 w^{\mathrm{II}}(\theta^{\mathrm{II}},\ t)}{\partial\theta^{\mathrm{II}2}}-\frac{\partial^3 u^{\mathrm{II}}(\theta^{\mathrm{II}},\ t)}{\partial\theta^{\mathrm{II}3}}\right)+\frac{\rho^{\mathrm{II}}I^{\mathrm{II}}}{R}\frac{\partial^2}{\partial t^2}\left(\frac{\partial u^{\mathrm{II}}(\theta^{\mathrm{II}},\ t)}{\partial\theta^{\mathrm{II}}}-w^{\mathrm{II}}(\theta^{\mathrm{II}},\ t)\right)-\rho^{\mathrm{II}}A^{\mathrm{II}}R\frac{\partial^2 w^{\mathrm{II}}(\theta^{\mathrm{II}},\ t)}{\partial t^2}=0 \tag{9.52}$$

These partial differential equations are coupled through the radial and tangential displacement. By assuming a harmonic solution (with frequency ω^{II}) of the form

$$u^{\mathrm{II}}(\theta^{\mathrm{II}},t)=U^{\mathrm{II}}(\theta^{\mathrm{II}})e^{i\omega^{\mathrm{II}}t} \tag{9.53}$$

$$w^{\mathrm{II}}(\theta^{\mathrm{II}},t)=W^{\mathrm{II}}(\theta^{\mathrm{II}})e^{i\omega^{\mathrm{II}}t} \tag{9.54}$$

Equations (9.51) and (9.52) become

$$\left(-\frac{\partial^4}{\partial\theta^{\mathrm{II}4}}-\frac{\partial^2}{\partial\theta^{\mathrm{II}2}}k\lambda+k-\frac{1}{\lambda}\right)U^{\mathrm{II}}-\left[-\frac{\partial^3}{\partial\theta^{\mathrm{II}3}}+\frac{\partial}{\partial\theta^{\mathrm{II}}}\left(\frac{1}{\lambda}-k\lambda\right)\right]W^{\mathrm{II}}\equiv L_1U^{\mathrm{II}}-L_2W^{\mathrm{II}}=0 \tag{9.55}$$

$$\left[-\frac{\partial^3}{\partial\theta^{\mathrm{II}3}}+\frac{\partial}{\partial\theta^{\mathrm{II}}}\left(\frac{1}{\lambda}-k\lambda\right)\right]U^{\mathrm{II}}-\left[\frac{\partial^2}{\partial\theta^{\mathrm{II}2}}\left(-1-\frac{1}{\lambda}\right)-k\lambda-k\right]W^{\mathrm{II}}\equiv L_3U^{\mathrm{II}}-L_4W^{\mathrm{II}}=0 \tag{9.56}$$

in which $k=\rho^{\mathrm{II}}A^{\mathrm{II}}R^4\omega^{\mathrm{II}2}/(E^{\mathrm{II}}I^{\mathrm{II}})$, $\lambda=I^{\mathrm{II}}/(A^{\mathrm{II}}R^2)$, and U^{II} and W^{II} are the normal functions of u^{II} and w^{II}. The system of equations can be decoupled as

$$\left(L_1L_4 - L_2L_3\right)U^{\mathrm{II}} = 0 \tag{9.57}$$

$$\left(L_1L_4 - L_2L_3\right)W^{\mathrm{II}} = 0 \tag{9.58}$$

Thereby, the decoupled differential equations of the radial and tangential displacements are identical and are expressed respectively as

$$U^{\mathrm{II}(6)} + U^{\mathrm{II}(4)}\left(2+2k\lambda\right) + U^{\mathrm{II}(2)}\left(1-k+k\lambda+k^2\lambda^2\right) + U^{\mathrm{II}}\left(k+k\lambda-k^2\lambda-k^2\lambda^2\right) = 0 \tag{9.59}$$

$$W^{\mathrm{II}(6)} + W^{\mathrm{II}(4)}\left(2+2k\lambda\right) + W^{\mathrm{II}(2)}\left(1-k+k\lambda+k^2\lambda^2\right) + W^{\mathrm{II}}\left(k+k\lambda-k^2\lambda-k^2\lambda^2\right) = 0 \tag{9.60}$$

in which $U^{\mathrm{II(n)}}$ and $W^{\mathrm{II(n)}}$ denote the *n*th partial derivative of U^{II} and W^{II} with respect to θ^{II}.

To the authors' best knowledge, this is the first time that the decoupled equations of free vibration of an extensible circular arch with rotary inertia (by ignoring shear deformation) are correctly derived. The usual practice is to either include or ignore both rotary inertia and shear deformation. In this study we deal with the problem of thin rings in which the effect of shear deformation is insignificant.

9.4.1 Dispersion curves

The dynamic response of the system can be evaluated through dynamic dispersion curves [109], based on the wave propagation theory. We assume that the radial and tangential displacements are expressed by waves of the type

$$u^{\mathrm{II}}(\theta^{\mathrm{II}}, t) = U^{\mathrm{II}} e^{i\left(b_w\theta^{\mathrm{II}}R - \omega^{\mathrm{II}}t\right)} \tag{9.61}$$

$$w^{\mathrm{II}}(\theta^{\mathrm{II}}, t) = W^{\mathrm{II}} e^{i\left(b_w\theta^{\mathrm{II}}R - \omega^{\mathrm{II}}t\right)} \tag{9.62}$$

where b_w denotes the wave number. The wave equations along the circular ring are

$$U^{\mathrm{II}}(\theta^{\mathrm{II}}) = U^{\mathrm{II}} e^{ib_w\theta^{\mathrm{II}}R} \tag{9.63}$$

$$W^{\mathrm{II}}(\theta^{\mathrm{II}}) = W^{\mathrm{II}} e^{ib_w\theta^{\mathrm{II}}R} \tag{9.64}$$

The expression $V_P = \omega^{\mathrm{II}} / b_w$ denotes the phase velocity of the system. The differential equations of the radial and tangential displacement are identical, therefore by substituting

Equation (9.63) in Equation (9.59) and solving for the normalized phase velocity $V_p/(\sqrt{E^{\mathrm{II}}/\rho^{\mathrm{II}}})$, one obtains the dispersion relations of the circular ring as

$$\frac{V_P}{\sqrt{\frac{E^{\mathrm{II}}}{\rho^{\mathrm{II}}}}}=\sqrt{\frac{\left(2b_w{}^4R^4+\frac{b_w{}^2R^2}{\lambda}-b_w{}^2R^2+\frac{1}{\lambda}+1\right)}{b_w{}^2R^2\left(b_w{}^2R^2+\frac{1}{\lambda}+1\right)}}\sqrt{\frac{\pm\sqrt{\left(2b_w{}^4R^4+\frac{b_w{}^2R^2}{\lambda}-b_w{}^2R^2+\frac{1}{\lambda}+1\right)^2-4b_w{}^2R^2\left(b_w{}^2R^2-1\right)^2\left(b_w{}^2R^2+\frac{1}{\lambda}+1\right)}}{b_w{}^2R^2\left(b_w{}^2R^2+\frac{1}{\lambda}+1\right)}} \tag{9.65}$$

In the case where the centerline of the ring is inextensible, the dispersion relation is given by

$$\frac{V_P}{\sqrt{\frac{E^{\mathrm{II}}}{\rho^{\mathrm{II}}}}}=\sqrt{\lambda}\,\frac{1-b_w{}^2R^2}{\sqrt{1+b_w{}^2R^2}} \tag{9.66}$$

Figure 9-6 plots the dispersion curves of the system. All the curves decrease with increased wave number, indicating that the system is dispersive and its energy attenuates. Therefore, there is no concern of exhibiting abnormal increase of amplitude under dynamic loading.

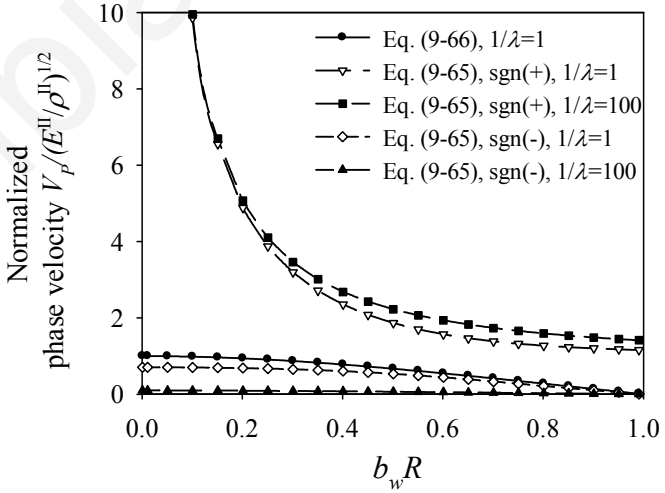

Figure 9-6: Dispersion curves of the normalized phase velocity of the system as a function of b_wR, by considering extensible and inextensible centerline of the ring, and for different values of parameter λ.

9.4.2 Frequency curves

The system is also evaluated by investigating the natural frequencies of the system. The problem of a pinned rigid semi-circle can be parallelized to the pinned structural arch problem. The free vibration of circular arches has been studied thoroughly by many researchers [15–20]. Veletsos et al. [110] and Austin and Veletsos [111] proposed approximate formulas to calculate the frequency coefficient spectrum of pinned circular arches. These formulas have proven to have adequate accuracy and are suitable for calculating easily the natural frequencies of such systems.

The final frequency curves are a combination of the bending and extensional frequency coefficient curves. The bending (including rotary inertia) antisymmetric and symmetric frequency coefficients are expressed respectively as

$$C_{n_f} = {m_f}^4 \pi^4 \frac{\left[1-\left(\frac{1}{m_f}\right)^2\right]^2}{1+3\left(\frac{1}{m_f}\right)^2} \frac{\frac{S_f}{m_f \pi r_f}}{\sqrt{\left(\frac{S_f}{m_f \pi r_f}\right)^2 + \Omega_f + \left[1+\Omega_f\left(\frac{m_f \pi r_f}{S_f}\right)^2\right]^{-1}}}, \quad m_f = 2n_f \tag{9.67}$$

$$C_{n_f} = {m_f}^4 \pi^4 \frac{\left[1-\left(\frac{1}{m_f}\right)^2\right]^2}{1+\frac{1}{{m_f}^2}+2\left(\frac{1}{m_f}\right)^2} \frac{\frac{S_f}{m_f \pi r_f}}{\sqrt{\left(\frac{S_f}{m_f \pi r_f}\right)^2 + \Omega_f + \left[1+\Omega_f\left(\frac{m_f \pi r_f}{S_f}\right)^2\right]^{-1}}}, \quad m_f = 2n_f + 1 \tag{9.68}$$

where n_f is the number of mode, S_f is equal to πR, and r_f is the radius of gyration $\sqrt{I^{II} / A^{II}}$. In order to neglect shear deformation, the shear flexibility factor Ω_f is set equal to 10.

The extensional frequency coefficients are expressed as

$$C_{m_f} = m_f \pi \frac{S_f}{r_f} \sqrt{1+\left(\frac{1}{m_f}\right)^2} \tag{9.69}$$

Odd values of m_f represent antisymmetric modes, whereas even values of m_f represent symmetric modes of vibration.

Note that, the mathematical relation of the natural circular frequency ω^{II} to the frequency coefficient C_n is $\omega^{II} = C_n / (R^2\pi^2)\sqrt{E^{II}I^{II}/(\rho^{II}A^{II})}$.

As shown in Figure 9-7 the resultant frequency curve and subsequently the free-vibration characteristics of the system are dominated by the first antisymmetric bending mode. It is clear that the natural frequency of a two-hinged artery is much larger than the frequency of the applied force (the frequency of a typical cardiac pulse is about 7 rad/sec). Therefore, the dynamic response of the system can be adequately approximated by the static response.

In conclusion, the dynamic investigation revealed that the dynamic effect is not significant for the long-term behavior of the two-hinged model. The first natural frequency of the two-hinged circular arch appears to be large compared to the loading frequency (at least ten times larger). Additionally, the system is dispersive. Therefore, the static analysis constitutes an adequate approach of the anastomosis response.

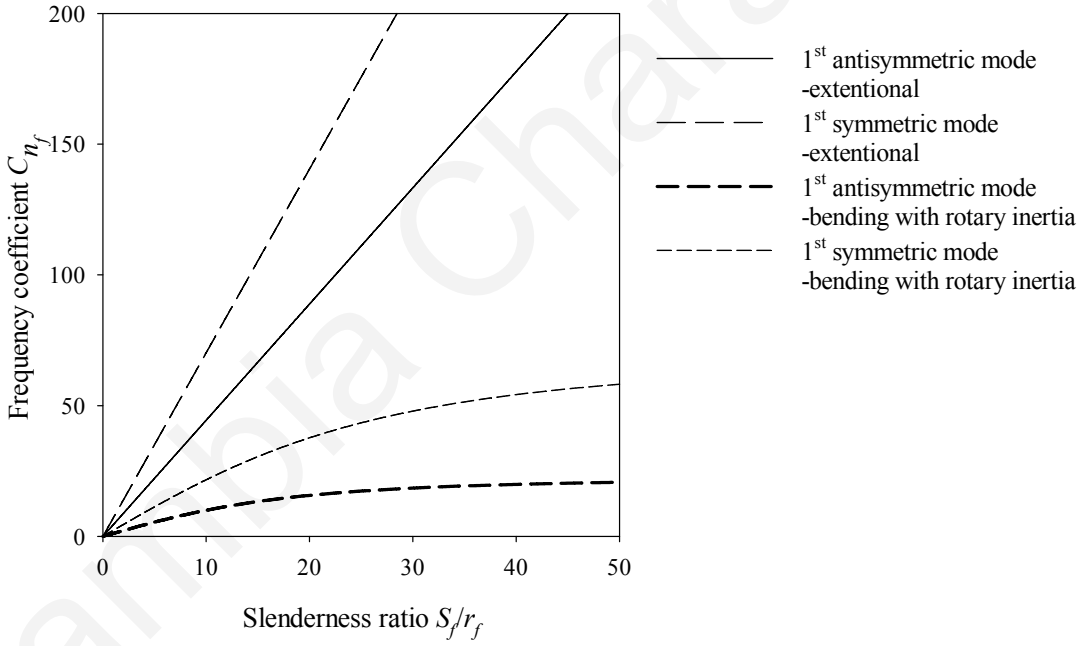

Figure 9-7: Frequency curves of first antisymmetric and symmetric modes.

9.5 Numerical example related to end-to-side anastomosis

The applicability of the proposed analytical model, simulating the end-to-side anastomosis problem, is demonstrated through a numerical example in which the geometric and mechanical properties of the models of Perktold et al. [12] are used. The far-field stress values of this study are verified against the finite-element calculations of Perktold et al.

Table 9-1 lists the problem parameters of a conventional anastomosis (artery/ePTFE graft) and a Taylor-patch anastomosis (artery/vein-patch/ePTFE-graft).

Table 9-1: Parameters of end-to-side anastomosis models of Perktold et al.

	Artery (II) /vein (I)	*Artery (II) /ePTFE graft (I)*
Parameters		
	$p = 13.33$ kPa, $R = 2$ mm, $E^{II} = 410$ kPa, $t^{II} = 0.5$ mm	
E^{I} (kPa)	820	7500
t^{I} (mm)	0.5	0.35

Table 9-2 lists the calculated response values. The radial displacement of the junction appears to be larger in the case of artery/vein anastomosis than in the case of artery/ePTFE anastomosis, whereas the stiffer the blood vessel or graft, the lower the developed strain is. The far-field stresses are approximated according to Hooke's law ($\sigma^i = E^i \varepsilon^i$). It can be observed that the stresses are not affected by the mechanical properties of the blood vessels, due to the fact that a stiffer graft (large elasticity modulus) will develop lower strains than a soft blood vessel (low elasticity modulus). The far-field stress of the graft would be exactly equal to the far-field stress of the artery if they had the same thicknesses. For the artery and vein the far-field stress as calculated in this study is 53 kPa and for the ePTFE graft the far-field stress is 75 kPa. The finite-element results of Perktold et al. are 50 kPa and 60 kPa respectively, which they compare well with our results.

Of particular interest is the rotation of each cross-section at the junction. Table 9-3 reports the rotation of each cross-section, as calculated by Equation (9.20). In both cases, element I is stiffer than the host artery, causing larger rotations angles for the host artery than the graft or vein. When the ePTFE graft is used, instead of the vein, the rotation angle of the artery is increased, creating larger incompatible angles that may cause injury of the arterial tissue and may promote the development of intimal hyperplasia. Figure 9-8 shows the incompatible angles at the junction of the artery/vein anastomosis and the artery/ePTFE graft anastomosis.

Table 9-2: Results of the proposed methodology for the end-to-side anastomosis models of Perktold et al.

	Artery (II) /vein (I)	*Artery (II) /ePTFE graft (I)*
	Response Values	
B^{I} (m/N)	0.3678	0.1175
B^{II} (m/N)	0.7356	0.7356
C^{I} (m/N)	2.439e-3	3.809e-4
C^{II} (m/N)	4.878e-3	4.878e-3
A	0.00221	0.005271
$\varepsilon^{I}(0) / \varepsilon^{I}(\pi/2)$	0.0650/0.0652	0.0101/0.0102
$\varepsilon^{II}(\pi/2)$	0.13	0.13
$u^{I}(0) / u^{I}(\pi/2)$ (mm)	0.173/0.092	0.053/-0.0006
σ^{I} (kPa)	53.33	75.00
σ^{II} (kPa)	53.32	53.32

Table 9-3: Rotation angles at the anastomosis junction as proposed by this study.

	Artery(II) /vein(I)	*Artery(II) /ePTFE graft(I)*
$\varphi^{I}(0)$ (degrees)	-1.58	-1.20
$\varphi^{II}(\pi/2)$ (degrees)	-3.16	-7.52

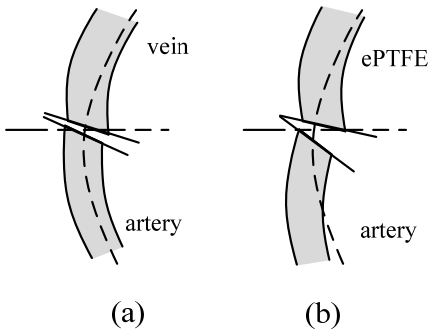

Figure 9-8: Rotation of the cross-sections at the junction of (a) artery/vein anastomosis, (b) artery/ePTFE anastomosis.

9.6 Numerical examples related to artery patching

The behavior of the patched artery is investigated through numerical examples, based on typical data. Furthermore, the peak far-field stress and strain values calculated by the proposed methodology are compared against the results of Kamenskiy et al. [108].

9.6.1 Typical examples of patched arteries

In this section, four numerical examples are investigated, considering different values of the mechanical and geometrical parameters of the two elements, the intraluminal pressure, and the angle θ_0. Table 9-4 lists the parameters of each example.

Table 9-4: Parameters of typical patched arteries examples.

	Example A	*Example B*	*Example C*	*Example D*
	Parameters			
p (kPa)	13.33	13.332	13.332	15.99
R (mm)	2	2	2	2
t^{I} (mm)	0.5	0.35	0.35	1
t^{II} (mm)	0.5	0.5	0.5	1
E^{I} (kPa)	820	7500	7500	7500
E^{II} (kPa)	410	410	410	410
θ_0 (degrees)	25	25	45	25

As follows from the calculated response values, reported in Table 9-5, the hinges placement (angle θ_0) or the elastic mismatch between the two blood vessels do not promote elevated stress concentration at the suture line ($f_s/(pR)$). Increased elastic mismatch results in a decrease of the displacements and rotation of the graft, whereas the strain and far-field stresses depend on the mechanical and geometric properties of each individual blood vessel. Furthermore, from examples B and C, it can be observed that by increasing angle θ_0 the relative rotation angle of the cross-sections at the junction is decreased.

It can be concluded that the behavior of the patched artery model exhibits similar behavior to that of the side-to-side related anastomosis model. To elaborate on the effect of angle θ_0 on the system response we investigate the rotation angle at the junction for different values

of the parameter θ_0. Figure 9-9(a) plots the relative rotation at the junction, and Figure 9-9(b) plots the rotation of the artery and graft cross sections at the junction, for each numerical example. Observe that an increase of the absolute value of angle θ_0 frequently decreases the relative and individual cross-sections rotations at the junction. Additionally, the rotation of the graft, in most cases, is lower than the rotation of the artery due to the fact that the graft is stiffer than the artery (Figure 9-9(b)).

Table 9-5: Results of the proposed methodology for typical patched arteries examples.

	Example A	*Example B*	*Example C*	*Example D*
	Response Values			
D_1^{II} (N/m)	-0.0308	-0.0588	-0.0290	-0.2907
D_2^{II} (m)	1.68E-04	2.20E-04	2.34E-04	1.34E-04
$f_s/(pR)$	1.0005	1.0009	1.0008	1.0039
$\varepsilon^{\mathrm{I}}(0)$	0.0651	0.0102	0.0102	0.0043
$\varepsilon^{\mathrm{II}}(\pi/2+\theta_0)$	0.1301	0.1302	0.1302	0.0783
$u_x^{\mathrm{I}}(0)$ (mm)	-0.1236	-0.0219	-0.0147	-0.0085
$\lvert u_{\max}^{\mathrm{I}} \rvert$ (mm)	0.1121	0.0198	0.0104	0.0077
$\lvert u_{\max}^{\mathrm{II}} \rvert$ (mm)	0.4034	0.4336	0.4560	0.2608
$\lvert w_{\max}^{\mathrm{I}} \rvert$ (mm)	0.0523	0.0092	0.0104	0.0036
$\lvert w_{\max}^{\mathrm{II}} \rvert$ (mm)	0.1128	0.1236	0.1594	0.0750
$\varphi^{\mathrm{I}}(0)$ (degrees)	-0.3532	-0.2148	-0.0377	-0.0455
$\varphi^{\mathrm{II}}(\pi/2+\theta_0)$ (degrees)	-2.9039	-5.5394	-3.6989	-3.4207

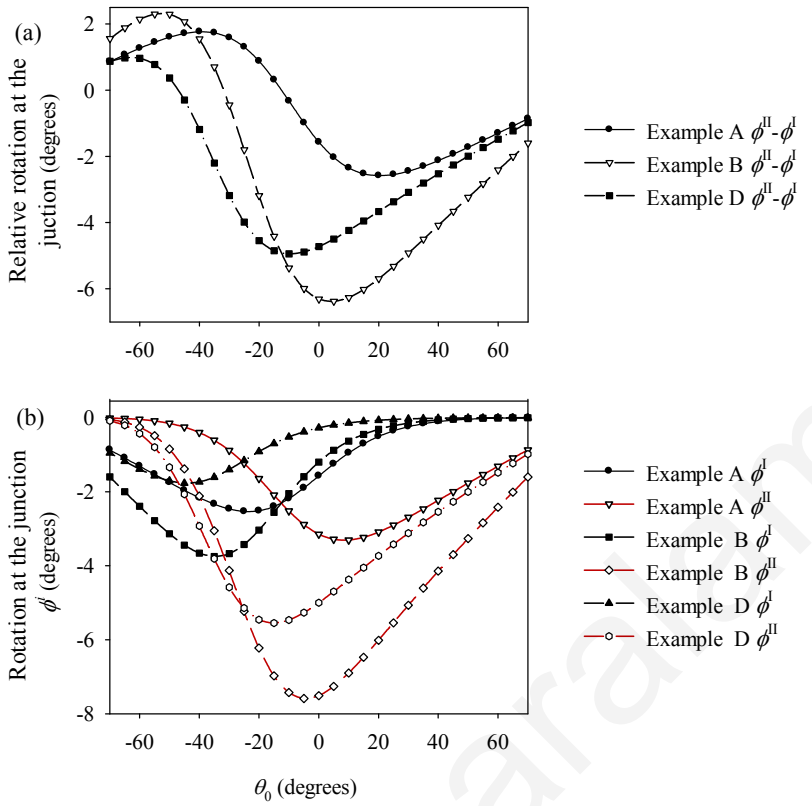

Figure 9-9: Rotation at the junction as a function of angle θ_0 : (a) Relative rotation at the junction, (b) Rotation of the artery and graft cross-section.

9.6.2 Patched carodit artery example based on the data of Kamenskiy et al.

Kamenskiy et al. [108] studied a finite-element model of a patched carotid artery. They used an exponential hyperelastic material law and modeled the stitches as fixed rigid contacts. Table 9-6 lists the properties used in the analysis. The geometric data of the model of Kamenskiy et al. were not given explicitly, therefore we used their figures and typical values for carotid arteries from the literature [56, 112]. The patch width was taken from Kamenskiy et al. [108] to be about 2.7 mm. For our calculations the elasticity modulus is taken to be equal to the tangent elasticity modulus under applied longitudinal pre-stretch equal to 1.08.

Figure 9-10 plots the total displacements along the PTFE patch and the artery, for equal scales of the undeformed and deformed configurations. It can be observed that the artery response is much larger than the patch response and that the most significant response value appear to be the relative rotation, $\varphi^{II}(\pi/2+\theta_0)-\varphi^{I}(0)$ between the artery and the patch at the junction. Table 9-7 lists the response values derived from our analysis. Note

also that, the forces and strains are found to be almost uniform along the patch and the carotid.

Table 9-6: Parameters of patched carotid model of Kamenskiy et al. [108].

Parameter	Value
p (kPa)	17.332
R (mm)	5.5
t^{I} (mm)	0.3
t^{II} (mm)	0.6
E^{I} (kPa)	8000
E^{II} (kPa)	845
θ_0 (degrees)	76

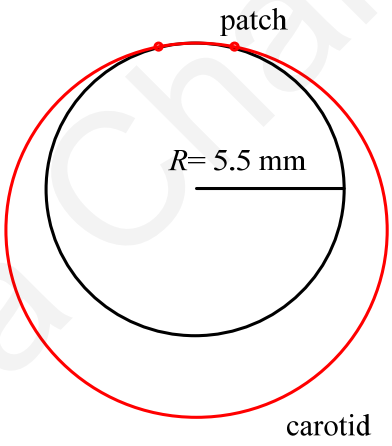

Figure 9-10: Global deformation distribution in of patched carotid model.

Kamenskiy et al. calculated the cyclic strain (the difference of Von Misses strain between systole and diastole) and the Misses effective stress σ_{eff} values. Table 9-8 lists a comparison of results obtained by Kamenskiy et al. and by this study, in terms of the maximum cyclic strain and the far-field stresses. Evidently, our calculations are in good agreement with the finite-element calculations of Kamenskiy et al. Note that, Kamenskiy et al. modeled the stitches as rigid contacts, resulting in stress concentrations at the suture line. The model proposed in this study incorporates hinges that result in relative rotations of the connected parts.

Table 9-7: Results of the proposed methodology for the patched carotid model of Kamenskiy et al.

Response values	
D_1^{II} (N/m)	-0.00398
D_2^{II} (m)	0.000993
$f_s/(pR)$	1
$\varepsilon^{\mathrm{I}}(0)$	0.0397
$\varepsilon^{\mathrm{II}}(\pi/2+\theta_0)$	0.188
$\sigma^{\mathrm{I}}(0)$ (kPa)	317.76
$\sigma^{\mathrm{II}}(\pi/2+\theta_0)$ (kPa)	158.88
$u_x^{\mathrm{I}}(0)$ (mm)	-0.0529
$\lvert u_{\max}^{\mathrm{I}} \rvert$ (mm)	0.0128
$\lvert u_{\max}^{\mathrm{II}} \rvert$ (mm)	1.985
$\lvert w_{\max}^{\mathrm{I}} \rvert$ (mm)	0.0513
$\lvert w_{\max}^{\mathrm{II}} \rvert$ (mm)	0.908
$\varphi^{\mathrm{I}}(0)$ (degrees)	-0.00185
$\varphi^{\mathrm{II}}(\pi/2+\theta_0)$ (degrees)	-1.386
$\varphi^{\mathrm{II}}-\varphi^{\mathrm{I}}$ (degrees)	-1.384

If the size of the patch is increased, and therefore the angle θ_0 is decreased, the relative rotation of the carotid and the patch at the junction would be increased (Figure 9-11). The largest relative rotation at the stitched junction is developed when $\theta_0 \approx 30°$. Therefore, thinner strips of patches seem to be more appropriate in order to prevent post-surgery complications.

9.7 Concluding remarks

This chapter investigated the problem of side-to-side related anastomosis and artery patching by examining the correlation of elastic (compliance) mismatch on the suture stress concentration and development of intimal hyperplasia at the suture line. The static analysis of the system under internal pressure appears to give an adequate estimation of the

long-term response, compared to the dynamic analysis, and is utilized to calculate the displacement at the junction (Equation (9.22)), the strains developed at each blood vessel (Equation (9.19)), and the incompatible angles at the junction (Equation (9.20)). It should be noted that the applicability of this study is limited to the analysis of anastomosis regions that can be approximated by the idealized two-hinged circular model of Figure 9-2(a).

Table 9-8: Comparison between results of Kamenskiy et al. [108] and this study.

	Kamenskiy et al.	*This study*
Patch maximum cyclic strain	0.02	0.0214
Carotid maximum cyclic strain	0.1	0.1012
Patch far-field stress $\log_{10}(\sigma_{eff})$ (Pa)	5.5	5.502
Carotid far-field stress $\log_{10}(\sigma_{eff})$ (Pa)	5.4	5.201

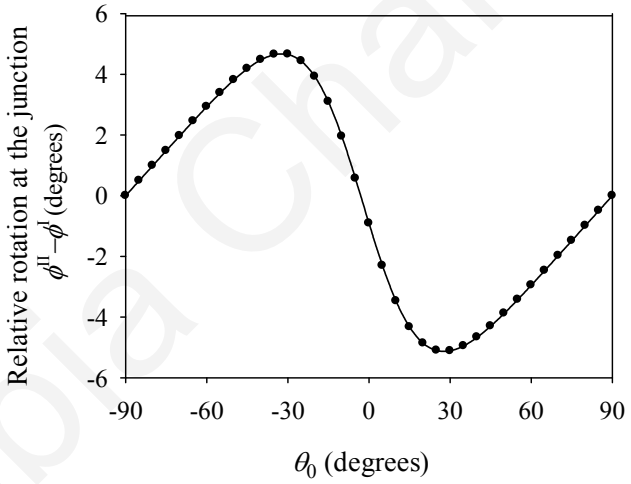

Figure 9-11: Relative rotation of the cross-section of the PTFE patch and the carotid artery at the junction as a function of angle θ_0. Large values of θ_0 correspond to thinner patches.

Results of this study suggest that elevated elastic mismatch between the artery and graft does not affect the internal forces of the blood vessels and that the system is dominated by almost uniform axial hoop stress $N = pR$. Furthermore, elevated elastic mismatch reduces the radial displacements and strains of the graft and the radial displacement at the junction, whereas the far-field stresses are of the same magnitude regardless of the material used. For typical geometrical and mechanical properties of the artery, parameter A has very low values. This favors the suture response by indicating insignificant stress concentration at the suture line in the presence of elastic mismatch (Equation (9.21)).

The response parameter that is primarily affected by the difference between the mechanical properties of the two blood vessels, appears to be the incompatible angle of the junction (Figures 9-3(b) and 9-8). Whenever blood flow creates almost zero shear stresses at the artery wall (e.g. stagnation points, low fluid velocities, reverse flows etc.), conditions for hyperplasia set in. At such cases, the compliance mismatch between the prosthetic graft and the host artery plays an important role in the development of intimal hyperplasia in the following sense: the higher the compliance mismatch, the higher the incompatible angle at the junction between the graft and the artery, implying that the blood flow at the suture line is disturbed even more. In order to minimize the rotation of the arterial cross-section and avoid elevated intimal thickening, the term $A^{\mathrm{I}}E^{\mathrm{I}}$ must be equal to $A^{\mathrm{II}}E^{\mathrm{II}}$. Frequently, the graft is stiffer than the host artery. Therefore, in order to obtain zero rotation the graft thickness has to be decreased to satisfy the equality $A^{\mathrm{I}}E^{\mathrm{I}} = A^{\mathrm{II}}E^{\mathrm{II}}$.

In regard to the geometric mismatch (i.e. when the thicknesses of the two blood vessels differ), the far-field stresses, and therefore the embedding stresses, of the host artery and the graft are not equal. Their values are of the same magnitude as long as thicknesses are also of the same magnitude. Additionally, increased graft thickness yields an increase of the compliance parameter A.

For the case that the hinges are placed at the edges of any chord of the full circle, the response value that is significantly affected is the rotation at the junction. By increasing the absolute value of angle θ_0, the relative rotation at the junction is decreased (Figure 9-11). In the case of the patched artery, the arterial part exhibits large displacements that may lead to softening of the tissue and development of aneurysm after a long time period. Additionally, it is likely that the large rotation angle at the junction promotes (along with other parameters) the development of intimal hyperplasia, injury of the arterial tissue, and infection of the patched region.

Through the proposed model and analysis the optimal graft characteristics can be obtained to minimize the incompatible angle at the anastomosis junction and the development of intimal hyperplasia. In order to minimize the post-surgery complications of end-to-side anastomosis, side-to-side anastomosis or artery patching the following practical techniques are proposed for surgical application: (a) Ideally, the graft and the host artery should have the same elasticity modulus and same thickness; (b) If the graft is stiffer than the host artery, the graft thickness should be smaller than the artery thickness (aiming to satisfy the equality $A^{\mathrm{I}}E^{\mathrm{I}} = A^{\mathrm{II}}E^{\mathrm{II}}$); and (c) In the case of artery patching, given that the patch is stiffer than the artery, the patch width should be as small as possible.

CHAPTER 10

Stress Concentration at the Stitching Hole

10.1 Introduction

The stress concentration at the stitching hole due to suture-artery interaction is a complex phenomenon. In Section 7.2.1 we calculated the peak embedding stress σ_s based on the approximation that the total force of each stitch af_s is applied over an area $2r_s h$, resulting in the approximation $\sigma_s = \alpha f_s / (2r_s h)$ (Equation (7.17)). When the embedding stresses due to suture-artery contact interaction exceed the limit value of the artery-wall shear strength, arterial-wall rupture or injury may occur.

The anastomosis is more likely to fail due to tissue tearing than suture failure, since the suture strength is frequently much larger than the induced suture force. A simple experimental setup to determine the suture force required to tear the arterial tissue, could be a suture loop that permeates a thin strip of arterial tissue through a hole that is close to the strip's edge. The loop and the arterial tissue can be axially loaded until tissue failure is observed, in the form of tearing of the hole. If the suture breaks, then we repeat the test by increasing the number of loops (sufficiently apart from each other), or by selecting a thicker suture.

Figure 10-1 shows two possible failure modes, caused by the suture-artery contact interaction. The first failure mode concerns the tearing towards the artery edge, in the longitudinal direction (direction that the suture is loaded) (Figure 10-1(a)). This is the most frequently-encountered failure mode [113]. The second failure mode concerns the tearing of the arterial wall in the circumferential direction, due to interaction of the embedding stresses of stitches arranged in a row (Figure 10-1(b)) [114].

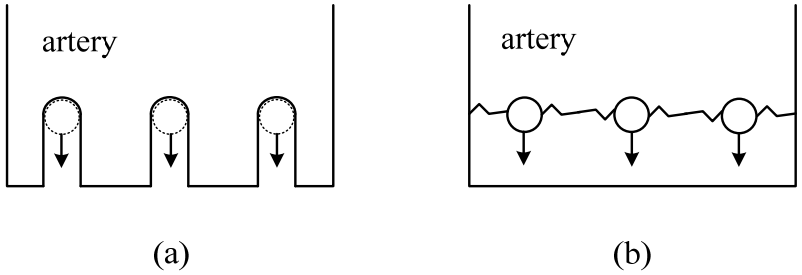

Figure 10-1: Failure modes due to suture-artery interaction. Arterial-wall tearing: (a) in the longitudinal direction, (b) in the circumferential direction.

The problem of stress concentration at the stitching hole can be parallelized with mechanics problems investigated thoroughly in the literature, such as the problem of pinned-loaded holes in plates [115–120] or the problem of internal indentation between two cylindrical surfaces [121, 122]. Such studies provide more sophisticated and accurate expressions than the approximation utilized in Chapters 7 and 8.

The following section presents closed-form solutions to the problem of the stress concentration around a pinned loaded hole [119].

10.2 Closed-form solution proposed by Echavarría et al.

In their study, Echavarría et al. [119] investigated the stress concentration around a pin-loaded hole in elastic orthotropic plates. They developed analytical closed-form expressions for the peak perpendicular and longitudinal stresses along the edge of the hole. Their formulas provide sufficient accuracy compared to other analytical studies that may require numerical methods for the problem solution. Figure 10-2 shows the geometry and considered loading of the problem. A force F_y is applied to one side of the plate, in the longitudinal direction (y-axis), resulting in a sinusoidal load distribution at the hole. The radius of the hole is denoted by R_h, and the distance from the center of the hole to the edge of the plate is denoted by e. Note that, the stitching holes and the suture have almost equal diameters.

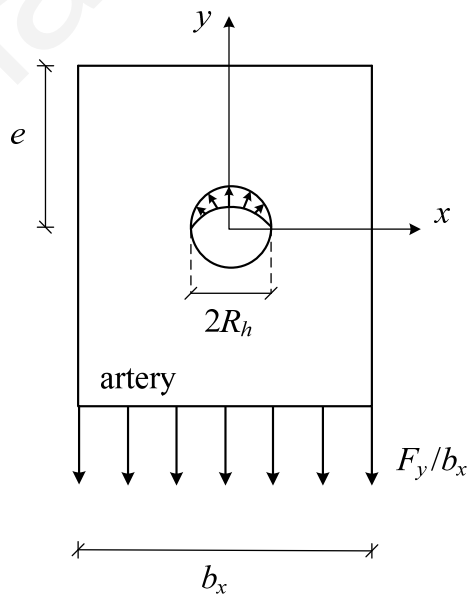

Figure 10-2: Geometry and loading of the pin-loaded hole problem [119].

The derived equations for the peak perpendicular and longitudinal stresses are expressed respectively as

$$\sigma_x = \frac{(4+\pi)F_y}{2R_h\pi^2}\left[2\left(\sqrt{\frac{E_x}{E_y}} - v_{yx}\frac{E_x}{E_y}\right) + \frac{E_x}{G_{xy}}\right]^{1/2} - \left(\frac{F_y}{2b_x} + \frac{3F_y}{2R_h\pi}\right)\sqrt{\frac{E_x}{E_y}} - v_{yx}\frac{E_x}{E_y}\frac{F_y}{2R_h\pi} \quad (10.1)$$

$$\sigma_y = \frac{\left(\frac{F_y}{2b_x} + \frac{2F_y}{R_h\pi^2}\right)\left[2\left(\sqrt{\frac{E_x}{E_y}} - v_{yx}\frac{E_x}{E_y}\right) + \frac{E_x}{G_{xy}}\right]^{1/2}}{\sqrt{\frac{E_x}{E_y}}} + \frac{F_y}{2b_x} \quad (10.2)$$

in which v_{xy} is the Poisson's ratio of the arterial tissue (0.5 for incompressible materials), G_{xy} is the shear modulus of elasticity, E_x and E_y are the perpendicular and longitudinal Young's modulus, respectively, and b_x is the width of the plate.

The problem parameters of the aforementioned expressions can be parallelized to the problem parameters of Chapters 7 and 8, according to Table 10-1, in order to be applied to the problem of end-to-end or end-to-side anastomosis, respectively.

Table 10-1: Parallelization of parameters of Echavarría et al. model to the parameters of end-to-end and end-to-side anastomosis models.

Echavarría et al. model	End-to-end anastomosis model	End-to-side anastomosis model
R_h	r_s	$d_r / 2$, $d_s / 2$
E_x	E_θ	circumferential Young's modulus
E_y	E_L	longitudinal Young's modulus
b_x	distance between sequential stitches	s
F_y	F_L / N_s	$\sigma_a^{local} s H_a$, $\sigma_a^{local} s H_g$

In conclusion, the use of Equations (10.1) and (10.2) provides a more refined solution to the stress-concentration problem at the stitching hole (embedding stresses), caused by the suture-artery interaction.

CHAPTER 11

Conclusions

11.1 Summary and conclusions

This dissertation focuses on the mathematical modeling of arterial anastomoses and their suture-line response. The mathematical formulation of the problem is carried out on the basis of dynamic analysis, suture-artery interaction, and different material constitutive laws. The aim of this dissertation is to investigate the response of different arterial anastomosis techniques in a general manner, develop closed-form expressions for the problem solution (wherever possible), and provide useful conclusions about the optimum suturing details and graft properties to prevent post-surgery complications.

Comprehensive failure criteria that account for short-term (immediately after the blood flow is restored) and long-term (weeks after the operation) anastomosis failure scenarios have been established. In particular, the suture may fail when its maximum tensile force f_s exceeds its tensile strength or the tensile strength of the deteriorated suture. Furthermore, the knots that bind the stitches together may fail (slip or relaxation of the knot) when the maximum tensile force of the suture exceeds the strength of the knot. Another failure mode is the rupture or injury of the blood vessel wall, caused when the embedding stresses σ_s, due to suture-wall contact interaction (at the stitching holes), exceed the limit value of wall shear strength. Moreover, high stress values promote the development of intimal hyperplasia at the suture line and cause the arterial wall to increase its cross-section. Another complication may be caused if the distance between the edges of the two anastomosed blood-vessels exceeds the typical size of a few red blood cells, leading to internal bleeding. Short-term blood leaking (immediately after the restoration of the blood flow) can be repaired by the surgeon, whereas long-term blood leaking may lead to thrombosis, weeks after the surgery. The established failure criteria can be utilized for the development of guidelines for vascular-anastomosis practice.

The far-field arterial response has been studied by assuming linear, hyperelastic, and viscoelastic material behaviors. The analysis of the linear arterial model demonstrated that arterial systems are characterized by high natural frequencies and that the smoother the pressure increase from zero to the peak systolic pressure is, the lower the peak radial displacement is, tending to become equal to the static displacement. By considering the

worst-case loading scenario (first cardiac cycle), the resulting response values have been found to be up to two times the static response values.

In regard to the hyperelastic arterial response, three different strain-energy functions corresponding to healthy (hardening behavior), atheromatic (exponential hardening behavior), and aneurysmatic (softening behavior) arteries, have been studied. In this way, the material strain-hardening effect on the dynamic response of arteries was revealed. The linear-elastic model appears to be a good approximation of the healthy artery response. Moreover, the linear-elastic model yields lower radial displacements than the aneurysmatic artery, whereas it does not approximate well the behavior of the atheromatic artery, due to the fact that the slope of its stress-strain curve is almost zero at low strains and becomes steeper at higher strains. We expect that a linear model with elasticity modulus equal to the tangent Young's modulus (of the nonlinear material law) corresponding to circumferential elongations 10%-20% will yield better approximations. As follows from this investigation, the arterial response depends on the increased hardening or softening behavior of the respective material stress-strain relationship.

The most important factors influencing the peak response of the hyperelastic models are found to be the longitudinal pre-stretch λ_z^0 and the normalized pressure. The normalized radial displacement decreases with increasing values of pre-stretch, implying that the gradual decrease of arterial strength, caused by aging, can be balanced by the decreased radial response (caused by the longitudinal pre-stretch). On the other hand, in old age the longitudinal pre-stretch is slightly decreased, causing an increase of the radial displacement, which cannot easily balance the low strength of the (aged) artery (Figure 5-28). Increased normalized pressure implies the existence of hypertension or soft (aneurysmatic) arterial tissue. In each case, the normalized pressure value is increased by a factor of 5/3 or 10, respectively, resulting in increased arterial response.

Important metrics, such as the radial deformation and the maximum energy density, are found to be influenced heavily by the strain-hardening characteristics of the model, as well as the longitudinal pre-stressing. It is worth noting that in some cases, the stress value is not an appropriate criterion for distinguishing the limit values of different systems, as opposed to the corresponding strain-energy density and displacement response, which are distinctive. Moreover, the normalized strain energy increases with increasing values of the absolute normalized displacement $\left|u_r / \mathrm{R}\right|$.

The analysis of the viscoelastic arterial model refined the results obtained from the analysis of the hyperelastic arterial model. Increased viscoelasticity burdens the cardiovascular system, due to increased energy loss during each cardiac cycle. The viscoelastic behavior was simulated by adopting a generalized Maxwell model and the sophisticated Bonet-Holzapfel approach. The resulting response is mainly affected by the relaxation time τ_1 and the free-energy parameter β_1^{∞}. Furthermore, two different loading approximations were considered, revealing the strong influence of the pressure time-profile approximation on the system response.

The first arterial pulse time-profile approximation analysis (Figure 6-4(b)), which constitutes a conservative scenario, showed that the system is characterized by high-frequency vibrations, and that an increase of the relaxation time τ_1 increases the values of the response time-histories. The second loading approximation analysis, in which the pressure is quasi-statically applied up to the diastolic pressure, demonstrated that the response is not always characterized by high-frequency vibrations, and that an increase of the relaxation time τ_1 results in a decrease of the response. In general, a decrease of the material parameter β_1^{∞} monotonically increases the normalized radial displacement.

Findings obtained from the suture-tissue interaction (displacement-based) analysis of the end-to-end anastomosis model demonstrated that the most influential parameter in drastically reducing the anastomotic gap, the (embedding) stresses at the arterial tissue, and the suture force, is the number of utilized stitches. Increased suture diameter reduces the embedding stress, whereas the influence of the ratio of suture-to-artery elastic modulus on the embedding stress and suture force is insignificant. Furthermore, the use of stiffer suturing material, larger suture diameter, and smaller stitch length reduce the anastomotic gap. In regard to the pre-tension of the suture, when the total pre-tension force is higher than the induced tensile arterial force ($F_L(t) \le \alpha N_s f_s^0$) and when the value of pre-tension f_s^0 exceeds a certain value (derived from $\alpha f_s^0 / 2 r_s H_p > \sigma_{s.u} / 2$) the arterial wall is likely to fail. On the other hand, for lower values of pre-tension and for $F_L(t) > \alpha N_s f_s^0$, the application of suture pre-tension can result in reducing the anastomotic gap, while not affecting considerably the embedding stress (which constitutes the critical response parameter), or the suture tensile force.

The end-to-side anastomosis stress-based analysis revealed that lower values of the graft-to-artery radii ratio R_g^o / R_a^o, the graft-to-artery thicknesses ratio H_g / H_a, and the ratio of

artery radius to artery thickness R_a^o / H_a, frequently decrease the stress-concentration factors (SCFs) at the junction. Furthermore, low values of anastomosis angle θ typically reduce the SCF. In general, for the suture-line response, when the distance between two sequential stitches is decreased (implying that the number of stitches is increased), or the stitch diameter/thickness is increased, the embedding stress and the gap created between the two blood vessels are decreased. In the case of the continuous stitching technique, when stronger sutures are used, the gap developed between the two blood vessels is decreased, and when the distance between two sequential stitches is increased, the suture tensile force is increased. In the case that pre-tension is applied to the suture, the knot strength, the suture tensile force, and the embedding stress are increased, whereas a gap between the two blood vessels will be formed only if the suture tensile force due to blood pressure exceeds the pre-tension value.

Finally, the effect of elastic mismatch on the response of end-to-side anastomosis, side-to-side anastomosis and artery patching has been investigated. By analyzing an idealized two-hinged circular model, it has been found that the elastic mismatch does not cause stress concentration at the anastomotic region. Elevated elastic mismatch reduces the radial displacements and strains of the graft, reduces the radial displacement at the junction, and causes large rotation angles at the junction. The incompatible angle at the junction may disturb the blood flow at the suture line, and thus promote the development of intimal hyperplasia. In order to minimize the rotation of the arterial cross-section, given that the graft is stiffer than the host artery, the graft thickness has to be decreased aiming to satisfy the equality $A^{\mathrm{I}}E^{\mathrm{I}} = A^{\mathrm{II}}E^{\mathrm{II}}$. Furthermore, the far-field stresses of the host artery and the graft are mainly affected by the thickness of each blood vessel. The far-field stresses of the two blood vessels are of the same magnitude as long as thicknesses are also of the same magnitude.

In the case of the patched artery, thinner patches demonstrate better behavior (smaller relative rotations at the junction). Increased elastic mismatch, causes large displacements of the arterial part that may lead to softening of the tissue and development of aneurysm after a long time period. Moreover, it is likely that the large rotation angle at the junction promotes (along with other parameters) the development of intimal hyperplasia, injury of the arterial tissue, and infection of the patched region.

In summary, the following practical techniques, leading to reduced displacements, rotations, and/or stresses at the suture line, are proposed for surgical application:

a) The number of stitches should be as high as possible (distance between sequential stitches as low as possible), minimizing the response values of Equations (7.15), (7.16), and (7.18) for the case of end-to-end anastomosis, or the response values of Equations (8.25) through (8.29) for the case of end-to-side anastomosis.
b) The suture or clip thickness should be as large as possible, minimizing the response values of Equations (7.15), and (7.18) for the case of end-to-end anastomosis, or the response values of Equations (8.25), (8.28), and (8.29) for the case of end-to-side anastomosis.
c) The pre-tension of the suture should be as low as possible, merely to secure the strength of the knot, reducing the response values of Equations (7.16) and (7.18) for the case of end-to-end anastomosis, or the response values of Equations (8.27) and (8.28) for the case of end-to-side anastomosis.
d) The stitch length should not be very long, minimizing the gap created between the two blood vessels as calculated by Equations (7.15) and (8.29) for the end-to-end anastomosis and the end-to-side anastomosis techniques, respectively.
e) The suture should have high elasticity modulus, when it is necessary to reduce the gap between the edges of the two blood vessels (Equations (7.15) and (8.29) for the end-to-end anastomosis and the end-to-side anastomosis techniques, respectively).
f) Ideally, the graft and the host artery should have the same elasticity modulus and the same thickness (side-to-side related anastomosis). If the graft is stiffer than the host artery, the graft thickness should be smaller than the artery thickness, minimizing the rotation at the junction as calculated by Equation (9.20).
g) In the case of end-to-side anastomosis, the anastomosis angle should be relatively low, reducing the SCFs of Equations (8.20) through (8.23).
h) For the end-to-side anastomosis technique, the graft radius should be smaller than the artery radius, reducing the SCFs of Equations (8.20) through (8.23), and the tensile force along the graft axis, calculated by Equation (8.16).
i) In the case of artery patching, given that the patch is stiffer than the artery, the patch width should be as small as possible, minimizing the rotation at the stitching region (Equation (9.42)).

In conclusion, the principal contribution of this dissertation lies in the development of fundamental analytical models to predict the far-field and suture-line behavior of arterial anastomoses. The mathematical formulation, together with the derived closed-form solutions for the suture-line response, reveals useful interrelations among the problem parameters, thus making the proposed model a valuable tool for the optimal selection of

materials and improved functionality of the sutures. By virtue of their generality and directness of application, the findings of this study can ultimately form the basis for the development of vascular anastomosis guidelines pertaining to the prevention of post-surgery complications.

11.2 Recommendations for future research

This dissertation studied the mechanics of arterial suturing by using strong simplifications, aiming to investigate the macroscopic response of the anastomotic region. The possibilities for further research through more enhanced models related to the arterial suturing problem are indeed great. Nevertheless, the researcher should keep in mind that for some problems simplicity is often better than sophistication.

Future research directions could potentially include the development of more sophisticated models in order to refine the results of the present study. Such models may consider the following: (a) elliptic geometry of the artery cross-section; (b) inhomogeneous arterial wall, by considering two (adventitia, media) or three arterial layers (adventitia, media, intimal); (c) anisotropic arterial tissue; (d) viscous blood flow; and (e) cardiac arrhythmia pressure time-profile.

References

1. Migliavacca F, Dubini G. Computational modeling of vascular anastomoses. Biomech. Model. Mechanobiol. 2005;3:235–50.
2. Haruguchi H, Teraoka S. Intimal hyperplasia and hemodynamic factors in arterial bypass and arteriovenous grafts: a review. J. Artif. Organs Off. J. Jpn. Soc. Artif. Organs. 2003;6:227–35.
3. Owida AA, Do H, Morsi YS. Numerical analysis of coronary artery bypass grafts: An over view. Comput. Methods Programs Biomed. 2012;108:689–705.
4. Ghista DN, Kabinejadian F. Coronary artery bypass grafting hemodynamics and anastomosis design: a biomedical engineering review. Biomed. Eng. OnLine. 2013;12:129.
5. Tiwari A, Cheng K-S, Salacinski H, Hamilton G, Seifalian AM. Improving the patency of vascular bypass grafts: the role of suture materials and surgical techniques on reducing anastomotic compliance mismatch. Eur. J. Vasc. Endovasc. Surg. Off. J. Eur. Soc. Vasc. Surg. 2003;25:287–95.
6. Paasche PE, Kinley CE, Dolan FG, Gozna ER, Marble AE. Consideration of suture line stresses in the selection of synthetic grafts for implantation. J. Biomech. 1973;6:253–9.
7. Melbin J, Ho PC. Stress reduction by geometric compliance matching at vascular graft anastomoses. Ann. Biomed. Eng. 1997;25:874–81.
8. Rachev A, Manoach E, Berry J, Moore Jr. J. A Model of Stress-induced Geometrical Remodeling of Vessel Segments Adjacent to Stents and Artery/Graft Anastomoses. J. Theor. Biol. 2000;206:429–43.
9. Hofer M, Rappitsch G, Perktold K, Trubel W, Schima H. Numerical study of wall mechanics and fluid dynamics in end-to-side anastomoses and correlation to intimal hyperplasia. J. Biomech. 1996;29:1297–308.
10. Ballyk PD, Walsh C, Butany J, Ojha M. Compliance mismatch may promote graft-artery intimal hyperplasia by altering suture-line stresses. J Biomech. 1998;31:229–37.

11. Leuprecht A, Perktold K, Prosi M, Berk T, Trubel W, Schima H. Numerical study of hemodynamics and wall mechanics in distal end-to-side anastomoses of bypass grafts. J Biomech. 2002;35:225–36.

12. Perktold K, Leuprecht A, Prosi M, Berk T, Czerny M, Trubel W, et al. Fluid Dynamics, Wall Mechanics, and Oxygen Transfer in Peripheral Bypass Anastomoses. Ann Biomed Eng. 2002;30:447–60.

13. Cacho F, Doblaré M, Holzapfel GA. A procedure to simulate coronary artery bypass graft surgery. Med. Biol. Eng. Comput. 2007;45:819–27.

14. Schiller NK, Franz T, Weerasekara NS, Zilla P, Reddy BD. A simple fluid–structure coupling algorithm for the study of the anastomotic mechanics of vascular grafts. Comput. Methods Biomech. Biomed. Engin. 2010;13:773–81.

15. Ngoepe MN, Reddy BD, Kahn D, Meyer C, Zilla P, Franz T. A Numerical Tool for the Coupled Mechanical Assessment of Anastomoses of PTFE Arterio-venous Access Grafts. Cardiovasc. Eng. Technol. 2011;2:160–72.

16. Lyman DJ, Fazzio FJ, Voorhees H, Robinson G, Albo D. Compliance as a factor effecting the patency of a copolyurethane vascular graft. J. Biomed. Mater. Res. 1978;12:337–45.

17. Hasson JE, Megerman J, Abbott WM. Increased compliance near vascular anastomoses. J. Vasc. Surg. 1985;2:419–23.

18. Hasson JE, Megerman J, Abbott WM. Suture technique and para-anastomotic compliance. J. Vasc. Surg. 1986;3:591–8.

19. Patel DJ, Janicki JS, Carew TE. Static Anisotropic Elastic Properties of the Aorta in Living Dogs. Circ. Res. 1969;25:765–79.

20. Abbott WM, Megerman J, Hasson JE, L'Italien G, Warnock DF. Effect of compliance mismatch on vascular graft patency. J. Vasc. Surg. 1987;5:376–82.

21. Ulrich M, Staalsen N-H, Djurhuus C., Christensen T., Nygaard H, Hasenkam J. In Vivo Analysis of Dynamic Tensile Stresses at Arterial End-to-end Anastomoses. Influence of Suture-line and Graft on Anastomotic Biomechanics. Eur. J. Vasc. Endovasc. Surg. 1999;18:515–22.

22. Baguneid MS, Goldner S, Fulford PE, Hamilton G, Walker MG, Seifalian AM. A comparison of para-anastomotic compliance profiles after vascular anastomosis: Nonpenetrating clips versus standard sutures. J. Vasc. Surg. 2001;33:812–20.

23. Bassiouny HS, White S, Glagov S, Choi E, Giddens DP, Zarins CK. Anastomotic intimal hyperplasia: mechanical injury or flow induced. J. Vasc. Surg. 1992;15:708–16; discussion 716–7.

24. Norberto JJ, Sidawy AN, Trad KS, Jones BA, Neville RF, Najjar SF, et al. The protective effect of vein cuffed anastomoses is not mechanical in origin. J. Vasc. Surg. 1995;21:558–66.

25. Noori N, Scherer R, Perktold K, Czerny M, Karner G, Trubel M, et al. Blood flow in distal end-to-side anastomoses with PTFE and a venous patch: results of an in vitro flow visualisation study. Eur. J. Vasc. Endovasc. Surg. 1999;18:191–200.

26. Vural KM, Sener E, Taşdemir O. Long-term patency of sequential and individual saphenous vein coronary bypass grafts. Eur. J. Cardiothorac. Surg. 2001;19:140–4.

27. Song Min-Ho, Tokuda Yoshiyuki, Ito Toshiaki. Revival of the side-to-side approach for distal coronary anastomosis. 2007;2:2.

28. Li H, Xie B, Gu C, Gao M, Zhang F, Wang J, et al. Distal end side-to-side anastomoses of sequential vein graft to small target coronary arteries improve intraoperative graft flow. BMC Cardiovasc. Disord. 2014;14:65.

29. Demiray H, Vito RP. On large periodic motions of arteries. J. Biomech. 1983;16:643–8.

30. Humphrey JD, Na S. Elastodynamics and Arterial Wall Stress. Ann. Biomed. Eng. 2002;30:509–23.

31. Kalita P, Schaefer R. Mechanical Models of Artery Walls. Arch. Comput. Methods Eng. 2008;15:1–36.

32. Westerhof N, Noordergraaf A. Arterial viscoelasticity: A generalized model. J. Biomech. 1970;3:371–9.

33. Cox RH. A model for the dynamic mechanical properties of arteries. J. Biomech. 1972;5:135–52.

34. Papageorgiou GL, Jones NB. Frequency response of the arterial wall. J. Biomed. Eng. 1988;10:231–6.

35. Holzapfel GA, Gasser TC. A viscoelastic model for fiber-reinforced composites at finite strains: Continuum basis, computational aspects and applications. Comput. Methods Appl. Mech. Eng. 2001;190:4379–403.

36. Holzapfel GA, Gasser TC, Stadler M. A structural model for the viscoelastic behavior of arterial walls: Continuum formulation and finite element analysis. Eur. J. Mech. - ASolids. 2002;21:441–63.

37. Haslach Jr HW. Nonlinear viscoelastic, thermodynamically consistent, models for biological soft tissue. Biomech. Model. Mechanobiol. 2005;3:172–89.

38. Čanić S, Hartley CJ, Rosenstrauch D, Tambača J, Guidoboni G, Mikelić A. Blood Flow in Compliant Arteries: An Effective Viscoelastic Reduced Model, Numerics, and Experimental Validation. Ann. Biomed. Eng. 2006;34:575–92.

39. Zhong L, Ghista DN, Ng EYK, Lim ST, Chua TSJ. Determination of Aortic Pressure-Time Profile,, along with Aortic Stiffness and Peripheral Resistance. J. Mech. Med. Biol. 2004;4:499–509.

40. Mills CJ, Gabe IT, Gault JH, Mason DT, Ross J, Braunwald E, et al. Pressure-flow relationships and vascular impedance in man. Cardiovasc. Res. 1970;4:405–17.

41. Rushmer RF. Cardiovascular dynamics. 3rd edition. W.B. Saunders; 1970.

42. Members AF, Mancia G, Fagard R, Narkiewicz K, Redon J, Zanchetti A, et al. 2013 ESH/ESC Guidelines for the management of arterial hypertension. Eur. Heart J. 2013;eht151.

43. Humphrey JD. Review Paper: Continuum biomechanics of soft biological tissues. Proc. R. Soc. Math. Phys. Eng. Sci. 2003;459:3–46.

44. Gozna ER, Marble AE, Shaw A, Holland JG. Age-related changes in the mechanics of the aorta and pulmonary artery of man. J. Appl. Physiol. 1974;36:407–11.

45. Holzapfel G, Gasser T, Ogden R. A New Constitutive Framework for Arterial Wall Mechanics and a Comparative Study of Material Models. J. Elast. 2000;61:1–48.

46. Wertheim G. Mémoire sur l'élasticité et la cohésion des principaux tissus du corps humain. Ann Chim Phys. 1847;21:385–414.

47. Mohan D, Melvin JW. Failure properties of passive human aortic tissue. II—Biaxial tension tests. J. Biomech. 1983;16:31–44.

48. Carew TE, Vaishnav RN, Patel DJ. Compressibility of the Arterial Wall. Circ. Res. 1968;23:61–8.

49. Rhodin JAG. Architecture of the vessel wall. Handb. Physiol. Sec 2 Cardiovasc. Syst. II Vasc. Smooth Muscle. American Physiological Society Bethesda, MD. John Wiley & Sons, Inc.; 1980.

50. Fung Y. Biodynamics: circulation. Springer-Verlag; 1984.

51. Mooney M. A Theory of Large Elastic Deformation. J. Appl. Phys. 1940;11:582–92.

52. Chadwick P. The existence and uniqueness of solutions to two problems in the Mooney-Rivlin theory for rubber. J. Elast. 1972;2:123–8.

53. Fung YC. Biomechanics: Mechanical Properties of Living Tissues. Springer; 1993.

54. Gent AN. A New Constitutive Relation for Rubber. Rubber Chem. Technol. 1996;69:59–61.

55. Skalak R, Tozeren A, Zarda RP, Chien S. Strain Energy Function of Red Blood Cell Membranes. Biophys. J. 1973;13:245–64.

56. Delfino A, Stergiopulos N, Moore Jr JE, Meister J-J. Residual strain effects on the stress field in a thick wall finite element model of the human carotid bifurcation. J. Biomech. 1997;30:777–86.

57. Alastrué V, Peña E, Martínez MÁ, Doblaré M. Assessing the Use of the "Opening Angle Method" to Enforce Residual Stresses in Patient-Specific Arteries. Ann. Biomed. Eng. 2007;35:1821–37.

58. Schanzer A, Messina L. Two Decades of Endovascular Abdominal Aortic Aneurysm Repair: Enormous Progress With Serious Lessons Learned. J. Am. Heart Assoc. 2012;1:e000075.

59. Paravastu SCV, Jayarajasingam R, Cottam R, Palfreyman SJ, Michaels JA, Thomas SM. Endovascular repair of abdominal aortic aneurysm. Cochrane Database Syst. Rev. 2014;1:CD004178.

60. Erickson KM, Cole DJ. Carotid artery disease: stenting vs endarterectomy. Br. J. Anaesth. 2010;105:i34–49.

61. Sfyroeras GS, Koutsiaris A, Karathanos C, Giannakopoulos A, Giannoukas AD. Clinical relevance and treatment of carotid stent fractures. J. Vasc. Surg. 2010;51:1280–5.

62. Kapadia MR, Popowich DA, Kibbe MR. Modified Prosthetic Vascular Conduits. Circulation. 2008;117:1873–82.

63. Lee S, Fung YC, Matsuda M, Xue H, Schneider D, Han K. The development of mechanical strength of surgically anastomosed arteries sutured with Dexon. J. Biomech. 1985;18:81–9.

64. Schajer GS, Green SI, Davis AP, Hsiang YN-H. Influence of Elastic Nonlinearity on Arterial Anastomotic Compliance. J. Biomech. Eng. 1996;118:445.

65. Shadwick RE. Mechanical design in arteries. J. Exp. Biol. 1999;202:3305–13.

66. Demetriou D. Dynamic response of sutures connecting human arteries and implications to vascular surgery operations. [Msc Thesis]. [Nicosia, Cyprus]: University of Cyprus; 2013.

67. MATLAB R2011b. Natick, Massachusetts: The MathWorks, Inc.; 2011.

68. Fung YC. Biomechanics: Motion, Flow, Stress, and Growth. New York: Springer; 1998.

69. Holzapfel GA, Sommer G, Gasser CT, Regitnig P. Determination of layer-specific mechanical properties of human coronary arteries with nonatherosclerotic intimal thickening and related constitutive modeling. Am. J. Physiol. - Heart Circ. Physiol. 2005;289:H2048–58.

70. Hariton I. Vascular Biomechanics: Functional Adaptation, Anisotropy and Seeds of Micromechanics [PhD Thesis]. [Beer-Sheva, Israel]: Ben Gurion University; 2007.

71. Shampine L, Reichelt M. The MATLAB ODE Suite. SIAM J. Sci. Comput. 1997;18:1–22.

72. Hatch MR. Vibration Simulation Using MATLAB and ANSYS. CRC Press; 2000.

73. Shampine LF. Implementation of Rosenbrock Methods. ACM Trans Math Softw. 1982;8:93–113.

74. Zedan H. Avoiding the exactness of the Jacobian matrix in Rosenbrock formulae. Comput. Math. Appl. 1990;19:83–9.

75. Hosea ME, Shampine LF. Analysis and implementation of TR-BDF2. Appl. Numer. Math. 1996;20:21–37.

76. Blatz PJ, Chu BM, Wayland H. On the Mechanical Behavior of Elastic Animal Tissue. Trans. Soc. Rheol. 1957-1977. 1969;13:83–102.

77. Chuong CJ, Fung YC. Three-Dimensional Stress Distribution in Arteries. J. Biomech. Eng. 1983;105:268–74.

78. Zafiropoulou VI. The contact mechanics of rubber materials: Analysis of penetration tests and applications to human arteries [PhD Thesis]. [Volos, Greece]: University of Thessaly; 2013.

79. Apter JT, Marquez E. Correlation of Visco-Elastic Properties of Large Arteries with Microscopic Structure V. Effects of Sinusoidal Forcings at Low and at Resonance Frequencies. Circ. Res. 1968;22:393–404.

80. Shah AD, Humphrey JD. Finite strain elastodynamics of intracranial saccular aneurysms. J. Biomech. 1999;32:593–9.

81. Bonet J. Large strain viscoelastic constitutive models. Int. J. Solids Struct. 2001;38:2953–68.

82. Taylor RL, Pister KS, Goudreau GL. Thermomechanical analysis of viscoelastic solids. Int. J. Numer. Methods Eng. 1970;2:45–59.

83. Newmark NM. A Method of Computation for Structural Dynamics. J. Eng. Mech. Div. 1959;85:67–94.

84. Géradin M, Rixen D. Mechanical Vibrations : Theory and Applications to Structural Dynamics. 2 edition. Chichester ; New York: Wiley; 1997.

85. Armentano RL, Barra JG, Levenson J, Simon A, Pichel RH. Arterial Wall Mechanics in Conscious Dogs Assessment of Viscous, Inertial, and Elastic Moduli to Characterize Aortic Wall Behavior. Circ. Res. 1995;76:468–78.

86. Veress AI, Vince DG, Anderson PM, Cornhill JF, Herderick EE, Klingensmith JD, et al. Vascular mechanics of the coronary artery. Z. Für Kardiologie. 2000;89:S092–100.

87. Van den Broek CN, van der Horst A, Rutten MCM, van de Vosse FN. A generic constitutive model for the passive porcine coronary artery. Biomech. Model. Mechanobiol. 2011;10:249–58.

88. Baumgartner N, Dobrin PB, Morasch M, Dong QS, Mrkvicka R. Influence of suture technique and suture material selection on the mechanics of end-to-end and end-to-side anastomoses. J Thor Cardiov Surg. 1996;111:1063–72.

89. Dobrin PB. Polypropylene suture stresses after closure of longitudinal arteriotomy. J. Vasc. Surg. 1988;7:423–8.

90. Brouwers J, Oosting D, D de H, Pj K. Dynamic loading of surgical knots. Surg. Gynecol. Obstet. 1991;173:443–8.

91. Seltmann M, Achenbach S, Muschiol G, Feyrer R. Suture-induced right coronary artery stenosis. J. Cardiovasc. Comput. Tomogr. 2010;4:215–7.

92. Salmon CG, Johnson EJ. Steel Structures–Design and Behavior Emphasizing Load and Resistance Factor Design. 4th Edition. Harper Collins; 1996.

93. Gozna ER, Marble AE, Shaw AJ, Winter DA. Mechanical properties of the ascending thoracic aorta of man. Cardiovasc. Res. 1973;7:261–5.

94. Marble AE, Sarwal SN, Watts KC, Kinley CE. A mathematical assessment of suture line stress in the end-to-side anastomosis--I. Steady flow. J. Biomech. 1979;12:941–4.

95. American Petroleum Institute. Recommended practice for planning, designing and constructing fixed offshore platforms. 1st edn. Washington D.C.: API RP2A-LRFD; 1993.

96. American Welding Society. Structural welding code-steel. 14th edn. Miami: ANSI/AWS; 1994.

97. Thubrikar MJ, Roskelley SK, Eppink RT. Study of stress concentration in the walls of the bovine coronary arterial branch. J. Biomech. 1990;23:15–26.

98. Lee CK, Chiew SP, Lie ST, Nguyen TBN. Fatigue study of partially overlapped circular hollow section K-joints. Part 1: Geometrical models and mesh generation. Eng. Fract. Mech. 2009;76:2445–63.

99. Shao Y-B, Du Z-F, Lie S-T. Prediction of hot spot stress distribution for tubular K-joints under basic loadings. J. Constr. Steel Res. 2009;65:2011–26.

100. Karamanos SA, Romeijn A, Wardenier J. Stress concentrations in tubular gap K-joints: mechanics and fatigue design. Eng. Struct. 2000;22:4–14.

101. Johnson KL. Contact Mechanics. Cambridge University Press; 1987.

102. Fett T, Mattheck C, Munz D. On the calculation of crack opening displacement from the stress intensity factor. Eng. Fract. Mech. 1987;27:697–715.

103. Berguer R, Higgins RF. Deterioration of grafts and prostheses. J. Cardiovasc. Surg. (Torino). 1976;17:493–501.

104. Klein SR GL. Effect of suture technique on arterial anastomotic compliance. Arch. Surg. 1982;117:45–7.

105. Li X-M, Rittgers SE. Computational simulation of biomechanics in e-PTFE and venous Miller's cuffs: implications for intimal hyperplasia. J. Med. Eng. Technol. 2005;29:187–96.

106. Love AEH. A Treatise on the mathematical theory of elasticity. 4th edition. New York, NY: Dover; 1944.

107. Rao SS. Vibration of Continuous Systems. John Wiley & Sons; 2007.

108. Kamenskiy AV, Pipinos II, Desyatova AS, Salkovskiy YE, Yu Kossovich L, Kirillova IV, et al. Finite element model of the patched human carotid. Vasc. Endovascular Surg. 2009;43:533–41.

109. Graff KF. Wave Motion in Elastic Solids. Courier Dover Publications; 1975.

110. Veletsos AS, Austin WJ, Pereia L, A C, Wung S-J. Free In-Plane Vibration of Circular Arches. J. Eng. Mech. Div. 1972;98:311–29.

111. Austin WJ, Veletsos AS. Free vibration of arches flexible in shear. J. Eng. Mech. Div. 1973;99:735–53.

112. Kamenskiy AV, MacTaggart JN, Pipinos II, Bikhchandani J, Dzenis YA. Three-Dimensional Geometry of the Human Carotid Artery. J. Biomech. Eng. 2012;134:064502–064502.

113. Liu Y, Wang S, Hu SJ, Qiu W. Mechanical analysis of end-to-end silk-sutured anastomosis for robot-assisted surgery. Int. J. Med. Robot. Comput. Assist. Surg. MRCAS. 2009;5:444–51.

114. Gu L, Kasavajhala ARM, Lang H, Hammel J. Numerical and Experimental Investigation of Vascular Suture Closure. Mech. Mater. Eng. Fac. Publ. [Internet]. 2012; Available from: http://digitalcommons.unl.edu/mechengfacpub/79

115. Rao AK. Elastic analysis of pin joints. Comput. Struct. 1978;9:125–44.

116. Zhang K, Ueng CES. Stresses around a pin-loaded hole in orthotropic plates with arbitrary loading direction. Compos. Struct. 1985;3:119–43.

117. Mangalgiri PD, Ramamurthy TS, Dattaguru B, Rao AK. Elastic analysis of pin joints in plates under some combined pin and plate loads. Int. J. Mech. Sci. 1987;29:577–85.

118. Liu C-S, Zhang K, Yang R. The FEM analysis and approximate model for cylindrical joints with clearances. Mech. Mach. Theory. 2007;42:183–97.

119. Echavarría C, Haller P, Salenikovich A. Analytical study of a pin–loaded hole in elastic orthotropic plates. Compos. Struct. 2007;79:107–12.

120. Aluko O, Whitworth HA. Analysis of stress distribution around pin loaded holes in orthotropic plates. Compos. Struct. 2008;86:308–13.

121. Noble B, Hussain MA. Exact solution of certain dual series for indentation and inclusion problems. Int. J. Eng. Sci. 1969;7:1149–61.

122. Pereira CM, Ramalho AL, Ambrósio JA. A critical overview of internal and external cylinder contact force models. Nonlinear Dyn. 2011;63:681–97.

Appendix A: Stress and strain tensors

The arterial tissue is an incompressible material. In this study the deformation and loading conditions are considered to be axis-symmetric and therefore only the principal stresses and strains exist. The deformation gradient is equal to

$$\mathbf{F} = \begin{pmatrix} \lambda_r & 0 & 0 \\ 0 & \lambda_\theta & 0 \\ 0 & 0 & \lambda_z \end{pmatrix} = \begin{pmatrix} \dfrac{1}{\lambda_\theta \lambda_z^0} & 0 & 0 \\ 0 & \lambda_\theta & 0 \\ 0 & 0 & \lambda_z^0 \end{pmatrix} \tag{A.1}$$

The right Cauchy-Green strain $\mathbf{C}$ and left Cauchy-Green strain $\mathbf{B}$ are identical because of the symmetry of the deformation gradient:

$$\mathbf{C} = \mathbf{F}^{\mathbf{T}}\mathbf{F} = \mathbf{F}\mathbf{F}^{\mathbf{T}} = \mathbf{B} = \begin{pmatrix} \dfrac{1}{\left(\lambda_\theta \lambda_z^0\right)^2} & 0 & 0 \\ 0 & (\lambda_\theta)^2 & 0 \\ 0 & 0 & (\lambda_z^0)^2 \end{pmatrix} \tag{A.2}$$

and the Green deformation is

$$\mathbf{e} = \frac{1}{2}(\mathbf{C} - \mathbf{I}) = \begin{pmatrix} \dfrac{1}{2}\left[\dfrac{1}{\left(\lambda_\theta \lambda_z^0\right)^2} - 1\right] & 0 & 0 \\ 0 & \dfrac{1}{2}\left[(\lambda_\theta)^2 - 1\right] & 0 \\ 0 & 0 & \dfrac{1}{2}\left[(\lambda_z^0)^2 - 1\right] \end{pmatrix} \tag{A.3}$$

The strain-energy density functions are usually expressed as a function of the principal invariants

$$W = f\left(I_1, I_2, ..\right) \tag{A.4}$$

and the Cauchy principal stresses are frequently expressed as

$$\boldsymbol{\sigma} = -\mathbf{P}\mathbf{I} + 2\mathbf{F}\frac{\partial \mathbf{W}}{\partial \mathbf{C}}\mathbf{F}^{\mathbf{T}} \tag{A.5}$$

Appendix B: Solution of artery/graft end-to-end anastomosis

This section presents the general solution of an end-to-end anastomosis between a host artery and a graft, each one having different geometrical and mechanical properties. The artery segment has length L_{pa}, radius R_{pa}, thickness H_{pa}, and Young's modulus in the longitudinal direction and circumferential direction E_{La} and $E_{\theta a}$, respectively, whereas the graft has length L_{pg}, radius R_{pg}, thickness H_{pg}, and Young's modulus in the longitudinal direction and circumferential direction E_{Lg} and $E_{\theta g}$, respectively (Figure (a)). Note that, if one or both blood vessels are not longitudinally pre-stressed, their geometric parameters will be equal to the that of the underformed state (e.g $H_{pa} = H_a$ and $H_{pg} = H_g$).

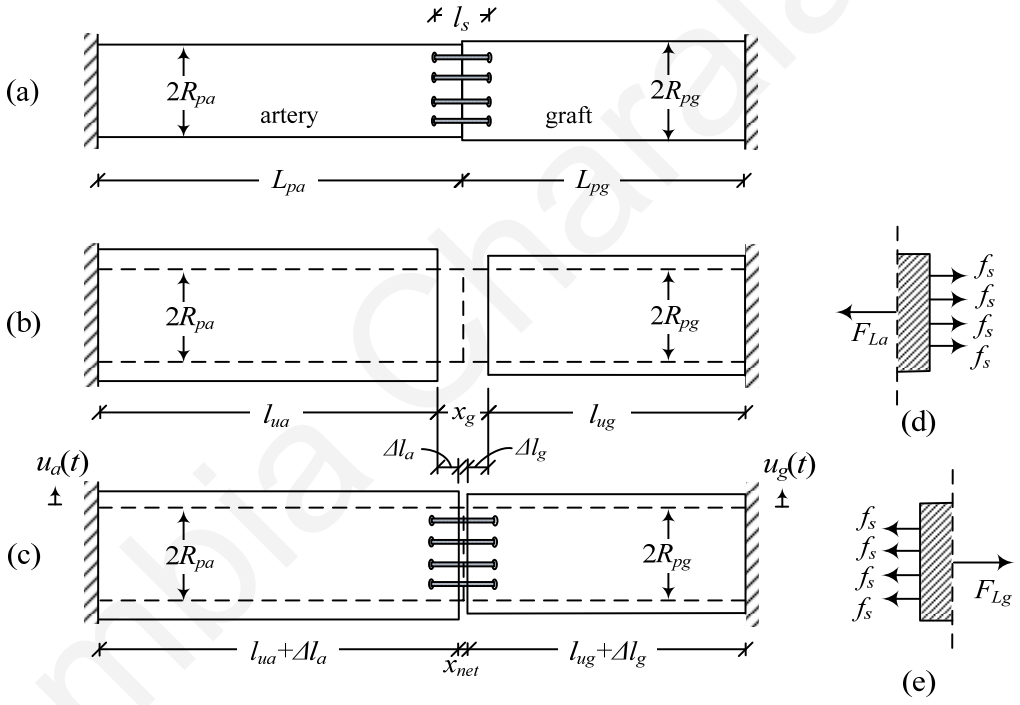

Figure B-1: Artery-graft end-to-end anastomosis analysis. (a) Anastomosis model (at-rest state); the artery and graft are clamped at the far ends and no pressure is transmitted at this stage since the artery is emptied from the blood, (b) unrestrained deformed state (without sutures); the blood volume is conserved, (c) deformed state of anastomotic region due to dynamic loading, (d) forces acting on end-element of artery segment, (e) forces acting on end-element of graft segment.

The conservation of the blood volume requires that the artery initial length L_{pa} decrease to l_{ua} and the graft initial length L_{pg} decrease to l_{ug} (Figure (b)) according to:

$$l_{ua} = \frac{L_{pa} {R_{pa}}^2}{(R_{pa} + u_a(t))^2} \tag{B.1}$$

$$l_{ug} = \frac{L_{pg} {R_{pg}}^2}{(R_{pg} + u_g(t))^2} \tag{B.2}$$

where u_a and u_g are the radial deformations of the artery and graft, respectively. Note that the graft has not initial radial displacement due to residual stresses. The gap developed in the unrestrained (without sutures) state of the artery is determined as

$$x_g(t) = L_{pa} + L_{pg} - l_{ua}(t) - l_{ug}(t) = L_{pa} + L_{pg} - \frac{L_{pa} {R_{pa}}^2}{(R_{pa} + u_a(t))^2} - \frac{L_{pg} {R_{pg}}^2}{(R_{pg} + u_g(t))^2} \tag{B.3}$$

Therefore, the resulting net gap developed in the restrained (with sutures) anastomotic region can be derived from

$$x_{net}(t) = x_g(t) - \Delta l_a(t) - \Delta l_g(t) \tag{B.4}$$

where Δl_a is the tensile deformation due to the artery/stitches interaction, and Δl_g is the tensile deformation due to the graft/stitches interaction (Figure (c)).

The tensile forces developed in the suture, arterial tissue, and graft are given respectively by

$$f_s(t) = A_s E_s \varepsilon_s(t) + f_s^0 = \frac{A_s E_s}{l_s} x_{net}(t) + f_s^0 \tag{B.5}$$

$$F_{La}(t) = 2\pi H_{pa} E_{L_a} \left(R_{pa} + u_a(t)\right) \frac{\Delta l_a(t)}{l_{ua}(t)} \tag{B.6}$$

$$F_{Lg}(t) = 2\pi H_{pg} E_{Lg} \left(R_{pg} + u_g(t)\right) \frac{\Delta l_g(t)}{l_{ug}(t)} \tag{B.7}$$

The unknown tensile deformations Δl_a and Δl_g can be derived from equilibrium of forces in the axial direction, $F_{La}(t) = F_{Lg}(t)$ and $F_{La}(t) = \alpha N_s f_s(t)$ (Figure (d,e)), yielding

$$\Delta l_a(t) = \frac{\alpha N_s f_s^0 + \alpha N_s A_s E_s \left\{ L_{pa} \left[1 - \frac{R_{pa}^{\ 2}}{\left(R_{pa} + u_a(t) \right)^2} \right] + L_{pg} \left[1 - \frac{R_{pg}^{\ 2}}{\left(R_{pg} + u_g(t) \right)^2} \right] \right\}}{\frac{2\pi E_{La} H_{pa}}{L_{pa} R_{pa}^{\ 2}} \left(R_{pa} + u_a(t) \right)^3 + \frac{\alpha N_s A_s E_s}{l_s} \left[1 + \frac{H_{pa} E_{La} L_{pg} R_{pg}^{\ 2} \left(R_{pa} + u_a(t) \right)^3}{H_{pg} E_{Lg} L_{pa} R_{pa}^{\ 2} \left(R_{pg} + u_g(t) \right)^3} \right]} \quad \text{(B.8)}$$

$$\Delta l_g(t) = \frac{H_{pa} E_{La} L_{pg} R_{pg}^{\ 2} \left(R_{pa} + u_a(t) \right)^3}{H_{pg} E_{Lg} L_{pa} R_{pa}^{\ 2} \left(R_{pg} + u_g(t) \right)^3} \Delta l_a(t) \quad \text{(B.9)}$$

Substituting Equations (B.3), (B.8) and (B.9) into Equation (B.4), we obtain the net gap between the anastomosed artery segments as

$$x_{net}(t) = \frac{2\pi E_{La} H_{pa} \left(R_{pa} + u_a(t) \right)^3 \left\{ L_{pa} \left[1 - \frac{R_{pa}^{\ 2}}{\left(R_{pa} + u_a(t) \right)^2} \right] + L_{pg} \left[1 - \frac{R_{pg}^{\ 2}}{\left(R_{pg} + u_g(t) \right)^2} \right] \right\}}{2\pi E_{La} H_{pa} \left(R_{pa} + u_a(t) \right)^3 + \frac{\alpha N_s A_s E_s L_{pa} R_{pa}^{\ 2}}{l_s} \left[1 + \frac{H_{pa} E_{La} L_{pg} R_{pg}^{\ 2} \left(R_{pa} + u_a(t) \right)^3}{H_{pg} E_{Lg} L_{pa} R_{pa}^{\ 2} \left(R_{pg} + u_g(t) \right)^3} \right]} \quad \text{(B.10)}$$
$$- \frac{\alpha N_s f_s^0 L_{pa} R_{pa}^{\ 2} \left[1 + \frac{H_{pa} E_{La} L_{pg} R_{pg}^{\ 2} \left(R_{pa} + u_a(t) \right)^3}{H_{pg} E_{Lg} L_{pa} R_{pa}^{\ 2} \left(R_{pg} + u_g(t) \right)^3} \right]}{2\pi E_{La} H_{pa} \left(R_{pa} + u_a(t) \right)^3 + \frac{\alpha N_s A_s E_s L_{pa} R_{pa}^{\ 2}}{l_s} \left[1 + \frac{H_{pa} E_{La} L_{pg} R_{pg}^{\ 2} \left(R_{pa} + u_a(t) \right)^3}{H_{pg} E_{Lg} L_{pa} R_{pa}^{\ 2} \left(R_{pg} + u_g(t) \right)^3} \right]}$$

Note that a gap across the anastomotic interface will be formed only if the tension developed in the arterial tissue exceeds the total suture pre-tension. The suture tensile force f_s developed in each stitch can be obtained from Equation (7.8). The embedding stresses induced on the arterial wall σ_{sa} and graft wall σ_{sg} must be compared to the strength of the artery $\sigma_{sa,u}$ and strength of the graft $\sigma_{sg,u}$, respectively:

$$\sigma_{sa}(t) = \frac{\alpha f_s(t)}{2 r_s H_{pa}} < \sigma_{sa,u} / 2 \quad \text{(B.11)}$$

$$\sigma_{sg}(t) = \frac{\alpha f_s(t)}{2 r_s H_{pg}} < \sigma_{sg,u} / 2 \quad \text{(B.12)}$$